frontiers | Research Topics

Climate-environment interactions under global warming, volume II

Edited by
Hainan Gong, Haipeng Yu, Zhiyuan Hu and Qinjian Jin

Published in
Frontiers in Environmental Science
Frontiers in Earth Science

ISSN 1664-8714
ISBN 978-2-8325-6087-7
DOI 10.3389/978-2-8325-6087-7

About Frontiers

Frontiers is more than just an open access publisher of scholarly articles: it is a pioneering approach to the world of academia, radically improving the way scholarly research is managed. The grand vision of Frontiers is a world where all people have an equal opportunity to seek, share and generate knowledge. Frontiers provides immediate and permanent online open access to all its publications, but this alone is not enough to realize our grand goals.

Frontiers journal series

The Frontiers journal series is a multi-tier and interdisciplinary set of open-access, online journals, promising a paradigm shift from the current review, selection and dissemination processes in academic publishing. All Frontiers journals are driven by researchers for researchers; therefore, they constitute a service to the scholarly community. At the same time, the *Frontiers journal series* operates on a revolutionary invention, the tiered publishing system, initially addressing specific communities of scholars, and gradually climbing up to broader public understanding, thus serving the interests of the lay society, too.

Dedication to quality

Each Frontiers article is a landmark of the highest quality, thanks to genuinely collaborative interactions between authors and review editors, who include some of the world's best academicians. Research must be certified by peers before entering a stream of knowledge that may eventually reach the public - and shape society; therefore, Frontiers only applies the most rigorous and unbiased reviews. Frontiers revolutionizes research publishing by freely delivering the most outstanding research, evaluated with no bias from both the academic and social point of view. By applying the most advanced information technologies, Frontiers is catapulting scholarly publishing into a new generation.

What are Frontiers Research Topics?

Frontiers Research Topics are very popular trademarks of the *Frontiers journals series*: they are collections of at least ten articles, all centered on a particular subject. With their unique mix of varied contributions from Original Research to Review Articles, Frontiers Research Topics unify the most influential researchers, the latest key findings and historical advances in a hot research area.

Find out more on how to host your own Frontiers Research Topic or contribute to one as an author by contacting the Frontiers editorial office: frontiersin.org/about/contact

Climate-environment interactions under global warming, volume II

Topic editors

Hainan Gong — Institute of Atmospheric Physics, Chinese Academy of Sciences (CAS), China

Haipeng Yu — Northwest Institute of Eco-Environment and Resources, Chinese Academy of Sciences (CAS), China

Zhiyuan Hu — Sun Yat-sen University, China

Qinjian Jin — University of Kansas, United States

Citation

Gong, H., Yu, H., Hu, Z., Jin, Q., eds. (2025). *Climate-environment interactions under global warming, volume II*. Lausanne: Frontiers Media SA.

doi: 10.3389/978-2-8325-6087-7

Table of contents

04 Spatiotemporal variations and trends of air quality in major cities in Guizhou
Fu Lu, Yang Yuan, Fu Hong and Liu Hao

21 Interdecadal variation of precipitation over Yunnan, China in summer and its possible causes
Zeyu Dong, Shu Gui, Ruowen Yang, Jinxin Cheng, Huan Yang and Ji Ma

35 Identifying the main drivers of the spatiotemporal variations in wetland methane emissions during 2001–2020
Yihan Hu, Xu Yue, Chenguang Tian, Hao Zhou, Weijie Fu, Xu Zhao, Yuan Zhao and Yuwen Chen

45 Research on the fugitive soil dust emission inventory in Western China based on wind erosion equation parameter optimization
Pengbo Wang, Min Chen, Weiming An, Yongle Liu and Feng Pan

63 Analysis of runoff variations in an arid catchment based on multi-model ensemble- a case study in the Tarim River Basin in Central Asia
Xiaoyu Gao, Gonghuan Fang, Yaning Chen and Xueqi Zhang

74 Historical global and regional spatiotemporal patterns in daily temperature
Md Adilur Rahim, Robert V. Rohli, Rubayet Bin Mostafiz, Nazla Bushra and Carol J. Friedland

86 Paulownia trees as a sustainable solution for CO_2 mitigation: assessing progress toward 2050 climate goals
Hesham S. Ghazzawy, Ahmed Bakr, Abdallah Tageldein Mansour and Mohamed Ashour

102 Research progress on the synergies between heat waves and canopy urban heat island and their driving factors
Tao Shi, Lei Liu, XiangCheng Wen and Ping Qi

113 Satellite-observed precipitation and total column water vapor
Sara E. A. Johnson, Hengchun Ye, Eric J. Fetzer and Jingjing Li

123 Comparative analysis of near-surface and surface urban heat islands in the Yangtze River Delta region
Xiao Shi, Ming Sun and Xiaochun Luo

frontiers | Frontiers in Environmental Science

TYPE Original Research
PUBLISHED 05 September 2023
DOI 10.3389/fenvs.2023.1254390

OPEN ACCESS

EDITED BY
Zhiyuan Hu,
Sun Yat-sen University, China

REVIEWED BY
Bo Hu,
Chinese Academy of Sciences (CAS), China
Zhang Xinmin,
Chinese Research Academy of Environmental Sciences, China

*CORRESPONDENCE
Yang Yuan,
gzhky_yy@163.com

RECEIVED 07 July 2023
ACCEPTED 21 August 2023
PUBLISHED 05 September 2023

CITATION
Lu F, Yuan Y, Hong F and Hao L (2023), Spatiotemporal variations and trends of air quality in major cities in Guizhou. *Front. Environ. Sci.* 11:1254390. doi: 10.3389/fenvs.2023.1254390

Spatiotemporal variations and trends of air quality in major cities in Guizhou

Fu Lu[1], Yang Yuan[2]*, Fu Hong[2] and Liu Hao[2]

[1]Guizhou Industry Polytechnic College, Guiyang, China, [2]Guizhou Research and Designing Institute of Environmental Sciences, Guizhou Academy of Environmental Science and Design, Guiyang, China

Tracking the evolution of air pollutants has a critical impact on our ability to further improve air quality, which have been extensively studied in the North China Plain (NCP), the Yangtze River Delta (YRD) and the Pearl River Delta (PRD) regions, but remain poorly characterized in Guizhou located in the east of Yunnan-Guizhou Plateau. Here, we analyzed spatiotemporal variations and trends of six criteria air pollutants, i.e., inhalable particles (PM_{10}), fine particle ($PM_{2.5}$), sulfur dioxide (SO_2), carbon monoxide (CO), nitrogen dioxide (NO_2) and ozone (O_3), from 2016 to 2020 in the focus major cities in Guizhou, taking advantage of the extensive network data available since 2016. The annual mean concentrations of the six criteria air pollutants were substantially lower than China's national ambient air quality standard (NAAQS-II), confirmed a significant improvement of air quality in Guizhou. The annual mean concentrations of PM_{10}, $PM_{2.5}$, SO_2, CO and NO_2 all decreased year by year during 2016–2020 in the focus major cities, and the highest decrease occurred in fall or winter. By contrast, O_3 increased with a rate ranged from 0.85 $\mu g \cdot m^{-3}$ yr^{-1} (95% CI: 0~1.78) to 3.71 $\mu g \cdot m^{-3}$ yr^{-1} (95% CI: 2.54~5.13), and the highest increase occurred in spring or summer, revealing a strong impetus for reducing O_3 pollution. Correlations among the six criteria air pollutants unveiled that the correlation coefficients between $PM_{2.5}$ and NO_2 were higher than those of between $PM_{2.5}$ and SO_2 in most focus major cities, mirroring a priority to control NO_x to further reduce $PM_{2.5}$ pollution in Guizhou. The focus of curbing O_3 pollution in Guizhou should be redesigned to mitigate multiple precursors from multiple sectors, and efficient control strategies to mitigate warm seasons O_3 pollution should also be implemented in cold seasons. Our results will benefit for our knowledge about current air pollution situation and police makers for future air pollution control in Guizhou.

KEYWORDS

air pollutants, air quality, $PM_{2.5}$, O_3, Guizhou

1 Introduction

Rising anthropogenic interferences for rapid and energy-intensive development in China has triggered a overwhelming quantities of tropospheric air pollutants (Hoesly et al., 2017), which not only impacts weather and climate (Guo et al., 2014) but weakens net primary productivity (Yue et al., 2017) and lowers Chinese urbanites' expressed happiness on social media (Zheng et al, 2019a), particularly in Beijing-Tianjin-Hebei (BTH), Sichuan Basin (SCB), Yangtze River Delta (YRD) and Pearl River Delta (PRD) regions (Lelieveld et al, 2015; Zhang et al., 2019a). Many epidemiological studies confirmed that both nonaccidental and cause-specific mortality have been associated with exposure to tropospheric air pollution (Burnett et al., 2018; Yin et al., 2020). A global atmospheric chemistry model estimated that

there were 2.5 million individuals in China die each year from the health effects of air pollution (Lim et al., 2012; Lelieveld et al., 2015).

Large-scale and long-lasting air pollution frequently descend on China. Since 2012, the China National Environmental Monitoring Center (CNEMC) network (http://106.37.208.233:20035/, last access: 03 November 2021) routinely measure levels of particulate matter measuring 10 μm (PM_{10}) and 2.5 μm ($PM_{2.5}$), sulfur dioxide (SO_2), nitrogen dioxide (NO_2), carbon monoxide (CO) and ozone (O_3) to improve our understanding of air pollution under different conditions and regions and help formulate more effective air pollution control strategies. According to monitoring results from 74 cities throughout China showed that the daily average concentrations of $PM_{2.5}$ exceeded the national ambient air quality standard of 75 ug m^{-3} for 69% of days in January in 2013, with a record-breaking daily concentration of 772 ug m^{-3} (Huang et al., 2014). High O_3 concentrations exceeding the national ambient air quality standards have frequently been observed in the aforementioned regions (Guo et al., 2017; Wang et al., 2017a). In response to the extremely severe and persistent haze pollution experienced by about 800 million people during the first quarter of 2013 (Huang et al., 2014), the Chinese government launched the Air Pollution Prevention and Control Action Plan (APPCAP, 2013–2017) to reduce anthropogenic emissions with a focus on the BTH, the YRD, and the PRD regions (www.gov.cn/zwgk/2013-09/12/content_2486773.htm, last access: 05 November 2021). The three metropolitan regions were required to reduce the five-year $PM_{2.5}$ concentrations by 25%, 20%, and 15%, respectively. The APPCAP launched a series of aggressive control measures including "ultralow" emission standard for power plants, strengthening industrial emission standards and phasing out outdated industrial capacity and so on. According to the evaluation of the effectiveness of the APPCAP, the national level of $PM_{2.5}$ exposure has dropped by 32% from 61.8 to 42.0 μg·m^{-3} in 5 years (Zhang et al., 2019b). In order to further reduce the $PM_{2.5}$ concentration, significantly improve the environmental air quality, and enhance the people's blue sky happiness, the State Council issued the three-year Action Plan for winning the battle to protect the blue sky (hereinafter referred to as the "Action Plan," 2018–2020) (http://www.gov.cn/zhengce/content/2018-07/03/content_ 5303158.htm, last access: 05 November 2021). The Action Plan proposed that by 2020, the concentration of $PM_{2.5}$ in cities below the prefecture level will decrease by more than 18%, and the total SO_2 and NO_x emissions will be reduced by more than 15%, respectively, compared with 2015. The Action Plan clarified five categories of measures, including optimizing industrial structure, adjusting energy structure, adjusting transportation structure, optimizing land use structure and implementing special actions (Zheng, et al., 2018a; Chu et al., 2020). Consequently, the total emission of major air pollutants and the number of days of heavy pollution in corresponding regions have been significantly reduced (Jiang et al., 2021), resulting in more blue-sky days (https://www.mee.gov.cn/ywdt/hjywnews/201607/t20160706_357205.shtml, last access: 06 November 2021). To further improve the country's ecological environment, the Communist Party of China Central Committee and the State Council jointly released a Circular on Further Promoting the Nationwide Battle to Prevent and Control Pollution (http://www.gov.cn/zhengce/2021-11/07/content_5649656.htm, last access: 06 November 2021). According to the circular, by 2025, in cities at or above the prefectural level, both the intensity of $PM_{2.5}$ and NO_x will be decreased by 10 percent and the growth trend of O_3 concentration will be effectively curbed. Success in controlling air pollution in China has changed the concentrations of air pollutants in China, decreasing the concentrations of CO, SO_2, NO_2, $PM_{2.5}$, and PM_{10} and increasing the concentrations of O_3 (Zheng, et al., 2018b; Li et al., 2019a; Li et al., 2019a; Zhang et al., 2019b; Guo et al., 2019; Wang et al., 2020b; Chu et al., 2020). From 2013 to 2018, the concentrations of PM_{10}, $PM_{2.5}$, SO_2, CO, and NO_2 decreased by 37%, 45%, 71%, 37%, and 19%, respectively, while O_3 increased by 17% (Chu et al., 2020), and the warm-season (April-September) daily maximum 8-h average (MDA8) O_3 levels increase by 2.4 ppb (5.0%) $year^{-1}$ from 2013 to 2019, with over 90% of the nationwide ozone monitoring sites showing positive trends and 30% with trends larger than 3.0 ppb·$year^{-1}$ (Lu et al., 2020), indicating a increasing photochemical pollution. To lessen particulate matter pollution, policies have focused on the reduction of primary emissions such as SO_2 and NO_x, while proposed efforts to reduce O_3 pollution target volatile organic compounds (VOCs) (Huang et al., 2020). However, efforts to reduce one pollutant can have perverse effects on others (Kulmala, 2015) and enhanced secondary pollution may offset reduction of primary emissions (Huang et al., 2020), hence further improvement of air quality depends upon a coordinated and balanced strategy for controlling multiple pollutants (Li et al., 2019c; Zhao et al., 2021).

Guizhou is located in Southwest China, bounded by 24°37′~29°13′N and 103°36′~109°35′E. The climate is diverse with an annual precipitation of 1,100–1,300 mm. The overall terrain is high in the southwest and low in the northeast. Most areas belong to the Karst Hilly landform of Yunnan Guizhou Plateau, and the cities and towns are basically distributed in the flat mountains. With the continuous advancement of urbanization in Central Guizhou, it is preliminarily predicted that by 2025, the new amount of NO_x, particulate matter and VOCs in Central Guizhou will increase by 9%, 11%, and 24%, respectively, compared with 2019 (https://sthj.guizhou.gov.cn/zwgk/zfxxgk1/fdzdgknr/tzgg/gggs_5619746/202111/t20211105_71562742.html, last access: 07 November 2021). The source structure of air pollutants will change from large and medium-sized industrial pollution sources in the past to a composite structure of industrial sources, living sources, mobile sources and dust sources. To address air pollution issues and protect public health, in recent years, the government, research institutions and universities have done the following efforts. By 2020, a total of 87 automatic air quality monitoring stations above the provincial level have been built in Central Guizhou, ensuring more than 2 automatic air quality monitoring stations in each county-level city, and forming a 6-index air quality monitoring system networked with the provincial level and covering all counties (districts and cities). The Guizhou Air Pollution Prevention and Control Action Plan (Guizhou_APPCAP, 2014–2017) (https://www.guizhou.gov.cn/zwgk/zcfg/szfwj/qff/201709/t20170925_70477126.html, last access: 08 November 2021) clarified that by 2017, the air quality in the province will be improved, the number of good days will increase year by year, and the concentration of PM_{10} will be reduced by more than 5% compared with that in 2012. The ambient air quality of Guiyang should be kept in the forefront of key cities in China. Guizhou Province's three-year Action Plan for winning the battle to protect the blue sky (hereinafter referred to as the Guizhou_Action Plan, 2018–2020) (https://www.guizhou.gov.cn/zwgk/zcfg/szfwj/qff/201809/t20180925_70477270.html, last access: 08 November 2021) clearly stipulated that by 2020, the total emissions of sulfur dioxide and nitrogen oxides in the province will be reduced by more than 7% respectively compared with 2015 and the main pollution

indicators such as $PM_{2.5}$ and PM_{10} have been effectively controlled. Since the implementation of Guizhou_APPCAP and Guizhou_ Action Plan, all departments have deeply implemented the relevant requirements, and the industrial structure, energy structure, transportation structure and land use structure have been continuously optimized and adjusted; Special actions have been carried out for the control of construction and road dust, the control of diesel truck pollution, the air pollution prevention and control of industrial enterprises, the comprehensive treatment of air pollution of industrial furnaces and kilns, the comprehensive treatment of VOCs in key industries, the treatment of loose burning coal and substitution of coal consumption reduction. These attempts has been highly effective in continuously improving air quality and further enhancing people's sense of blue sky in Guizhou. To reduce continuous flake air pollution in Central Guizhou, Guizhou Provincial Department of Ecological Environment issued the Plan for Joint Prevention and Control of Air Pollution in Central Guizhou Urban Agglomeration (https://sthj.guizhou.gov.cn/zwgk/zfxxgk1/fdzdgknr/tzgg/gggs_5619746/202111/t20211105_71562742.html, last access: 09 November 2021). According to the plan, by 2025, the average annual concentration of six indicators of urban ambient air in Central Guizhou will stably reach the secondary standard, and the aggravating trend of O_3 pollution will be effectively curbed. The ratio of excellent days in central cities is more than 95%, and that in county-level cities is more than 96.5%. In order to fight the tough battle against heavy pollution weather and O_3 pollution, it is important to fully understand the trends and variations of air pollutants.

Meeting the set targets, realizing the coordinated control of $PM_{2.5}$ and O_3, quantifying the impacts of different emission control policies on air quality and assessing the associations between exposure and human health will require a comprehensive understanding of the spatiotemporal variations and trends of conventional air pollutants in different regions. Compared with the increasing rich studies of spatiotemporal variability of air pollutants and assessing the impact of APPCAP and Action Plan on air quality trends on the national scale (Bai et al., 2020; Chu et al., 2020; Feng et al., 2019; Guo et al., 2019; Jiang et al., 2021; Kong et al., 2021a; Li et al., 2019b; Ma et al., 2019a; Sun et al., 2018; Wang et al., 2017a; Wanget al., 2020a; Zhang et al., 2019a; Zheng et al., 2018b) and in some key areas where photochemical smog pollution has become increasingly worse over recent decades (Bai et al., 2020; Bian et al., 2019; Chen et al., 2019a; Kong et al., 2021b; Li et al., 2020; Liu et al., 2021; Shi et al., 2019; Vu et al., 2019a; Wang et al., 2017b), a provincial long-term estimate of the surface concentrations of six air pollutants in Guizhou on an hourly scale are still lacking. To fill the blank, in this study, the spatiotemporal variations and trends of air quality and the correlations among air pollutants during 2016–2020 were studied based on the automatic monitoring data of air quality in Guizhou. To our knowledge, this study represents the first provincial estimate of air pollutants in Guizhou. The results of this study are of great significance for completing and advancing our understanding of air pollution and formulating accurate and effective air pollution prevention and control strategies.

2 Materials and methods

2.1 Monitoring network and data quality control

According to the requirements of ambient air quality standard (GB 3095-2012, https://www.mee.gov.cn/ywgz/fgbz/bz/bzwb/dqhjbh/dqhjzlbz/201203/t20120302_224165.shtml, last access: 09 November 2021) (hereinafter referred to as the new standard), the Guizhou Provincial Environmental Monitoring Central Station network, established by the Department of Ecology and Environment of Guizhou Province began measuring six air pollutants concentrations in Guizhou in 2016. The network includes 164 sites in 98 counties/districts, as visualized in Supplementary Figure S1. PM_{10}, $PM_{2.5}$, SO_2, NO_2, O_3 and CO are measured following the specifications and test procedures for ambient air quality continuous automated monitoring system released by the Ministry of Ecology and Environment of China (MEE) (HJ 653-2013, https://www.mee.gov.cn/ywgz/fgbz/bz/bzwb/jcffbz/201308/t20130802_256852.shtml, last access: 10 November 2021, and HJ 654-2013, https://www.mee.gov.cn/ywgz/fgbz/bz/bzwb/jcffbz/201308/t20130802_256853.htm, last access: 10 November 2021). Particulate matter concentrations are measured using β absorption and/or oscillating microbalance; SO_2 and NO_2 concentrations are measured by ultraviolet (UV) fluorescence and by a molybdenum converter and chemiluminescence, respectively; O_3 and CO concentrations are measured using UV and infrared absorption, respectively. In addition, both the gross domestic product (GDP) and permanent population at the year-end by region were obtained from the statistical yearbook compiled by the Guizhou Provincial Bureau of Statistics (http://stjj.guizhou.gov.cn/tjsj_35719/, last access: 10 November 2021). The possession of civil vehicles were obtained from the Vehicle Management Office of the Provincial Traffic Police Corps.

Data quality control has been applied to the hourly PM_{10}, $PM_{2.5}$, SO_2, NO_2, O_3 and CO measurements prior to further analysis because the presence of the outliers, due to instrument malfunctions, the influence of harsh environments and the limitation of measuring methods, may lead to unrealistic spatiotemporal variations. First, the raw observation data with zero or negative value were defined as missing (Chu et al., 2020; Shi et al., 2018). Second, the repeated values for no less than 3 times, which were likely to be duplicated by the reporting system of the monitoring network due to communication error, were also set as missing, except for the first value (Rohde and Muller, 2015; Chu et al., 2020). Third, the unreasonable extreme values were deleted following (Chu et al., 2020). Fourth, spatially and temporally inconsistent outliers and lower PM_{10} than $PM_{2.5}$ outliers were removed following (Wu et al., 2018). These procedures remove 7% of the hourly records. In addition, similar data quality control methods with (Lu et al., 2020) were also used here for trend analyses that can be sensitive to data outliers: For each year, there should be more than 60% of available hourly records. If not, all records of this year are removed from the analysis. For each site, we calculate the yearly mean levels of PM_{10}, $PM_{2.5}$, SO_2, NO_2, O_3 and CO (averaged over all available hourly records) for each year. Year with its mean value falls outside the 5-year mean values ±300% standard deviation range are removed from the analysis. These procedures removed 2% of the remaining hourly records.

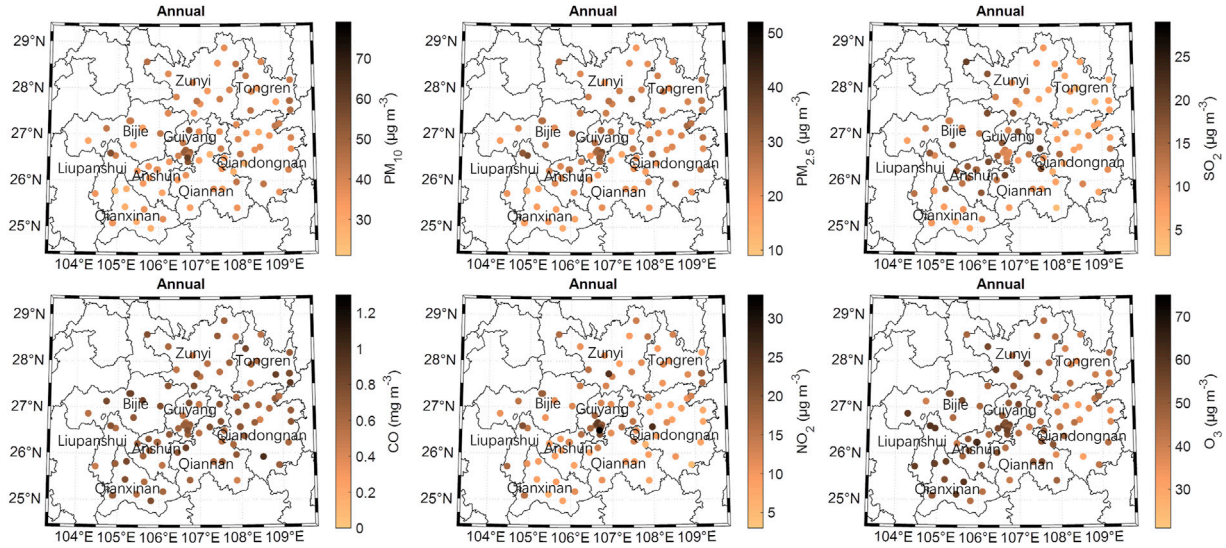

FIGURE 1
Spatiotemporal distributions of PM_{10}, $PM_{2.5}$, SO_2, CO, NO_2 and O_3 in Guizhou. The map was prepared in MATLAB R2019a using political boundaries from the Global Database of Administrative Areas.

2.2 Trend analyses using Theil–Sen estimator

In this study, for the trend analyses, the Theil-Sen method has been used, which has been implemented in the R "openair" package (Carslaw and Ropkins, 2012) and are freely available at https://cran.r-project.org/web/packages/openair/index.html (last access: 11 November 2021). Theil-Sen approach, which computes the slopes of all possible pairs of pollutant concentrations and takes the median value (Sen and Kumar, 1968; Theil, 1992), is typically used to determine trends in pollutant concentrations over several years (Lu et al., 2020; Olstrup et al., 2018; Pal and Masum, 2021; Vu et al., 2019b). The advantage of using the Theil-Sen estimator is that it tends to yield accurate confidence intervals, by selecting the median of the slopes, even with non-normal data and heteroscedasticity (Kong et al., 2021a; Lu et al., 2020; Vu et al., 2019a; Wu et al., 2018). The trend estimate, confidence intervals for the trend and significance level are estimated through bootstrap resampling. In our calculations, the trends were based on the deseasonalised monthly mean concentrations of PM_{10}, $PM_{2.5}$, SO_2, NO_2, O_3 and CO.

3 Results and discussions

3.1 Observed levels and spatial variability of six criteria pollutants in Guizhou

Figure 1 and Supplementary Figures S2–S7 show the PM_{10}, $PM_{2.5}$, SO_2, CO, NO_2 and O_3 values at all available sites for each year in 2015–2020. The observed levels of PM_{10}, $PM_{2.5}$, SO_2, CO, NO_2 and O_3 during 2016–2020 were on average 38.8 $\mu g \cdot m^{-3}$ [95% confidence interval (CI) of 37.4~41.2], 23.3 $\mu g \cdot m^{-3}$ (95% CI: 22.5~24.2), 10.5 $\mu g \cdot m^{-3}$ (95% CI: 9.6~11.3), 0.7 $mg \cdot m^{-3}$ (95% CI: 0.6~0.7), 13.2 $\mu g \cdot m^{-3}$ (95% CI: 13.1~14.2) and 47.2 $\mu g \cdot m^{-3}$ (95% CI: 45.8~48.6), respectively, which were significantly lower than those in BTH, SCB, YRD and PRD regions (Chu et al., 2020; Guo et al., 2019; Kong et al., 2021b; Li et al., 2019c; Wang et al., 2020a; Zhang et al., 2019a; Zheng et al., 2018a). The corresponding maxima of PM_{10}, $PM_{2.5}$, SO_2, CO, NO_2 and O_3 were 52.8 $\mu g \cdot m^{-3}$ (95% CI: 52.5~53.2), 27.1 $\mu g \cdot m^{-3}$ (95% CI: 27.0~27.3), 16.7 $\mu g \cdot m^{-3}$ (95% CI: 16.5~17.0), 0.8 $mg \cdot m^{-3}$ (95% CI: 0.7~0.8), 24.7 $\mu g\ m^{-3}$ (95% CI: 24.6~24.8) and 58.3 $\mu g \cdot m^{-3}$ (95% CI: 58.0~58.6), occurred in Tongren, Liupanshui, Qianan, Bijie, Zunyi and Anshun, respectively (Table 1). The mean concentrations of PM_{10}, SO_2, CO, NO_2 and O_3 were lower than China's national ambient air quality standard (NAAQS-I) (https://www.mee.gov.cn/ywgz/fgbz/bz/bzwb/dqhjbh/dqhjzlbz/201203/t20120302_224165.shtml, last access: 15 November 2021) of 40, 20, 4, 80, and 160 $\mu g \cdot m^{-3}$, respectively, whereas the level of $PM_{2.5}$ was still substantially higher than NAAQS-I of 15 $\mu g \cdot m^{-3}$ and the WHO guideline of 10 $\mu g \cdot m^{-3}$ (https://www.euro.who.int/en/health-topics/environment-and-health/air-quality, last access: 15 November 2021). The percentage of counties/districts with PM_{10}, $PM_{2.5}$, SO_2, CO, NO_2 and O_3 concentrations higher than 40, 15, 20, 4, 80 and 160 $\mu g \cdot m^{-3}$ were 36.7%, 100.0%, 0.0%, 0.0%, 0.0% and 0.0%, respectively. These results confirmed that Guizhou presented a cleaner atmospheric environment as a whole, compared with the cities in eastern and central China hit by serious air pollution caused by the development of urbanization and industrialization.

Contrasting spatial variations of O_3 and the others in Guizhou from 2016 to 2020 were observed (Supplementary Figures S2–S7), which was similar to what has been reported in previous studies conducted in eastern and southern China (Bian et al., 2019; Chen et al., 2019b; Chu et al., 2020; Guo et al., 2019; Li et al., 2019a; Zhang et al., 2019a). During 2016–2020, the spatial distribution shrunk for the high values of PM_{10}, $PM_{2.5}$, SO_2, CO and NO_2, while the scope of O_3 pollution expanded, and demonstrated a lower spatial heterogeneity than that of the others, which were attributed the success to the reduced anthropogenic emissions and the nonexistence of tailored control measures for O_3 in current

TABLE 1 Statistics for the annual-average concentrations of criteria pollutants in the nine major cities in Guizhou.

Central cities	PM_{10} (μg·m^{-3})	$PM_{2.5}$ (μg·m^{-3})	SO_2 (μg·m^{-3})	CO (mg·m^{-3})	NO_2 (μg·m^{-3})	O_3 (μg·m^{-3})
Guiyang	46.4 (95% CI: 46.2~46.7)	26.8 (95% CI: 26.6~27.0)	10.7 (95% CI: 10.6~10.8)	0.6 (95% CI: 0.6~0.6)	22.5 (95% CI: 22.4~22.6)	50.0 (95% CI: 49.7~50.3)
Zunyi	42.2 (95% CI: 41.9~42.4)	25.6 (95% CI: 25.4~25.8)	10.9 (95% CI: 10.8~11.0)	0.7 (95% CI: 0.7~0.7)	24.7 (95% CI: 24.6~24.8)	44.8 (95% CI: 44.5~45.1)
Liupanshui	45.3 (95% CI: 45.0~45.5)	27.1 (95% CI: 27.0~27.3)	14.8 (95% CI: 14.7~14.9)	0.7 (95% CI: 0.7~0.7)	20.2 (95% CI: 20.0~20.3)	56.1 (95% CI: 55.9~56.3)
Anshun	32.3 (95% CI: 32.1~32.6)	23.5 (95% CI: 23.3~23.6)	16.4 (95% CI: 16.2~16.5)	0.6 (95% CI: 0.6~0.6)	12.7 (95% CI: 12.6~12.7)	58.3 (95% CI: 58.0~58.6)
Bijie	39.0 (95% CI: 38.7~39.3)	25.3 (95% CI: 25.1~25.5)	10.5 (95% CI: 10.4~10.6)	0.8 (95% CI: 0.7~0.8)	18.7 (95% CI: 18.6~18.8)	51.8 (95% CI: 51.6~52.2)
Tongren	52.8 (95% CI: 52.5~53.2)	24.6 (95% CI: 24.3~24.8)	7.7 (95% CI: 7.6~7.9)	0.8 (95% CI: 0.8~0.8)	18.2 (95% CI: 18.1~18.4)	42.5 (95% CI: 42.2~42.8)
Qiandongnan	37.7 (95% CI: 37.4~38.0)	25.9 (95% CI: 25.7~26.1)	13.3 (95% CI: 13.1~13.5)	0.7 (95% CI: 0.7~0.7)	21.3 (95% CI: 21.1~21.4)	44.7 (95% CI: 44.4~45.0)
Qianxinan	31.2 (95% CI: 31.0~31.3)	16.4 (95% CI: 16.3~16.6)	7.7 (95% CI: 7.6~7.8)	0.7 (95% CI: 0.6~0.7)	14.9 (95% CI: 14.7~15.0)	45.3 (95% CI: 45.0~45.5)
Qiannan	32.7 (95% CI: 32.5~33.0)	20.4 (95% CI: 20.3~20.6)	16.7 (95% CI: 16.5~17.0)	0.6 (95% CI: 0.5~0.6)	13.4 (95% CI: 13.3~13.5)	47.6 (95% CI: 47.3~47.9)

policies. The increasing spatial distribution of O_3 pollution coincided with the decreasing spatial distribution of $PM_{2.5}$ pollution. This coincidence was largely attributable to the model simulations results that the decrease in $PM_{2.5}$ could drive the increase in O_3 because $PM_{2.5}$ scavenges hydroperoxy (HO_2) and NO_x radicals that would otherwise produce O_3 (Li et al., 2019c). Ground-based observation also showed that when the concentrations of $PM_{2.5}$ were less than 100 μg·m^{-3}, O_3 concentrations rapidly increased with the decrease in $PM_{2.5}$ concentrations (Tie et al., 2019). Spatially, the high values of PM_{10} and $PM_{2.5}$ appeared in Guiyang and Liupanshui (Supplementary Figures S2, S3), whereas SO_2 and NO_2 occurred in Guiyang and its neighbouring areas (Supplementary Figures S4, S6), which could be accounted for by the facts that Guiyang and its neighbouring areas concentrated 46% of the province's population, produced 61% of the province's total economic output and distributed 53% of the province's industrial parks, and industrial coal consumption accounted for 42% of theprovince's total coal consumption (https://sthj.guizhou.gov.cn/xwzx/tzgg/202111/t20211105_77740934.html, last access: 09 November 2021). The basic situation of heavy industrial structure, coal energy structure, and highway transportation structure has not been fundamentally changed in Guiyang and its neighbouring areas, and the problem of structural pollution needs further breakthroughs. In contrast, the high value of CO was widely distributed in inter-provincial border areas (Supplementary Figure S5), demonstrating that it is necessary to implement cross-provincial joint prevention and control measures of air pollution. Distinct exacerbation of O_3 pollution can be seen from 2016 to 2020 (Supplementary Figure S7). In 2016, the high value of O_3 was concentrated in Guiyang and its neighbouring areas. Since 2017, O_3 hot spots extended northwestward to Bijie and Liupanshui, and southwestward to Anshun and Qianxinan. In addition, smaller hotspots of O_3 pollution were observed in Zunyi and Tongren. The spatial evolution of O_3 pollution suggested that only from a regional perspective will Guizhou decrease O_3 pollution.

3.2 Diurnal variability of targeted pollutants in the nine major cities in Guizhou

Air pollutants display diurnal variations due to the diurnal cycles of their influencing factors including meteorological conditions, sources and sinks (Lin et al., 2011; Su et al., 2017). Diurnal regulations of air pollutants were adopted in some regions in China although ongoing research has documented that positive or negative impacts of diurnal regulation approach on air pollutants concentrations were both found at the city level (Wu et al., 2021). Supplementary Figure S8 depicts the annual average diurnal cycles of six criteria pollutants measured from 2016 to 2020 in Guiyang, Zunyi, Liupanshui, Anshun, Bijie, Tongren, Qiandongnan, Qianxinan and Qiannan. Generally, the diurnal variation patterns of PM_{10}, $PM_{2.5}$, SO_2, CO and NO_2 seemed fairly synchronous, while that of O_3 reversed, which was also observed in Wuqing (Xu et al., 2011), Beijing (Lin et al., 2011) and Nanjing (Ding et al., 2013a). It is apparent that the averages of PM_{10}, $PM_{2.5}$, SO_2, CO and NO_2 levels between 2016 and 2018 were higher than that between 2019 and 2020, while the opposite was true for O_3. Also it is noteworthy that the peak time for O_3 levels has slightly delayed. Additionally, different nighttime-afternoon differences of the six criteria pollutants occurred in the nine major cities.

Specifically, pronounced diurnal variation of $PM_{2.5}$ was observed in the nine major cities, with an obvious morning peak at around 09:00 to 11:00 (Beijing Time) and an afternoon valley between 14:00 and 16:00. This diurnal pattern was also observed in Beijing (Liu et al., 2015a), Shenyang, Chongqing, Lhasa, Dinghu, Gongga mountain (Liu et al., 2018), Lushan and Changde (Wang et al., 2015). The morning and evening peaks were contributed to by

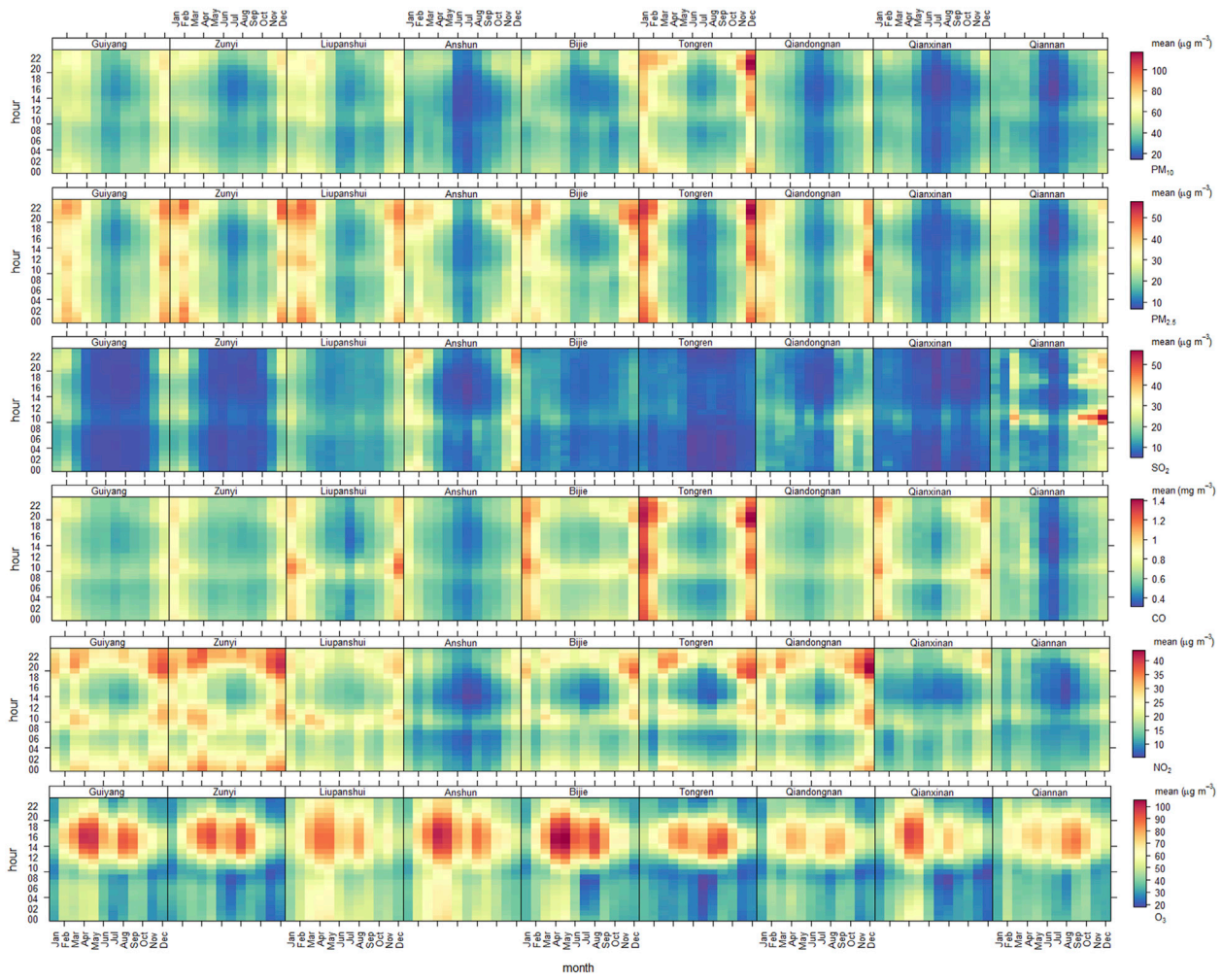

FIGURE 2
Monthly average diurnal cycles of criteria pollutants measured from 2016 to 2020 in Guiyang, Zunyi, Liupanshui, Anshun, Bijie, Tongren, Qiandongnan, Qianxinan and Qiannan.

enhanced anthropogenic activity during rush hour, and the afternoon valley was mainly due to a higher atmospheric mixing layer, which is beneficial for air pollution diffusion (Liu et al., 2018; Liu et al., 2015b). The diurnal variation in PM_{10} concentrations was similar to that of $PM_{2.5}$ in the nine major cities. The SO_2, CO and NO_2 concentrations showed similar diurnal patterns with elevated concentration during the night, a peak at around 08:00 to 10:00, and a broad valley in the afternoon. The morning peak was consistent with the rush hour emissions (Hao et al., 2000) and the large nighttime-afternoon differences should be mainly due to larger emissions from heating in combination with stronger temperature inversion during the nighttime (Lin et al., 2011). The diurnal variability of O_3 concentrations were opposite to the PM_{10}, $PM_{2.5}$, SO_2, CO and NO_2 concentrations, being lowest in the morning and reaching a peak in the afternoon when the photochemical reactions are more intense due to the higher temperature and stronger solar radiation (Shi et al., 2019; Tang et al., 2012). Similar diurnal patterns were also observed for the surface O_3 in Beijing (Tang et al., 2009; Tang et al., 2012; Wang et al., 2014a), Tianjin (Wang et al., 2014b), Hong Kong (Guo et al., 2013), Nanjing (Ding et al., 2013b). The lowest O_3 concentration during the rush-hours in the morning was mainly caused by the strong destruction of O_3 by chemical titration of NO owing to higher NO_x emissions (Lin et al., 2011; Lin et al., 2009; Lin et al., 2008).

For each month the average diurnal variations of six criteria pollutants were calculated from the hourly mean values in the corresponding month. Figure 2 shows the monthly average diurnal cycles of criteria pollutants measured from 2016 to 2020 in Guiyang, Zunyi, Liupanshui, Anshun, Bijie, Tongren, Qiandongnan, Qianxinan and Qiannan. As can be seen in Figure 2, the diurnal variations of PM_{10} and $PM_{2.5}$ were much more significant in winter than those in other seasons in the nine major cities. The summer-winter difference of the average diurnal amplitude in the PM_{10} concentration was by far not as large as that in the $PM_{2.5}$ concentration in the nine major cities. The seasonal average diurnal variations of PM_{10} and $PM_{2.5}$ in Qianxinan and Qianan were much less significant than in other cities. The monthly average diurnal cycles of SO_2 was much less significant compared with other pollutans, particularly in Bijie, Tongren and Qianxinan. The concentrations of O_3 precursors CO and NO_2 at night in winter

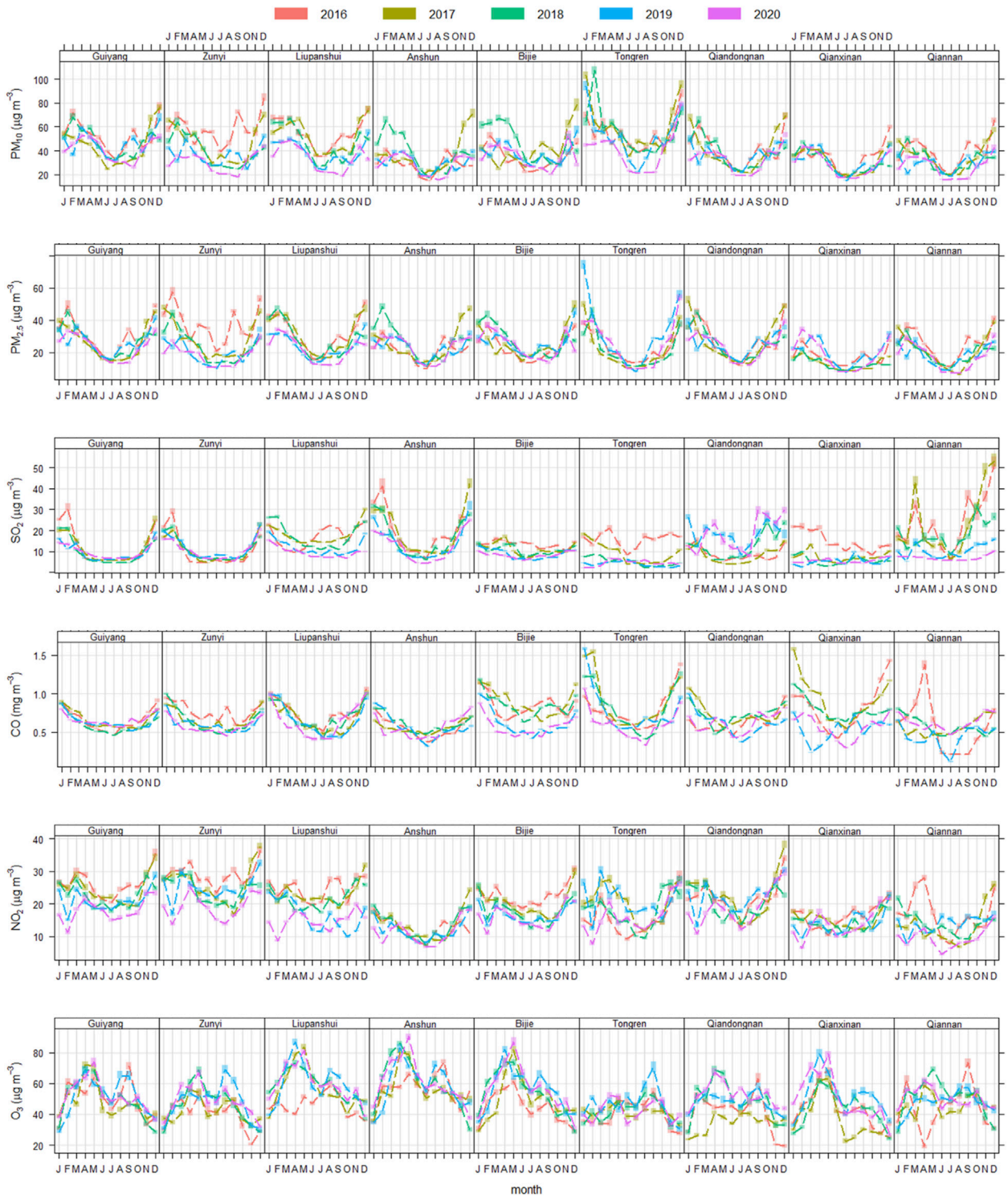

FIGURE 3
Seasonal variations of criteria pollutants measured from 2016 to 2020 in Guiyang, Zunyi, Liupanshui, Anshun, Bijie, Tongren, Qiandongnan, Qianxinan and Qiannan. The shading shows the 95 % confidence intervals of the average.

stayed at high levels, which might be resulted from larger emission from heating, in combined with strong temperature inversion and stable condition (Lin et al., 2009). The highest average diurnal amplitude for NO_2 appeared in Guiyang, Zunyi, Tongren and Qiandongnan, and the lowest average diurnal amplitude appeared in Anshun and Qianan. In contrast with the primary pollutants, the secondary pollutant O_3 showed a reverse seasonal average diurnal pattern with the highest average diurnal amplitude appearing in spring (particularly in April and May) and summer (particularly in August and September), and the lowest amplitude

appearing in winter (particularly in December and January), which was consistent with results observed in Beijing-Tianjin-Hebei region, Yangtze River Delta, Pearl River Delta, Chengdu-Chongqing region and the Fenhe-Weihe River Plain urban agglomeration (China's Air Ozone Pollution Prevention and Control Blue Book (2020): https://mp.weixin.qq.com/s/y9CJhur7v18aBhYcOTvgQA). It is worth noting that the durations of the high value interval of the seasonal average diurnal variation in O_3 concentrations in Guiyang, Zunyi, Anshun and Bijie were longer than that in other cities, and the higher the O_3 maximum was, the longer its duration was. Also As shown in Figure 2, the daily variation in the O_3 concentration was usually continuous. The change from high concentration to low concentration, or from low concentration to high concentration, was often a gradual process rather than a sudden change, which was consistent with prior study based on O_3 concentrations in 338 cities from 1 January 2016, to 28 February 2019 in China at a city level (Yang et al., 2020).

3.3 Seasonal behaviors of six criteria pollutants in the nine major cities in Guizhou

Criteria pollutants concentrations usually exhibit different seasonality in different regions owing to the differences of chemical processes, evolution of emission sources and meteorological conditions. Figure 3 illustrates the seasonal variations of criteria pollutants measured from 2016 to 2020 in Guiyang, Zunyi, Liupanshui, Anshun, Bijie, Tongren, Qiandongnan, Qianxinan and Qiannan. The six criteria pollutants showed well-defined seasonal patterns but also some unique month-to-month variations in different year. Overall, for PM_{10}, $PM_{2.5}$, SO_2, CO and NO_2, seasonal patterns looked similar, with the highest levels appearing in winter and the lowest levels appearing in summer. In contrast with the PM_{10}, $PM_{2.5}$, SO_2, CO and NO_2, O_3 concentrations showed a reverse seasonal pattern, with lower concentrations in winter and higher concentrations in late spring and early autumn in the nine major cities.

Both the PM_{10} and $PM_{2.5}$ concentrations exhibited an overall well-defined seasonal pattern with a maximum in winter (November or February) and a minimum in summer in all central cities. The observed winter peaks of PM_{10} and $PM_{2.5}$ can be attributed to the increased anthropogenic emissions related to enhanced power generation, industrial activities, fossil fuel burning for heating purposes (Li et al., 2017) and unfavourable meteorological conditions (Kong et al., 2021a). The observed summer valleys of PM_{10} and $PM_{2.5}$ can be attributed to the low emission rate and intense mixing processes (Kong et al., 2021b). The SO_2, CO and NO_2 concentrations exhibited a profound seasonal cycle but also some unique month-to-month variation patterns in different city in different year. These seasonal variations of SO_2, CO and NO_2 have been studied by previous authors in the western Yangtze River Delta during August 2011-July 2012 (Ding et al., 2013a). These seasonal and month-to-month variation patterns could be due to the change of anthropogenic emissions and atmospheric conditions in different seasons and months. O_3 showed a distinguished seasonal pattern, with two peaks in late spring and early autumn (a maximum in April or May and a secondary maximum in August or September) and a minimum in winter. Specifically, the highest O_3 level in April or May appeared in Liupanshui, Anshun, Bijie and Qianxinan, and in August or September appeared in Tongren, while the two peaks in Guiyang, Zunyi, Qiandongnan and Qiannan were basically the same. The observed valleys of O_3 in winter can be attributed to lower vertical mixing due to lower planetary boundary layer heights, stronger titration by NO_x due to higher emissions related to heating and lower photochemical production due to lower temperature and solar radiation (Tang et al., 2012). The observed peaks of O_3 in late spring and early autumn could be due to the large emissions of local and regional O_3 precursor and related meteorological variables (Ding et al., 2008; Wang et al., 2008). Given that summer (June, July and August) had the highest temperature predicted by Gaussian process regression method (He et al., 2021), higher O_3 concentrations were expected in this season. Therefore, the fact that the O_3 concentration in summer was much lower than that in late spring and early autumn is of great interest. The observed seasonal behavior of O_3 in the nine major cities in Guizhou was different from what has been reported in previous studies conducted in PRD region (China's Air Ozone Pollution Prevention and Control Blue Book (2020): https://mp.weixin.qq.com/s/y9CJhur7v18aBhYcOTvgQA). For instance, a summer minimum of O_3 was recorded at Hong Kong in southern China (Wang et al., 2009) and an early summer broad maximum was reported in Beijing (Lin et al., 2009; Lin et al., 2008). Available observations from either surface measurement at Lin'an (Xu et al., 2008) and satellite retrievals at Shanghai (Dufour et al., 2010) in the YRD region also suggested a later spring (May) maximum and early autumn (September) secondary maximum of O_3, which was attributed to the summer minimum of O_3 associated with the Asian summer monsoon that brings clean air masses from the Pacific during summer.

3.4 Trends of six criteria pollutants in the nine major cities in Guizhou

Air pollutants concentrations changed markedly and contrasting trends of all primary pollutants (PM_{10}, $PM_{2.5}$, SO_2, CO and NO_2) and secondary pollutant O_3 concentrations were observed in Guizhou from 2016 to 2020 (Figure 4), which were decoupling from gross domestic product, population and vehicles growth (Supplementary Figure S9). For PM_{10}, the average trends for the focus central cities were $-1.58\ \mu g{\cdot}m^{-3}\ yr^{-1}$ (95% CI: -2.57~-0.49) for Guiyang, $-6.16\ \mu g{\cdot}m^{-3}\ yr^{-1}$ (95% CI: -7.37~-4.68) for Zunyi, $-5.41\ \mu g{\cdot}m^{-3}\ yr^{-1}$ (95% CI: -6.35~-4.59) for Liupanshui, $0.11\ \mu g{\cdot}m^{-3}\ yr^{-1}$ (95% CI: -1.12~1.11) for Anshun, $-0.11\ \mu g{\cdot}m^{-3}\ yr^{-1}$ (95% CI: -1.85~1.5) for Bijie, $-4.54\ \mu g{\cdot}m^{-3}\ yr^{-1}$ (95% CI: -6.03~-2.73) for Tongren, $-1.82\ \mu g{\cdot}m^{-3}\ yr^{-1}$ (95% CI: -2.97~-0.63) for Qiandongnan, $-0.94\ \mu g{\cdot}m^{-3}\ yr^{-1}$ (95% CI: -1.51~-0.38) for Qianxinan, and $-2.81\ \mu g{\cdot}m^{-3}\ yr^{-1}$ (95% CI: -3.76~-2.07) for Qiannan. The highest decrease in $PM_{2.5}$ was observed in Zunyi, with a average value of $-4.22\ \mu g{\cdot}m^{-3}\ yr^{-1}$ (95% CI: -5.21~-3.12); the reductions in Guiyang, Liupanshui, qiandongnan and Qiannan were $-0.99\ \mu g{\cdot}m^{-3}\ yr^{-1}$ (95% CI: -1.88~-0.43), $-2.53\ \mu g{\cdot}m^{-3}\ yr^{-1}$ (95% CI: -3.26~-1.93), $-0.74\ \mu g{\cdot}m^{-3}\ yr^{-1}$ (95% CI: -1.57~0.11) and $-1.69\ \mu g{\cdot}m^{-3}\ yr^{-1}$ (95% CI: -2.27~-1.05), respectively; while upward trends occurred in Anshun, Bijie, Tongren and Qianxinan

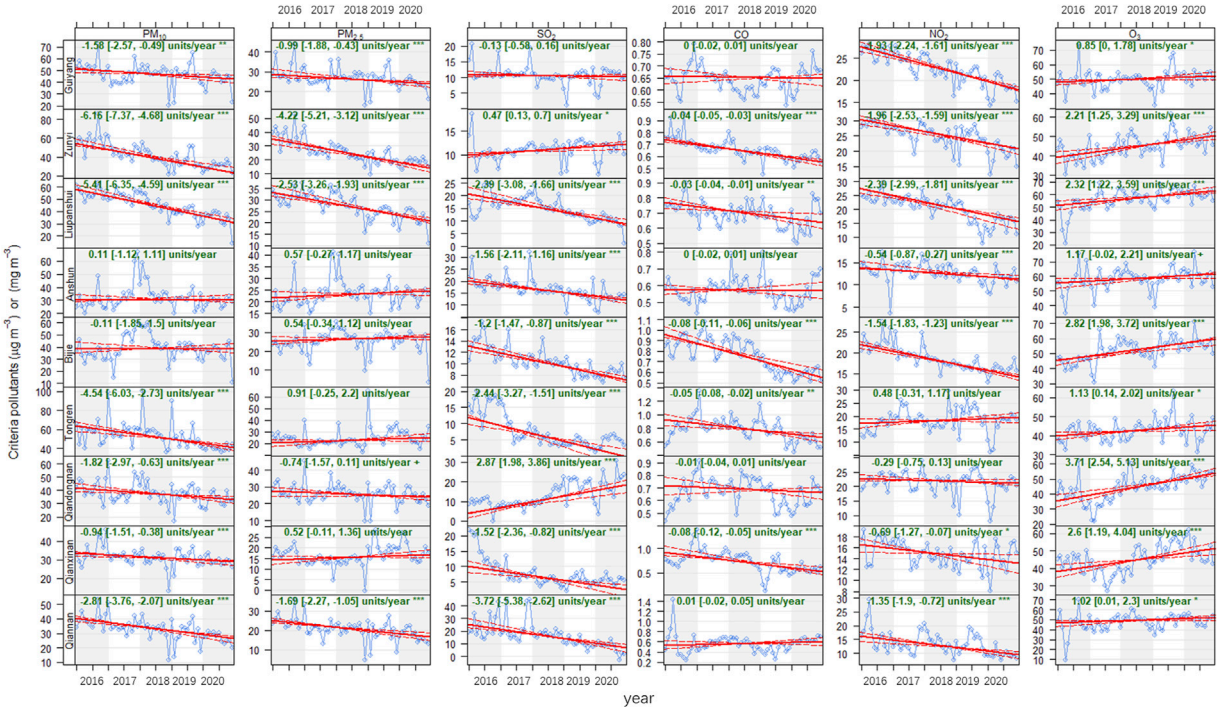

FIGURE 4
Trends of criteria pollutants measured from 2016 to 2020 in Guiyang, Zunyi, Liupanshui, Anshun, Bijie, Tongren, Qiandongnan, Qianxinan and Qiannan. The solid red line shows the trend estimate and the dashed red lines show the 95 % confidence intervals for the trend based on resampling methods. Note also that the symbols shown next to each trend estimate relate to how statistically significant the trend estimate is: $p < 0.001 = ***$, $p < 0.01 = **$, $p < 0.05 = *$ and $p < 0.1 = +$.

with the corresponding average trends being 0.57 μg·m^{-3} yr^{-1} (95% CI: -0.27~1.17), 0.54 μg·m^{-3} yr^{-1} (95% CI: -0.34~1.12), 0.91 μg·m^{-3} yr^{-1} (95% CI: -0.25~2.2) and 0.52 μg·m^{-3} yr^{-1} (95% CI: -0.11~1.36). The average trends of PM_{10} and $PM_{2.5}$ for the focus central cities fell within the ranges reported for other Chinese cities and regions (Cai et al., 2017; Chu et al., 2020; Guo et al., 2019; Huang et al., 2018; Jiang et al., 2015; Silver et al., 2018; Wang et al., 2020a; Xu et al., 2020; Xue et al., 2019; Zhang et al., 2019a; Zheng et al., 2017). These results demonstrated that Guizhou government was successful in the reduction of particulate matter in central cities from 2016 to 2020, although its concentration has increased slightly in several cities. Although interannual meteorological variations could significantly alter PM_{10} and $PM_{2.5}$ concentrations, the relative contribution of emission control and interannual meteorological variation to reductions in PM_{10} and $PM_{2.5}$ concentrations revealed that the effects of meteorological conditions on the trends of PM_{10} and $PM_{2.5}$ were relatively small (Ding et al., 2019b; Zhai et al., 2019; Zhang et al., 2019a; Zhang et al., 2019b), demonstrating that the improvement in PM_{10} and $PM_{2.5}$ air quality was dominated by abatements in anthropogenic emissions. The control of anthropogenic emissions accounted for 78.6% of the decrease in $PM_{2.5}$ concentrations in Beijing from 2013 to 2017, with the relative contribution of local and regional emission reduction being 53.7% and 24.9%, respectively (Chen et al., 2019b). The drivers of improved PM_{10} and $PM_{2.5}$ air quality could be attributed to the strengthening industrial emission standards (power plants and emission-intensive industrial sectors), upgrading on industrial boilers, phasing out outdated industrial capacities, and promoting clean fuels in the residential sector (Zhang et al., 2019a; Zheng et al., 2018a).

The relative change rates of SO_2 in the focus central cities during 2016–2020 were −0.13 μg·m^{-3} yr^{-1} (95% CI: -0.58~0.16) for Guiyang, 0.47 μg·m^{-3} yr^{-1} (95% CI: 0.13~0.7) for Zunyi, −2.39 μg·m^{-3} yr^{-1} (95% CI: -3.08~-1.66) for Liupanshui, −1.56 μg·m^{-3} yr^{-1} (95% CI: -2.11~-1.16) for Anshun, −1.2 μg·m^{-3} yr^{-1} (95% CI: -1.47~-0.87) for Bijie, −2.44 μg·m^{-3} yr^{-1} (95% CI: -3.27~-1.51) for Tongren, 2.87 μg·m^{-3} yr^{-1} (95% CI: 1.98~3.86) for Qiandongnan, −1.52 μg·m^{-3} yr^{-1} (95% CI: -2.36~-0.82) for Qianxinan, and −3.72 μg·m^{-3} yr^{-1} (95% CI: -5.38~-2.62) for Qiannan. The SO_2 concentration substantially increased in Qiandongnan should gaine growing attention and emphasis. SO_2 emissions are mainly from coal combustion in power plant and residential heating (Lu et al., 2010; Vu et al., 2019b; Zheng et al., 2018a), hence the negative trends of SO_2 in most central cities in Guizhou should be driven by the decreased emissions of these factors. During the 11th-13th Five-Year Plans (FYPs) and APPCAP the Chinese government set strict emissions reduction measures including the installation of flue-gas desulfurization (FGD) and selective catalytic reduction systems, construction of large units, decommissioning of small units, and replacement of coal with cleaner energies (Kong et al., 2021b; Li et al., 2017; Liu et al., 2015b; Sun et al., 2018; Zheng et al., 2018a), resulting in SO_2 anthropogenic emissions in China decreased by 10% from 2005 to 2010 (Sun et al., 2018), 62% during 2010–2017 (Zheng et al., 2018b), 59% during 2013–2017 (Zheng et al., 2018b) and 6.2 μg·m^{-3} yr^{-1} during 2013–2018 (Kong et al., 2021b). The CO concentration in the focus central cities in Guizhou during

2016–2020 were estimated to have decreased with the rate of around −0.04 $mg{\cdot}m^{-3}$ yr^{-1} (95% CI: -0.05~-0.03) for Zunyi, −0.03 $mg{\cdot}m^{-3}$ yr^{-1} (95% CI: -0.04~-0.01) for Liupanshui, −0.08 $mg{\cdot}m^{-3}$ yr^{-1} (95% CI: -0.11~-0.06) for Bijie, −0.05 $mg{\cdot}m^{-3}$ yr^{-1} (95% CI: -0.08~-0.02) for Tongren, −0.01 $mg{\cdot}m^{-3}$ yr^{-1} (95% CI: -0.04~0.01) for Qiandongnan and −0.08 $mg{\cdot}m^{-3}$ yr^{-1} (95% CI: -0.12~-0.05) for Qianxinan, whereas CO concentration in Guiyang, Anshun and Qiannan changed little, with the corresponding change rates being 0.0 $mg{\cdot}m^{-3}$ yr^{-1} (95% CI: -0.02~0.01), 0.0 $mg{\cdot}m^{-3}$ yr^{-1} (95% CI: -0.02~0.01) and 0.01 $mg{\cdot}m^{-3}$ yr^{-1} (95% CI: -0.02~0.05). The negative trends of CO concentration have also been observed in BTH, YRD and PRD using long-term comprehensive data sets from 2013 to 2017, the corresponding percentage of the decrease being 21%, 12% and 12% (Wang et al., 2020a). According to the estimates using a combination of bottom-up emission inventory and index decomposition analysis approaches, during 2010–2017, the relative change rates of China's anthropogenic emission of CO decreased by 27% (Zheng et al., 2018a). Such negative trends have also been observed in satellite measurements, such as MOPITT observations (Zheng et al., 2018b), which are mainly attributed to the reduced anthropogenic emissions in China, as suggested by both bottom-up and top-down methods (Zheng et al., 2019b). Incomplete combustion of coal, biomass, and gasoline are recognized as the major CO emissions sources (Sun et al., 2018), hence these factors should be the main drivers of CO reduction. Between 2016 and 2020, observed average NO_2 levels in the focus central cities decreased by −1.93 $\mu g{\cdot}m^{-3}$ yr^{-1} (95% CI: -2.24~-1.61) for Guiyang, −1.96 $\mu g{\cdot}m^{-3}$ yr^{-1} (95% CI: -2.53~-1.59) for Zunyi, −2.39 $\mu g{\cdot}m^{-3}$ yr^{-1} (95% CI: -2.99~-1.81) for Liupanshui, −0.54 $\mu g{\cdot}m^{-3}$ yr^{-1} (95% CI: -0.87~-0.27) for Anshun, −1.54 $\mu g{\cdot}m^{-3}$ yr^{-1} (95% CI: -1.83~-1.23) for Bijie, 0.48 $\mu g{\cdot}m^{-3}$ yr^{-1} (95% CI: -0.31~1.17) for Tongren, −0.29 $\mu g{\cdot}m^{-3}$ yr^{-1} (95% CI: -0.75~0.13) for Qiandongnan, −0.69 $\mu g{\cdot}m^{-3}$ yr^{-1} (95% CI: -1.27~-0.07) for Qianxinan, and −1.35 $\mu g{\cdot}m^{-3}$ yr^{-1} (95% CI: -1.9~-0.72) for Qiannan. These decreases were comparable to the reductions reported by (Chu et al., 2020), who used the data from the China National Environmental Monitoring Center (CNEMC) and observations at more rural sites. From 2013 to 2020, with the implementation of the APPCAP and Action Plan in China, significant declines in NO_2 concentrations occurred nationwide. For instance, compared to levels in 2013, the concentration of NO_2 in 2018 decreased by 19% (Chu et al., 2020), and from 2017 to 2020, decreased by 17% (Li et al., 2021a). The reduced emissions of fossil fuel combustion, on-road vehicles, biomass burning, and non-road mobile sources may be responsible for the reductions of NO_2 (Sun et al., 2018; Zheng et al., 2018b).

The O_3 concentration exhibited the opposite trend to that exhibited by the other air pollutants, which revealed significant positive trends in the focus central cities, indicating enhanced photochemical pollution in Guizhou. The highest increase in O_3 was observed in Qiandongnan, with a average value of 3.71 $\mu g{\cdot}m^{-3}$ yr^{-1} (95% CI: 2.54~5.13), followed by 2.82 $\mu g{\cdot}m^{-3}$ yr^{-1} (95% CI: 1.98~3.72) for Bijie, 2.6 $\mu g{\cdot}m^{-3}$ yr^{-1} (95% CI: 1.19~4.04) for Qianxinan, 2.32 $\mu g{\cdot}m^{-3}$ yr^{-1} (95% CI: 1.22~3.59) for Liupanshui, 2.21 $\mu g{\cdot}m^{-3}$ yr^{-1} (95% CI: 1.25~3.29) for Zunyi, 1.17 $\mu g{\cdot}m^{-3}$ yr^{-1} (95% CI: -0.02~2.21) for Anshun, 1.13 $\mu g{\cdot}m^{-3}$ yr^{-1} (95% CI: 0.14~2.02) for Tongren and 1.02 $\mu g{\cdot}m^{-3}$ yr^{-1} (95% CI: 0.01~2.3) for Qiannan, while the lowest increase occurred in Guiyang with a average value of 0.85 $\mu g{\cdot}m^{-3}$ yr^{-1} (95% CI: 0~1.78). The increase rate of O_3 in most focus central cities in Guizhou was comparable to the Chinese average of 2.1 $\mu g{\cdot}m^{-3}$ yr^{-1} from 2013 to 2018 (Chu et al., 2020). The increasing O_3 levels have been found in many locations in China. For instance, a 6-year-long high-resolution Chinese air quality reanalysis (CAQRA) dataset obtained from the assimilation of surface observations from the CNEMC revealed significant positive trends in NCP, northeast, southeast, northwest, southwest and central regions, ranging from 2.3 to 5.4 $\mu g{\cdot}m^{-3}$ yr^{-1} (Kong et al., 2021a). The multiple analytical approaches also unveiled that O_3 had increased by 20.86%, 14.05% and 12.64% in North, Central and South regions during 2015–2018 (Kalsoom et al., 2021). Using an observation-based box 15 model (OBM) coupled with CB05 mechanism (Wang et al., 2017c), found that both monthly-averaged O_3 and monthly maximum O_3 increased with a rate of 0.56 ± 0.01 ppbv yr^{-1} (p <0.01) and 1.92 ± 0.15 ppbv yr^{-1} (p <0.05), respectively. At the national scale, significant increases in O_3 concentrations occurred. For instance, taking advantage of CNEMC, observations and Tropospheric Ozone Assessment Report (TOAR) dataset (Chu et al., 2020), found that the O_3 concentration increased 17% from 2013 to 2018 and (Lu et al., 2020) revealed that O_3 levels at the 5th, 50th, and 95th percentiles increase at, respectively, 0.4 (7%), 1.7 (7%), 2.8 (4%) ppb $year^{-1}$ (all with p <0.05) averaged over CNEMC network based on the linear trend estimate. The maximum 8-hour-average 90-percentile (MDA8-90) O_3 concentration is suggested by MEE of China to characterize the statistic potential damage of O_3. Supplementary Figure S10 shows that the MDA8-90 O_3 measured from 2016 to 2020 in Guiyang, Zunyi, Liupanshui, Anshun, Bijie, Tongren, Qiandongnan, Qianxinan and Qiannan increased by −0.43 $\mu g{\cdot}m^{-3}$ yr^{-1} (95% CI: -2.26~2.02), 2.96 $\mu g{\cdot}m^{-3}$ yr^{-1} (95% CI: 0.7~6.05), 4 $\mu g{\cdot}m^{-3}$ yr^{-1} (95% CI: 1.99~6.55), 0.48 $\mu g{\cdot}m^{-3}$ yr^{-1} (95% CI: -2.45~3.53), 1.74 $\mu g{\cdot}m^{-3}$ yr^{-1} (95% CI: 0.07~3.68), 1.71 $\mu g{\cdot}m^{-3}$ yr^{-1} (95% CI: -0.88~5.45), 0.69 $\mu g{\cdot}m^{-3}$ yr^{-1} (95% CI: -1.25~2.68), 4.65 $\mu g{\cdot}m^{-3}$ yr^{-1} (95% CI: 2.33~6.9), and 0.04 $\mu g{\cdot}m^{-3}$ yr^{-1} (95% CI: -2.41~2.97), respectively. The most significant increase of MDA8-90 O_3 occurred in Qianxinan, Liupanshui and Zunyi, which were even faster in some Chinese cities compared with the urban MDA8-90 O_3 trends in any other region worldwide reported in TOAR (Lu et al., 2020), suggesting these localities should further do solid efforts in the prevention and control of O_3 pollution. The MDA8-90 O_3 levelled off in Qianan during 2016–2020, while decreasing MDA8-90 O_3 in Guiyang, confirming the effectiveness of emergency control measures for O_3 pollution in Guiyang. It can be also found from comparisons with O_3 concentrations that the increase rates of MDA8-90 O_3 higher than that O_3 in Zunyi, Liupanshui, Tongren and Qianxinan that required our urgent attention, while the opposite was true for the other focus central cities. The O_3 increases could partially be explained by the following aspects. Anthropogenic emission reductions, particularly $PM_{2.5}$ and NO_x reductions, could lead to O_3 increases. The decrease of $PM_{2.5}$ can slow down the aerosol sink of hydroperoxy (HO_2) radicals and thus enhanced O_3 concentration (Li et al., 2019a). Simulations using GEOS-Chem model indicated that a more important factor for the

increase in summer O_3 in the NCP was the reduction in summer $PM_{2.5}$ concentration by about 40% over the 2013–2017 period (Li et al., 2019b). Decreasing $PM_{2.5}$ concentrations can increase solar radiation, especially ultraviolet radiation, which could photolysis more NO_2 into NO, and consequently, increase O_3 production (Wang et al., 2020b). Based on the synchronous monitoring of $PM_{2.5}$ and broadband solar radiation (Hu et al., 2017), found that the solar radiation intensity increased by 1.93 W^{-2} per year between 2005 and 2015 in Beijing, while the $PM_{2.5}$ concentration showed a decreasing trend. Elevated $PM_{2.5}$ may suppress mixing layer height (Wilcox et al., 2016), demoting the vertical diffusion of O_3 precursors, and $PM_{2.5}$ may affect cloud formation (Koren et al., 2004; Koren et al., 2008) and cloud radiative properties (Zamora et al., 2016; Zheng et al., 2018a), affecting photolysis rates and temperature, and hence facilitating O_3 production chemistry. Reductions in anthropogenic NO_x would enhance O_3 in urban areas where O_3 production is expected to be NO_x-saturated (Li et al., 2019a; Lu et al., 2019a; Wang et al., 2021) due to a decrease of the titration effect of NO. High daytime nitrous acid concentrations, which as an important source of OH radicals in the atmosphere, may to some extent enhance the photochemical production of O_3, particularly during late spring and early fall (Tie et al., 2019). In addition, interannual meteorological conditions had a significant influence on the annual variability in O_3 concentrations (Han et al., 2020; Ma et al., 2019a; Yang et al., 2019), and O_3 can increase as much as 8.1 ppbv due to meteorology (Zhang et al., 2021), which can be attributed to increasing temperature and increasing solar radiation (Ding et al., 2019a; Ma et al., 2021; Wang et al., 2020b; Zhang et al., 2021b). Factors contributing to the O_3 enhancements in 2017 compared to 2016 over China were the higher background O_3 driven by hotter and drier weather conditions rather than anthropogenic emission change (Lu et al., 2018), highlighting strong effects of meteorological variations on the interannual variability of surface O_3 over China.

Supplementary Figures S11–S16 display the trends of six criteria pollutants in four seasons in the focus central cities. Overall, decreasing PM_{10}, $PM_{2.5}$, SO_2, CO and NO_2 occurred in four seasons, despite the upward trend in a certain city at some season. The highest decrease of PM_{10}, $PM_{2.5}$, SO_2, CO and NO_2 occurred in fall or winter, with the corresponding maximum being −7.77 $\mu g \cdot m^{-3}$ yr^{-1} (95% CI: -9.39~-6.67), −5.73 $\mu g \cdot m^{-3}$ yr^{-1} (95% CI: -6.62~-5.05), −8.12 $\mu g \cdot m^{-3}$ yr^{-1} (95% CI: -8.8~-7.5), −0.11 $mg \cdot m^{-3}$ yr^{-1} (95% CI: -0.13~-0.1), and −3.04 $\mu g \cdot m^{-3}$ yr^{-1} (95% CI: -3.67~-2.5), which appeared in Liupanshui, Zunyi, Qiannan, Qianxinan and Guiyang, respectively. These results confirmed the effectiveness of air pollution prevention and control in fall and winter. However, O_3 concentrations showed increasing trends in four seasons in the focus central cities, revealing rapid broadening of the O_3 pollution season in Guizhou. The extension of the O_3 pollution season into winter-spring was also observed not only for the North China Plain but across China (Li et al., 2021a), which were attributable to the rapid photochemical production of O_3, driven by HO_x radicals from carbonyl photolysis, and increasing background O_3 in cold seasons. The highest increase of O_3 and MDA8-90 O_3 occurred in spring or summer, with the corresponding maximum being 5.87 $\mu g \cdot m^{-3}$ yr^{-1} (95% CI: 5.86~5.87) and 10.26 $\mu g \cdot m^{-3}$ yr^{-1} (95% CI: 8.6~11.77), which appeared in Qianxinan (Supplementary Figure S17). In general, in contrast to its initial focus on control actions in O_3 pollution season (April-September), the prevention and control of O_3 pollution should extend to four seasons through extensive coordination at the regional level.

3.5 Correlations of six criteria pollutants in the nine major cities in Guizhou

The correlations between air pollutants can yield quiet a few rewarding information about the related mechanisms/processes and how they change over time in different regions (Chu et al., 2020; Ding et al., 2013a; Guo et al., 2019; Othman and Latif, 2021; Wang et al., 2014a). The relationships between air pollutants in the nine major cities in Guizhou during the period of study are illustrated in Figure 5. Overall, strong correlations were observed between PM_{10} and $PM_{2.5}$ for all focus central cities with r = 0.92 for Guiyang, r = 0.92 for Zunyi, r = 0.95 for Liupanshui, r = 0.96 for Anshun, r = 0.94 for Bijie, r = 0.8 for Tongren, r = 0.96 for Qiandongnan, r = 0.81 for Qianxinan and r = 0.91 for Qiannan, suggesting that $PM_{2.5}$ accounted for a large fraction of PM_{10} (Wang et al., 2017d). O_3 was weakly to moderately anti-correlated with other gaseous pollutants, which was is partially the result of O_3 depletion during the oxidation of NO to NO_2 (Wang et al., 2014b). Weak positive correlations ($0 < r \leq 0.47$) were observed between O_3 and PM_{10} as well as $PM_{2.5}$, indicating the simultaneous formation of secondary O_3 and particulate matter by photochemical reactions under favorable weather conditions. Discriminating correlations between $PM_{2.5}$ and primary gaseous pollutants were observed in Guiyang, Zunyi and Anshun. Pleasurable relationships between $PM_{2.5}$ and CO were observed because almost all combustion sources contribute CO and most gaseous precursors of $PM_{2.5}$, such as NO_x and SO_2 (Chu et al., 2020). The positive correlations between $PM_{2.5}$ and SO_2, with r = 0.55 for Guiyang, r = 0.42 for Zunyi, r = 0.3 for Liupanshui, r = 0.46 for Anshun, r = 0.28 for Bijie, r = 0.19 for Qiandongnan, r = 0.19 for Qianxinan and r = 0.25 for Qiannan, indicated that coal burning is an important source of $PM_{2.5}$ (Yang et al., 2011), particularly in Guiyang, Zunyi and Anshun. The favorable relationship between $PM_{2.5}$ and NO_2, with r = 0.43 for Guiyang, r = 0.42 for Zunyi, r = 0.27 for Liupanshui, r = 0.53 for Anshun, r = 0.42 for Bijie, r = 0.23 for Tongren, r = 0.39 for Qiandongnan, r = 0.25 for Qianxinan and r = 0.48 for Qiannan, implied that vehicle emissions are another important source of $PM_{2.5}$ (Chu et al., 2020), particularly in Guiyang, Zunyi and Anshun, Bijie and Qiannan. The lower correlation between $PM_{2.5}$ and NO_2 than that between $PM_{2.5}$ and SO_2 occurred in Guiyang and Liupanshui, indicating a relative higher contribution of SO_2 emission to $PM_{2.5}$ in these in these two cities. The higher correlation between $PM_{2.5}$ and NO_2 than that between $PM_{2.5}$ and SO_2 occurred in Anshun, Bijie, Tongren, Qiandongnan, Qianxinan and Qiannan, accounting for about 67% of the total focus central cities, which may be resulted from the slower reduction of NO_x than SO_2 in the past decade in Guizhou, highlighting regulation of NO_x emissions is pressing for mitigating $PM_{2.5}$ pollution in Guizhou. Field and laboratory studies indicated NO_2 can enhance atmospheric oxidation capacity, hence contributing secondary $PM_{2.5}$ production (Cheng et al., 2016;

FIGURE 5
The matrix of Pearson correlation coefficients between air pollutants in Guiyang, Zunyi, Liupanshui, Anshun, Bijie, Tongren, Qiandongnan, Qianxinan and Qiannan. Leave blank on no significant coefficient.

Chu et al., 2019; He et al., 2014; Russell et al., 1988). Aerosol pollution in the NCP gradually changed from sulfate-driven to nitrate-driven was observed based on intensive field observations and model simulations (Huang et al., 2021; Li et al., 2019b; Li et al., 2021c; Wen et al., 2018). High concentrations of NO_x, as a catalyst or an oxidants, can promote the heterogeneous reaction of SO_2 with NO_2, particularly under NH_3-rich conditions (Chu et al., 2020; He et al., 2014; Ma et al., 2018; Wang et al., 2016; Xue et al., 2016; Zhang et al., 2021a). These heterogeneous processes and aqueous reactions further indicated that NO_2 played an vital role in enhancing the secondary $PM_{2.5}$ production and explained why $PM_{2.5}$ concentrations were highly related to changes in NO_2 than in SO_2 in most central cities in Guizhou, highlighting the urgency for curbing NO_x to further mitigate $PM_{2.5}$ pollution in Guizhou.

In general, as shown in Supplementary Figures S18–S20, the correlation between $PM_{2.5}$ and NO_2/SO_2 were higher in the winter and autumn seasons with lower correlation coefficient between $PM_{2.5}$ and SO_2 than that between $PM_{2.5}$ and NO_2, indicating the presence of NO_x-related secondary $PM_{2.5}$ production in the winter and autumn seasons. Generally, higher correlation between $PM_{2.5}$ and O_3 were observed in winter in the focus central cities, except in Liupanshui where the highest value occurred in spring. Speculatively, one reason of this phenomenon is that there is strong O_3 photochemical production due to carbonyl photolysis and photodissociation of nitrous acid in these seasons (Edwards et al., 2014; Li et al., 2021a; Schnell et al., 2009; Tie et al., 2019). A comprehensive observations of atmospheric radicals and relevant parameters during several haze events in winter 2016 Beijing revealed surprisingly high hydroxyl radical oxidation rates up to 15 ppbv·h^{-1} facilitating the production of secondary pollutants, which was is mainly initiated by the photolysis of nitrous acid and ozonolysis of olefins and maintained by an extremely efficiently

radical cycling process driven by nitric oxide (Lu et al., 2019b). There was also often strong O_3 photochemical production due to the photodissociation of nitrous acid, causing a copresence of high $PM_{2.5}$ and O_3 concentrations during late spring in eastern China (Tie et al., 2019).

4 Environmental policy implication

Research on spatiotemporal variations and trends of criteria air pollutants can help policymakers develop strategies and policies for emission reductions and track the progress of those policies. Our study quantified the spatiotemporal variations and trends of criteria air pollutants in nine central cities in Guizhou based on datasets obtained from Guizhou Provincial Environmental Monitoring Central Station network. Our results showed that the dramatic reductions in PM_{10}, $PM_{2.5}$, SO_2, CO and NO_2, indicating the remarkable air quality improvements in Guizhou. Our results confirmed that driven by a series of active explorations and practices, the air quality in Guizhou has continued to improve steadily. However, the annual mean concentration of $PM_{2.5}$ is still substantially higher than China's national ambient air quality standard (NAAQS-I) of 15 $\mu g \cdot m^{-3}$ and the WHO guideline of 10 $\mu g \cdot m^{-3}$. VOCs, SO_2, NO_x, and NH_3 are key precursors of secondary $PM_{2.5}$ (Gu et al., 2021; Li et al., 2016; Liu et al., 2013; Yang et al., 2009). VOCs, including volatile chemical products (VCPs), which are responsible for half of the petrochemical VOCs emitted in major urban areas (McDonald et al., 2018; Coggon et al., 2021), can produce amounts of the photochemical organic $PM_{2.5}$. In addition, the latest study showed that abating NH_3 is more cost-effective than NO_x for mitigating $PM_{2.5}$ air pollution (Gu et al., 2021). Both VOCs and NH_3 are derived from a wealth of sources, with a lack of effective control measures, and the lower correlation between $PM_{2.5}$ and NO_2 than that between $PM_{2.5}$ and SO_2. Therefore, we suggest that a reduction of NO_x emissions is currently urgent for further reducing $PM_{2.5}$ pollution in Guizhou. However, further mitigating $PM_{2.5}$ pollution in the future because of the benefit for public health, tailored control measures for VOCs and NH_3 emissions should be put on the agenda.

Our results showed an increasing trend of O_3 concentrations and an extension of the O_3 pollution season, hence curbing O_3 concentrations has become the focus of Guizhou's next air quality control strategies. Both ground measurements and simulations indicated that decreasing $PM_{2.5}$ and NO_x emissions can increase O_3 in urban areas where O_3 production is expected to be VOC-limited, calling for decreasing NO_x and VOC emissions to overcome that effect (Li et al., 2019a; Li et al., 2019b). In addition, the photodissociation of nitrous acid (Lu et al., 2019c; Tie et al., 2019), carbonyl photolysis (Edwards et al., 2014; Li et al., 2021a), increasing background O_3 (Li et al., 2021b) and meteorological conditions (Han et al., 2020; Ma et al., 2019b; Yang et al., 2019) could also contribute to the increase in surface O_3 pollution. Therefore, curbing O_3 pollution in Guizhou will require comprehensive measurements, and the focus should be redesigned to mitigate multiple precursors from multiple sectors through extensive coordination at the regional or national level, instead of its initial focus on control actions for a single pollutant or in a single sector. Meanwhile, efficient control strategies to mitigate cold season O_3 pollution in Guizhou may require measures similar as implemented to avoid O_3 pollution in warm season in pursuit of cleaner air.

5 Concluding remarks

Based on the extensive network data available since 2016, we analyzed the spatiotemporal variations and trends of air quality in the nine major cities in Guizhou during 2016–2020 for the first time to the best of our knowledge. The provincewide 5-year PM_{10}, $PM_{2.5}$, SO_2, CO, NO_2 and O_3 were 38.8 $\mu g \cdot m^{-3}$ (95% CI 37.4~41.2), 23.3 $\mu g \cdot m^{-3}$ (95% CI: 22.5~24.2), 10.5 $\mu g \cdot m^{-3}$ (95% CI: 9.6~11.3), 0.7 $mg \cdot m^{-3}$ (95% CI: 0.6~0.7), 13.2 $\mu g \cdot m^{-3}$ (95% CI: 13.1~14.2) and 47.2 $\mu g \cdot m^{-3}$ (95% CI: 45.8~48.6), respectively, with corresponding maxima occurred in Tongren, Liupanshui, Qianan, Bijie, Zunyi and Anshun. PM_{10}, $PM_{2.5}$, SO_2, CO and NO_2 exhibited similar spatiotemporal variation with nighttime and wintertime peaks, and the polluted areas had shrunk, wihle O_3 presented distinguished diurnal and seasonal pattern with an afternoon maximum and two peaks in late spring and early autumn, and the polluted areas had expanded. The annual mean concentrations of PM_{10}, $PM_{2.5}$, SO_2, CO and NO_2 all decreased year by year during 2016–2020 with the corresponding rate rangs being -6.16 $\mu g \cdot m^{-3}$ yr^{-1} (95% CI: -7.37~-4.68) - 0.11 $\mu g \cdot m^{-3}$ yr^{-1} (95% CI: -1.12~1.11), -4.22 $\mu g \cdot m^{-3}$ yr^{-1} (95% CI: -5.21~-3.12)- 0.91 $\mu g \cdot m^{-3}$ yr^{-1} (95% CI: -0.25~2.2), -3.72 $\mu g \cdot m^{-3}$ yr^{-1} (95% CI: -5.38~-2.62)- 2.87 $\mu g \cdot m^{-3}$ yr^{-1} (95% CI: 1.98~3.86), -0.08 $mg \cdot m^{-3}$ yr^{-1} (95% CI: -0.11~-0.06)- 0.01 $mg \cdot m^{-3}$ yr^{-1} (95% CI: -0.02~0.05) and -2.39 $\mu g \cdot m^{-3}$ yr^{-1} (95% CI: -2.99~-1.81) -0.48 $\mu g \cdot m^{-3}$ yr^{-1} (95% CI: -0.31~1.17), and the highest decrease occurred in fall or winter. In contrast with the PM_{10}, $PM_{2.5}$, SO_2, CO and NO_2, O_3 concentrations increased year by year, with increase rates ranged from 0.85 $\mu g \cdot m^{-3}$ yr^{-1} (95% CI: 0~1.78) to 3.71 $\mu g \cdot m^{-3}$ yr^{-1} (95% CI: 2.54~5.13), and the highest increase occurred in spring or summer. The correlations among the six criteria pollutants indicated the $PM_{2.5}$-NO_2 correlation coefficients were higher than those of $PM_{2.5}$-SO_2, hence a priority to control NO_x to further reduce $PM_{2.5}$ pollution in Guizhou. However, tailored control measures for VOCs and NH_3 emissions should be put on the agenda in order to continuously improve $PM_{2.5}$ air quality in the future because of the benefit for public health. Comprehensive measurements, including carbonyls and nitrous acid, and the focus redesigned to mitigate multiple precursors from multiple sectors are indispensable for curbing O_3 pollution.

This study can provide a theoretical basis for the formulation of future air-pollution control policy in Guizhou. Importantly, Guizhou urgently needs to conduct observation of multiple pollutants, formulate O_3 control policies, and setting up cost-effective measures to mitigate both $PM_{2.5}$ and O_3. Cleaning up city air will require simultaneous tracking of all air pollutants relevant to health and their feedbacks and interactions. We need to understand how the mixture and its toxicity changes as air quality measures are implemented. Therefore, in the future, we will estimate the drivers of the contrasting trends of $PM_{2.5}$ and surface O_3 air quality, and the associated health benefits in Guizhou, and also quantify the effectiveness of Guizhou's action plan by decoupling the impact of meteorology on ambient air quality.

Data availability statement

The original contributions presented in the study are included in the article/Supplementary Material, further inquiries can be directed to the corresponding author.

Author contributions

FL: Data curation, Formal Analysis, Investigation, Methodology, Software, Visualization, Writing–original draft. YY: Conceptualization, Funding acquisition, Project administration, Supervision, Validation, Writing–review and editing. FH: Software, Visualization, Writing–review and editing. LH: Software, Visualization, Writing–review and editing.

Funding

This research has been supported by the Guizhou Province Science and Technology Plan Project "Research and demonstration of ozone formation mechanism and control policies in Bijie Pilot Zone [Qianke joint support (2021) general 498]," and the Science and Technology Planned Project in Guizhou Province [Qian Kehe Foundation (2020)1Y175].

Acknowledgments

All referenced supplemental figures and tables can be found in the supporting information. The authors are grateful to all staff and workers from Guizhou Provincial Environmental Monitoring Central Station network for maintaining the instruments used in the current study.

Conflict of interest

The authors declare that the research was conducted in the absence of any commercial or financial relationships that could be construed as a potential conflict of interest.

Publisher's note

Supplementary material

The Supplementary Material for this article can be found online at: https://www.frontiersin.org/articles/10.3389/fenvs.2023.1254390/full#supplementary-material

References

Bai, K., Li, K., Wu, C., Chang, N. B., and Guo, J. (2020). A homogenized daily *in situ* PM_{2.5} concentration dataset from the national air quality monitoring network in China. *Earth Syst. Sci. Data* 12 (4), 3067–3080. doi:10.5194/essd-12-3067-2020

Bian, Y., Huang, Z., Ou, J., Zhong, Z., Xu, Y., Zhang, Z., et al. (2019). Evolution of anthropogenic air pollutant emissions in Guangdong Province, China, from 2006 to 2015. *Atmos. Chem. Phys.* 19 (18), 11701–11719. doi:10.5194/acp-19-11701-2019

Burnett, R., Chen, H., Szyszkowicz, M., Fann, N., Hubbell, B., PopeSpadaro, C. A. J. V., et al. (2018). Global estimates of mortality associated with long-term exposure to outdoor fine particulate matter. *Proc. Natl. Acad. Sci. U. S. A.* 115 (38), 9592–9597. doi:10.1073/pnas.1803222115

Cai, S., Wang, Y., Zhao, B., Wang, S., Chang, X., and Hao, J. (2017). The impact of the "air pollution prevention and control action plan" on PM2.5 concentrations in jing-jin-ji region during 2012–2020. *Sci. Total Environ.* 580, 197–209. doi:10.1016/j.scitotenv.2016.11.188

Carslaw, D. C., and Ropkins, K. (2012). Openair — an R package for air quality data analysis. *Environ. Model. Softw.* 27-28, 52–61. doi:10.1016/j.envsoft.2011.09.008

Chen, Z., Chen, D., Kwan, M.-P., Chen, B., Gao, B., Zhuang, Y., et al. (2019a). The control of anthropogenic emissions contributed to 80 % of the decrease in PM_{2.5} concentrations in Beijing from 2013 to 2017. *Atmos. Chem. Phys.* 19 (21), 13519–13533. doi:10.5194/acp-19-13519-2019

Chen, Z., Chen, D., Wen, W., Zhuang, Y., Kwan, M.-P., Chen, B., et al. (2019b). Evaluating the "2+26" regional strategy for air quality improvement during two air pollution alerts in Beijing: variations in PM_{2.5} concentrations, source apportionment, and the relative contribution of local emission and regional transport. *Atmos. Chem. Phys.* 19 (10), 6879–6891. doi:10.5194/acp-19-6879-2019

Cheng, Y., Zheng, G., Wei, C., Mu, Q., Zheng, B., Wang, Z., et al. (2016). Reactive nitrogen chemistry in aerosol water as a source of sulfate during haze events in China. *Sci. Adv.* 2 (12), e1601530. doi:10.1126/sciadv.1601530

Chu, B., Ma, Q., Liu, J., Ma, J., Zhang, P., Chen, T., et al. (2020). Air pollutant correlations in China: Secondary air pollutant responses to NO_x and SO_2 control. *Environ. Sci. Technol. Lett.* 7 (10), 695–700. doi:10.1021/acs.estlett.0c00403

Chu, B., Wang, Y., Yang, W., Ma, J., Ma, Q., Zhang, P., et al. (2019). Effects of NO₂ and C₃H₆ on the heterogeneous oxidation of SO₂ on TiO₂ in the presence or absence of UV–Vis irradiation. *Atmos. Chem. Phys.* 19 (23), 14777–14790. doi:10.5194/acp-19-14777-2019

Coggon, M. M., Gkatzelis, G. I., McDonald, B. C., Gilman, J. B., Schwantes, R. H., Abuhassan, N., et al. (2021). Volatile chemical product emissions enhance ozone and modulate urban chemistry. *Proc. Natl. Acad. Sci.* 118 (32), e2026653118. doi:10.1073/pnas.2026653118

Ding, A. J., Fu, C. B., Yang, X. Q., Sun, J. N., Zheng, L. F., Xie, Y. N., et al. (2013a). Ozone and fine particle in the western Yangtze River Delta: An overview of 1 yr data at the SORPES station. *Atmos. Chem. Phys.* 13 (11), 5813–5830. doi:10.5194/acp-13-5813-2013

Ding, A. J., Fu, C. B., Yang, X. Q., Sun, J. N., Zheng, L. F., Xie, Y. N., et al. (2013b). Ozone and fine particle in the western Yangtze River Delta: An overview of 1 yr data at the SORPES station. *Atmos. Chem. Phys.* 13 (11), 5813–5830. doi:10.5194/acp-13-5813-2013

Ding, A. J., Wang, T., Thouret, V., Cammas, J. P., and Nédélec, P. (2008). Tropospheric ozone climatology over Beijing: analysis of aircraft data from the MOZAIC program. *Atmos. Chem. Phys.* 8 (1), 1–13. doi:10.5194/acp-8-1-2008

Ding, D., Xing, J., Wang, S., Chang, X., and Hao, J. (2019a). Impacts of emissions and meteorological changes on China's ozone pollution in the warm seasons of 2013 and 2017. *Front. Environ. Sci. Eng.* 13 (5), 76. doi:10.1007/s11783-019-1160-1

Ding, D., Xing, J., Wang, S., Liu, K., and Hao, J. (2019b). Estimated contributions of emissions controls, meteorological factors, population growth, and changes in baseline mortality to reductions in ambient [formula: See text] and [formula: See text]-related mortality in China, 2013-2017. *Environ. Health Perspect.* 127 (6), 067009. doi:10.1289/EHP4157

Dufour, G., Eremenko, M., Orphal, J., and Flaud, J. M. (2010). IASI observations of seasonal and day-to-day variations of tropospheric ozone over three highly populated areas of China: Beijing, Shanghai, and Hong Kong. *Atmos. Chem. Phys.* 10 (8), 3787–3801. doi:10.5194/acp-10-3787-2010

Edwards, P. M., Brown, S. S., Roberts, J. M., Ahmadov, R., Banta, R. M., deGouw, J. A., et al. (2014). High winter ozone pollution from carbonyl photolysis in an oil and gas basin. *Nature* 514 (7522), 351–354. doi:10.1038/nature13767

Feng, Y., Ning, M., Lei, Y., Sun, Y., Liu, W., and Wang, J. (2019). Defending blue sky in China: Effectiveness of the "air pollution prevention and control action plan" on air quality improvements from 2013 to 2017. *J. Environ. Manag.* 252, 109603. doi:10.1016/j.jenvman.2019.109603

Gu, B., Zhang, L., Dingenen, R. V., Vieno, M., Grinsven, H. J. V., Zhang, X., et al. (2021). Abating ammonia is more cost-effective than nitrogen oxides for mitigating $PM_{2.5}$ air pollution. *Science* 374 (6568), 758–762. doi:10.1126/science.abf8623

Guo, H., Gu, X., Ma, G., Shi, S., Wang, W., Zuo, X., et al. (2019). Spatial and temporal variations of air quality and six air pollutants in China during 2015-2017. *Sci. Rep.* 9 (1), 15201. doi:10.1038/s41598-019-50655-6

Guo, H., Ling, Z. H., Cheng, H. R., Simpson, I. J., Lyu, X. P., Wang, X. M., et al. (2017). Tropospheric volatile organic compounds in China. *Sci. Total Environ.* 574, 1021–1043. doi:10.1016/j.scitotenv.2016.09.116

Guo, H., Ling, Z. H., Cheung, K., Jiang, F., Wang, D. W., Simpson, I. J., et al. (2013). Characterization of photochemical pollution at different elevations in mountainous areas in Hong Kong. *Atmos. Chem. Phys.* 13 (8), 3881–3898. doi:10.5194/acp-13-3881-2013

Guo, S., Hu, M., Zamora, M. L., Peng, J., Shang, D., Zheng, J., et al. (2014). Elucidating severe urban haze formation in China. *Proc. Natl. Acad. Sci.* 111 (49), 17373–17378. doi:10.1073/pnas.1419604111

Han, H., Liu, J., Shu, L., Wang, T., and Yuan, H. (2020). Local and synoptic meteorological influences on daily variability in summertime surface ozone in eastern China. *Atmos. Chem. Phys.* 20 (1), 203–222. doi:10.5194/acp-20-203-2020

Hao, J., He, D., Wu, Y., Fu, L., and He, K. (2000). A study of the emission and concentration distribution of vehicular pollutants in the urban area of Beijing. *Atmos. Environ.* 34 (3), 453–465. doi:10.1016/S1352-2310(99)00324-6

He, H., Wang, Y., Ma, Q., Ma, J., Chu, B., Ji, D., et al. (2014). Mineral dust and NOx promote the conversion of SO2 to sulfate in heavy pollution days. *Sci. Rep.* 4 (1), 4172. doi:10.1038/srep04172

He, Q., Wang, M., Liu, K., Li, K., and Jiang, Z. (2021). GPRChinaTemp1km: A high-resolution monthly air temperature dataset for China (1951–2020) based on machine learning. *Earth Syst. Sci. Data Discuss.* 2021, 1–29. doi:10.5194/essd-2021-267

Hoesly, R., Smith, S., Feng, L., Klimont, Z., Janssens-Maenhout, G., Pitkanen, T., et al. (2017). Historical (1750–2014) anthropogenic emissions of reactive gases and aerosols from the Community Emission Data System (CEDS). *Geosci. Model Dev. Discuss.*, 1–41. doi:10.5194/gmd-2017-43

Hu, B., Zhao, X., Liu, H., Liu, Z., Song, T., Wang, Y., et al. (2017). Quantification of the impact of aerosol on broadband solar radiation in North China. *Sci. Rep.* 7 (1), 44851. doi:10.1038/srep44851

Huang, J., Pan, X., Guo, X., and Li, G. (2018). Health impact of China's air pollution prevention and control action plan: An analysis of national air quality monitoring and mortality data. *Lancet Planet. Health* 2 (7), e313–e323. doi:10.1016/S2542-5196(18)30141-4

Huang, R. J., Zhang, Y., Bozzetti, C., Ho, K. F., Cao, J. J., Han, Y., et al. (2014). High secondary aerosol contribution to particulate pollution during haze events in China. *Nature* 514 (7521), 218–222. doi:10.1038/nature13774

Huang, W., Yang, Y., Wang, Y., Gao, W., Li, H., Zhang, Y., et al. (2021). Exploring the inorganic and organic nitrate aerosol formation regimes at a suburban site on the North China Plain. *Sci. Total Environ.* 768, 144538. doi:10.1016/j.scitotenv.2020.144538

Huang, X., Ding, A., Gao, J., Zheng, B., Zhou, D., Qi, X., et al. (2020). Enhanced secondary pollution offset reduction of primary emissions during COVID-19 lockdown in China. *Natl. Sci. Rev.* 8, nwaa137. doi:10.1093/nsr/nwaa137

Jiang, X., Hong, C., Zheng, Y., Zheng, B., Guan, D., Gouldson, A., et al. (2015). To what extent can China's near-term air pollution control policy protect air quality and human health? A case study of the Pearl River Delta region. *Environ. Res. Lett.* 10 (10), 104006. doi:10.1088/1748-9326/10/10/104006

Jiang, X., Li, G., and Fu, W. (2021). Government environmental governance, structural adjustment and air quality: A quasi-natural experiment based on the three-year action plan to win the blue sky defense war. *J. Environ. Manag.* 277, 111470. doi:10.1016/j.jenvman.2020.111470

Kalsoom, U., Wang, T., Ma, C., Shu, L., Huang, C., and Gao, L. (2021). Quadrennial variability and trends of surface ozone across China during 2015–2018: A regional approach. *Atmos. Environ.* 245, 117989. doi:10.1016/j.atmosenv.2020.117989

Kong, L., Tang, X., Zhu, J., Wang, Z., Li, J., Wu, H., et al. (2021a). A 6-year-long (2013–2018) high-resolution air quality reanalysis dataset in China based on the assimilation of surface observations from CNEMC. *Earth Syst. Sci. Data* 13 (2), 529–570. doi:10.5194/essd-13-529-2021

Kong, L., Tang, X., Zhu, J., Wang, Z., Li, J., Wu, H., et al. (2021b). A 6-year-long (2013–2018) high-resolution air quality reanalysis dataset in China based on the assimilation of surface observations from CNEMC. *Earth Syst. Sci. Data* 13 (2), 529–570. doi:10.5194/essd-13-529-2021

Koren, I., Kaufman, Y. J., Remer, L. A., and Martins, J. V. (2004). Measurement of the effect of amazon smoke on inhibition of cloud formation. *Science* 303 (5662), 1342–1345. doi:10.1126/science.1089424

Koren, I., Martins, J. V., Remer, L. A., and Afargan, H. (2008). Smoke invigoration versus inhibition of clouds over the amazon. *Science* 321 (5891), 946–949. doi:10.1126/science.1159185

Kulmala, M. (2015). Atmospheric chemistry: China's choking cocktail. *Nature* 526 (7574), 497–499. doi:10.1038/526497a

Lelieveld, J., Evans, J. S., Fnais, M., Giannadaki, D., and Pozzer, A. (2015). The contribution of outdoor air pollution sources to premature mortality on a global scale. *Nature* 525 (7569), 367–371. doi:10.1038/nature15371

Li, H., Cheng, J., Zhang, Q., Zheng, B., Zhang, Y., Zheng, G., et al. (2019c). Rapid transition in winter aerosol composition in Beijing from 2014 to 2017: Response to clean air actions. *Atmos. Chem. Phys.* 19 (17), 11485–11499. doi:10.5194/acp-19-11485-2019

Li, J., Gao, W., Cao, L., Xiao, Y., Zhang, Y., Zhao, S., et al. (2021a). Significant changes in autumn and winter aerosol composition and sources in Beijing from 2012 to 2018: Effects of clean air actions. *Environ. Pollut.* 268, 115855. doi:10.1016/j.envpol.2020.115855

Li, J., Wu, R., Li, Y., Hao, Y., Xie, S., and Zeng, L. (2016). Effects of rigorous emission controls on reducing ambient volatile organic compounds in Beijing, China. *Sci. Total Environ.* 557-558, 531–541. doi:10.1016/j.scitotenv.2016.03.140

Li, K., Jacob, D. J., Liao, H., Zhu, J., Shah, V., Shen, L., et al. (2019b). A two-pollutant strategy for improving ozone and particulate air quality in China. *Nat. Geosci.* 12 (11), 906–910. doi:10.1038/s41561-019-0464-x

Li, K., Jacob, D. J., Liao, H., Qiu, Y., Shen, L., Zhai, S., et al. (2021b). Ozone pollution in the North China Plain spreading into the late-winter haze season. *Proc. Natl. Acad. Sci.* 118 (10), e2015797118. doi:10.1073/pnas.2015797118

Li, K., Jacob, D. J., Liao, H., Shen, L., Zhang, Q., and Bates, K. H. (2019a). Anthropogenic drivers of 2013-2017 trends in summer surface ozone in China. *Proc. Natl. Acad. Sci.* 116 (2), 422–427. doi:10.1073/pnas.1812168116

Li, M., Liu, H., Geng, G., Hong, C., Liu, F., Song, Y., et al. (2017). Anthropogenic emission inventories in China: A review. *Natl. Sci. Rev.* 4 (6), 834–866. doi:10.1093/nsr/nwx150

Li, W., Shao, L., Wang, W., Li, H., Wang, X., Li, Y., et al. (2020). Air quality improvement in response to intensified control strategies in Beijing during 2013–2019. *Sci. Total Environ.* 744, 140776. doi:10.1016/j.scitotenv.2020.140776

Li, Y., Shi, G., and Chen, Z. (2021c). Spatial and temporal distribution characteristics of ground-level nitrogen dioxide and ozone across China during 2015-2020. *Environ. Res. Lett.* 16, 124031. doi:10.1088/1748-9326/ac3794

Lim, S. S., Vos, T., Flaxman, A. D., Danaei, G., Shibuya, K., Adair-Rohani, H., et al. (2012). A comparative risk assessment of burden of disease and injury attributable to 67 risk factors and risk factor clusters in 21 regions, 1990-2010: A systematic analysis for the global burden of disease study 2010. *Lancet* 380 (9859), 2224–2260. doi:10.1016/S0140-6736(12)61766-8

Lin, W., Xu, X., Ge, B., and Liu, X. (2011). Gaseous pollutants in Beijing urban area during the heating period 2007–2008: Variability, sources, meteorological, and chemical impacts. *Atmos. Chem. Phys.* 11 (15), 8157–8170. doi:10.5194/acp-11-8157-2011

Lin, W., Xu, X., Ge, B., and Zhang, X. (2009). Characteristics of gaseous pollutants at Gucheng, a rural site southwest of Beijing. *J. Geophys. Res. Atmos.* 114 (D2), D00G14. doi:10.1029/2008JD010339

Lin, W., Xu, X., Zhang, X., and Tang, J. (2008). Contributions of pollutants from North China plain to surface ozone at the shangdianzi GAW station. *Atmos. Chem. Phys.* 8 (19), 5889–5898. doi:10.5194/acp-8-5889-2008

Liu, F., Zhang, Q., Tong, D., Zheng, B., Li, M., Huo, H., et al. (2015a). High-resolution inventory of technologies, activities, and emissions of coal-fired power plants in China from 1990 to 2010. *Atmos. Chem. Phys.* 15 (23), 13299–13317. doi:10.5194/acp-15-13299-2015

Liu, J., Li, X., Liu, S., Liu, L., Wu, J., Wang, R., et al. (2021). Assessment of the emission mitigation effect on the wintertime air quality in the Guanzhong Basin, China from 2013 to 2017. *Atmos. Pollut. Res.* 12 (10), 101196. doi:10.1016/j.apr.2021.101196

Liu, X. G., Li, J., Qu, Y., Han, T., Hou, L., Gu, J., et al. (2013). Formation and evolution mechanism of regional haze: A case study in the megacity Beijing, China. *Atmos. Chem. Phys.* 13 (9), 4501–4514. doi:10.5194/acp-13-4501-2013

Liu, Z., Gao, W., Yu, Y., Hu, B., Xin, J., Sun, Y., et al. (2018). Characteristics of PM_{2.5} mass concentrations and chemical species in urban and background areas of China: Emerging results from the CARE-China network. *Atmos. Chem. Phys.* 18 (12), 8849–8871. doi:10.5194/acp-18-8849-2018

Liu, Z., Hu, B., Wang, L., Wu, F., Gao, W., and Wang, Y. (2015b). Seasonal and diurnal variation in particulate matter (PM10and PM2.5) at an urban site of Beijing: analyses from a 9-year study. *Environ. Sci. Pollut. Res.* 22 (1), 627–642. doi:10.1007/s11356-014-3347-0

Lu, H., Lyu, X., Cheng, H., Ling, Z., and Guo, H. (2019a). Overview on the spatial-temporal characteristics of the ozone formation regime in China. *Environ. Science-Processes Impacts* 21 (6), 916–929. doi:10.1039/c9em00098d

Lu, K., Fuchs, H., Hofzumahaus, A., Tan, Z., Wang, H., Zhang, L., et al. (2019b). Fast photochemistry in wintertime haze: Consequences for pollution mitigation strategies. *Environ. Sci. Technol.* 53 (18), 10676–10684. doi:10.1021/acs.est.9b02422

Lu, X., Zhang, L., Chen, Y., Zhou, M., Zheng, B., Li, K., et al. (2019c). Exploring 2016–2017 surface ozone pollution over China: Source contributions and meteorological influences. *Atmos. Chem. Phys.* 19 (12), 8339–8361. doi:10.5194/acp-19-8339-2019

Lu, X., Zhang, L., Wang, X., Gao, M., Li, K., Zhang, Y., et al. (2020). Rapid increases in warm-season surface ozone and resulting health impact in China since 2013. *Environ. Sci. Technol. Lett.* 7 (4), 240–247. doi:10.1021/acs.estlett.0c00171

Lu, Z., Liu, X., Zhang, Z., Zhao, C., Meyer, K., Rajapakshe, C., et al. (2018). Biomass smoke from southern Africa can significantly enhance the brightness of stratocumulus over the southeastern Atlantic Ocean. *Proc. Natl. Acad. Sci.* 115 (12), 2924–2929. doi:10.1073/pnas.1713703115

Lu, Z., Streets, D. G., Zhang, Q., Wang, S., Carmichael, G. R., Cheng, Y. F., et al. (2010). Sulfur dioxide emissions in China and sulfur trends in East Asia since 2000. *Atmos. Chem. Phys.* 10 (13), 6311–6331. doi:10.5194/acp-10-6311-2010

Ma, J., Chu, B., Liu, J., Liu, Y., Zhang, H., and He, H. (2018). NO promotion of SO2 conversion to sulfate: An important mechanism for the occurrence of heavy haze during winter in Beijing. *Environ. Pollut.* 233, 662–669. doi:10.1016/j.envpol.2017.10.103

Ma, M., Gao, Y., Wang, Y., Zhang, S., Leung, L. R., Liu, C., et al. (2019a). Substantial ozone enhancement over the North China Plain from increased biogenic emissions due to heat waves and land cover in summer 2017. *Atmos. Chem. Phys.* 19 (19), 12195–12207. doi:10.5194/acp-19-12195-2019

Ma, X., Huang, J., Zhao, T., Liu, C., Zhao, K., Xing, J., et al. (2021). Rapid increase in summer surface ozone over the North China plain during 2013–2019: A side effect of particulate matter reduction control? *Atmos. Chem. Phys.* 21 (1), 1–16. doi:10.5194/acp-21-1-2021

Ma, Z., Liu, R., Liu, Y., and Bi, J. (2019b). Effects of air pollution control policies on PM_{2.5} pollution improvement in China from 2005 to 2017: A satellite-based perspective. *Atmos. Chem. Phys.* 19 (10), 6861–6877. doi:10.5194/acp-19-6861-2019

McDonald, B. C., de Gouw, J. A., Gilman, J. B., Jathar, S. H., Akherati, A., Cappa, C. D., et al. (2018). Volatile chemical products emerging as largest petrochemical source of urban organic emissions. *Science* 359 (6377), 760–764. doi:10.1126/science.aaq0524

Olstrup, H., Forsberg, B., Orru, H., Spanne, M., Nguyen, H., Molnár, P., et al. (2018). Trends in air pollutants and health impacts in three Swedish cities over the past three decades. *Atmos. Chem. Phys.* 18 (21), 15705–15723. doi:10.5194/acp-18-15705-2018

Othman, M., and Latif, M. T. (2021). Air pollution impacts from COVID-19 pandemic control strategies in Malaysia. *J. Clean. Prod.* 291, 125992. doi:10.1016/j.jclepro.2021.125992

Pal, S. K., and Masum, M. M. H. (2021). Spatiotemporal trends of selected air quality parameters during force lockdown and its relationship to COVID-19 positive cases in Bangladesh. *Urban Clim.* 39, 100952. doi:10.1016/j.uclim.2021.100952

Rohde, R. A., and Muller, R. A. (2015). Air pollution in China: Mapping of concentrations and sources. *Plos One* 10 (8), e0135749. doi:10.1371/journal.pone.0135749

Russell, A. G., McCue, K. F., and Cass, G. R. (1988). Mathematical modeling of the formation of nitrogen-containing pollutants. 2. Evaluation of the effect of emission controls. *Environ. Sci. Technol.* 22 (11), 1336–1347. doi:10.1021/es00176a014

Schnell, R. C., Oltmans, S. J., Neely, R. R., Endres, M. S., Molenar, J. V., and White, A. B. (2009). Rapid photochemical production of ozone at high concentrations in a rural site during winter. *Nat. Geosci.* 2 (2), 120–122. doi:10.1038/ngeo415

Sen, and Kumar, P. (1968). Estimates of the regression coefficient based on kendall's tau. *Publ. Am. Stat. Assoc.* 63 (324), 1379–1389. doi:10.1080/01621459.1968.10480934

Shi, X., Zhao, C., Jiang, J. H., Wang, C., Yang, X., and Yung, Y. L. (2018). Spatial representativeness of PM2.5 concentrations obtained using observations from network stations. *J. Geophys. Res. Atmos.* 123 (6), 3145–3158. doi:10.1002/2017JD027913

Shi, Z., Vu, T., Kotthaus, S., Harrison, R. M., Grimmond, S., Yue, S., et al. (2019). Introduction to the special issue "In-depth study of air pollution sources and processes within Beijing and its surrounding region (APHH-Beijing)". *Atmos. Chem. Phys.* 19 (11), 7519–7546. doi:10.5194/acp-19-7519-2019

Silver, B., Reddington, C. L., Arnold, S. R., and Spracklen, D. V. (2018). Substantial changes in air pollution across China during 2015–2017. *Environ. Res. Lett.* 13 (11), 114012. doi:10.1088/1748-9326/aae718

Su, W., Liu, C., Hu, Q., Fan, G., Xie, Z., Huang, X., et al. (2017). Characterization of ozone in the lower troposphere during the 2016 G20 conference in Hangzhou. *Sci. Rep.* 7 (1), 17368. doi:10.1038/s41598-017-17646-x

Sun, W., Shao, M., Granier, C., Liu, Y., Ye, C. S., and Zheng, J. Y. (2018). Long-term trends of anthropogenic SO2, NOx, CO, and NMVOCs emissions in China. *Earth's Future* 6 (8), 1112–1133. doi:10.1029/2018ef000822

Tang, G., Li, X., Wang, Y., Xin, J., and Ren, X. (2009). Surface ozone trend details and interpretations in Beijing, 2001–2006. *Atmos. Chem. Phys.* 9 (22), 8813–8823. doi:10.5194/acp-9-8813-2009

Tang, G., Wang, Y., Li, X., Ji, D., Hsu, S., and Gao, X. (2012). Spatial-temporal variations in surface ozone in Northern China as observed during 2009–2010 and possible implications for future air quality control strategies. *Atmos. Chem. Phys.* 12 (5), 2757–2776. doi:10.5194/acp-12-2757-2012

Theil, H. (1992). A rank-invariant method of linear and polynomial regression analysis. *Nederl. Akad. wetensch.Proc.* 12 (2), 345–381. doi:10.1007/978-94-011-2546-8_20

Tie, X., Long, X., Li, G., Zhao, S., Cao, J., and Xu, J. (2019). Ozone enhancement due to the photodissociation of nitrous acid in eastern China. *Atmos. Chem. Phys.* 19 (17), 11267–11278. doi:10.5194/acp-19-11267-2019

Vu, T. V., Shi, Z., Cheng, J., Zhang, Q., He, K., Wang, S., et al. (2019a). Assessing the impact of clean air action on air quality trends in Beijing using a machine learning technique. *Atmos. Chem. Phys.* 19 (17), 11303–11314. doi:10.5194/acp-19-11303-2019

Vu, T. V., Shi, Z., Cheng, J., Zhang, Q., He, K., Wang, S., et al. (2019b). Assessing the impact of clean air action on air quality trends in Beijing using a machine learning technique. *Atmos. Chem. Phys.* 19 (17), 11303–11314. doi:10.5194/acp-19-11303-2019

Wang, G., Kawamura, K., Xie, M., Hu, S., Cao, J., An, Z., et al. (2009). Organic molecular compositions and size distributions of Chinese summer and autumn aerosols from nanjing: Characteristic haze event caused by wheat straw burning. *Environ. Sci. Technol.* 43 (17), 6493–6499. doi:10.1021/es803086g

Wang, G., Zhang, R., Gomez, M. E., Yang, L., Levy Zamora, M., Hu, M., et al. (2016). Persistent sulfate formation from London Fog to Chinese haze. *Proc. Natl. Acad. Sci.* 113 (48), 13630–13635. doi:10.1073/pnas.1616540113

Wang, T., Xue, L., Brimblecombe, P., Lam, Y. F., Li, L., and Zhang, L. (2017a). Ozone pollution in China: A review of concentrations, meteorological influences, chemical precursors, and effects. *Sci. Total Environ.* 575, 1582–1596. doi:10.1016/j.scitotenv.2016.10.081

Wang, W.-N., Cheng, T.-H., Gu, X.-F., Chen, H., Guo, H., Wang, Y., et al. (2017b). Assessing spatial and temporal patterns of observed ground-level ozone in China. *Sci. Rep.* 7 (1), 3651. doi:10.1038/s41598-017-03929-w

Wang, W. N., Cheng, T. H., Gu, X. F., Chen, H., Guo, H., Wang, Y., et al. (2017c). Assessing spatial and temporal patterns of observed ground-level ozone in China. *Sci. Rep.* 7 (1), 3651. doi:10.1038/s41598-017-03929-w

Wang, W., Parrish, D. D., Li, X., Shao, M., Liu, Y., Mo, Z., et al. (2020a). Exploring the drivers of the increased ozone production in Beijing in summertime during 2005–2016. *Atmos. Chem. Phys.* 20 (24), 15617–15633. doi:10.5194/acp-20-15617-2020

Wang, W., van der A, R., Ding, J., van Weele, M., and Cheng, T. (2021). Spatial and temporal changes of the ozone sensitivity in China based on satellite and ground-based observations. *Atmos. Chem. Phys.* 21 (9), 7253–7269. doi:10.5194/acp-21-7253-2021

Wang, Y. H., Gao, W. K., Wang, S., Song, T., Gong, Z. Y., Ji, D. S., et al. (2020b). Contrasting trends of PM2.5 and surface-ozone concentrations in China from 2013 to 2017. *Natl. Sci. Rev.* 7 (8), 1331–1339. doi:10.1093/nsr/nwaa032

Wang, Y. H., Hu, B., Ji, D. S., Liu, Z. R., Tang, G. Q., Xin, J. Y., et al. (2014b). Ozone weekend effects in the Beijing–Tianjin–Hebei metropolitan area, China. *Atmos. Chem. Phys.* 14 (5), 2419–2429. doi:10.5194/acp-14-2419-2014

Wang, Y., McElroy, M. B., Munger, J. W., Hao, J., Ma, H., Nielsen, C. P., et al. (2008). Variations of O₃ and CO in summertime at a rural site near Beijing. *Atmos. Chem. Phys.* 8 (21), 6355–6363. doi:10.5194/acp-8-6355-2008

Wang, Y. Q., Zhang, X. Y., Sun, J. Y., Zhang, X. C., Che, H. Z., and Li, Y. (2015). Spatial and temporal variations of the concentrations of PM₁₀, PM_{2.5} and PM₁ in China. *Atmos. Chem. Phys.* 15 (23), 13585–13598. doi:10.5194/acp-15-13585-2015

Wang, Y., Wang, H., Guo, H., Lyu, X., Cheng, H., Ling, Z., et al. (2017d). Long-term O₃–precursor relationships in Hong Kong: Field observation and model simulation. *Atmos. Chem. Phys.* 17 (18), 10919–10935. doi:10.5194/acp-17-10919-2017

Wang, Y., Ying, Q., Hu, J., and Zhang, H. (2014a). Spatial and temporal variations of six criteria air pollutants in 31 provincial capital cities in China during 2013-2014. *Environ. Int.* 73, 413–422. doi:10.1016/j.envint.2014.08.016

Wen, L., Xue, L., Wang, X., Xu, C., Chen, T., Yang, L., et al. (2018). Summertime fine particulate nitrate pollution in the North China plain: Increasing trends, formation mechanisms and implications for control policy. *Atmos. Chem. Phys.* 18 (15), 11261–11275. doi:10.5194/acp-18-11261-2018

Wilcox, E. M., Thomas, R. M., Praveen, P. S., Pistone, K., Bender, F. A. M., and Ramanathan, V. (2016). Black carbon solar absorption suppresses turbulence in the atmospheric boundary layer. *Proc. Natl. Acad. Sci.* 113 (42), 11794–11799. doi:10.1073/pnas.1525746113

Wu, H., Tang, X., Wang, Z., Wu, L., Lu, M., Wei, L., et al. (2018). Probabilistic automatic outlier detection for surface air quality measurements from the China national environmental monitoring network. *Adv. Atmos. Sci.* 35 (12), 1522–1532. doi:10.1007/s00376-018-8067-9

Wu, W., Xue, W., Zheng, Y., Wang, Y., Lei, Y., and Wang, J. (2021). Diurnal regulation of VOCs may not be effective in controlling ozone pollution in China. *Atmos. Environ.* 256, 118442. doi:10.1016/j.atmosenv.2021.118442

Xu, W., Kuang, Y., Bian, Y., Liu, L., Li, F., Wang, Y., et al. (2020). Current challenges in visibility improvement in southern China. *Environ. Sci. Technol. Lett.* 7 (6), 395–401. doi:10.1021/acs.estlett.0c00274

Xu, W. Y., Zhao, C. S., Ran, L., Deng, Z. Z., Liu, P. F., Ma, N., et al. (2011). Characteristics of pollutants and their correlation to meteorological conditions at a suburban site in the North China Plain. *Atmos. Chem. Phys.* 11 (9), 4353–4369. doi:10.5194/acp-11-4353-2011

Xu, X., Lin, W., Wang, T., Yan, P., Tang, J., Meng, Z., et al. (2008). Long-term trend of surface ozone at a regional background station in eastern China 1991–2006: Enhanced variability. *Atmos. Chem. Phys.* 8 (10), 2595–2607. doi:10.5194/acp-8-2595-2008

Xue, J., Yuan, Z., Griffith, S. M., Yu, X., Lau, A. K. H., and Yu, J. Z. (2016). Sulfate Formation enhanced by a cocktail of high NO_x, SO_2, particulate matter, and droplet pH during haze-fog events in megacities in China: An observation-based modeling investigation. *Environ. Sci. Technol.* 50 (14), 7325–7334. doi:10.1021/acs.est.6b00768

Xue, T., Liu, J., Zhang, Q., Geng, G., Zheng, Y., Tong, D., et al. (2019). Rapid improvement of PM2.5 pollution and associated health benefits in China during 2013–2017. *Sci. China Earth Sci.* 62 (12), 1847–1856. doi:10.1007/s11430-018-9348-2

Yang, F., Tan, J., Zhao, Q., Du, Z., He, K., Ma, Y., et al. (2011). Characteristics of PM_{2.5} speciation in representative megacities and across China. *Atmos. Chem. Phys.* 11 (11), 5207–5219. doi:10.5194/acp-11-5207-2011

Yang, G., Liu, Y., and Li, X. (2020). Spatiotemporal distribution of ground-level ozone in China at a city level. *Sci. Rep.* 10 (1), 7229. doi:10.1038/s41598-020-64111-3

Yang, L., Luo, H., Yuan, Z., Zheng, J., Huang, Z., Li, C., et al. (2019). Quantitative impacts of meteorology and precursor emission changes on the long-term trend of ambient ozone over the Pearl River Delta, China, and implications for ozone control strategy. *Atmos. Chem. Phys.* 19 (20), 12901–12916. doi:10.5194/acp-19-12901-2019

Yang, S., Yuesi, W., and Changchun, Z. (2009). Measurement of the vertical profile of atmospheric SO2 during the heating period in Beijing on days of high air pollution. *Atmos. Environ.* 43 (2), 468–472. doi:10.1016/j.atmosenv.2008.09.057

Yin, P., Guo, J., Wang, L., Fan, W., Lu, F., Guo, M., et al. (2020). Higher risk of cardiovascular disease associated with smaller size-fractioned particulate matter. *Environ. Sci. Technol. Lett.* 7 (2), 95–101. doi:10.1021/acs.estlett.9b00735

Yue, X., Unger, N., Harper, K., Xia, X., Liao, H., Zhu, T., et al. (2017). Ozone and haze pollution weakens net primary productivity in China. *Atmos. Chem. Phys.* 17 (9), 6073–6089. doi:10.5194/acp-17-6073-2017

Zamora, L. M., Kahn, R. A., Cubison, M. J., Diskin, G. S., Jimenez, J. L., Kondo, Y., et al. (2016). Aircraft-measured indirect cloud effects from biomass burning smoke in the Arctic and subarctic. *Atmos. Chem. Phys.* 16 (2), 715–738. doi:10.5194/acp-16-715-2016

Zhai, S., Jacob, D. J., Wang, X., Shen, L., Li, K., Zhang, Y., et al. (2019). Fine particulate matter (PM_{2.5}) trends in China, 2013–2018: Separating contributions from anthropogenic emissions and meteorology. *Atmos. Chem. Phys.* 19 (16), 11031–11041. doi:10.5194/acp-19-11031-2019

Zhang, Q., Zheng, Y., Tong, D., Shao, M., Wang, S., Zhang, Y., et al. (2019a). Drivers of improved PM2.5 air quality in China from 2013 to 2017. *Proc. Natl. Acad. Sci.* 116 (49), 24463–24469. doi:10.1073/pnas.1907956116

Zhang, S., Li, D., Ge, S., Liu, S., Wu, C., Wang, Y., et al. (2021a). Rapid sulfate formation from synergetic oxidation of SO2 by O3 and NO2 under ammonia-rich conditions: Implications for the explosive growth of atmospheric PM2.5 during haze events in China. *Sci. Total Environ.* 772, 144897. doi:10.1016/j.scitotenv.2020.144897

Zhang, X., Xu, X., Ding, Y., Liu, Y., Zhang, H., Wang, Y., et al. (2019b). The impact of meteorological changes from 2013 to 2017 on PM2.5 mass reduction in key regions in China. *Sci. China Earth Sci.* 62, 1885–1902. doi:10.1007/s11430-019-9343-3

Zhang, Y., Shindell, D., Seltzer, K., Shen, L., Lamarque, J. F., Zhang, Q., et al. (2021b). Impacts of emission changes in China from 2010 to 2017 on domestic and intercontinental air quality and health effect. *Atmos. Chem. Phys.* 21 (20), 16051–16065. doi:10.5194/acp-21-16051-2021

Zhao, H., Chen, K., Liu, Z., Zhang, Y., Shao, T., and Zhang, H. (2021). Coordinated control of PM2.5 and O3 is urgently needed in China after implementation of the "Air pollution prevention and control action plan". *Chemosphere* 270, 129441. doi:10.1016/j.chemosphere.2020.129441

Zheng, B., Chevallier, F., Ciais, P., Yin, Y., Deeter, M., Worden, H., et al. (2018a). Rapid decline in carbon monoxide emissions and export from East Asia between years 2005 and 2016. *Environ. Res. Lett.* 13, 044007. doi:10.1088/1748-9326/aab2b3

Zheng, B., Chevallier, F., Yin, Y., Ciais, P., Fortems-Cheiney, A., Deeter, M., et al. (2019a). Global atmospheric carbon monoxide budget 2000-2017 inferred from multi-species atmospheric inversions. *Earth Syst. Sci. Data* 11, 1411–1436. doi:10.5194/essd-11-1411-2019

Zheng, B., Tong, D., Li, M., Liu, F., Hong, C., Geng, G., et al. (2018b). Trends in China's anthropogenic emissions since 2010 as the consequence of clean air actions. *Atmos. Chem. Phys.* 18 (19), 14095–14111. doi:10.5194/acp-18-14095-2018

Zheng, S., Wang, J., Sun, C., Zhang, X., and Kahn, M. E. (2019b). Air pollution lowers Chinese urbanites' expressed happiness on social media. *Nat. Hum. Behav.* 3 (3), 237–243. doi:10.1038/s41562-018-0521-2

Zheng, Y., Xue, T., Zhang, Q., Geng, G., Tong, D., Li, X., et al. (2017). Air quality improvements and health benefits from China's clean air action since 2013. *Environ. Res. Lett.* 12, 114020. doi:10.1088/1748-9326/aa8a32

frontiers | Frontiers in Environmental Science

TYPE Original Research
PUBLISHED 25 September 2023
DOI 10.3389/fenvs.2023.1281202

OPEN ACCESS

EDITED BY
Hainan Gong,
Chinese Academy of Sciences (CAS), China

REVIEWED BY
Cheng Sun,
Beijing Normal University, China
Zhiqiang Gong,
Beijing Climate Center (BCC), China

*CORRESPONDENCE
Ruowen Yang,
yangruowen@ynu.edu.cn

†These authors have contributed equally to this work

RECEIVED 22 August 2023
ACCEPTED 12 September 2023
PUBLISHED 25 September 2023

CITATION
Dong Z, Gui S, Yang R, Cheng J, Yang H and Ma J (2023), Interdecadal variation of precipitation over Yunnan, China in summer and its possible causes. *Front. Environ. Sci.* 11:1281202. doi: 10.3389/fenvs.2023.1281202

Interdecadal variation of precipitation over Yunnan, China in summer and its possible causes

Zeyu Dong[1,2†], Shu Gui[1,3†], Ruowen Yang[1,3*†], Jinxin Cheng[1,4], Huan Yang[1] and Ji Ma[1]

[1]Yunnan Key Laboratory of Meteorological Disasters and Climate Resources in the Greater Mekong Subregion, Yunnan University, Kunming, China, [2]Kunming Meteorological Bureau, Kunming, China, [3]Collaborative Innovation Center on Forecast and Evaluation of Meteorological Disasters (CIC-FEMD), Nanjing University of Information Science and Technology, Nanjing, China, [4]Yunnan Climate Center, Kunming, China

In recent decades, severe drought conditions have become increasingly frequent in Yunnan, Southwest China. The extreme drought events cause huge losses to agricultural economy, ecological security and human health. To uncover the reasons behind the worsening drought conditions, this study investigates the interdecadal variability (IDV) of summer precipitation in Yunnan during 1961–2019 and its association with the Indo-Pacific Sea surface temperature (SST) configuration based on gauge observation and reanalysis data. The dominant mode of summer precipitation IDV in Yunnan shows a uniform pattern characterizing the alternations of flood and drought. Specifically, a relatively wet period persists from the early 1990s to the early 2000s, followed by a relatively dry period from the early 2000s to the late 2010s. The IDV of precipitation is consistent with the IDV of the column-integrated water vapor flux divergence, where the wind anomalies play a major role in modulating the moisture supply. The main SST forcings of the IDV of precipitation include the sea surface temperature anomalies (SSTAs) over the Bay of Bengal (BOB), the Western Pacific Warm Pool (WPWP), and the western North Pacific (WNP). The negative SSTAs over the BOB and the WPWP trigger a Gill-Matsuno-type response that enhances the cyclonic curvature over Yunnan. The SSTAs over the WNP show a tripole pattern that weakens the WNP subtropical high and further enhances the cyclonic anomaly over Yunnan. The above SST configuration also favors moisture transport to Yunnan. Numerical experiments verify the key physical processes.

KEYWORDS

precipitation, interdecadal variation, SST configuration, Gill-Matsuno response, Bay of Bengal, western Pacific warm pool, western North Pacific subtropical high

1 Introduction

Yunnan is the main part of the low-latitude highland of China, encompassing the confluence zone of the East Asian summer monsoon (EASM) and Indian summer monsoon (ISM). The interaction between the EASM and the ISM superimposes onto the complex terrain of Yunnan, making a unique plateau-mountain monsoon climate (Cao et al., 2012; Cao et al., 2016; Guo et al., 2016; Tao et al., 2016). The moisture source of Yunnan originates from the Bay of Bengal (BOB) and the Arabian Sea to the Southwest, and tropical Western North Pacific (WNP) the Southeast. The rainy season of Yunnan lasts from May to October, when the cumulative rainfall accounts for more than 83% of the total annual precipitation

regionwide. The rainfall variation in Yunnan is independent from other parts of China, primarily because of the combined modulation of the EASM–ISM interaction and the complex terrain of Yunnan (Qin, 1998; Cheng et al., 2009; Yan et al., 2018; He et al., 2021).

The IDV of precipitation in Yunnan has been a hot topic since the 2009 megadrought (Duan et al., 2000; Huang et al., 2012; Lü et al., 2012; Pradhan et al., 2017; Zheng et al., 2017; Zheng et al., 2017; Liu et al., 2018a; Han and Jiang, 2018; Wang et al., 2018; Li et al., 2019a; Wang et al., 2023). From 2009 to 2012, Yunnan encountered a severe drought for four consecutive years, not only in the dry season (from October to April of the following year), but also in the wet season (from May to September). The persistent drought in Yunnan directly caused major economic losses over 40 billion Chinese Yuan (CNY) and reduced the terrestrial ecosystem Gross Primary Productivity (GPP) by 8.6%, 17.48% and 13.85% in 2009, 2010, and 2011 (Tao et al., 2014; Li et al., 2022). Since then, Yunnan has been experiencing recurrent drought conditions especially in spring and early summer (Wang et al., 2021; Liu et al., 2022; Gao et al., 2023). The IDV of precipitation also manifests as the interdecadal variations of the daytime and nighttime precipitation amount and the number of rainy days (Zhu et al., 2022). Given the severity of summer drought, many studies investigated the IDV of summer precipitation around Yunnan and revealed the possible causes.

Previous studies so far suggest that the IDV of summer precipitation in the neighborhood of Yunnan is attributed to multiple SST forcings (SSTAs) over tropical Indian Ocean (IO) and the tropical Pacific (Nitta and Hu, 1996; Hu, 1997; Xie et al., 2009; Park and An, 2014). For instance, the tropical IO affects the IDV of summer rainfall in Southwestern China by the interdecadal IO basin mode (the main driver) and the interdecadal IO dipole (the secondary driver) (Liu et al., 2018b). The tropical Pacific modulates the IDV of summer precipitation in the Greater Mekong Subregion by the SSTAs over the western Pacific warm pool (Wen et al., 2021). The configuration of SSTAs over tropical IO and tropical Pacific is identified as the primary cause of the summer precipitation IDV around Yunnan. The tropical IO and the tropical eastern Pacific modulate the IDV of summer precipitation over Eastern China by altering the western Pacific subtropical high (Gong and Ho, 2002). The SSTAs over the western Pacific warm pool and the eastern IO warm pool are the main driver of the IDV of heavy precipitation events during the wet-season over the low-latitude highland of China (Liu et al., 2011). The anomalous warming of western Pacific and western IO suppresses summer precipitation over the Hengduan Mountains through inducing anomalous moisture divergence and downward motions over the area (Dong et al., 2019). The IDV of summer precipitation around Yunnan is also related to the extratropical SST modes such as the PDO (Lü et al., 2014), and the combined effect of the tropical IO SST and the Tibetan Plateau snow cover (Wu et al., 2010).

Most previous studies put Yunnan and the surrounding areas together for investigation (for example, Southwestern China or Eastern China), which weakens the representability of precipitation pattern in Yunnan and potentially underplays the impact of tropical SST patterns on the IDV of summer precipitation in Yunnan. Since the correlation between the summer precipitation variability in Yunnan and the surrounding areas is statistically insignificant, we need to isolate Yunnan from the surrounding areas for investigation. If only Yunnan is considered, the IDV of summer precipitation and its main driver could be different from the previous findings. Since the IDV of precipitation in the neighborhood of Yunnan is affected by the SSTAs over different oceans, we could assume that the IDV of summer precipitation in Yunnan is also attributed to the coordinated influence of multiple SSTAs. To reveal the main reason of the increasing drought in recent decades, a detailed analysis on the IDV of summer precipitation in Yunnan is urgently needed. This study aims to reveal the main characteristics of the IDV of summer precipitation in Yunnan and elucidates its association with the SSTAs over the ocean areas surrounding Yunnan.

The remainder of this paper is as follows. Section 2 introduces the reanalysis data, methodology, and the atmospheric model. Section 3 presents the main characteristics of the IDV of summer precipitation in Yunnan. Section 4 investigates the physical processes of the IDV of summer precipitation and clarifies the impact mechanism of tropical SSTA configuration. Section 5 presents the model results to verify the causal link between the IDV of summer precipitation in Yunnan and the tropical SSTA configuration. Section 6 presents a discussion and our conclusion.

2 Data, method, and AGCM

2.1 Data

This study employs the observed precipitation data from 124 observation stations in Yunnan provided by Yunnan Climate Center. The 5th generation European Centre for Medium-range Weather Forecasts atmospheric reanalysis (ERA5) is used for the atmospheric variables including horizontal wind, vertical velocity, and specific humidity. The ERA5 data has a horizontal resolution of 0.25° and 37 pressure levels from 1,000 to 1 hPa. The Hadley Centre Sea Ice and Sea Surface Temperature (HadISST) dataset version 1.1 is used for monthly SST with a horizontal resolution of 1°. The time span of the above data is 1961–2019.

2.2 Method

This study adopts the empirical orthogonal function (EOF) analysis to extract the leading mode of summer rainfall variation in Yunnan (von Storch and Zwiers, 2002). A 7-year low-pass filtering is used to extract the interdecadal component of the research data. The investigation uses the least squares regression and the composite method to identify key physical processes. The significance test uses the two-tailed Student's *t*-test with the effective degree of freedom $N_{dof} = N\left(\sum_{k=-\infty}^{\infty}\rho_{XX,k}\rho_{YY,k}\right)^{-1}$, where N is the sample size and $\rho_{XX,k}$ and $\rho_{YY,k}$ are the lag-k autocorrelations of the time series (Afyouni et al., 2019).

To unveil the primary cause of moisture transport anomalies, we decomposed the column-integrated water vapor flux divergence (CIWVFD) as follows:

$$-\frac{1}{g}\int_{p_s}^{100\,hPa}\nabla\cdot(q\boldsymbol{V})'dp = \left(-\frac{1}{g}\int_{p_s}^{100\,hPa}\nabla\cdot\bar{q}\boldsymbol{V}'dp\right) + \left(-\frac{1}{g}\int_{p_s}^{100\,hPa}\nabla\cdot q'\bar{\boldsymbol{V}}dp\right) + \left(-\frac{1}{g}\int_{p_s}^{100\,hPa}\nabla\cdot q'\boldsymbol{V}'dp\right) \quad (1)$$

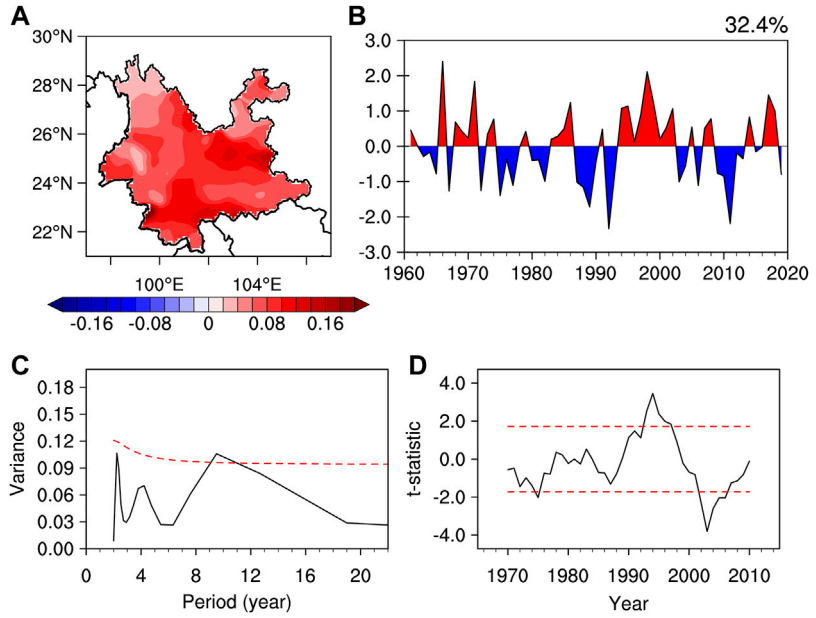

FIGURE 1
(A) Spatial distribution of the first EOF mode (EOF1) of summer rainfall over the Yunnan, **(B)** normalized detrended principal component (PC1) of the EOF1, **(C)** continuous power spectra of the detrended PC1, **(D)** the sliding *t*-test of the PC1 with window length of 7 years. The red dashed lines in **(C,D)** represent the 95% confidence level.

where p_s represents the surface pressure, q is the specific humidity, $\boldsymbol{V}$ is the horizontal wind, dp is the integral variable, and g is the gravitational acceleration. In Eq. 1, the overbar denotes the climatological mean state, and the prime denotes the anomalies. The three terms on the right-hand side of the equation are respectively the dynamical term, the thermodynamical term, and the perturbation term. Since the only time-varying factor in the dynamical term $(-\frac{1}{g}\int_{p_s}^{100\,hPa}\nabla\cdot\bar{q}V'dp)$ is the wind anomalies, this term represents the dynamical effect of wind anomalies on the CIWVFD. Likewise, the thermodynamical term $(-\frac{1}{g}\int_{p_s}^{100\,hPa}\nabla\cdot q'\bar{V}dp)$ represents the thermodynamical effect of specific humidity anomalies on the CIWVFD. The perturbation term $(-\frac{1}{g}\int_{p_s}^{100\,hPa}\nabla\cdot q'V'dp)$ represents the perturbation effect of both specific humidity anomalies and wind anomalies on the CIWVFD.

2.3 Model

This study uses the simplified parameterizations primitive equation dynamics (SPEEDY) model (the latest version 41) to verify the proposed mechanism (Kucharski et al., 2013). The SPEEDY model is a hydrostatic spectral-transform model developed at the Abdus Salam International Centre for Theoretical Physics. The SPEEDY model has simplified physical parameterizations of radiation, convection, large-scale condensation, clouds, surface fluxes, etc., which resemble those in operational weather forecast models (Molteni, 2003). The spatial resolution of SPEEDY model is T30L8, corresponding to a horizontal resolution of approximately 3.75° × 3.75° on a Gaussian grid with 8 vertical levels on the terrain-following σ-coordinate. The model output is interpolated on 8 pressure levels at 30, 100, 200, 300, 500, 700, 850, and 925 hPa.

3 Interdecadal variation of summer precipitation in Yunnan

We used the EOF analysis to reveal the spatiotemporal characteristics of precipitation in Yunnan during summer (June–July–August: JJA). The leading EOF mode (EOF1) characterizes a uniform pattern with positive centers over the southern and central-eastern Yunnan (Figure 1A). The spatial pattern of EOF1 suggests a region-wide uniform increase or decrease of precipitation in Yunnan. The variation contribution rate of the EOF1 is 32.4%. The first principal component (PC1) shows an intense interannual-to-interdecadal variability (Figure 1B). The power spectral analysis of the first principal component (PC1) shows a significant IDV period of 9–11 years (Figure 1C). To determine the IDV phase change, we performed a 11-year sliding *t*-test on the PC1. Results show three interdecadal dry-wet transitions during 1961–2019, including a relatively wet period before 1974, a relatively dry period of 1983–1992, a relatively wet period of 1993–2002, and a relatively dry period of 2003–2019 (Figure 1D). The mean value of the PC1 is 0.71 for the relatively wet period and −0.70 for the relatively dry period. The mean value change of PC1 is significant at 99% confidence level. Thus, the summer precipitation in Yunnan has undergone significant IDV. Given the significant period of the IDV (9–11 years), we adopted the nine-year binomial smoothing method to extract the interdecadal component of PC1 (ID-PC1).

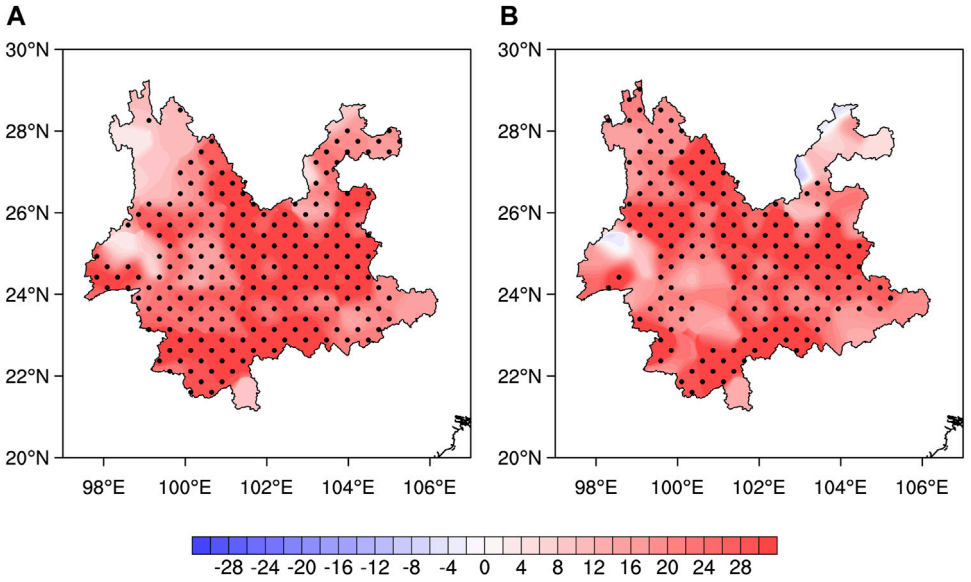

FIGURE 2
The anomalies of JJA mean precipitation calculated by **(A)** regression against the standardized ID-PC1, **(B)** composite between the wet and dry periods (units: mm). The stippling denotes significance at the 95% confidence levels.

The magnitude of the IDV of precipitation is investigated and cross-validated with regression and composite methods. The observed summer rainfall data is regressed against the ID-PC1. The regression result shows positive anomalies regionwide, with significant changes over the southern and central-eastern Yunnan. The composite of summer precipitation between wet and dry periods shows a similar pattern (Figure 2B). The precipitation increases for all observation stations, with significant changes mainly over central-eastern and Southern Yunnan. The regressed anomalies of precipitation are significant at 98 weather stations, and the composites of precipitation are significant at 71 weather stations. The composite analysis only accounts the IDV anomaly years, making the precipitation variation larger than the regression result. The maximum of precipitation anomalies is around 30 mm for the regression result, and around 60 mm for the composite result. The spatial pattern of EOF1, the regression and composite results are consistent with each other. Thus, the IDV of summer rainfall in Yunnan is associated with a robust change in the precipitation amount over most parts of Yunnan.

4 Possible mechanism

4.1 Large-scale circulation

To reveal the large-scale circulation pattern, we regressed the 7-year low-pass filtered horizontal wind against the ID-PC1. The 200 hPa horizontal wind field characterizes a significant cyclonic anomaly to the north of Yunnan (Figure 3A). This cyclonic anomaly indicates a weakened South Asian high associated with enhanced low-level easterly anomalies over the North of Yunnan (Figure 3B). The 700 hPa horizontal wind field characterizes two anomalous anticyclones over the Indo-Pacific warm pool, one over the BOB (point A) and the other over the WPWP (point C). The anomalous anticyclone over the BOB enhances westerly anomalies over the Southern Yunnan, and the anomalous anticyclone over the WPWP intensifies the Southwesterly over the Southeastern Yunnan. The joint effect of these two anomalous anticyclones induces an anomalous cyclonic curvature over Yunnan (point B). This cyclonic curvature is enhanced by the easterly anomalies over the North of Yunnan. The cyclonic anomaly over Yunnan stretches to subtropical WNP, suggesting a weakened Western North Pacific subtropical high (WNPSH). The composite of horizontal wind field between wet and dry periods shows a similar pattern as the regression results (Figures 3C, D). The consistency between the regression and composite results confirms the horizontal wind pattern of the IDV of summer precipitation.

The link between the anomalous anticyclones over the Indo-Pacific warm pool and the anomalous cyclone over Yunnan is evident on the regression map of vertical circulation (Figure 4A). The anomalous descent over the BOB (point A) is associated with anomalous ascent to the southwest of Yunnan, which further enhances the ascending motion over Yunnan (point B). The anomalous ascent over Yunnan and the anomalous descent over the WPWP (point C) forms an anomalous anticlockwise circulation. Thus, the enhanced descending motion associated with anomalous anticyclones over the BOB and the WPWP would simultaneously intensify the rising motion over Yunnan. The composite result resembles the regression pattern (Figure 4B). The anomalous ascent over Yunnan is associated with an anomalous ascent over the East Asia coastal areas and an anomalous descent over the WNP (Figure 4C). The composite vertical circulation resembles the regression pattern (Figure 4D). Thus, the anomalous anticyclones over the BOB and the WPWP, and the anomalous descent over the WNP are main boosters of the rising motion over Yunnan. The

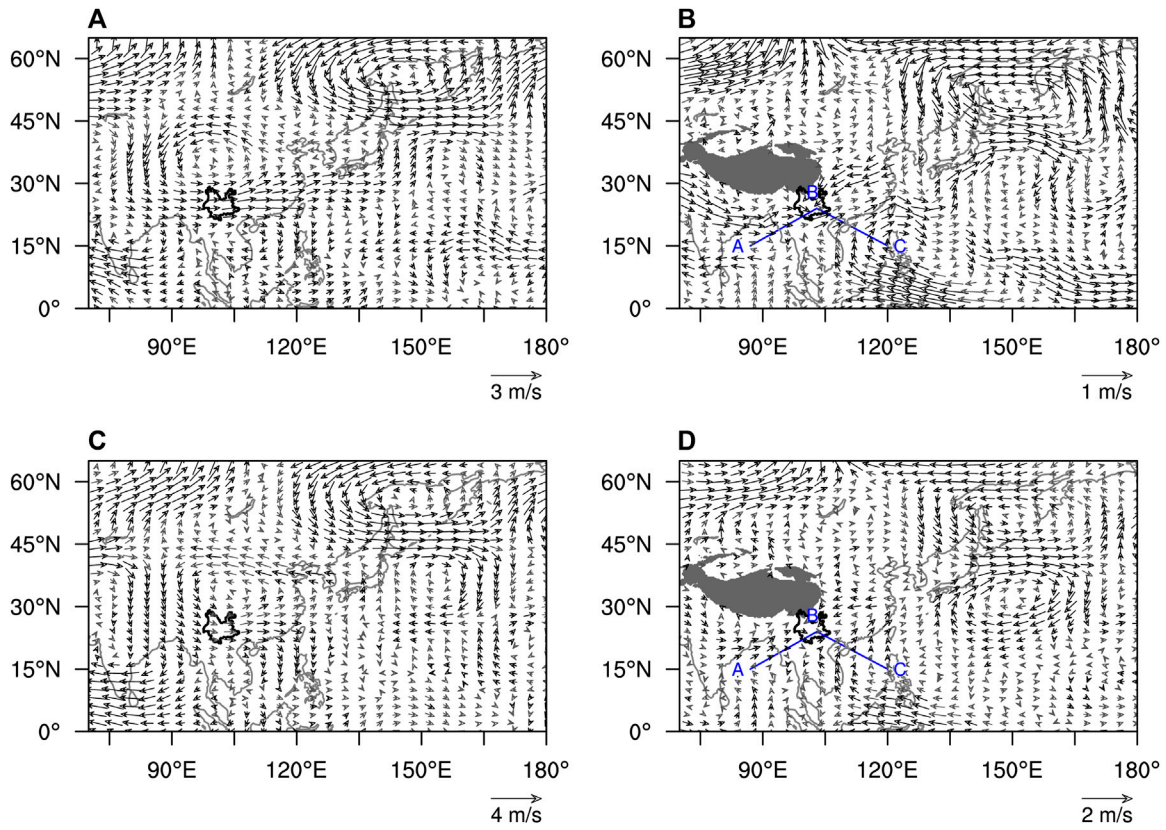

FIGURE 3
Regression of the interdecadal component of the JJA mean **(A)** 200 hPa horizontal winds (vector, units: ms^{-1}), **(B)** 700 hPa horizontal winds (vector, units: ms^{-1}) against the ID-PC1. Panels **(C,D)** are the same as **(A,B)**, except for the composite of the JJA mean variables between the wet and dry periods. The black vectors denote significance at the 95% confidence level. The letters **(A–C)** stand for three anomaly centers. The black solid line marks the boundary of Yunnan. The gray shadings in **(B,D)** represent the topography.

enhanced convection over Yunnan provides the dynamical condition for precipitation.

4.2 Decomposition of moisture transport

The column-integrated water vapor flux (CIWVF) shows an anomalous pattern basically consistent with the 700 hPa horizontal wind pattern (Figures 3B, D). Specifically, the anomalous anticyclone over the BOB facilitates the moisture transport from northern BOB to Yunnan (Figure 5A). The anomalous anticyclone over the WPWP also pushes the water vapor from the WPWP to southeastern Yunnan. The anomalous cyclone over Yunnan reinforces the water vapor supply from the BOB and the WPWP. The divergence of CIWVF (CIWVFD) shows significant negative anomalies over Yunnan, suggesting a strengthened moisture convergence favoring precipitation (Figure 5B). The composite results resemble the regression patterns of both the CIWVF and the CIWVFD (Figures 5C, D). Compared with the regression pattern, the composite pattern shows larger variation magnitude and more areas passing the significance test.

The CIWVFD can be decomposed into three terms that represent the dynamical effect of wind anomalies, the thermodynamical effect of specific humidity anomalies, and the perturbation effect of both wind anomalies and specific humidity anomalies (Eq. 1). The regressed anomalies of dynamical term $(-\frac{1}{g}\int_{p_s}^{100\,hPa}\nabla\cdot\bar{q}V'dp)$ bear the closest resemblance to the CIWVFD pattern among the three terms (Figure 6A). The thermodynamical term $(-\frac{1}{g}\int_{p_s}^{100\,hPa}\nabla\cdot q'\bar{V}dp)$ shows a weak moisture divergence over Yunnan, which counteracts the effect of dynamical term (Figure 6C). The impact of perturbation term over Yunnan is the smallest of three terms and is statistically insignificant (Figure 6E). Thus, the dynamical term plays a major role in the IDV of the CIWVFD. The composite results have similar patterns to the regression results of all decomposed terms (Figures 6B, D, F). The consistency between the regression pattern and the composite pattern validates the central role of wind anomalies in the IDV of the CIWVFD.

4.3 SST configuration

To identify the SST drivers for the IDV of summer rainfall in Yunnan, we regressed the JJA mean SST against the ID-PC1. The JJA mean SST was detrended and 7-year low-pass filtered before regression. Results show a uniform decrease in the SST over the BOB and the WPWP regions, and a tripole SSTA pattern over the WNP (Figure 7A). The significant SST decrease over the BOB and the WPWP is mainly over the equatorial parts of these two regions. Whereas the tripole SSTA pattern characterizes a significant SST

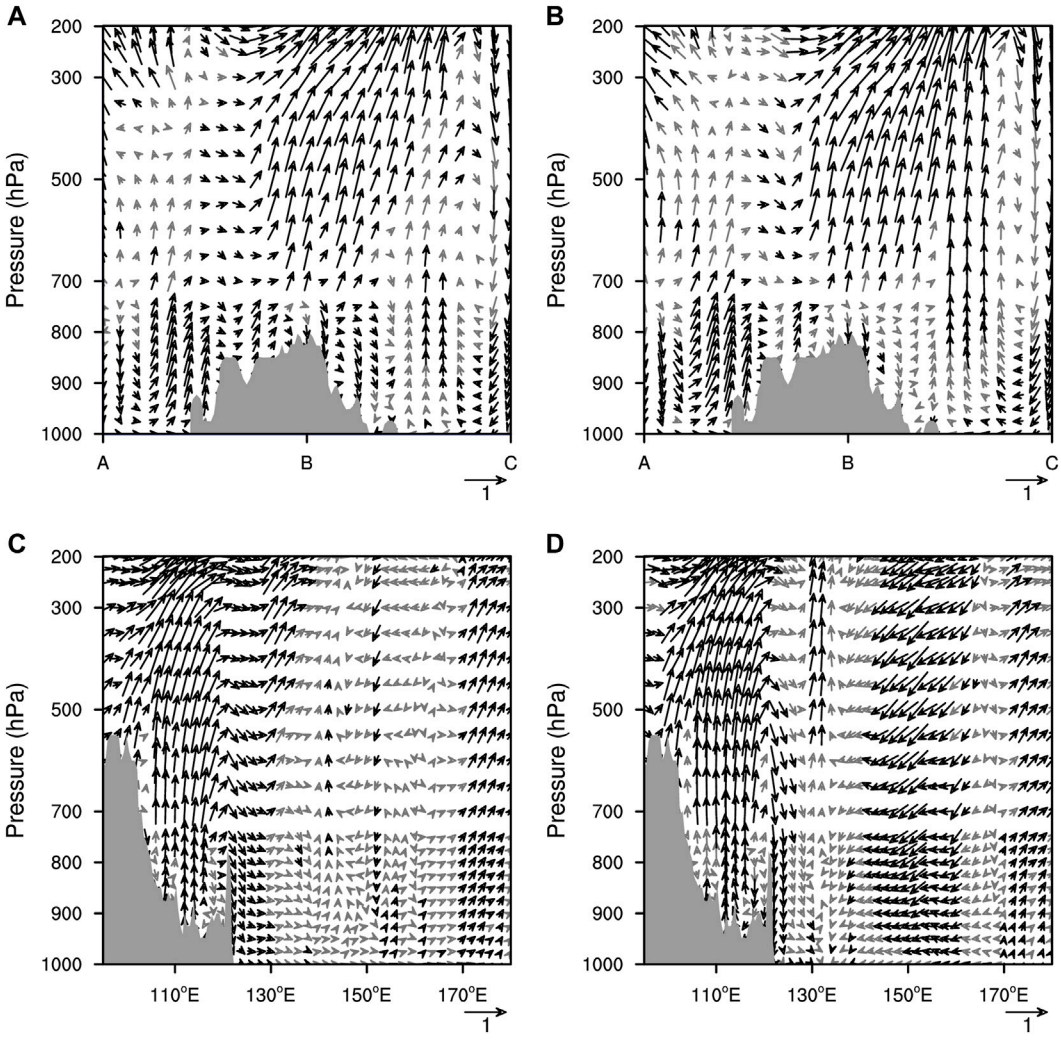

FIGURE 4
The anomalous vertical circulation derived from **(A)** regression against the ID-PC1 and **(B)** composite between the wet and dry periods along the line ABC of Figure 3A, and the anomalous vertical circulation averaged between 20°N and 30°N for **(C)** regression against the ID-PC1 and **(D)** composite between the wet and dry periods (unit: ms^{-1} for horizontal wind and 10^{-2} Pa s^{-1} for vertical velocity). The black vectors denote significance at the 95% confidence level. The gray shading represents the topography.

decrease over the tropical WNP and the northern WNP, with a significant SST increase in between the two regions. The composite SSTAs have a similar pattern to the correlation pattern (Figure 7B). We defined three SST indices to describe the IDV of the SSTAs over the BOB, the WPWP, and the WNP regions. The SST index for the BOB region is defined as the area average SST over (2.5°N–22.5°N, 80°E–105°E), and the SST index for the WPWP region is defined as the area average SST over (2.5°N–22.5°N, 105°E–130°E). Since the WNP tripole (WNPT) pattern resembles the North Atlantic tripole (NAT) but positioned at the WNP, we referred to Wu's definition of the NAT index to define the index of the WNPT pattern (Wu et al., 2011). The WNPT index is defined as (S* + N*)/2 − M*, where S*, N*, and M* refer to the normalized SST anomalies averaged over (2.5°N–17.5°N, 130°E–150°E), (25°N–40°N, 140°E–160°E), and (45°N–60°N, 140°E–160°E), respectively.

The IDV of summer precipitation in Yunnan is forced by the combined effect of the SSTAs over the BOB, the WPWP, and the WNP regions. To determine their relative contribution to the IDV of summer precipitation, we adopted the relative weights analysis to calculate the contribution rate of each SSTA (Johnson, 2000; Tonidandel and LeBreton, 2011). Specifically, the SST indices defined above represent the SSTAs over respective regions. The 7-year low-pass filtered average summer precipitation in Yunnan represents the IDV of summer precipitation. Results indicate that the contribution rate is 34% for the SSTA over the BOB, 20% for the SSTA over the WPWP, and 46% for the SST tripole over the WNP. Since the BOB and the WPWP regions constitute a major part of the northern Indo-Pacific warm pool, the combined effect of the BOB and the WPWP (54%) approximately equals to that of the WNP. Thus, we could assume that the northern Indo-Pacific warm pool and the WNP share an equal contribution to the IDV of summer precipitation in Yunnan.

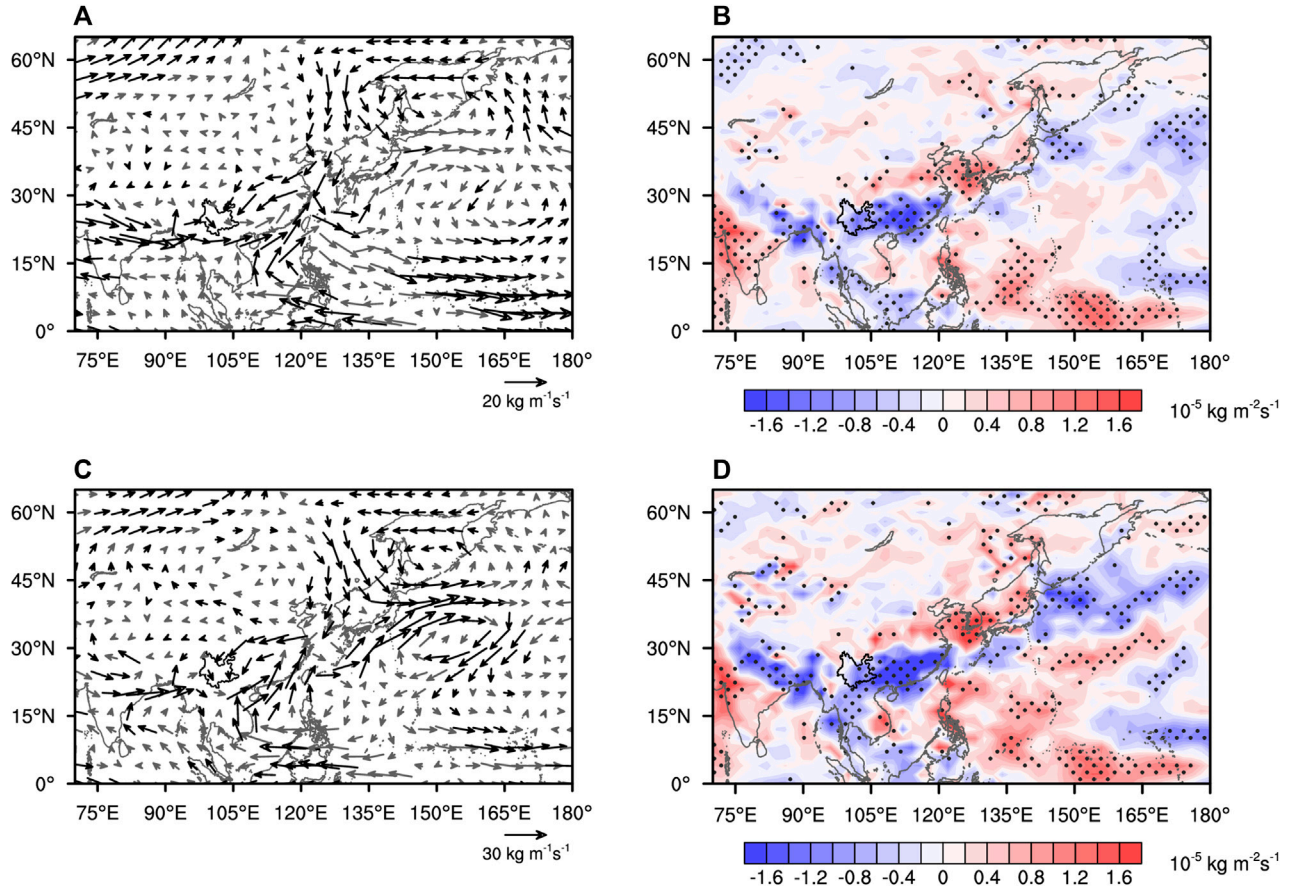

FIGURE 5
The anomalous CIWVF in summer derived from **(A)** regression against the ID-PC1 and **(C)** composite between the wet and dry periods (units: kg m^{-1} s^{-1}). Panels **(B,D)** are the same as **(A,C)** except for the CIWVFD (units: 10^{-5} kg m^{-2} s^{-1}). The black vectors denote significance at the 95% confidence level. The stippling in **(B,D)** denotes significance at the 95% confidence level. The black solid line marks the boundary of Yunnan.

5 Modelling results

We used the SPEEDY model to verify the effect of the SSTAs over the BOB and the WPWP on the IDV of summer precipitation in Yunnan. The SST forcing is set to the composite SSTA in Figure 7 over respective regions. Specifically, the negative SSTA over the BOB (BOB-) is used in the experiment No. 1 (EXP1, Figure 8A), the reversed SSTA over the BOB (BOB+) is used in the experiment No. 2 (EXP2, Figure 8B), the negative SSTA over the WPWP (WPWP-) is used in the experiment No. 3 (EXP3, Figure 8C), the reversed SSTA (WPWP+) is used in the experiment No. 4 (EXP4, Figure 8D), the WNP tripole (WNPT-) is used in the experiment No. 5 (EXP5, Figure 8E), the reversed SSTA (WNPT+) is used in the experiment No. 6 (EXP6, Figure 8F), the negative SSTAs over the BOB and the WPWP regions (BOB-&WPWP-) are used in the experiment No. 7 (EXP7, Figure 8G), and the reversed SSTAs (BOB+&WPWP+) are used in the experiment NO. 8 (EXP6, Figure 8H), the SSTAs over three regions (BOB-&WPWP-&WNPT-) are used in the experiment No. 9 (EXP9, Figure 8I), and the reversed SSTAs (BOB+&WPWP+&WNPT+) are used in the experiment No. 10 (EXP10, Figure 8J). In each experiment, the SSTAs are superimposed onto the climatological monthly mean SST in summer. For other seasons, the SSTAs are set to zero. The air-sea coupling is activated outside the prescribed SSTA regions. The model is integrated for 31 years in each experiment, and the first year of model integration is treated as the spin-up period. The model output of the last 30 years is used for analysis.

The negative SSTA over the BOB induces a significant low-level anticyclonic anomaly over the Indian subcontinent and the BOB (Figure 9A). This anomalous anticyclone is centered to the northwest of the SSTA, suggesting a Gill-Matsuno-type response. The westerly anomalies over the northern flank of the anticyclone favor the water vapor transport from the BOB to Yunnan. The westerly anomalies also conduce to the formation of an anomalous convergence over Yunnan. Consequently, the precipitation increases over Yunnan, but the significant changes are located to the South of Yunnan (Figure 9B). The negative SSTA over the WPWP induces an anomalous anticyclone stretching from tropical Northern IO to tropical WNP (Figure 9C). This elongated anticyclone also resembles the Gill-Matsuno-type response to the SSTA over the WPWP. The anomalous anticyclone enhances the anomalous convergence over Yunnan, causing a significant increase in precipitation (Figure 9D). Compared with the atmospheric response to the SSTA over the BOB, the SSTA over the WPWP further strengthens the Southwesterly anomalies over southeastern Yunnan. The WNPT induces an anticyclonic anomaly over the northern WNP and a cyclonic anomaly over the central WNP

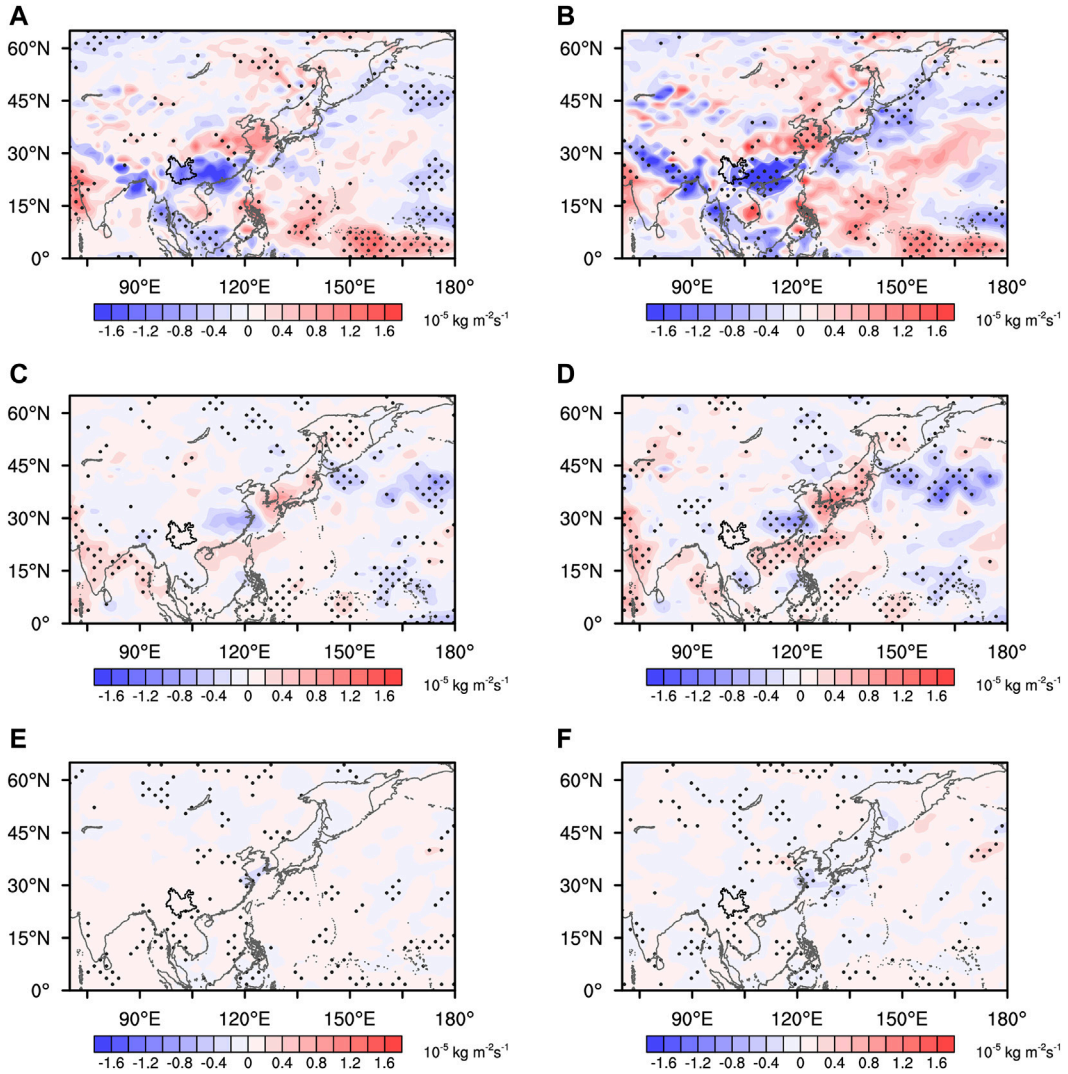

FIGURE 6
Regression coefficient of **(A)** dynamical term ($-\frac{1}{g}\int_{p_s}^{100\,hPa}\nabla\cdot\bar{q}V'dp$), **(C)** thermodynamical term ($-\frac{1}{g}\int_{p_s}^{100\,hPa}\nabla\cdot q'\bar{V}dp$), and **(E)** perturbation term ($-\frac{1}{g}\int_{p_s}^{100\,hPa}\nabla\cdot q'V'dp$) against the ID-PC1 (units: 10^{-5} kg m^{-2} s^{-1}). Panels **(B)**, **(D)**, and **(F)** are the same as **(A)**, **(C)**, and **(E)** except for the composite between the wet and dry periods. The stippling denotes significance at the 95% confidence level. The black solid line marks the boundary of Yunnan.

(Figure 9E). This anomalous anticyclone–cyclone pair resembles the atmospheric response to the North Atlantic tripole. The cyclonic anomaly over the central WNP weakens the WNPSH that further strengthens the anomalous convergence over Yunnan. The negative SSTA over the tropical WNP induces an anomalous anticyclone that also strengthens the cyclonic curvature over Yunnan. Consequently, the precipitation increases in Yunnan (Figure 9F).

The combined SSTAs over the BOB and the WPWP induce a stronger anticyclonic anomaly over the tropical IO and tropical WNP, making a stronger cyclonic anomaly over Yunnan (Figure 9G). The precipitation increases more than that in the single SSTA forcing experiments (Figure 9H). The WNPT reinforces the cyclonic anomaly over Yunnan by inducing a stronger anticyclonic anomaly over the Indo-Pacific warm pool and a stronger cyclonic over the WNP (Figure 9I). The horizontal wind pattern suggests an intensified cyclonic curvature over southern Yunnan, associated with a weakened WNPSH. Consequently, the combined SSTAs over the three regions induces the largest increase in precipitation (Figure 9J). The anticyclonic anomaly over the central WNP (Figures 3B, D) is located to the east of 150°E in the model results, suggesting that the local air-sea coupling (not applicable in the prescribed SST forcing) also matters to the horizontal wind patterns.

The CIWVF resembles the 700 hPa horizontal wind pattern in each experiment (Figures 10A, D, G, J, 10 m). The SSTA over the BOB mainly enhances the moisture transport from tropical IO to Yunnan (Figure 10B). Likewise, the SSTA over the WPWP intensifies the moisture transport from the WPWP to Yunnan (Figure 10E). The WNPT induces the water vapor divergence over the tropical BOB, the WPWP, and the tropical WNP, which favors the moisture transport to Yunnan from the three regions (Figure 10H). The combined SSTAs over the BOB and the WPWP intensifies the water vapor divergence to the South of Yunnan, causing more moisture supply to Yunnan than under the single

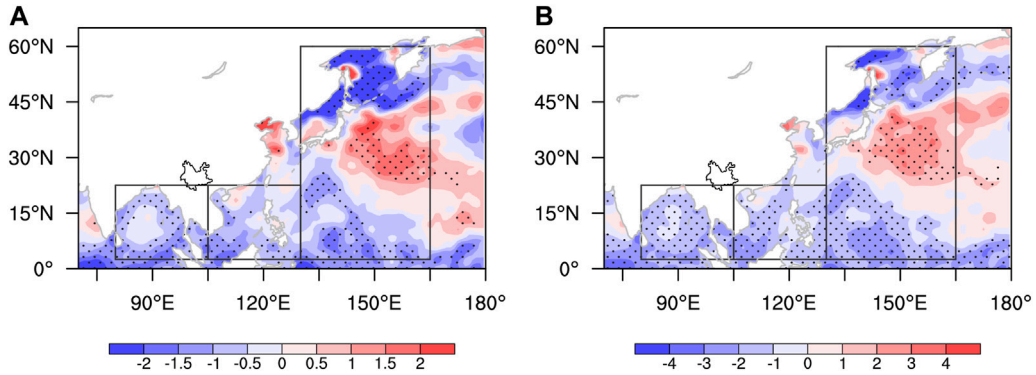

FIGURE 7
Regression coefficient of the JJA mean SST (units: K 10 years^{-1}), **(B)** are the same as **(A)**, except for composite differences of the JJA mean variables between the relatively wet period and the relatively dry period. The stippling denotes the differences significant at the 95% confidence levels. The region bounded by the black solid line indicates the Yunnan. Black boxes are SST key zones of the BOB, the WPWP, and the WNPT.

SSTA forcing (Figure 10K). The presence of WNPT reinforces the water vapor divergence over the tropical WNP and the WPWP (Figure 10J). Consequently, the moisture convergence over Yunnan is the strongest among all cases. The major contributor to the CIWVF, the dynamical term $(-\frac{1}{g}\int_{p_s}^{100\,hPa}\nabla\cdot\bar{q}V'dp)$, shows a consistent pattern with the total CIWVFD (Figures 10C, F, I, L, O). The gradual increase in moisture convergence over Yunnan also highlights the synergistic effect of the SSTAs over the BOB, the WPWP, and the WNPT on the IDV of summer precipitation in Yunnan. The above model results confirm the modulating effect of the SSTAs over the three regions, and the dominant role of dynamical term $(-\frac{1}{g}\int_{p_s}^{100\,hPa}\nabla\cdot\bar{q}V'dp)$ in modulating the moisture supply.

6 Discussion and conclusion

In this study, the IDV of summer precipitation in Yunnan and its possible causes were investigated with the ground-observation data, the ERA5 and the HadISST reanalysis data during 1961–2019. Results suggest that the IDV of summer precipitation in Yunnan has a significant period of 9–11 years. The IDV pattern characterizes consistent changes regionwide, with large amplitude over the Southern and central-eastern Yunnan. The IDV of summer precipitation has undergone three dry-wet transitions since 1961. The phase change of the IDV characterizes a relatively wet period before 1974, a relatively dry period of 1983–1992, a relatively wet period of 1993–2002, and a relatively dry period of 2003–2019. The IDV of moisture transport is essential to the IDV of summer precipitation. The IDV of moisture supply over Yunnan is ascribed mainly to the dynamical term $(-\frac{1}{g}\int_{p_s}^{100\,hPa}\nabla\cdot\bar{q}V'dp)$, where the wind anomalies play a central role in modulating the water vapor transport.

The IDV of summer precipitation in Yunnan is attributed mainly to the SSTAs over the BOB, the WPWP, and the WNP regions. The negative SSTA over the BOB induces a Gill-Matsuno-type response that manifests as an anticyclonic anomaly over the Indian subcontinent—BOB region. This anomalous anticyclone intensifies westerly anomalies over the northern BOB that facilitates the moisture transport to Yunnan and strengthens the cyclonic anomaly over Yunnan. Likewise, the negative SSTA over the WPWP induces an elongated anticyclonic anomaly over the Northern Indo-Pacific warm pool. The anomalous anticyclone enhances the water vapor transport from the WPWP to Yunnan, and also strengthens the cyclonic anomaly over Yunnan. The SSTAs over the WNP characterizes a tripole pattern (WNPT) that favors the moisture transport from the BOB, the WPWP, and the WNP to Yunnan. The joint effect of SSTAs over the BOB and the WPWP intensifies the cyclonic anomaly over Yunnan and enhances the moisture transport from the BOB and the WPWP to Yunnan. The WNPT reinforces the moisture convergence over Yunnan by intensifying the anticyclonic anomaly over the Indo-Pacific warm pool and weakening the WNPSH. Consequently, Yunnan experienced a relatively wet period. The positive SSTAs over the BOB and the WPWP would induce the opposite atmospheric response that further reduces the precipitation in Yunnan. Numerical experiments confirm the modulating effect of the SSTAs over the three regions, and the primary contribution of the dynamical term $(-\frac{1}{g}\int_{p_s}^{100\,hPa}\nabla\cdot\bar{q}V'dp)$ to the changes in moisture transport.

The main characteristics of anomalous circulation patterns associated with the IDV of summer precipitation in Yunnan still remain unchanged using the JRA55 dataset (Kobayashi et al., 2015) (Supplementary Figures S1, S2). The horizontal wind pattern characterizes an elongated anticyclonic anomaly over the Indo-Pacific warm pool associated with a weakened WNPSH. When the WNPSH is strengthened, the western ridge point shifts west and South that would form a high-pressure barrier from the WNP to the Indian subcontinent. This high-pressure barrier would impede the moisture transport to Yunnan and hence reduce the precipitation. When the WNPSH is weakened, the opposite condition occurs that conduces to summer precipitation in Yunnan. Note that the anomalous patterns also resemble the EAP teleconnection. For instance, the 850 hPa wind field characterizes an anticyclonic anomaly over the Western Pacific warm pool and a cyclonic anomaly over Northeast Asia. This dipole structure resembles the 850 hPa wind pattern during the EAP positive phase (Huang and Sun, 1992; Wu et al., 2016). The IDV of moisture flux and the SST pattern also resemble the EAP-related changes in the water vapor

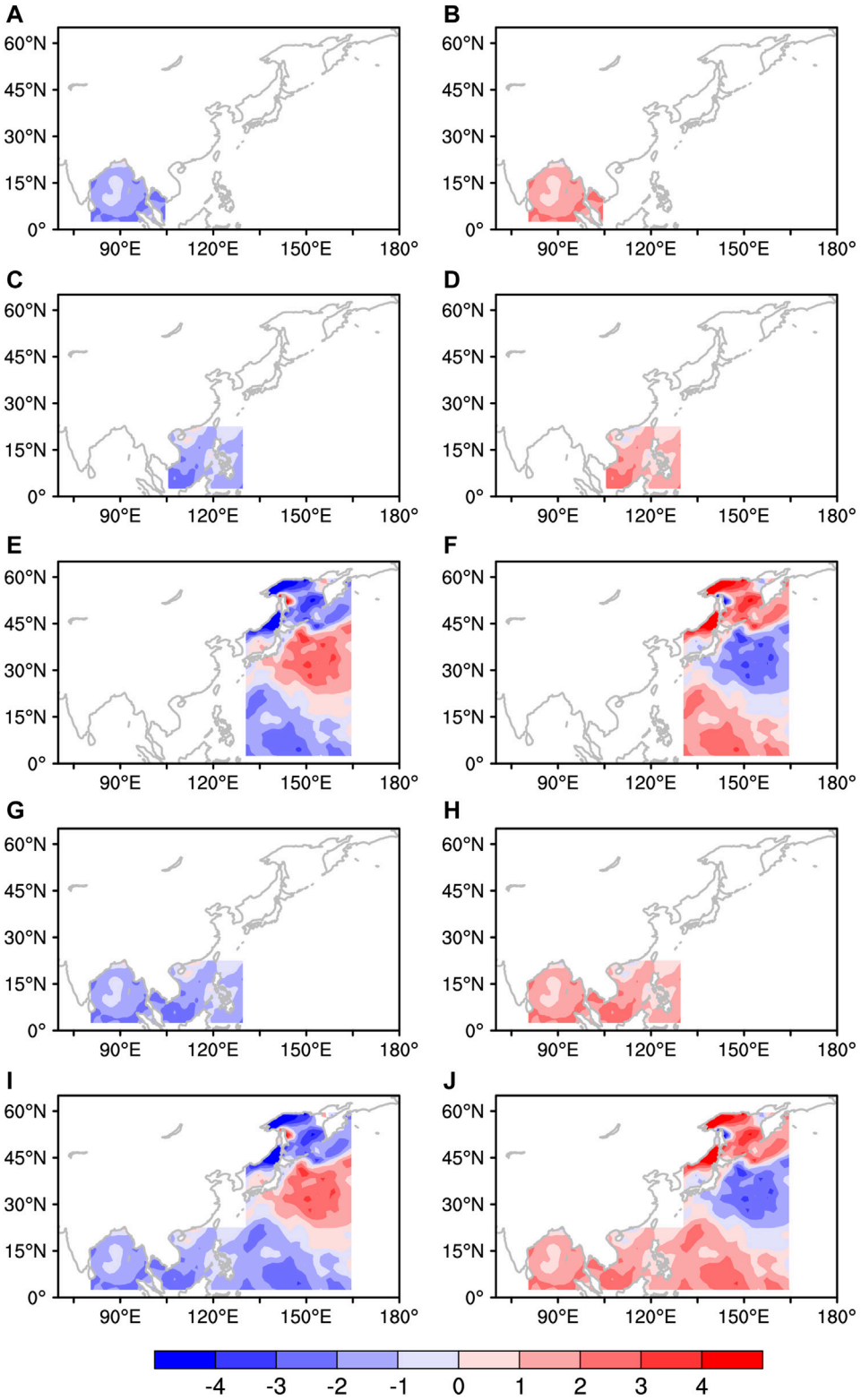

FIGURE 8
The SSTAs superimposed onto the SPEEDY model for **(A)** the BOB^{-}, **(B)** the BOB^{+}, **(C)** $WPWP^{-}$, **(D)** $WPWP^{+}$, **(E)** $WNPT^{-}$, **(F)** $WNPT^{+}$, **(G)** BOB^{-}&$WPWP^{-}$, **(H)** BOB^{+}&$WPWP^{+}$, **(I)** BOB^{-}&$WPWP^{-}$&$WNPT^{-}$, **(J)** BOB^{+}&$WPWP^{+}$&$WNPT^{+}$ experiments (units: K 10 $years^{-1}$).

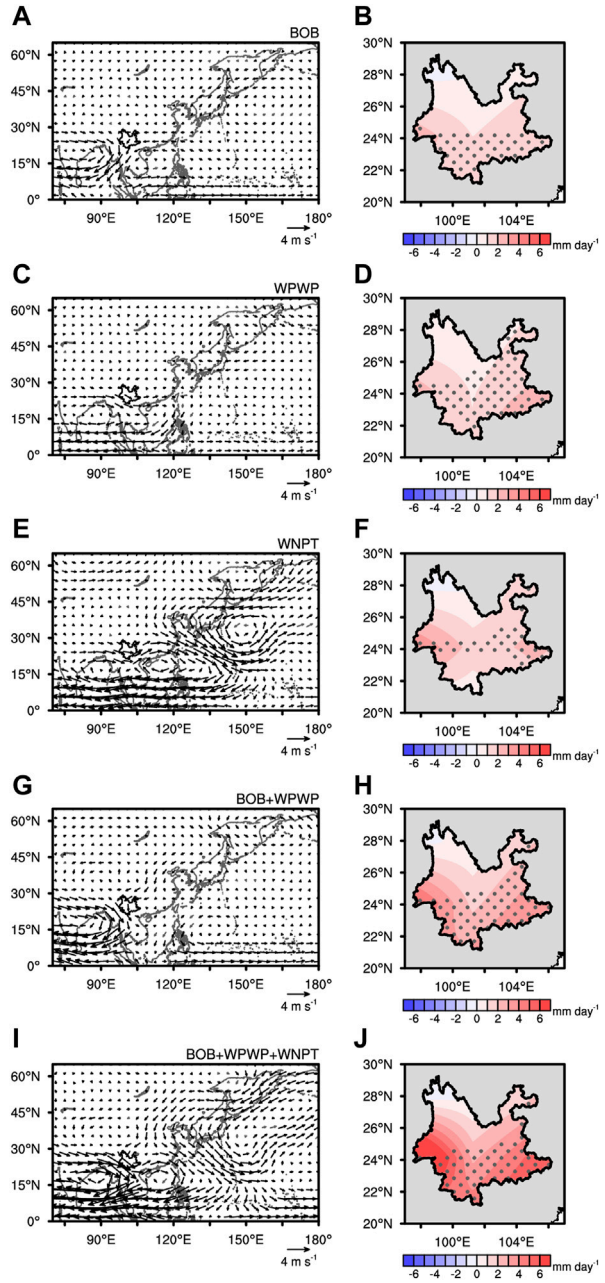

FIGURE 9
Difference in **(A)** 700 hPa horizontal wind and **(B)** precipitation between the BOB$^-$ and the BOB$^+$ experiments. Panels **(C,D)** are the same as **(A,B)** except for the difference between the WPWP$^-$ and the WPWP$^+$ experiments. Panels **(E,F)** are the same as **(A,B)** except for the difference between the WNPT$^-$ and the WNPT$^+$ experiments. Panels **(G,H)** are the same as **(A,B)** except for the difference between the BOB$^-$&WPWP$^-$ and the BOB$^+$&WPWP$^+$ experiments. Panels **(I,J)** are the same as **(A,B)** except for the difference between the BOB$^-$&WPWP$^-$&WNPT$^-$ and the BOB$^+$&WPWP$^+$&WNPT$^+$ experiments. The black vectors in **(A)**, **(C)**, **(E)**, **(G)**, **(I)** denote the difference is significant at the 95% confidence level, and the stippling in **(B)**, **(D)**, **(F)**, **(H)**, **(J)** denote significant difference at the 95% confidence level.

flux and the SST (Li et al., 2019b; Yin et al., 2021). Thus, the EAP pattern could be a primary factor of the IDV of summer precipitation in Yunnan. Since the EAP-related changes in precipitation are statistically insignificant over many parts of Yunnan, the EAP could indirectly affect the IDV of summer precipitation in Yunnan by reinforcing the anomalous wind patterns over Eastern China.

The IDV of summer precipitation in Yunnan could also link to the interdecadal oceanic modes in the Northern Indian Ocean and the Northern Pacific, such as the Pacific Decadal Oscillation (PDO), North Pacific Gyre Oscillation (NPGO) and the Indian Ocean Dipole (IOD). We calculated the correlation coefficient between the ID-PC1 of summer precipitation in Yunnan and the indices of oceanic decadal modes. The oceanic indices include the PDO index provided by the National Centers for Environmental Information (NCEI) (Deser and Trenberth, 2022), the NPGO index provided by Dr. Di Lorenzo (Di et al., 2008), and the IOD index provided by NOAA Physical Sciences Laboratory. The correlation coefficient is −0.10 between the ID-PC1 and the IOD index, −0.59 between the ID-PC1 and the NPGO index, and 0.15 between the ID-PC1 and the PDO index. Thus, only the NPGO is a potential driver of the IDV of summer precipitation in Yunnan. We further regressed the horizontal wind against the NPGO index normalized by its standard deviation. To facilitate comparison with the manuscript, a negative sign is added to the NPGO index before regression. Results show significant increases in precipitation over some parts of Yunnan (Supplementary Figure S3).

The regressed wind anomalies against the NPGO index characterize an anticyclonic anomaly over central Asia at 200 hPa (Supplementary Figure S4A). This anticyclonic anomaly resembles the regression pattern against the ID-PC1, but the anomalous anticyclone is centered to the North of 40°N. For the regression pattern against the ID-PC1, the anticyclonic anomaly is centered to the South of 40°N. The anomalous wind pattern at 850 hPa characterizes a cyclonic anomaly over western Pacific warm pool (to the East of point C), a weak cyclonic anomaly over subtropical Western Pacific, and an anticyclonic anomaly to the east of Japan (Supplementary Figure S4B). The anomalous cyclone over the western Pacific warm pool is opposite to the regression pattern against the ID-PC1. The regressed wind anomalies are statistically insignificant over the BOB (point A). The above wind anomalies resemble the regression pattern against the ID-PC1 over the Western North Pacific, but nearly opposite to the regression pattern against the ID-PC1 over the tropical Indian Ocean and the Western Pacific warm pool. This circulation pattern weakens the cyclonic curvature over Yunnan (point B). Consequently, the variation in precipitation is statistically insignificant over many parts of Yunnan. The above results suggest that the NPGO could affect the IDV of summer precipitation in Yunnan by inducing a wind anomaly pattern over the western North Pacific.

This study indicates that the IDV of summer precipitation in Yunnan is affected mainly by the WNP rather than the IO. Nevertheless, previous studies suggest that the interannual variation of summer precipitation in Yunnan is attributed mainly to the IO (Cao et al., 2014; Wang et al., 2018). Thus, the major contributor to the summer precipitation in Yunnan varies with the timescales of variability. The SST configuration involves the SSTAs over three regions, i.e., the BOB, the WPWP, and the WNP regions. To reveal the potential linkage among the SSTAs, we calculated the correlation coefficients between each pair of the SST indices (Supplementary Figure S5). Only the SST indices of the BOB and the WPWP are significantly correlated with each other

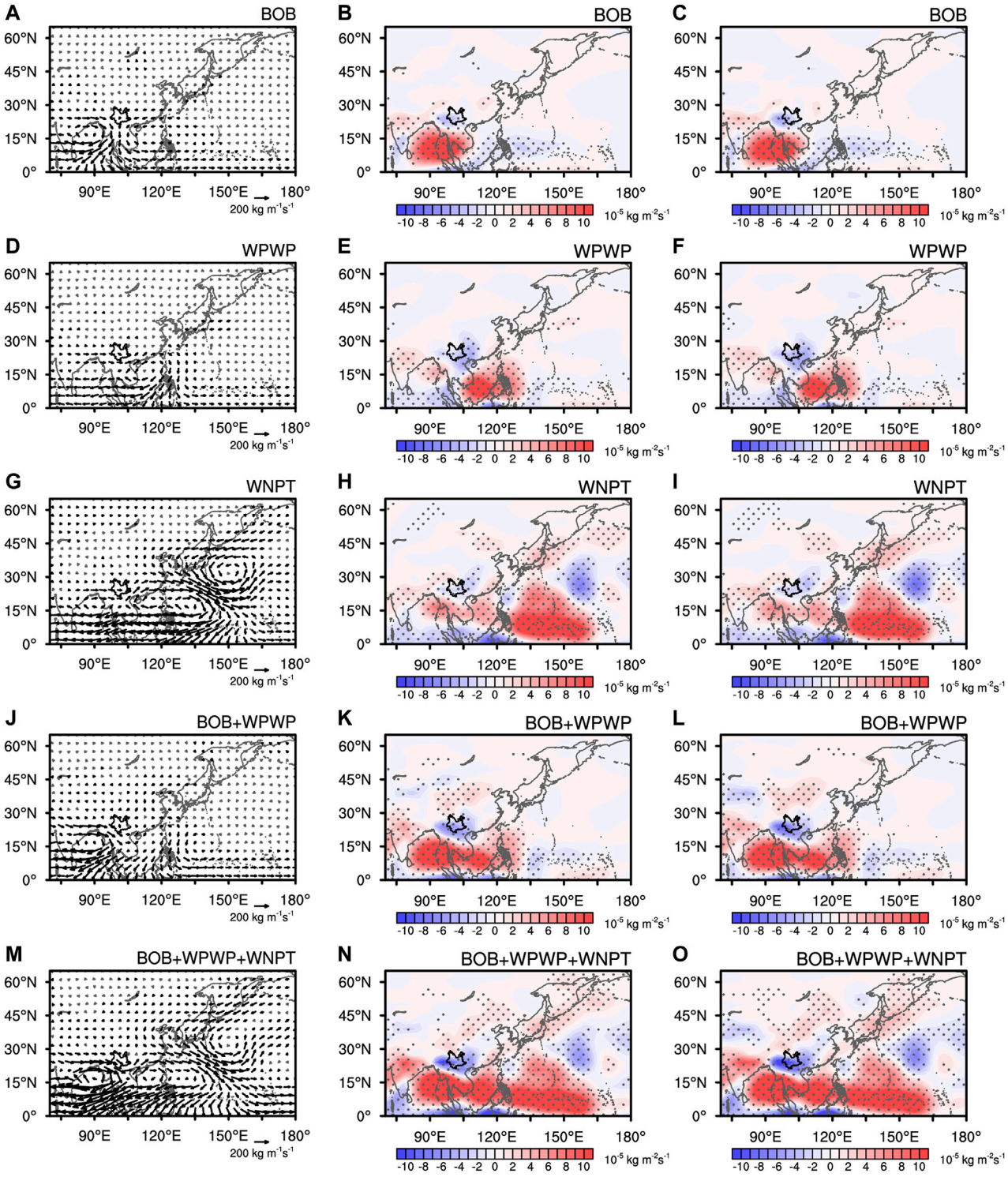

FIGURE 10
Difference in **(A)** the CIWVF, **(B)** the CIWVFD, and **(C)** the divergence of the dynamical term ($-\frac{1}{g}\int_{p_s}^{100\,hPa}\nabla\cdot\bar{q}V'dp$) between the BOB$^-$ and the BOB$^+$ experiments. Panels **(D–F)** are the same as **(A–C)** except for the difference between the WPWP$^-$ and the WPWP$^+$ experiments. Panels **(G–I)** are the same as **(A–C)** except for the difference between the WNPT$^-$ and the WNPT$^+$ experiments. Panels **(J–L)** are the same as **(A–C)** except for the difference between the BOB$^-$&WPWP$^-$ and BOB$^+$&WPWP$^+$ experiments. Panels **(M–O)** are the same as **(A–C)** except for the difference between the BOB$^-$&WPWP$^-$&WNPT$^-$ and the BOB$^+$&WPWP$^+$&WNPT$^+$ experiments. The black vectors and the stippling denote significance at the 95% confidence level.

(Supplementary Table S1). We further calculated the correlation coefficient between each SST index and the interdecadal SST data (Supplementary Figure S6). The correlation maps also show significant SSTAs over the BOB and the WPWP regions using the SST indices of the BOB and the WPWP (Supplementary Figures S6A, B), whereas the WNPT has little connection with the SSTA patterns over the BOB and the WPWP (Supplementary Figure S6C). Thus, there is a high possibility that the SSTAs over the BOB join forces with the SSTAs over the WPWP, but a low possibility for them to synergize with the WNPT pattern. There is a high possibility that the SSTAs over the BOB join forces with the SSTAs over the WPWP, but a slight lower possibility for them to synergize with the WNPT pattern. Given the coordinated variation in the SSTAs over different ocean areas, the impact of tropical Eastern Pacific and tropical North Atlantic still needs clarification. Other external forcings such as the snow cover and soil moisture, and the land-atmosphere interaction could also affect the IDV of summer precipitation in Yunnan. A further investigation from the above angles would greatly deepen the understanding of the IDV of summer precipitation in Yunnan.

Data availability statement

The ERA5 dataset for this study can be found at the Copernicus Climate Data Store [https://www.ecmwf.int/en/forecasts/dataset/ecmwf-reanalysis-v5]. The HadISST data can be found at the Met Office Hadley Centre [https://www.metoffice.gov.uk/hadobs/hadisst].

Author contributions

ZD: Data curation, Formal Analysis, Investigation, Writing–review and editing. SG: Formal Analysis, Investigation, Writing–original draft. RY: Conceptualization, Funding acquisition, Project administration, Resources, Supervision, Writing–review and editing. JC: Methodology, Visualization, Writing–review and editing. HY: Methodology, Visualization, Writing–review and editing. JM: Writing–review and editing.

Funding

National Natural Science Foundation of China, grant numbers 41975093, 42022035, and 42375050, the Natural Science Foundation of Yunnan Province, grant number 202302AN360006 and 202301AV070001.

Acknowledgments

The authors are thankful to Prof. Jie Cao from Yunnan University, Prof. Chuanfeng Zhao from Peking University, and Prof. Lin Wang from the Institute of Atmospheric Physics, Chinese Academy of Science, for their constructive comments of research analysis.

Conflict of interest

The authors declare that the research was conducted in the absence of any commercial or financial relationships that could be construed as a potential conflict of interest.

Publisher's note

All claims expressed in this article are solely those of the authors and do not necessarily represent those of their affiliated organizations, or those of the publisher, the editors and the reviewers. Any product that may be evaluated in this article, or claim that may be made by its manufacturer, is not guaranteed or endorsed by the publisher.

Supplementary material

The Supplementary Material for this article can be found online at: https://www.frontiersin.org/articles/10.3389/fenvs.2023.1281202/full#supplementary-material

References

Afyouni, S., Smith, S. M., and Nichols, T. E. (2019). Effective degrees of freedom of the Pearson's correlation coefficient under autocorrelation. *NeuroImage* 199, 609–625. doi:10.1016/j.neuroimage.2019.05.011

Cao, J., Gui, S., Su, Q., and Yang, Y. (2016). The variability of the Indian–East Asian summer monsoon interface in relation to the spring seesaw mode between the Indian Ocean and the central-western pacific. *J. Clim.* 29, 5027–5040. doi:10.1175/JCLI-D-15-0839.1

Cao, J., Hu, J., and Tao, Y. (2012). An index for the interface between the Indian summer monsoon and the East Asian summer monsoon. *J. Geophys. Res. Atmos.* 117. doi:10.1029/2012JD017841

Cao, J., Yao, P., Wang, L., and Liu, K. (2014). Summer rainfall variability in low-latitude highlands of China and subtropical Indian Ocean Dipole. *J. Clim.* 27 (2), 880–892. doi:10.1175/JCLI-D-13-00121.1

Chen, Y., Guo, S., Liu, Y., Ju, J., and Ren, J. (2017). Interannual variation of the onset of yunnan's rainy season and its relationships with the arctic oscillation of the preceding winter. *Atmos. Clim. Sci.* 7, 210–222. doi:10.4236/acs.2017.72015

Cheng, J. G., Yan, H. M., and Yan, H. S. (2009). *Characteristics and causes of major climate disasters in Yunnan*. Beijing: Meteorological Publishing House.

Deser, C., and Trenberth, K. (2022). "Atmospheric research staff," in *Last modified 2022-09-09 "the climate data guide: Pacific decadal oscillation (PDO): Definition and indices*. Available at: https://climatedataguide.ucar.edu/climate-data/pacific-decadal-oscillation-pdo-definition-and-indices on 2023-09-04.

Di, L. E., Schneider, N., Cobb, K. M., Chhak, K., Franks, P. J. S., Miller, A. J., et al. (2008). North Pacific Gyre Oscillation links ocean climate and ecosystem change. *Geophys. Resarch Lett.* 35, L08607. doi:10.1029/2007GL032838

Dong, D. H., Tao, W. C., Lau, L., Li, Z. Q., Huang, G., and Wan, P. F. (2019). Interdecadal variation of precipitation over the hengduan mountains during rainy seasons. *J. Clim.* 32, 3743–3760. doi:10.1175/JCLI-D-18-0670.1

Duan, X., Ju, J. H., and Xiao, Z. N. (2000). *Research on physical processes and prediction signals of climate anomalies in Yunnan*. Beijing: Meteorological Press, 1–154.

Gao, L., Han, X., Chen, X. L., Liu, B. Q., and Li, Y. (2023). The spring drought in yunnan province of China: Variation characteristics, leading impact factors, and physical mechanisms. *Atmosphere* 14, 294. doi:10.3390/atmos14020294

Gong, D. Y., and Ho, C. H. (2002). Shift in the summer rainfall over the Yangtze River valley in the late 1970s. *Geophys. Res. Lett.* 29, 78-1–78-4. doi:10.1029/2001GL014523

Guo, Y. R., Cao, J., Li, H., Wang, J., and Ding, Y. C. (2016). Simulation of the interface between the Indian summer monsoon and the East Asian summer monsoon: Intercomparison between MPI-ESM and ECHAM5/MPI-OM. *Adv. Atmos. Sci.* 33, 294–308. doi:10.1007/s00376-015-5073-z

Han, Y., Jiang, X. J., He, T., Wang, D., Guo, N., Zhang, X., et al. (2018). PD-1/PD-L1 inhibitor screening of caffeoylquinic acid compounds using surface plasmon resonance spectroscopy. *Water Resour. Dev. Manag.* 2, 52–56. doi:10.1016/j.ab.2018.02.003

He, Y., Zhou, C., and Ahmed, T. (2021). Vulnerability assessment of rural social-ecological system to climate change: A case study of yunnan province, China. *Int. J. Clim. Change Strategies Manag.* 13, 162–180. doi:10.1108/IJCCSM-08-2020-0094

Hu, Z. Z. (1997). Interdecadal variability of summer climate over East Asia and its association with 500 hPa height and global sea surface temperature. *J. Geophys. Res. Atmos.* 102, 19403–19412. doi:10.1029/97JD01052

Huang, R. H., Liu, Y., Wang, L., and Wang, L. (2012). Analyses of the causes of severe drought occurring in southwest China from the fall of 2009 to the spring of 2010. *Atmos. Sci.* 36, 443–457. doi:10.3878/j.issn.1006-9895.2011.11101

Huang, R., and Sun, F. (1992). Impacts of the tropical western Pacific on the East Asian summer monsoon. *J. Meteorological Soc. Jpn.* 70, 243–256. doi:10.2151/jmsj1965.70.1B_243

Johnson, J. W. (2000). A heuristic method for estimating the relative weight of predictor variables in multiple regression. *Multivar. Behav. Res.* 35, 1–19. doi:10.1207/S15327906MBR3501_1

Kobayashi, S., Ota, Y., Harada, Y., Ebita, A., Moriya, M., Onoda, H., et al. (2015). The JRA-55 Reanalysis: General specifications and basic characteristics. *J. Meteorological Soc. Jpn.* 93, 5–48. doi:10.2151/jmsj.2015-001

Kucharski, F., Molteni, F., King, M. P., Farneti, R., Kang, I.-S., and Feudale, L. (2013). On the need of intermediate complexity general circulation models: A "SPEEDY" example. *Bull. Am. Meteorological Soc.* 94, 25–30. doi:10.1175/BAMS-D-11-00238.1

Li, C., Peng, L., Zhou, M., Wei, Y., Liu, L., Li, L., et al. (2022). SIF-based GPP is a useful index for assessing impacts of drought on vegetation: An example of a mega-drought in yunnan province, China. *Remote Sens.* 14, 1509. doi:10.3390/rs14061509

Li, S., Feng, G., Hou, W., and Cheng, J. (2019a). Characteristics of atmospheric circulation patterns over East Asia and their impacts on precipitation in summer. *Clim. Res.* 78, 117–133. doi:10.3354/cr01544

Li, Y. J., Wang, Z. X., Zhang, Y. Y., Li, X., and Huang, W. (2019b). Drought variability at various timescales over yunnan province, China: 1961-2015. *Theor. Appl. Climatol.* 138, 743–757. doi:10.1007/s00704-019-02859-z

Liu, F., Ouyang, Y., Wang, B., Yang, J., Li, J., and Hsu, P. C. (2020). Seasonal evolution of the intraseasonal variability of China summer precipitation. *Clim. Dyn.* 54, 4641–4655. doi:10.1007/s00382-020-05251-0

Liu, J. P., Ren, H. L., Li, W. J., and Zuo, J. (2018b). Remarkable impacts of Indian Ocean sea surface temperature on interdecadalvariability of summer rainfall in Southwestern China. *Atmosphere* 9, 103. doi:10.3390/atmos9030103

Liu, L., Cao, J., and He, D. (2011). Interdecadal variation of heavy precipitation events and their causes in the low latitude plateau of China. *Atmos. Sci.* 35, 435–443.

Liu, S. G., Leng, X. X., Sun, G. Z., Peng, Y. L., Huang, Y. F., and Yang, Q. L. (2018a). Assessment of drought characteristics in Yunnan Province based on SPI and SPEI from 1961-2100. *J. Agric. Mach.* 49, 236–245+299. doi:10.6041/j.issn.1000-1298.2018.12.029

Liu, Y. Y., Hu, Z. Z., Wu, R. G., and Yuan, X. (2022). Causes and predictability of the 2021 spring southwestern China severe drought. *Adv. Atmos. Sci.* 39, 1766–1776. doi:10.1007/s00376-022-1428-4

Lü, J. M., Ju, J. H., Ren, J. Z., and Gan, W. W. (2012). The influence of the Madden-Julian Oscillation activity anomalies on Yunnan's extreme drought of 2009-2010. *Sci. Sin. Terrae* 42, 98–112. doi:10.1007/s11430-011-4348-1

Lü, J. M., Zhu, C. W., Ju, J. H., and Lin, X. (2014). Interdecadal variability in summer precipitation over east China during the past 100 Years and its possible causes. *Chin. J. Atmos. Sci.* 38, 782–794. doi:10.3878/j.issn.1006-9895.1401.13227

Molteni, F. (2003). Atmospheric simulations using a gcm with simplified physical parametrizations. I: Model climatology and variability in multi-decadal experiments. *Clim. Dyn.* 20, 175–191. doi:10.1007/s00382-002-0268-2

Nitta, T., and Hu, Z. Z. (1996). Summer climate variability in China and its association with 500 hPa height and tropical convection. *J. Meteorological Soc. Jpn.* 74, 425–445. doi:10.2151/jmsj1965.74.4_425

Park, J. H., and An, S. I. (2014). The impact of tropical western Pacific convection on the North Pacific atmospheric circulation during the boreal winter. *Clim. Dyn.* 43, 2227–2238. doi:10.1007/s00382-013-2047-7

Pradhan, N. S., Fu, Y., Zhang, L., and Yang, Y. (2017). Farmers' perception of effective drought policy implementation: A case study of 2009–2010 drought in yunnan province, China. *Land Use Policy* 67, 48–56. doi:10.1016/j.landusepol.2017.04.051

Qin, J. (1998). Climate change and analysis of agrometeorological hazards in Yunnan. *Meteorology* 24, 45–51.

Shi, Z., Sha, Y., and Liu, X. (2017). Effect of yunnan–guizhou topography at the southeastern Tibetan plateau on the Indian monsoon. *J. Clim.* 30, 1259–1272. doi:10.1175/JCLI-D-16-0105.1

Tao, Y., Cao, J., Lan, G., and Su, Q. (2016). The zonal movement of the Indian-East Asian summer monsoon interface in relation to the land-sea thermal contrast anomaly over East Asia. *Clim. Dyn.* 46, 2759–2771. doi:10.1007/s00382-015-2729-4

Tao, Y., Zhang, W. C., Duan, C. C., Chen, Y., Ren, J. Z., Xing, D., et al. (2014). Climatic causes of continuous drought over Yunnan Province from 2009 to 2012. *J. Yunnan Univ. Nat. Sci. Ed.* 36, 866–874. doi:10.7540/j.ynu.20140312

Tonidandel, S., and LeBreton, J. M. (2011). Relative importance analysis: A useful supplement to regression analysis. *J. Bus. Psychol.* 26, 1–9. doi:10.1007/s10869-010-9204-3

von Storch, H., and Zwiers, F. W. (2002). *Statistical analysis in climate research*. Cambridge: Cambridge University Press.

Wang, L., Gui, S., Cao, J., and Yan, H. (2018). Summer precipitation anomalies in the low-latitude highlands of China coupled with the subtropical Indian Ocean dipole-like sea surface temperature. *Clim. Dyn.* 51 (7), 2773–2791. doi:10.1007/s00382-017-4044-8

Wang, L., Huang, G., Chen, W., Zhou, W., and Wang, W. Q. (2018). Wet-to-dry shift over Southwest China in 1994 tied to the warming of tropical warm pool. *Clim. Dyn.* 51, 3111–3123. doi:10.1007/s00382-018-4068-8

Wang, S. S., Huang, J. P., and Yuan, X. (2021). Attribution of 2019 extreme spring-early summer hot drought over yunnan in southwestern China. *Bull. Am. Meteorological Soc.* 102, S91–S96. doi:10.1175/bams-d-20-0121.1

Wang, Y., Wang, Y., Chen, Y., Chen, H., Li, X., Ding, Z., et al. (2023). Spatial and temporal characteristics of drought events in southwest China over the past 120 years. *Remote Sens.* 15, 3008. doi:10.3390/rs15123008

Wen, D. Y., Cao, J., Zhao, C. X., Masiri, I., and Buntoung, S. (2021). Interdecadal variation of summer rainfall in the Greater Mekong Subregion and its possible causes. *Environ. Res. Lett.* 6, 084064–084069. doi:10.1088/1748-9326/ac188b

Wu, B., Zhou, T., and Li, T. (2016). Impacts of the pacific–Japan and circumglobal teleconnection patterns on the interdecadal variability of the East asian summer monsoon. *J. Clim.* 29, 3253–3271. doi:10.1175/JCLI-D-15-0105.1

Wu, R. G., Wen, Z. P., Yang, S., and Li, Y. Q. (2010). An interdecadal change in Southern China Summer Rainfall around 1992/93. *J. Clim.* 23, 2389–2403. doi:10.1175/2009JCLI3336.1

Wu, R., Yang, S., Liu, S., Sun, L., Lian, Y., and Gao, Z. (2011). Northeast China summer temperature and North Atlantic SST. *J. Geophys. Res. Atmos.* 116 (16), D16116. doi:10.1029/2011JD015779

Xie, S. P., Hu, K. M., Hafner, J., Tokinaga, H., Du, Y., Huang, G., et al. (2009). Indian ocean capacitor effect on indo-western pacific climate during the summer following el niño. *J. Clim.* 22, 730–747. doi:10.1175/2008JCLI2544.1

Yan, H. M., Li, Q. Q., and Wang, D. Q. (2018). Spatial and temporal characteristics of the rainy season in Yunnan and the relationship with atmospheric circulation changes. *J. Trop. Meteorology* 34, 12–22. doi:10.16032/j.issn.1004-4965.2018.01.002

Yin, X. X., Zhou, L. T., and Huang, J. F. (2021). Weakened connection between east China summer rainfall and the East asia-pacific teleconnection pattern. *Atmosphere* 12, 704. doi:10.3390/atmos12060704

Zheng, J., Huang, W., Chen, Y., and Zhou, J. (2017). Study on meteorological extreme-drought index for yunnan province. *Plateau Meteorol.* 36, 1039–1051. doi:10.7522/j.issn.1000-0534.2016.00067

Zhu, D., Yang, Q., Xiong, K., and Xiao, H. (2022). Spatiotemporal variations in daytime and night-time precipitation on the yunnan–guizhou plateau from 1960 to 2017. *Atmosphere* 13, 415. doi:10.3390/atmos13030415

frontiers | Frontiers in Environmental Science

TYPE Original Research
PUBLISHED 25 October 2023
DOI 10.3389/fenvs.2023.1275742

OPEN ACCESS

EDITED BY
Zhiyuan Hu,
Sun Yat-sen University, China

REVIEWED BY
Xiao Lu,
Sun Yat-sen University, China
Zhenzhong Zeng,
Southern University of Science and Technology, China

*CORRESPONDENCE
Xu Yue,
yuexu@nuist.edu.cn

RECEIVED 10 August 2023
ACCEPTED 12 October 2023
PUBLISHED 25 October 2023

CITATION
Hu Y, Yue X, Tian C, Zhou H, Fu W, Zhao X, Zhao Y and Chen Y (2023), Identifying the main drivers of the spatiotemporal variations in wetland methane emissions during 2001–2020.
Front. Environ. Sci. 11:1275742.
doi: 10.3389/fenvs.2023.1275742

Identifying the main drivers of the spatiotemporal variations in wetland methane emissions during 2001–2020

Yihan Hu[1], Xu Yue[1]*, Chenguang Tian[1], Hao Zhou[2], Weijie Fu[1], Xu Zhao[1], Yuan Zhao[1] and Yuwen Chen[1]

[1]School of Environmental Science and Engineering, Nanjing University of Information Science and Technology (NUIST), Nanjing, China, [2]Climate Change Research Center, Institute of Atmospheric Physics, Chinese Academy of Sciences, Beijing, China

Wetlands act as an important natural source of global methane (CH_4). The emission rate of wetland CH_4 is jointly affected by climate change, carbon dioxide (CO_2) fertilization, and wetland distribution. In this study, we implemented a wetland CH_4 emission module into the Yale Interactive Biosphere (YIBs) model to quantify the spatiotemporal variations of global wetland CH_4 emissions in 2001–2020. Site-level validations showed that the YIBs model reasonably captures the seasonality and magnitude of CH_4 emissions at 28 out of 33 sites with significantly positive correlations and low relative biases. On the global scale, the YIBs predicts an annual mean wetland CH_4 emission of 147.5 Tg yr^{-1} in 2000–2017, very close to the estimate of 147.9 Tg yr^{-1} from the ensemble of 13 process-based models. Global wetland CH_4 emissions showed a positive trend of 0.74 Tg yr^{-2} in the past 2 decades, leading to an increase of 7.4 Tg yr^{-1} (5.2%) in 2008–2017 than 2000–2009. Climate change and CO_2 fertilization accounted for over 70% of global wetland CH_4 emission changes. Among them, the impact of CO_2 grew steadily and became the dominant factor after the year 2008. The most significant changes in wetland CH_4 emissions were located in the tropical regions following the perturbations in temperature that drives the ecosystem productivity. We found limited changes in CH_4 emissions over high latitudes because of the moderate variations in wetland area fraction. The rise of wetland CH_4 emissions poses an emerging threat to the global warming and likely escalates the tropospheric air pollutants.

KEYWORDS

wetland, methane, climate change, CO_2 fertilization, YIBs model

1 Introduction

Atmospheric methane (CH_4) is an important greenhouse gas (Fletcher and Schaefer, 2019) and precursor of tropospheric ozone (Staniaszek et al., 2022). The CH_4 concentrations have been steadily increasing since the preindustrial period (Aben et al., 2017). Recent observations showed a CH_4 rise of 267 ppb (16.2%) from 1984 to 2022 though with large interannual variations (Lan et al., 2022). Such increase of CH_4 is mainly driven by the changes of emissions, especially from the anthropogenic sources that grew 26% during 1970–2012 (Turner et al., 2019). However, the natural emissions of CH_4 also account for

approximately 28% of the global CH_4 emissions and made important contributions to the growth of atmospheric CH_4 levels (Saunois et al., 2020).

The wetland CH_4 emission is the largest component of natural sources (Koffi et al., 2020). Production of wetland CH_4 involves complex biogeochemical processes and is highly sensitive to climatic and environmental perturbations. High temperature promotes CH_4 emissions with a Q_{10} metric and further escalates emissions with a warming feedback (Liu et al., 2020; Rößger et al., 2022; Zhang et al., 2023). Precipitation usually increases wetland emissions by enlarging the area of waterbody and increasing the water table depth (Lunt et al., 2021; Zou et al., 2022), the latter of which may further increase the temperature sensitivity of CH_4 emissions (Duval and Radu, 2018; Chen et al., 2021). The variation of wetland area caused by the shifts in precipitation and temperature patterns directly determine the area of wetland methane discharge (Kuhn et al., 2018; Zou et al., 2022). Increased CO_2 concentration can lead to an increase in microbial biomass of methanogens by promoting the ecosystem productivity and the mineralization of soil organic matter (Liu et al., 2019; Yuan et al., 2021). The changes of these environmental factors modulate the spatiotemporal variations in the regional to global wetland CH_4 emissions.

Different approaches have been applied to estimate global wetland CH_4 emissions, including the top-down estimates of 155.5–218.6 Tg yr^{-1} using the inverse modeling and satellite-based observations (Ishizawa et al., 2016; Bergamaschi et al., 2018), as well as the bottom-up estimates of 100.1–183.2 Tg yr^{-1} with process-based models and site-level measurements (Zhu et al., 2015; Arora et al., 2018). Among these methods, the process-based models show advantages in predicting historical emissions and identifying the dominant drivers. Most models consider the biogeochemical processes such as production, oxidation, and transport for CH_4 emissions (Wania et al., 2010; Nzotungicimpaye et al., 2021; Salmon et al., 2022). For example, the LPJ-WHyMe model reasonably captures the seasonal variations of CH_4 emissions at seven sites by adding a root exudate pool with stratified root distribution to the major biogeochemical processes (Wania et al., 2010). The WETMETH model also considers the above processes with dynamic predictions of soil water table and inundation areas, and shows consistent spatial patterns with three upscaled flux measurements (Nzotungicimpaye et al., 2021). The ORCHIDEE model with the permafrost dynamics and optimized parameters can reasonably simulate methane emissions from the northern wetlands (Salmon et al., 2022).

In addition to the above-mentioned individual simulations, the recent estimates with 13 models predicted natural wetland CH_4 emissions of 101–179 Tg yr^{-1} on the global scale during 2000–2017 (Saunois et al., 2020). These models were driven with the same meteorology and boundary conditions, so as to minimize the modeling uncertainties due to the forcing data. However, they prescribed the wetland net primary productivity (NPP) and ignored the CO_2 fertilization effects to the changes in substrate availability. As a result, the multi-model ensemble average suggests a very limited trend in wetland CH_4 emissions for 2000–2017 (Saunois et al., 2020), which are inconsistent with the fast growth of atmospheric CH_4 levels (Lan et al., 2022) and the recent increase of wetland emissions (Shaw et al., 2022). Furthermore, the drivers of the changes in wetland CH_4 emissions were not explored.

In this study, we implemented a process-based wetland CH_4 emissions scheme into the well-established Yale Interactive terrestrial Biosphere (YIBs) model (Yue and Unger, 2015). We evaluate the simulated wetland emissions against *in situ* measurements and the multi-model ensemble averages. The model is then driven with year-to-year CO_2 concentrations, meteorological parameters, and wetland extent to predict global wetland CH_4 emissions during 2000–2020. We perform sensitivity experiments to quantify the contributions of individual factors to the trends in CH_4 emissions. With these model configurations, we attempt to depict the spatiotemporal variations of wetland CH_4 emissions and identify their dominant drivers in the past two decades.

2 Methods and data

2.1 YIBs vegetation model

We use the YIBs model as the framework for wetland CH_4 emissions. The YIBs is a vegetation model that simulates carbon fluxes with prognostic leaf area index (LAI) and tree height (Yue and Unger, 2015). The model applies the Michaelis-Menten enzyme-kinetics scheme for leaf photosynthesis (Farquhar et al., 1980) and the two-leaf canopy radiative transfer scheme for light partitioning (Spitters et al., 1986). The gross primary productivity (GPP) is calculated by the integration of leaf photosynthesis along the LAI. The litterfall drives the carbon transitions among soil pools and the heterotrophic respiration (R_h). The accumulation of soil carbon provides substrate for the wetland CH_4 emissions. Simulated GPP and LAI have been validated against site-level and satellite-based observations (Yue et al., 2015). The YIBs model has joined the vegetation model intercomparison project since 2020 and showed reasonable performance in the simulation of major carbon metrics including GPP, LAI, vegetation biomass, soil carbon and so on (Friedlingstein et al., 2020).

2.2 Wetland CH4 emission module

We implement a process-based wetland CH_4 emission module into the YIBs with major biogeochemical processes, including production, oxidation, and transportation of CH_4. In the wetland areas, the production of CH_4 is calculated based on soil conditions (including soil temperature and pH) and the amount of carbon that is distributed for methanation, following the CH_4-related module in the TRIPLEX-GHG model (Zhu et al., 2014). The decomposition of organic matter is regulated by redox acceptors. Under anaerobic conditions, the presence of high organic substrates restricts the redox potential, controlling the decomposition rate of organic carbon and the emissions ratio of CH_4 and carbon dioxide. The R_h during anaerobic decomposition processes is derived as the remaining portion after subtracting net ecosystem productivity (NEP) from net primary productivity (NPP). The rate of CH_4 oxidation is computed using a Michaelis-Menten kinetic relationship that is dependent on temperature and CH_4

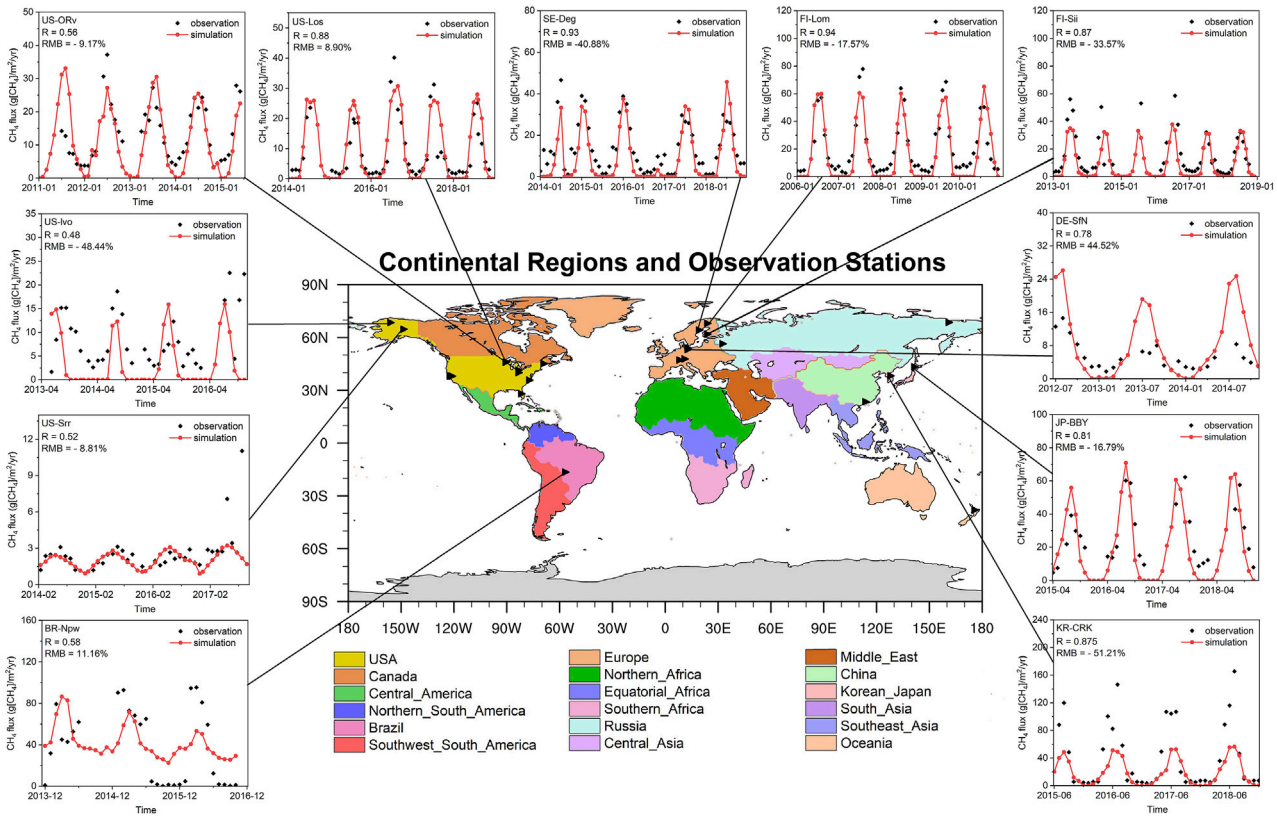

FIGURE 1
The distribution of 18 continental regions and the comparisons of site-level CH_4 emissions between observations (black points) and simulations (red lines) at 11 sites from the FLUXNET—CH_4 network. The statistics for all sites are listed in Supplementary Table S1.

concentrations in the corresponding soil layer (Dunfield et al., 1993). The transportation of CH_4 from soil to atmosphere is composed of three pathways including diffusion, ebullition, and plant-mediated transportation. The diffusion of CH_4 follows the Fick's law with the dependence on soil properties (soil texture, tortuosity and water content) and CH_4 concentration gradient between different soil layers (Walter and Heimann, 2000). The ebullition of CH_4 is triggered if the CH_4 concentration exceeds 750 μmol L^{-1} (Zhu et al., 2014). The plant-mediated transportation, which provides an impactful way to divert CH_4 from soil to atmosphere, is calculated based on the same aerenchyma factor of plants as those equations used in the TRIPLEX-GHG model (Zhu et al., 2014).

2.3 Data for simulations and validations

We use the meteorological variables from the MERRA-2 reanalysis (Gelaro et al., 2017) to drive the YIBs model. The surface variables include air temperature, specific humidity, solar radiation, air pressure, and wind speed. The soil variables include soil temperature and soil moisture at six vertical layers. All these variables are interpolated to the horizontal resolution of $1^\circ \times 1^\circ$ at the hourly time step. The year-to-year global mean atmospheric CO_2 concentrations are adopted from the protocol data for the input4MIPs (https://esgf-node.llnl.gov/projects/input4mips/).

For the wetland CH_4 scheme, we used the monthly global wetland extent dataset of WAD2M (Zhang Z. et al., 2021) derived from remote sensing and the soil pH map of SoilGrids250m dataset (Hengl et al., 2017) from the International Soil Reference and Information Centre. Other gridded soil parameters (e.g., particle composition, soil porosity) are obtained from the ISLSCP II Global Gridded Soil Characteristics dataset (Scholes et al., 2011) generated by the International Satellite Land-Surface Climatology Project.

We use site-level measurements from the FLUXNET-CH4 network (Delwiche et al., 2021) to validate the simulated CH_4 emissions. The monthly CH_4 fluxes are collected from all the available 33 sites with at least 3 years length of period. We also use the multi-model output from 13 bottom-up models and 9 top-down approaches to assess the simulated wetland emissions during 2000–2017. To facilitate the comparison, we separate the global land into 18 regions following the definitions in Saunois et al. (2020) (Figure 1).

2.4 Simulations

We perform four simulations to depict the spatiotemporal variations of wetland CH_4 emissions (Table 1). The BASE run is forced with year-to-year meteorology, wetland extent, and CO_2 concentrations during 2000–2020. Three "FIX" sensitivity

TABLE 1 Summary of sensitivity experiments.

Simulations	Climate	Wetland extent	CO_2 concentration
BASE	2000–2020	2000–2020	2000–2020
FIXCLIM	2000	2000–2020	2000–2020
FIXWET	2000–2020	2000	2000–2020
$FIXCO_2$	2000–2020	2000–2020	2000

experiments are conducted to distinguish the impacts of the changes in climate (CLIM), wetland area (WET), and CO_2 fertilization effects (CO_2) on CH_4 emissions. For each of these runs, all the forcings are the same as BASE run except that a specific forcing is fixed at the year 2000. The differences between the BASE and "FIX" runs indicate the contributions of changes in climate (BASE—FIXCLIM), wetland (BASE—FIXWET), and CO_2 (BASE—$FIXCO_2$) to the global wetland CH_4 emissions. For all simulations, the hourly meteorology is applied from 1900 to 2020 with the cycling of 2000 meteorology for the 1900–2000 period, which is used for the model spin up.

3 Result

3.1 Model evaluations and comparisons

We first evaluate the simulated CH_4 emissions at FLUXNET-CH4 sites (Figure 1). For the selected sites around the world, the YIBs model in general captures the seasonality of CH_4 emissions with the peak values in summer period. Among the total of 33 sites, simulations show significantly positive correlation coefficients (R) at 28 sites and reasonable relative mean biases (RMB) of −50%–50% at 23 sites (Supplementary Table S1). Emissions are usually higher nearby the tropical rainforest but lower in the semi-arid regions such as western United States. For the Amazon rainforest with dense vegetation, the non-flooded trees can absorb CH_4 from the soil through their roots, transport the gas through vascular systems to stems, and release it into the air subsequently (Gauci et al., 2021). The model fails to capture the CH_4 emissions at some sites. For example, simulated CH_4 fluxes are negatively correlated with a high RMB of 186% against measurements at site US-Snd. However, this site is within the same grid as US-Sne and US-Srr where the YIBs model yields reasonable emissions. A similar case could be found at US-Twt, US-Tw1, and US-Tw4 where the simulations share the same values due to the vicinity of sites but observations exhibit large deviations. As a result, the missing of site-specific parameters (such as vegetation types, soil characteristics) may in part cause the modeling biases at these sites.

We then compare the simulated global wetland CH_4 emissions with other estimates (Supplementary Table S2). On average, the emissions estimated by process-based models are 19.1% lower than those using the top-down approaches. Compared to the ensemble of 13 bottom-up models, the YIBs shows lower value of −2.1% in 2000–2009 and the higher estimate of 1.6% in 2008–2017. For the ensemble mean of models, limited differences are found between the two periods likely because of the omission of CO_2 fertilization effects on the wetland NPP (Saunois et al., 2020). However, for individual models, either positive (7 out of 13), negative (2 out of 13), or mild (4 out of 13) trends are predicted because of their varied representations of climatic impacts on CH_4 emissions. A similar conclusion is achieved with the nine top-down approaches utilizing the WAD2M wetland dataset. The maximum increases in CH_4 emissions between the two decades are predicted at 3.6% for the top-down and 5.2% for the bottom-up methods, respectively. The predicted trend of 5.2% with the YIBs model is at the high end of other estimates, though our simulations consider the CO_2 fertilization effect.

We compare the simulated trend of wetland CH_4 emissions with the top-down inversion (Zhang Y. et al., 2021) from the Greenhouse gases Observing Satellite (GOSAT). The growth rate of natural wetland CH_4 in the YIBs model shows increased emissions after the year 2010 (Supplementary Figure S1A). The simulated trend of 12.09% matches that of 12.29% from the posterior data of GOSAT, which shows a much larger interannual variability than the simulations. Such year-to-year variations are difficult to reproduce as the prior data fail to capture both the interannual perturbations and the long-term trend. Furthermore, we compare the simulated interannual variations with the results of LPJ model (Zhang et al., 2023) driven by meteorological fields from either Climatic Research Unit (CRU) or MERRA-2 reanalyses (Supplementary Figure S1B). The growth rates obtained from different meteorological fields exhibit a maximum deviation of up to 11.62%. Using the same meteorological field of MERRA2, the moderate difference of 2.03% is achieved between the simulations of YIBs and LPJ models. Such discrepancy is lower than the differences caused by the varied meteorological fields.

We divide global land into 18 regions (Figure 1) where the simulated wetland CH_4 emissions are compared to the values from multiple models and approaches (Figure 2). Comparing the results from different approaches, the assessment of natural wetland CH_4 emissions by bottom-up models tends to be lower than that of top-down approaches in most regions (Supplementary Figure S2A). Similar to other bottom-up models, the YIBs model yields lower emission estimates in multiple regions compared to the top-down models especially over the Canada, Brazil, and Southeast Asia regions. On average, the simulated CH_4 emissions match the medians of multiple models with a high R^2 of 0.77, though the former is in general lower than the latter estimates (Supplementary Figure S2B).

In all the 18 regions, YIBs model yields reasonable wetland CH_4 emissions with differences of $-15.2\ Tg\ yr^{-1} \sim 2.54\ Tg\ yr^{-1}$ from the multi-model ensemble medians. For comparison of top-down models and bottom-up models, both methods show the same top two emitters in Brazil and Southeast Asia, though the top-down approach predicts much higher emissions in Brazil than the latter region. The YIBs also yields the largest wetland CH_4 emissions in Brazil, but underestimates the emissions in Southeast Asia by 56.82%–63.37% compared to the multi-model ensemble mean. The median assessments of CH_4 emissions from the third-largest natural wetland region in Africa by bottom-up models, top-down approaches, and YIBs model are relatively close, ranging from 14.21 to $18.72\ Tg\ yr^{-1}$. However, there is a relatively significant divergence among different models in the assessments over high-emission regions, like Brazil, Southeast Asia and Equatorial Africa.

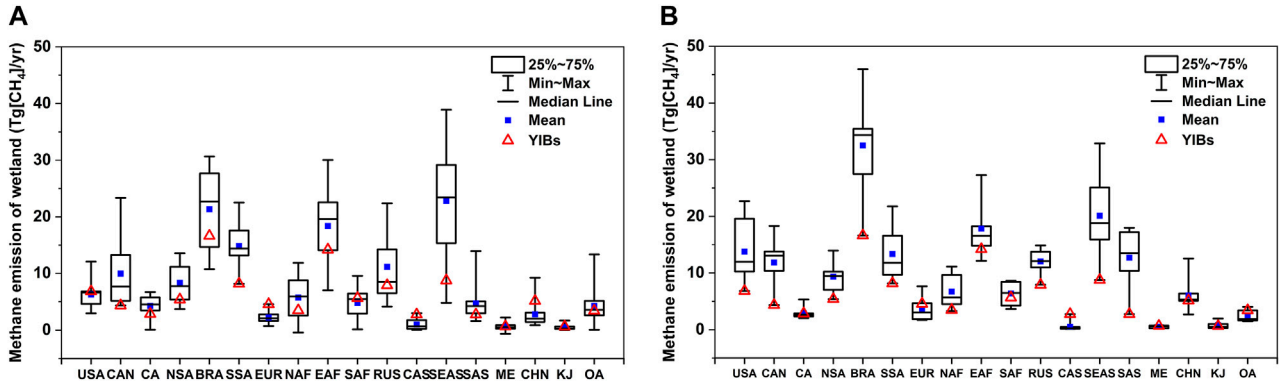

FIGURE 2
Comparisons of wetland CH_4 emissions at 18 regions averaged for 2000–2017 between simulations and the estimates by **(A)** 13 bottom-up approaches and **(B)** 9 top-down approaches. For each boxplot, the central black solid line indicates the median, and the blue solid square shows the ensemble mean of all approaches. The top and bottom edges represent the 25th and 75th percentiles, respectively, with the whiskers representing the data range. The results of YIBs are shown in red triangles.

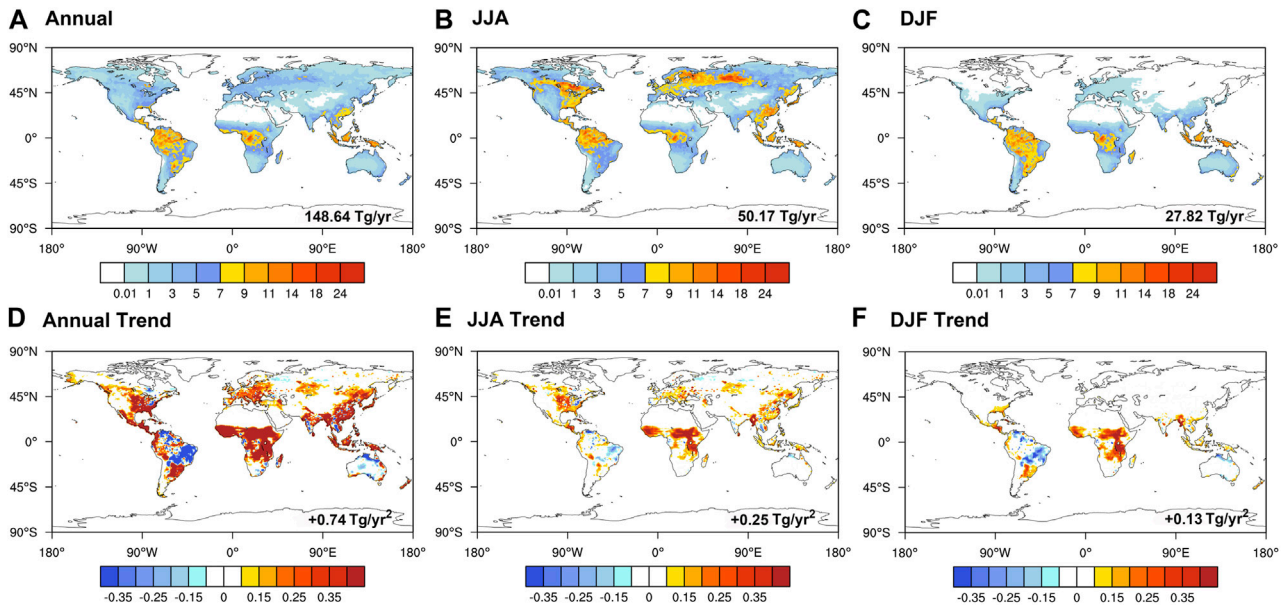

FIGURE 3
The (top) mean (mg [CH_4] m^{-2} day^{-1}) and (bottom) trend (mg [CH_4] m^{-2} day^{-1} yr^{-1}) of CH_4 emissions from wetland for **(A,D)** whole year **(B,E)**, June-August, and **(C,F)** December–February in 2001–2020. The global total values are shown on each panel.

We also found large inter-model variability in Canada and Russia though the emissions are much lower than the tropical region, which is likely associated with the varied sensitivity to climatic drivers among different models and approaches (Saunois et al., 2020). In most regions, the performance of the YIBs model is relatively close to the intermediate levels of other bottom-up models. However, it yields significantly higher assessment of emissions in Central Asia compared to most models, though it does not exceed the maximum values among the other 13 bottom-up models. The discrepancies underscore the substantial uncertainty in the current assessment of natural wetland CH_4 emissions, primarily attributed to the complex biogeochemical and ecological processes involved in the processes. The variations among models in different processes may further magnify the differences in the final emission estimates. In future researches, more observations are required to validate the simulated CH_4 emissions from natural wetlands in different regions.

3.2 Spatiotemporal variation in wetland CH_4 emissions

The wetland CH_4 emissions show distinct spatial and seasonal variations (Figure 3). Large emissions are located in the tropics

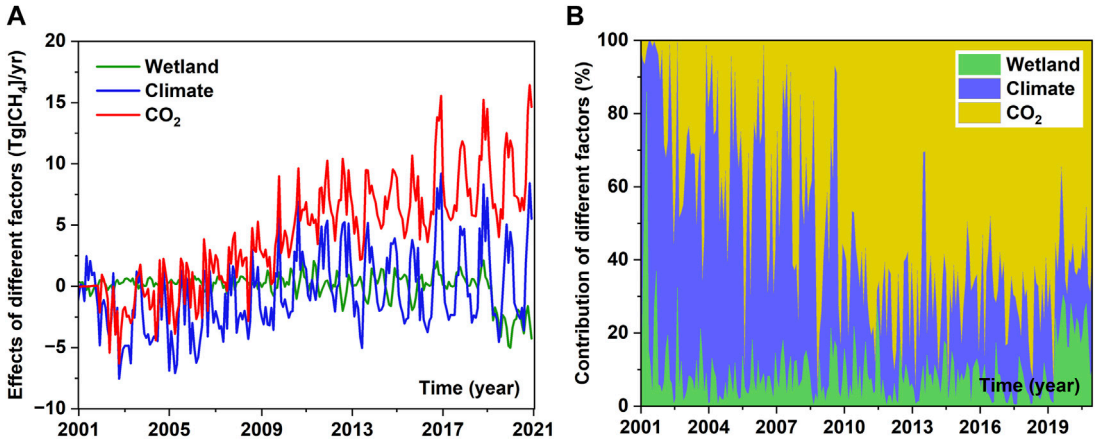

FIGURE 4
The **(A)** variations of wetland CH_4 emissions and **(B)** contributions of three key driving factors including wetland extent, climate change, and CO_2 fertilization during 2001–2020. The contribution percentages for individual factors are derived based on the absolute changes from baseline simulation caused by prescribing the specific factor.

(23.5°S–23.5°N), contributing 69.22% to the global total amount due to the optimal hydrothermal conditions and the adequate supply of substrate. The secondary hotspots are found in the temperate (23.5°N–60°N) regions of the Northern Hemisphere, which accounts for 24.32% of the global amount (Figure 3A). These centers become the strongest in the boreal summer (Figure 3B), when the high temperature promotes CH_4 emission rate and expand the wetland extent. The total global emissions in summer (from June to August) reach 50.2 Tg, accounting for 33.8% of the annual total amount. In contrast, limited emissions are predicted over the northern mid-high latitudes in boreal winter because of the low temperature and seasonally frozen ground. For this season, most of global wetland CH_4 emissions are confined in the tropical regions, leading to 45% lower emissions compared to the summertime on the global scale.

We further assess the trend of wetland CH_4 emissions during 2001–2020. Over the global grids with baseline emissions of at least 1 mg m^{-2} day^{-1}, 1.47% show significant increase in the past two decades. The most significant enhancement is located at the tropical Africa, eastern Asia, and eastern United States. (Figure 3D). The increase of CH_4 emissions in tropical Africa persist all year round, while those in Asia and US are more evident in boreal summer (Figures 3E, F). Meanwhile, large reduction is predicted over eastern South America, where the baseline emissions (Figure 3A) are low due to the moderate supply of substrate from grassland. Such regional decline is more evident in boreal winter (Figure 3F). On the global scale, the positive trend in summer almost doubles that in winter.

3.3 Drivers of the trends in wetland CH4 emissions

We isolate the contributions of climate change, CO_2 fertilization, and wetland extent to the trend of CH_4 emissions during 2001–2020 (Figure 4). Among these factors, the changes of wetland area show limited impacts while the other two factors cause large variabilities in CH_4 emissions (Figure 4A). For 2001–2008, the negative effects of climate change play the dominant role in regulating the total trend. However, after the year 2008, the impact of CO_2 fertilization is becoming more important year by year, accounting for 67.84% of the total changes in CH_4 emissions during 2010–2020 (Figure 4B). For the FIXCO_2 simulation, the average wetland CH_4 emissions are predicted to be 143.47 Tg yr^{-1} in 2000–2009 and 143.26 Tg yr^{-1} in 2008–2017. As a result, the YIBs model yields limited changes in wetland CH_4 emissions between the 2 decades, close to the estimate by the ensemble of 13 process-based models without the CO_2 fertilization effects (Supplementary Table S2).

We further identify the spatial distribution of wetland CH_4 changes induced by different factors (Figure 5). Climate change alone exerts strong impacts in tropical regions with CH_4 reductions in South America, South Africa, and Australia, but increased emissions in central Africa (Figure 5A). There are some moderately positive changes in CH_4 emissions induced by climate at the middle latitudes of Northern Hemisphere. The positive and negative changes are offsetting each other, leading to a limited contribution of −0.12 Tg yr^{-1} by climate change during 2001–2020. CO_2 fertilization causes widespread enhancement in CH_4 emissions especially over the tropical regions (Figure 5B). The changes in wetland area cause patchy responses in CH_4 emissions with moderate reductions in South America and central Africa (Figure 5C).

In anaerobic environments, the rate of organic carbon decomposition and the release ratio of carbon dioxide to methane are constrained by the presence of high organic matter substrates. Climate change decreases R_h in South America, South Africa, and Australia (Figure 6A), because increased temperature (Figure 6C) inhibits plant photosynthesis in the tropical regions (Piao et al., 2013). In contrast, the slight cooling over Sahel and central Africa promotes the regional R_h (Figure 6A) and the consequent

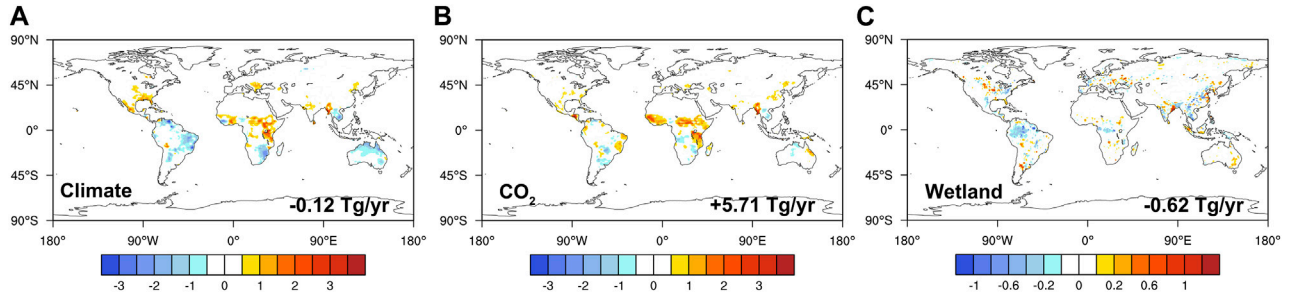

FIGURE 5
The mean differences in wetland CH_4 emissions (Units: mg[CH_4] m^{-2} day^{-1}) between simulations with all forcing (BASE) and that with fixed **(A)** climate (FIXCLIM), **(B)** CO_2 (FIXCO_2) and **(C)** wetland extent (FIXWET) during 2001–2020.

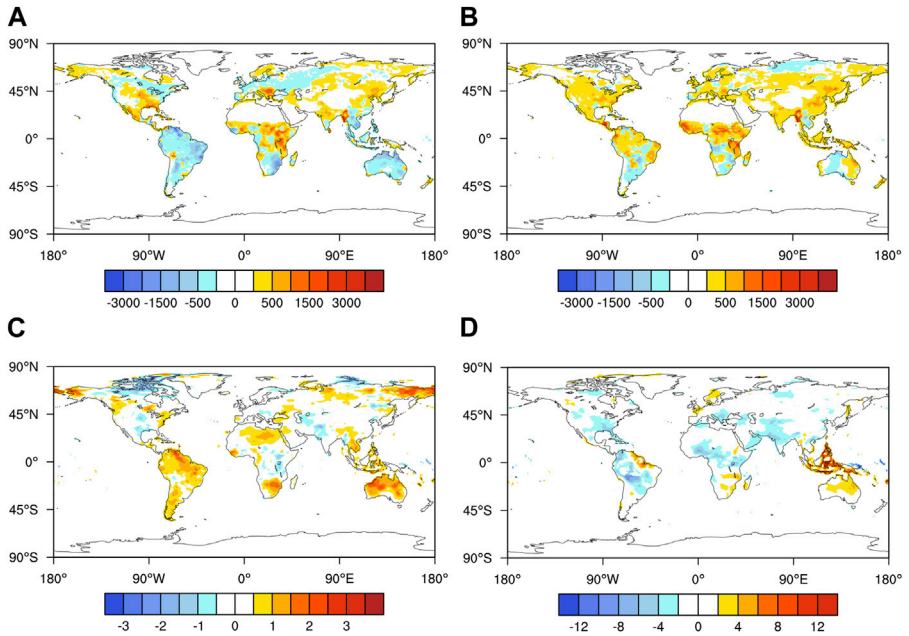

FIGURE 6
The trend of heterotrophic respiration (Units: mg[C] m^{-2} day^{-1}) induced by **(A)** climate change and **(B)** CO_2 fertilization, as well as the trend in **(C)** temperature (Units: °C) and **(D)** solar radiation (Units: W m^{-2}) during 2001–2020.

wetland CH_4 emissions (Figure 5A). Solar radiation shows widespread reductions except over Indonesia and Australia (Figure 6D). However, the effect of radiation change on R_h is secondary to that of temperature, as the warming-induced inhibition overweighs the benefit of increased radiation in Indonesia and Australia (Figure 6A). The CO_2 fertilization effect causes increases in R_h globally (Figure 6B), leading to significant enhancement of wetland CH_4 emissions. (Figure 5B).

4 Conclusion and discussion

We implemented a wetland CH_4 emission module into the YIBs vegetation model and validated its performance against available measurements and estimates. Simulated wetland CH_4 emissions matched observations with reasonable seasonality at 28 out of 33 sites. The model also yielded similar global wetland CH_4 emissions compared to the ensemble of 13 process-based models. We performed sensitivity experiments to identify the spatiotemporal variations of wetland CH_4 emissions and the associated drivers from 2001 to 2020. The results showed that the interannual variation of atmospheric CO_2 and meteorological conditions predominantly drive the changes in global wetland CH_4 emissions, with their combined contributions exceeding 70% in each month during the research period. The role of CO_2 fertilization grew gradually and became the dominant factor after 2008. The attribution analyses indicated that the changes of wetland CH_4 emissions followed the changes in R_h,

with widespread enhancement by CO_2 fertilization effects but patchy responses to climate change mainly following the trend of temperature.

Previous studies also revealed the strong impacts of CO_2 fertilization on wetland CH_4 emissions. For example, Yuan et al. (2021) suggested that increased CO_2 could promote the concentration of dissolved organic carbon (DOC) and acetate by enhancing ecosystem productivity and the mineralization of soil organic matter. This, in turn, leads to an increase in the microbial biomass of methanogens, ultimately resulting in enhanced CH_4 emissions. However, some recent estimates ignored the CO_2 fertilization effect in their simulations. For example, the observation-constrained study by Koffi et al. (2020) showed enhanced wetland CH_4 emissions of 50%–80% at the end of 21st century without considering CO_2 fertilization effect. The multi-model ensemble estimates by Saunois et al. (2020) also neglected the CO_2 fertilization and achieved limited trends in wetland CH_4 emissions for the recent two decades. We expect that the increasing rates of wetland CH_4 emissions are likely underestimated in above studies as the role of CO_2 fertilization becomes more dominant over the long-term period.

Many studies have emphasized the influences of climatic factors on wetland CH_4 emissions. Liu et al. (2020) highlighted the important role of air temperature, which affects CH_4 production directly through Q_{10} factors and indirectly by altering both NPP and wetland inundation area fraction. We also found that temperature accounts for most of climate-driven changes in CH_4 emissions through modulating ecosystem NPP (Figure 6). Furthermore, Chen et al. (2021) observed a positive correlation between wetland water level and temperature sensitivity in CH_4 emissions, though this relationship is not incorporated in our model. Zhang et al. (2023) compared the impacts of temperature and precipitation, and found that precipitation dominates the variability of CH_4 emissions in some tropical regions as rainfall alter the wetland extent. However, we prescribed the area of wetland in our simulations and constrained the effects of precipitation to some extent. Despite these discrepancies, we also found that the perturbations of tropical CH_4 dominates the global wetland emissions as concluded by Zhang et al. (2023).

In this study, we found limited changes of wetland CH_4 emissions at high latitudes. The melting permafrost in boreal regions of the Northern Hemisphere is expected to become a crucial source in the future, as projected by the Coupled Model Intercomparison Project (Canadell et al., 2021). However, there is considerable disagreement regarding the assessment of the impact of permafrost melting on CH_4 emissions. Zhang et al. (2017) estimated that CH_4 emissions could reach 347.8 Tg yr^{-1} by the end of the 21st century under the RCP8.5 scenario taking into account the wetland expansion from permafrost melting. Nonetheless, the inversion-constrained estimation showed much lower CH_4 emissions under the same climate change scenario (Koffi et al., 2020). Furthermore, Salmon et al. (2022) found that bottom-up models tend to overestimate CH_4 emissions in northern peatland sites in the model calibrations. These studies revealed the large uncertainties in estimating wetland CH_4 emissions due to the permafrost dynamics in process-based models. It should be noted that global wetland area distributions derived from satellite retrievals may also deviate from the actual conditions. The retrievals are influenced by the accuracy of prior data (Xi et al., 2022) and it is challenging to adequately validate retrieval results in regions lacking ground-based observations. Additionally, the low surface reflectance features such as limestone deposits may lead to overestimations of inundation levels in certain areas (Jensen and Mcdonald, 2019). Non-wetland areas in dynamic dataset with an inundation index of 0 do not necessarily imply the absence of wetlands. These limitations of the wetland area dataset may introduce uncertainties into our assessment of the global variations in wetland CH_4 emissions. Despite these uncertainties, we revealed an increasing tendency of wetland CH_4 emissions due to the joint effects of CO_2 fertilization and climate change in the past two decades. Such trend likely persists under global warming and poses an emerging threat to both climate and air quality.

Data availability statement

The original contributions presented in the study are included in the article/Supplementary Material, further inquiries can be directed to the corresponding author.

Author contributions

YH: Conceptualization, Data curation, Methodology, Writing–original draft, Writing–review and editing. XY: Conceptualization, Data curation, Methodology, Writing–original draft, Writing–review and editing, Funding acquisition. CT: Data curation, Investigation, Writing–review and editing. HZ: Data curation, Investigation, Writing–review and editing. WF: Data curation, Investigation, Writing–review and editing. XZ: Data curation, Investigation, Writing–review and editing. YZ: Data curation, Investigation, Writing–review and editing. YC: Data curation, Investigation, Writing–review and editing.

Funding

The authors declare financial support was received for the research, authorship, and/or publication of this article. This study was jointly supported by the National Natural Science Foundation of China (grant no. 42293323) and Natural Science Foundation of Jiangsu Province (grant no. BK20220031).

Acknowledgments

The authors thank the NASA for the MERRA-2 reanalysis datasets and ISLSCP II Global Gridded Soil Characteristics dataset, the ISRIC for SoilGrids 250m datasets, the ESGF for input4MIPs, the FLUXNET-CH4 community for methane observation data, and Zhang et al. for WAD2M dataset.

Conflict of interest

The authors declare that the research was conducted in the absence of any commercial or financial relationships that could be construed as a potential conflict of interest.

Publisher's note

All claims expressed in this article are solely those of the authors and do not necessarily represent those of their affiliated organizations, or those of the publisher, the editors and the reviewers. Any product that may be evaluated in this article, or claim that may be made by its manufacturer, is not guaranteed or endorsed by the publisher.

Supplementary material

The Supplementary Material for this article can be found online at: https://www.frontiersin.org/articles/10.3389/fenvs.2023.1275742/full#supplementary-material

References

Aben, R., Barros, N., Donk, E., Frenken, T., Hilt, S., Kazanjian, G., et al. (2017). Cross continental increase in methane ebullition under climate change. *Nat. Commun.* 8, 1682. doi:10.1038/s41467-017-01535-y

Arora, V. K., Melton, J. R., and Plummer, D. (2018). An assessment of natural methane fluxes simulated by the CLASS-CTEM model. *Biogeosciences* 15, 4683–4709. doi:10.5194/bg-15-4683-2018

Bergamaschi, P., Karstens, U., Manning, A. J., Saunois, M., Tsuruta, A., Berchet, A., et al. (2018). Inverse modelling of European CH_4 emissions during 2006–2012 using different inverse models and reassessed atmospheric observations. *Atmos. Chem. Phys.* 18, 901–920. doi:10.5194/acp-18-901-2018

Canadell, J. G., Scheel Monteiro, P., Costa, M. H., Cotrim da Cunha, L., Cox, P. M., Eliseev, A. V., et al. (2021). "Global carbon and other biogeochemical cycles and feedbacks," in *Climate change 2021: the physical science basis. Contribution of working group I to the sixth assessment report of the intergovernmental panel on climate change*. V. Masson-Delmotte, P. Zhai, A. Pirani, S. L. Connors, C. Péan, S. Berger, et al. (Cambridge, United Kingdom and New York, NY, USA: Cambridge University Press), 673–816. doi:10.1017/9781009157896.001

Chen, H., Xu, X., Fang, C., Li, B., and Nie, M. (2021). Differences in the temperature dependence of wetland CO2 and CH4 emissions vary with water table depth. *Nat. Clim. Change* 11, 766–771. doi:10.1038/s41558-021-01108-4

Delwiche, K. B., Knox, S. H., Malhotra, A., Fluet-Chouinard, E., McNicol, G., Feron, S., et al. (2021). FLUXNET-CH_4: a global, multi-ecosystem dataset and analysis of methane seasonality from freshwater wetlands. *Earth Syst. Sci. Data* 13, 3607–3689. doi:10.5194/essd-13-3607-2021

Dunfield, P., knowles, R., Dumont, R., and Moore, T. R. (1993). Methane production and consumption in temperate and subarctic peat soils: response to temperature and pH. *Soil Biol. biochem.* 25, 321–326. doi:10.1016/0038-0717(93)90130-4

Duval, T. P., and Radu, D. D. (2018). Effect of temperature and soil organic matter quality on greenhouse-gas production from temperate poor and rich fen soils. *Ecol. Eng.* 114, 66–75. doi:10.1016/j.ecoleng.2017.05.011

Farquhar, G. D., Von Caemmerer, S., and Berry, J. A. (1980). A biochemical model of photosynthetic CO2 assimilation in leaves of C3 species. *Planta* 149, 78–90. doi:10.1007/BF00386231

Fletcher, S. E. M., and Schaefer, H. (2019). Rising methane: a new climate challenge. *Science* 364, 932–933. doi:10.1126/science.aax1828

Friedlingstein, P., O'Sullivan, M., Jones, M. W., Andrew, R. M., Hauck, J., Olsen, A., et al. (2020). Global carbon budget 2020. *Earth Syst. Sci. Data* 12, 3269–3340. doi:10.5194/essd-12-3269-2020

Gauci, V., Figueiredo, V., Gedney, N., Pangala, S. R., Stauffer, T., Weedon, G. P., et al. (2021). Non-flooded riparian Amazon trees are a regionally significant methane source. *Philos. Trans. R. Soc. Math. Phys. Eng. Sci.* 380, 20200446. doi:10.1098/rsta.2020.0446

Gelaro, R., McCarty, W., Suárez, M. J., Todling, R., Molod, A., Takacs, L., et al. (2017). The modern-era retrospective analysis for research and applications, version 2 (MERRA-2). *J. Clim.* 30, 5419–5454. doi:10.1175/JCLI-D-16-0758.1

Hengl, T., Jesus, J. M., Heuvelink, G. B. M., Gonzalez, M. R., Kilibarda, M., Blagotić, A., et al. (2017). SoilGrids250m: global gridded soil information based on machine learning. *PLOS ONE* 12, e0169748. doi:10.1371/journal.pone.0169748

Ishizawa, M., Mabuchi, K., Shirai, T., Inoue, M., Morino, I., Uchino, O., et al. (2016). Inter-annual variability of summertime CO2 exchange in Northern Eurasia inferred from GOSAT XCO2. *Environ. Res. Lett.* 11, 105001. doi:10.1088/1748-9326/11/10/105001

Jensen, K., and Mcdonald, K. (2019). Surface water microwave product series version 3: a near-real time and 25-year historical global inundated area fraction time series from active and passive microwave remote sensing. *IEEE Geosci. Remote Sens. Lett.* 16, 1402–1406. doi:10.1109/LGRS.2019.2898779

Koffi, E. N., Bergamaschi, P., Alkama, R., and Cescatti, A. (2020). An observation-constrained assessment of the climate sensitivity and future trajectories of wetland methane emissions. *Sci. Adv.* 6, eaay4444. doi:10.1126/sciadv.aay4444

Kuhn, M., Lundin, E. J., Giesler, R., Johansson, M., and Karlsson, J. (2018). Emissions from thaw ponds largely offset the carbon sink of northern permafrost wetlands. *Sci. Rep.* 8, 9535. doi:10.1038/s41598-018-27770-x

Lan, X., Thoning, K. W., and Dlugokencky, E. J. (2022). Global monitoring laboratory - carbon cycle greenhouse gases. Available at: https://gml.noaa.gov/ccgg/trends_ch4/ (Accessed June 7, 2023).

Liu, L., Zhuang, Q., Oh, Y., Shurpali, N. J., Kim, S., and Poulter, B. (2020). Uncertainty quantification of global net methane emissions from terrestrial ecosystems using a mechanistically based biogeochemistry model. *J. Geophys. Res. Biogeosciences* 125. doi:10.1029/2019JG005428

Liu, Y., Piao, S., Gasser, T., Ciais, P., Yang, H., Wang, H., et al. (2019). Field-experiment constraints on the enhancement of the terrestrial carbon sink by CO2 fertilization. *Nat. Geosci.* 12, 809–814. doi:10.1038/s41561-019-0436-1

Lunt, M. F., Palmer, P. I., Lorente, A., Borsdorff, T., Landgraf, J., Parker, R. J., et al. (2021). Rain-fed pulses of methane from East Africa during 2018–2019 contributed to atmospheric growth rate. *Environ. Res. Lett.* 16, 024021. doi:10.1088/1748-9326/abd8fa

Nzotungicimpaye, C.-M., Zickfeld, K., MacDougall, A. H., Melton, J. R., Treat, C. C., Eby, M., et al. (2021). WETMETH 1.0: a new wetland methane model for implementation in Earth system models. *Geosci. Model Dev.* 14, 6215–6240. doi:10.5194/gmd-14-6215-2021

Piao, S., Sitch, S., Ciais, P., Friedlingstein, P., Peylin, P., Wang, X., et al. (2013). Evaluation of terrestrial carbon cycle models for their response to climate variability and to CO2 trends. *Glob. Change Biol.* 19, 2117–2132. doi:10.1111/gcb.12187

Rößger, N., Sachs, T., Wille, C., Boike, J., and Kutzbach, L. (2022). Seasonal increase of methane emissions linked to warming in Siberian tundra. *Nat. Clim. Change* 12, 1031–1036. doi:10.1038/s41558-022-01512-4

Salmon, E., Jégou, F., Guenet, B., Jourdain, L., Qiu, C., Bastrikov, V., et al. (2022). Assessing methane emissions for northern peatlands in ORCHIDEE-PEAT revision 7020. *Geosci. Model Dev.* 15, 2813–2838. doi:10.5194/gmd-15-2813-2022

Saunois, M., Stavert, A. R., Poulter, B., Bousquet, P., Canadell, J. G., Jackson, R. B., et al. (2020). The global methane budget 2000–2017. *Earth Syst. Sci. Data* 12, 1561–1623. doi:10.5194/essd-12-1561-2020

Scholes, R. J., Eric, B. D. C., Collatz, F. G. H., Meeson, B. W., Los, S. O., and Landis, D. R. (2011). *Data from: ISLSCP II global gridded soil characteristics*. USA: ORNL DAAC Oak Ridge Tenn. doi:10.3334/ORNLDAAC/1004

Shaw, J. T., Allen, G., Barker, P., Pitt, J. R., Pasternak, D., Bauguitte, S. J.-B., et al. (2022). Large methane emission fluxes observed from tropical wetlands in Zambia. *Glob. Biogeochem. Cycles* 36, e2021GB007261. doi:10.1029/2021GB007261

Spitters, C. J. T., Toussaint, H. A. J. M., and Goudriaan, J. (1986). Separating the diffuse and direct component of global radiation and its implications for modeling canopy photosynthesis Part I. Components of incoming radiation. *Agric. For. Meteorol.* 38, 217–229. doi:10.1016/0168-1923(86)90060-2

Staniaszek, Z., Griffiths, P. T., Folberth, G. A., O'Connor, F. M., Abraham, N. L., and Archibald, A. T. (2022). The role of future anthropogenic methane emissions in air quality and climate. *Npj Clim. Atmos. Sci.* 5, 21–28. doi:10.1038/s41612-022-00247-5

Turner, A. J., Frankenberg, C., and Kort, E. A. (2019). Interpreting contemporary trends in atmospheric methane. *Proc. Natl. Acad. Sci.* 116, 2805–2813. doi:10.1073/pnas.1814297116

Walter, B. P., and Heimann, M. (2000). A process-based, climate-sensitive model to derive methane emissions from natural wetlands: application to five wetland sites, sensitivity to model parameters, and climate. *Glob. Biogeochem. Cycles* 14, 745–765. doi:10.1029/1999GB001204

Wania, R., Ross, I., and Prentice, I. C. (2010). Implementation and evaluation of a new methane model within a dynamic global vegetation model: LPJ-WHyMe v1.3.1. *Geosci. Model Dev.* 3, 565–584. doi:10.5194/gmd-3-565-2010

Xi, Y., Peng, S., Ducharne, A., Ciais, P., Gumbricht, T., Jimenez, C., et al. (2022). Gridded maps of wetlands dynamics over mid-low latitudes for 1980–2020 based on TOPMODEL. *Sci. Data* 9, 347. doi:10.1038/s41597-022-01460-w

Yuan, F., Wang, Y., Ricciuto, D. M., Shi, X., Yuan, F., Hanson, P. J., et al. (2021). An integrative model for soil biogeochemistry and methane processes. II: warming and elevated CO2 effects on peatland CH4 emissions. *J. Geophys. Res. Biogeosciences* 126, e2020JG005963. doi:10.1029/2020JG005963

Yue, X., and Unger, N. (2015). The Yale Interactive terrestrial Biosphere model version 1.0: description, evaluation and implementation into NASA GISS ModelE2. *Geosci. Model Dev.* 8, 2399–2417. doi:10.5194/gmd-8-2399-2015

Yue, X., Unger, N., and Zheng, Y. (2015). Distinguishing the drivers of trends in land carbon fluxes and plant volatile emissions over the past 3 decades. *Atmos. Chem. Phys.* 15, 11931–11948. doi:10.5194/acp-15-11931-2015

Zhang, Y., Jacob, D. J., Lu, X., Maasakkers, J. D., Scarpelli, T. R., Sheng, J.-X., et al. (2021a). Attribution of the accelerating increase in atmospheric methane during 2010–2018 by inverse analysis of GOSAT observations. *Atmos. Chem. Phys.* 21, 3643–3666. doi:10.5194/acp-21-3643-2021

Zhang, Z., Fluet-Chouinard, E., Jensen, K., McDonald, K., Hugelius, G., Gumbricht, T., et al. (2021b). Development of the global dataset of wetland area and dynamics for methane modeling (WAD2M). *Earth Syst. Sci. Data* 13, 2001–2023. doi:10.5194/essd-13-2001-2021

Zhang, Z., Poulter, B., Feldman, A. F., Ying, Q., Ciais, P., Peng, S., et al. (2023). Recent intensification of wetland methane feedback. *Nat. Clim. Change* 13, 430–433. doi:10.1038/s41558-023-01629-0

Zhang, Z., Zimmermann, N. E., Stenke, A., Li, X., Hodson, E. L., Zhu, G., et al. (2017). Emerging role of wetland methane emissions in driving 21st century climate change. *Proc. Natl. Acad. Sci.* 114, 9647–9652. doi:10.1073/pnas.1618765114

Zhu, Q., Liu, J., Peng, C., Chen, H., Fang, X., Jiang, H., et al. (2014). Modelling methane emissions from natural wetlands by development and application of the TRIPLEX-GHG model. *Geosci. Model Dev.* 7, 981–999. doi:10.5194/gmd-7-981-2014

Zhu, Q., Peng, C., Chen, H., Fang, X., Liu, J., Jiang, H., et al. (2015). Estimating global natural wetland methane emissions using process modelling: spatio-temporal patterns and contributions to atmospheric methane fluctuations. *Glob. Ecol. Biogeogr.* 24, 959–972. doi:10.1111/geb.12307

Zou, J., Ziegler, A. D., Chen, D., McNicol, G., Ciais, P., Jiang, X., et al. (2022). Rewetting global wetlands effectively reduces major greenhouse gas emissions. *Nat. Geosci.* 15, 627–632. doi:10.1038/s41561-022-00989-0

frontiers | Frontiers in Environmental Science

TYPE Methods
PUBLISHED 30 November 2023
DOI 10.3389/fenvs.2023.1301934

OPEN ACCESS

EDITED BY
Zhiyuan Hu,
Sun Yat-sen University, China

REVIEWED BY
Guoyin Wang,
Fudan University, China
Jianhua Xiao,
Chinese Academy of Sciences (CAS), China
Qiuyan Du,
University of Science and Technology of China, China

*CORRESPONDENCE
Feng Pan,
panfeng@lzu.edu.cn

RECEIVED 25 September 2023
ACCEPTED 10 November 2023
PUBLISHED 30 November 2023

CITATION
Wang P, Chen M, An W, Liu Y and Pan F (2023), Research on the fugitive soil dust emission inventory in Western China based on wind erosion equation parameter optimization.
Front. Environ. Sci. 11:1301934.
doi: 10.3389/fenvs.2023.1301934

Research on the fugitive soil dust emission inventory in Western China based on wind erosion equation parameter optimization

Pengbo Wang, Min Chen, Weiming An, Yongle Liu and Feng Pan*

Lanzhou University, College of Atmospheric Sciences, Lanzhou, China

The Wind Erosion Equation, currently one of the primary methods for estimating fugitive soil dust emission inventory, is influenced by several factors. Taking the convergent areas of the Tibet Plateau, Loess Plateau, and Qinba Mountains in Western China, we have optimized the climate factor using the *WRF* model driven by *ERA5* reanalysis data. Additionally, we have modified the vegetation cover factors via normalized difference vegetation index and considered the impacts of the land use and cover change. Subsequently, other factors were allocated utilizing geographic information system, and the grid-based fugitive soil dust emission inventory for the study area for 2019 was derived through calculation. Based on the climate factor and vegetation cover factor, we have come up with the monthly allocation coefficients. The study has revealed the following findings: (1) Climate factors are unevenly distributed throughout the focused region, with the Loess Plateau showing the highest value, followed by the Tibet Plateau and the Qinba Mountains. There are also significant variations in the distribution of these factors among municipalities and counties; (2) The order of vegetation cover factor, primarily influenced by regional background as well as agricultural and pastoral activities, in the Loess Plateau, Tibetan Plateau and Qinba Mountains, is consistent with that of the wind erosion index; (3) In 2019, fugitive dust emissions from total suspended particles, PM_{10}, and $PM_{2.5}$ reached 9835.9, 2950.8, and 491.8 kt/a, respectively. The Loess Plateau exhibited the highest emission intensity due to factors such as low vegetation coverage, precipitation, high wind speed and wind erosion index; (4) Climate factor and vegetation cover factor are the primary factors influencing the monthly allocation coefficients. In 2019, the highest monthly fugitive dust emissions were estimated in April, accounting for approximately 36.21% of the total. The second and third-highest were found in August and June, respectively. This phenomenon can be explained climatically, as the Loess Plateau, semi-arid and arid regions, did not experience a significant increase in rainfall corresponding to rising temperatures.

KEYWORDS

WRF, wind erosion equation, climate factor, vegetation cover factor, fugitive soil dust emission inventory, monthly allocation coefficient

1 Introduction

Particulate matter (*PM*) in the atmosphere has detrimental effects on both human health and atmospheric visibility, with a particular concern for $PM_{2.5}$ (Apte et al., 2015; Liu et al., 2016; Ji et al., 2020). To address these challenges, China introduced the "Air Pollution Prevention and Control Action Plan" (The State Council, 2013) in 2013 and the "Three-Year Action Plan to Fight Air Pollution" (The State Council, 2018) in 2018. These plans aim to achieve targeted pollution control through pollution source inventories, numerical modeling, and receptor models, to continuously address PM_{10} and $PM_{2.5}$ pollution and improve urban air quality (Wang et al., 2014; Cheng et al., 2017; Zhang et al., 2017; Shang et al., 2018; Asian Clean Air Center, 2021). However, compiling emission inventories for certain atmospheric pollution sources in complex terrains still presents challenges, such as the fugitive soil dust (*FSD*) emission inventory. *FSD* refers to the *PM* generated directly from exposed surfaces, including agricultural fields, bare mountains, mudflats/tidal flats, dried river valleys, and undeveloped or unvegetated lands, due to natural forces such as wind erosion or anthropogenic activities (Ministry of Environmental Protection, 2014). *FSD* represents a major source of *PM* in the ambient air, particularly in the arid and semi-arid regions of Northwestern China (Song et al., 2016).

Wind erosion, categorized as soil erosion, involves the displacement of soil particles under the influence of certain wind forces, including migration, creeping, and suspension. It primarily encompasses fine dust in the form of aerosols, sand drifting, and coarse particles displacing on the ground (Zhang et al., 2002). The results of receptor models indicate that fugitive dust is responsible for 10%–24% of ambient PM_{10} in cities such as Urumqi, Taiyuan, Anyang, Tianjin, and Jinan. (Bi et al., 2007). However, due to the uncertainties associated with *FSD* emission inventory compilation, several regional emission inventory studies currently exclude *FSD* (Zheng et al., 2009; Fu et al., 2013; Qi et al., 2017; Liu H. et al., 2018).

In the 1960s, Woodruff and Siddoway, (1965) and the U.S. Department of Agriculture conduced extensive research on wind erosion in farmlands, leading to development of the Wind Erosion Equation (*WEQ*). This empirical model established relationships between wind erosion rates and various influencing factors (Skidmore and Woodruff, 1968). Subsequently, as the understanding of wind erosion mechanisms improved, several other models were subsequently developed, including the Revised Wind Erosion Equation (Fryrear et al., 2000), the Texas Erosion Analysis Model (Gregory et al., 2004), the Wind Erosion Assessment Model (Shao et al., 1996), and the Wind Erosion Prediction System (Buschiazzo and Zobeck, 2008). Although these later models offer more refined and accurate predictions compared with *WEQ* (Buschiazzo and Zobeck, 2008; Zou et al., 2014; Liu et al., 2021), they require more detailed input parameters and involve higher technical complexity, making them unsuitable for large-scale regional *FSD* emission inventory compilation. In contrast, the *WEQ* is widely adopted due to its simplicity, operational feasibility, and ease of implementation (Xuan et al., 2000; Panebianco and Buschiazzo, 2008; Mandakh et al., 2016; Xu et al., 2016; Liu A. B. et al., 2018). The *WEQ* has been endorsed by the United States Environmental Protection Agency (Cowherd et al., 1974; Jutze and Axetell, 1974) and the California Air Resources Board (Countess Environmental, 2006). In 2014, the Ministry of Ecology and Environment of the People's Republic of China officially designated the *WEQ* model as the recommended calculation method for *FSD* emission inventory compilation (Ministry of Environmental Protection, 2014).

Some researchers have utilized the *WEQ* and incorporated normalized difference vegetation index (*NDVI*) data for estimating vegetation cover and urban meteorological data for calculating regional climate factor to compute *FSD* emission inventory for the Beijing–Tianjin–Hebei region and the 2 + 26 cities across China (Li et al., 2020; Li et al., 2021; Song et al., 2021). However, in complex terrains, meteorological factors observed at national basic and general meteorological stations cannot fully represent the distribution of meteorological factors in administrative regions such as cities, counties, or districts, due to the influence of atmospheric circulation, topography, latitude, solar radiation, and water vapor conditions. Consequently, the climate factor required for *WEQ* calculations, such as annual mean wind speed, monthly precipitation, and monthly mean temperature, exhibit heterogeneity within the same city, county, or district.

To address these limitations, we propose a method in this study to further optimize the *WEQ*'s parameter and develop a high spatiotemporal-resolution *FSD* emission inventory. Our approach improves the accuracy of *WRF* simulations using the *ECMWF-ERA5* climate reanalysis dataset and calculates the climate factor of *WEQ* based on the *WRF* simulation results. This approach reduces the errors in calculating climate factor within the *WEQ* model caused by the uniform adoption of meteorological data from city, county, or district meteorological stations. According to the land use and cover change (*LUCC*) data, adjustments are made to the vegetation cover factor for grids representing construction land, paddy fields, water area, and areas with high vegetation coverage. Furthermore, monthly allocation coefficients are proposed based on the estimated annual mean fugitive soil dust emissions. We apply this methodology to estimate the *FSD* emission inventory in the convergence areas of the Tibet Plateau, Loess Plateau, and Qinba Mountains in Western China, and investigate the variations among different contributing factors.

2 Data and methods

2.1 Study area

The study area encompasses the eastern part of the Tibet Plateau, the southwestern part of the Loess Plateau, and the northwestern part of the Qinba Mountains in Western China. It includes several prefecture-level regions across different provinces. In Gansu Province, the cities of Tianshui, Longnan, Pingliang, Qingyang, Baiyin, Lanzhou, Linxia, Gannan, and Wuwei are within the study area. Qinghai Province is represented by Xining city, Haidong, Huangnan, and Hainan prefecture. The Shaanxi Province includes Xi'an, Xianyang, Yulin, Weinan, Hanzhong, Yan'an, Tongchuan, Shangluo, and Ankang cities. Zhongwei, Guyuan, and Wuzhong cities fall within the study area of Ningxia Autonomous Region. Lastly, Sichuan Province encompasses Guangyuan, Mianyang, Bazhong cities, and Aba prefecture. The study area displays diverse topography, with the

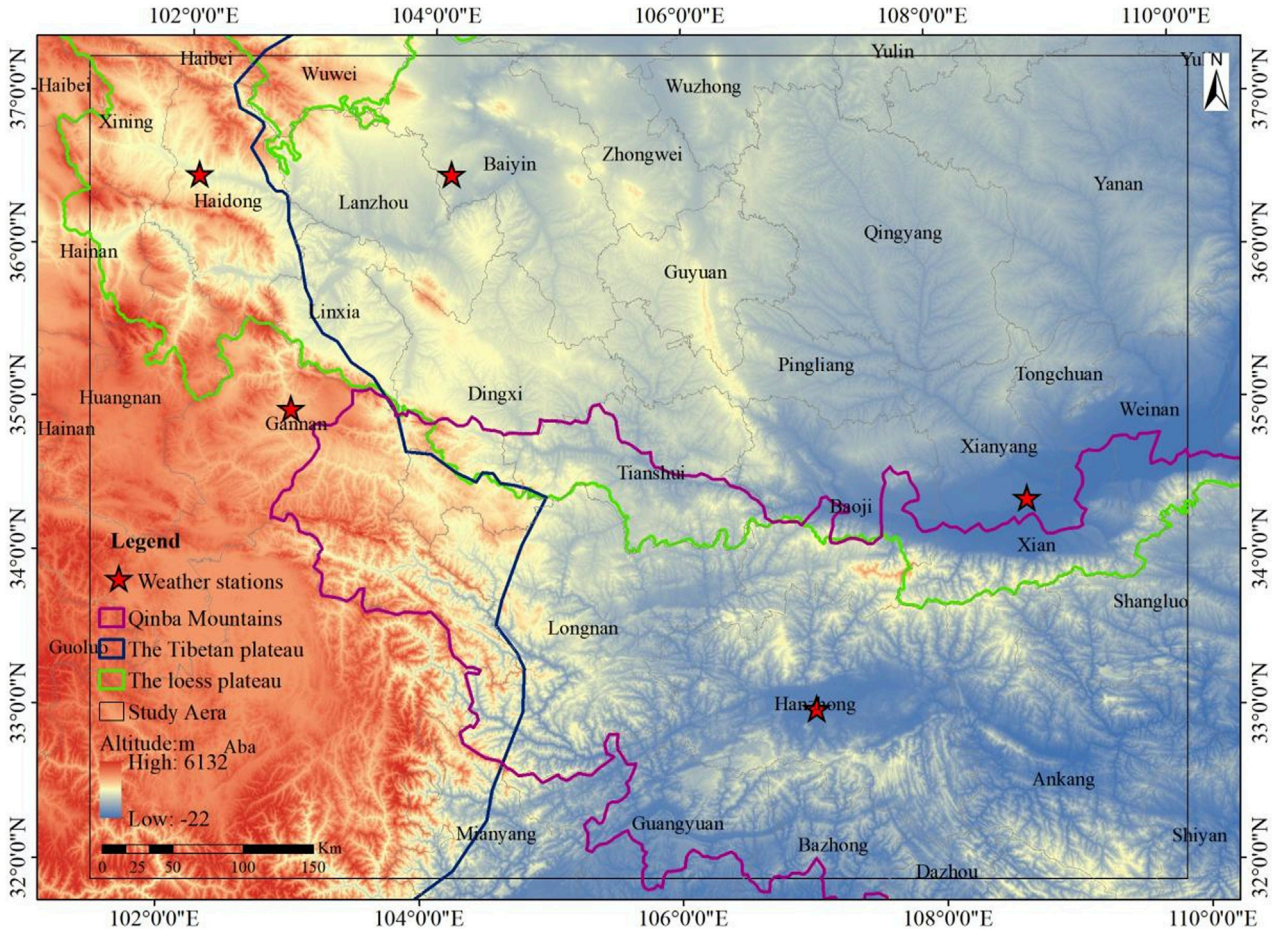

FIGURE 1
Geographical elevation and weather stations of the study area in Western China.

western region dominated by the Tibet Plateau, characterized by high-altitude terrain. In the northern and northeastern parts, the prominent feature is the Loess Plateau, characterized by relatively higher elevations and a network of gullies. The southern region is primarily occupied by the Qinba Mountains, featuring lower elevations but more intricate terrain compared to the Loess Plateau, as illustrated in Figure 1.

2.2 Introduction to the *WEQ*

The estimation model adopted in this paper is *WEQ*, which is represented as follows:

$$W = EF \times A \tag{2.1}$$

$$EF = \alpha \times k \times I \times K \times C \times L \times V \tag{2.2}$$

Where *W* represents the *FSD* emission, and *EF* denotes the annual emission intensity factor for wind-eroded *FSD*, measured in $t\cdot(hm^2\cdot a)^{-1}$. *A* corresponds to the area of the study area (unit: hm^2). α is the dimensionless proportion coefficient of total suspended particles (*TSP*) to the total loss induced by wind erosion, with a reference value of 2.5% recommended by the United States Environmental Protection Agency (*USEPA*). In this model, *k* represents the *PM* percentage in *FSD* and it is dimensionless whereas *TSP*, PM_{10}, $PM_{2.5}$ are set to be 1.0, 0.3, and 0.05, respectively. (Chepil, 1958; Craig and Turelle, 1964; Jutze and Axetell, 1976). *I* represents the wind erosion index, measured in $t\cdot(hm^2\cdot a)^{-1}$; *K* represents the surface roughness factor (dimensionless); *C* represents the climate factor (dimensionless), as presented in Eqs 2.3, 2.4 respectively; *L* represents the unshielded width factor (dimensionless). *V* represents the vegetation cover factor, which indicates the proportion of bare soil area to the total calculated area and is dimensionless (Jutze and Axetell, 1976; US. Environmental Protection Agency, 1977; Skidmore, 1986), as shown in Eq. 2.5.

$$C = 3.86 \times u^3 \Big/ (PE)^2 \tag{2.3}$$

$$PE = 3.16 \times \sum_{i=1}^{12} \left[\frac{Pi}{(1.8Ti+22)} \right]^{10/9} \tag{2.4}$$

$$V = 1 - VC \tag{2.5}$$

Where, *u* represents the annual mean wind speed, corresponding to the annual mean 10-m wind speed in meteorology, $(unit:m\cdot s^{-1})$. *PE* represents the Thornthwaite's precipitation–evapotranspiration

TABLE 1 *WRF* model simulations correlation validation for representative stations in the study area from January to December of 2019.

Item	Station	R	*RMSE*	*MFB*	*MFE* (%)
Monthly mean wind speed ($m \cdot s^{-1}$)	Ping'an	0.316	0.302	−3.7%	9.8
	Hezuo	0.628	0.205	−1.3%	6.5
	Baiyin	0.662	0.554	11.5%	14.9
	Qindu	0.569	0.360	−10.1%	12.6
	Hanzhong	0.811	0.204	18.8%	10.0
Monthly mean temperature (°C)	Ping'an	0.994	1.126	6.5%	7.6
	Hezuo	0.874	4.187	11.7%	5.4
	Baiyin	0.929	4.751	50.9%	19.5
	Qindu	0.920	4.820	25.2%	39.8
	Hanzhong	0.998	0.912	19.1%	6.1
Monthly precipitation (mm)	Ping'an	0.906	14.451	8.1%	32.8
	Hezuo	0.906	36.696	6.1%	37.4
	Baiyin	0.800	21.564	25.7%	63
	Qindu	0.883	30.826	0.1%	25.4
	Hanzhong	0.886	67.693	12.7%	35.2

index (dimensionless), calculated using Eq. 2.4. P_i denotes the monthly precipitation in month i (unit: mm), with a minimum value of 12.7 mm for $P_i < 12.7$ mm. T_i stands for the monthly mean temperature measured in °C, corresponding to monthly mean ground temperature in meteorology, with a minimum value of −1.7°C for $Ti < -1.7$°C (Lyles, 1983; Panebianco and Buschiazzo, 2008). *VC* refers to the proportion of the area covered by the vertical projection per unit area of the vegetation and is dimensionless (Gitelson et al., 2002). *VC* was calculated using the binary pixel model (Jia et al., 2013), as shown in Eq. 2.6.

$$\mathrm{VC} = (\mathrm{NDVI} - \mathrm{NDVI_{soil}}) \Big/ \left(\mathrm{NDVI_{veg}} - \mathrm{NDVI_{soil}}\right) \tag{2.6}$$

Where, *VC* represents the vegetation cover of the pixel, where *NDVI* and $NDVI_{soil}$ denote the *NDVI* values of the pixel and non-vegetated land, respectively, with the latter being the minimum *NDVI* value. $NDVI_{veg}$ is the *NDVI* value of vegetated land, which can be considered as the maximum *NDVI* value. In this study, the upper and lower thresholds of *NDVI* were defined to represent $NDVI_{soil}$ and $NDVI_{veg}$, respectively, at a 5% confidence level.

2.3 Data sources and processing methods

ERA5 is the fifth generation European Centre for Medium-Range Weather Forecasts (*ECMWF*) atmospheric reanalysis of the global climate. The *ECMWF-ERA5* reanalysis dataset has a horizontal grid resolution of 0.25 × 0.25 and comprises 137 pressure levels in the vertical direction, with a temporal resolution of 1 h. In this study, the *ECMWF-ERA5* dataset is used to provide initial boundary conditions for the WRF model simulations. Surface observation data of the stations in Baiyin (Baiyin station), Haidong (Ping'an station), Gannan (Hezuo station), Xianyang (Qindu station), and Hanzhong (Hanzhong station) for the year 2019 were obtained from the *CMA* Meteorological Data Centre (*http://data.cma.cn/data/detail/dataCode/A.0012.0001.html*), as presented in Figure 1. To quantitatively analyze the performance of the WRF model simulation, the model results will be assessed by using four commonly used statistical metrics, namely, the correlation coefficient (*R*), root mean square error (*RMSE*), mean fractional bias (*MFB*), and mean fractional error (*MFE*) (Taylor, 2001).

$$\mathrm{R} = \frac{\sum_{i=1}^{N}(P_i - \bar{P})(O_i - \bar{O})}{\sqrt{\sum_{i=1}^{N}(P_i - \bar{P})^2} \times \sqrt{\sum_{i=1}^{N}(O_i - \bar{O})^2}} \tag{2.7}$$

$$\mathrm{RMSE} = \sqrt{\frac{1}{N}\sum_{i=1}^{N}(P_i - O_i)^2} \tag{2.8}$$

$$MFB = \frac{1}{N}\sum_{i}^{N}\frac{P_i - O_i}{O_i + P_i/2} \tag{2.9}$$

$$MFE = \frac{1}{N}\sum_{i}^{N}\frac{|P_i - O_i|}{O_i + P_i/2} \tag{2.10}$$

Where, P_i and O_i represent the simulated and observed data, respectively, N denotes the number of samples, and $\bar{P}$ and $\bar{O}$ denote the mean of the stimulated and observed data, respectively.

The *NDVI* data used are derived from *MODIS* (*https://modis.gsfc.nasa.gov/*). The *MODIS NDVI* data product is identified as *MOD13Q1*, which is generated every 16 days. In this study, we used the 250 m spatial resolution *NDVI* values from the year 2019, resulting in total 46 *NDVI* datasets covering the study area. Regarding land use types, this study used the land use and cover change (*LUCC*) of 2020 with a spatial resolution of 1 km × 1 km (Xu et al., 2018).

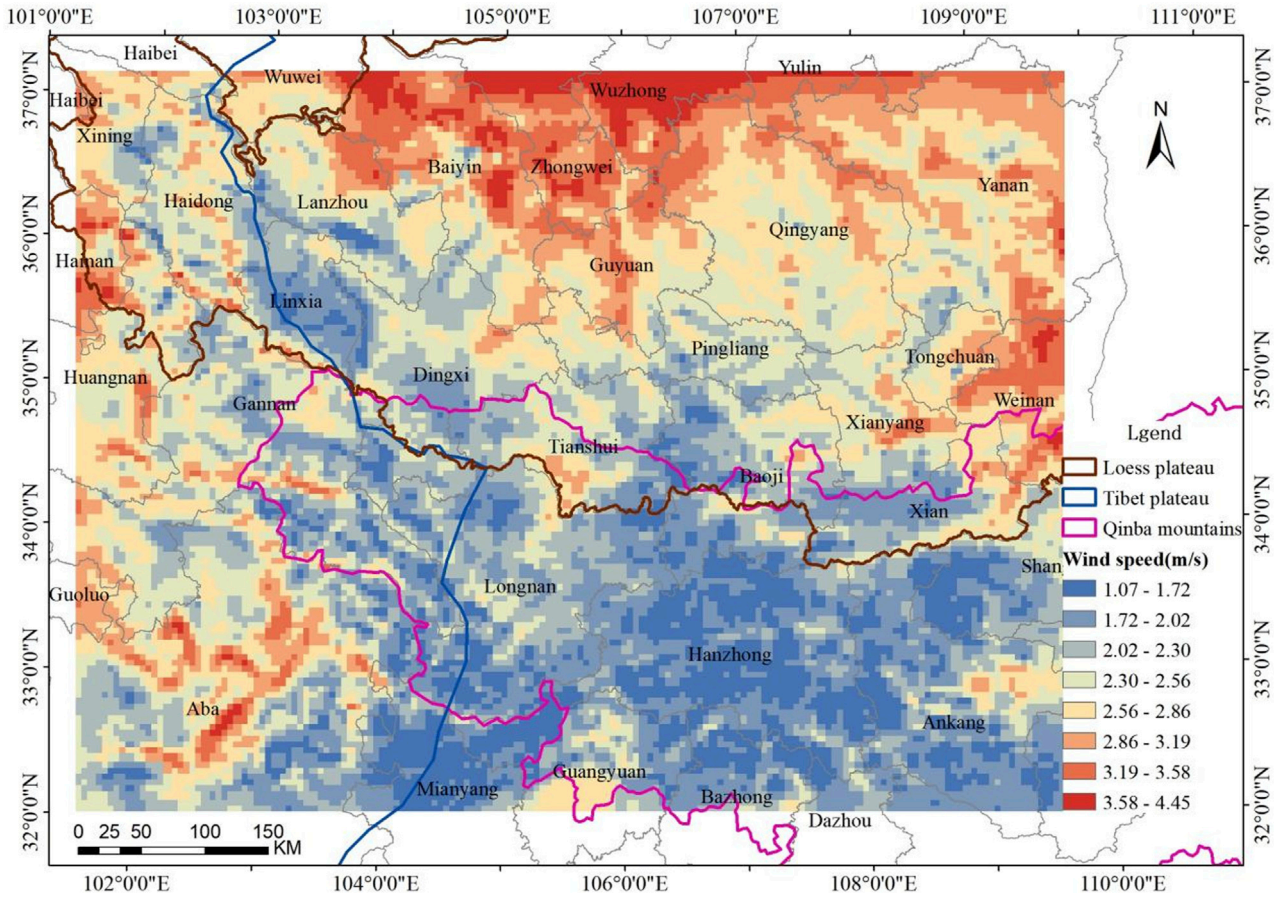

FIGURE 2
5 km × 5 km annual mean 10-m wind speed in the study area in 2019.

The soil texture data used in this study are obtained from the Chinese soil dataset from the "Harmonized World Soil Database (v1.1)" provided by the National Cryosphere Desert Data Center (*http://www.ncdc.ac.cn*) (Lu and Liu, 2019). This dataset, which has a spatial resolution of 1 km × 1 km, includes information on the percentage of sand, clay, and silt in the soil.

For data processing, the *WRF* simulation was initially conducted using *ERA5* reanalysis data as the initial field, allowing for the computation of *C* at each grid point. Subsequently, monthly and annual average *VC* for the study area were derived using the *NDVI* data at a spatial resolution of 250 m. These data were further optimized by integrating 1 km-resolution *LUCC* data with grids having *VC* values above 0.61, resulting in a refined *V* with a 1 km resolution. This refined dataset was then allocated to 5 km-resolution grids. Various relevant parameters, including *C*, *V*, *I*, and other related parameters were incorporated into a geographic information system (*GIS*) to generate multiple data layers. Finally, the annual *FSD* emissions were calculated utilizing the annual data of various parameters from the 5 km × 5 km grid; in the meantime, based on the monthly allocation coefficients proposed in this study, the monthly *FSD* emissions were calculated to derive the high spatiotemporal-resolution *FSD* emission inventory for the study area.

3 Results and discussion

3.1 Key parameter values

3.1.1 Climate factor

3.1.1.1 *WRF* simulation setup and parameterization scheme

In this study, *ECMWF-ERA5* data were used to provide initial boundary conditions for the *WRF* model. The simulation area was centered at 105.66°E and 34.62°N. The horizontal domain consisted of two nested model domains: the first nested domain had a grid size of 80 × 64 and a spacing of 25 km, while the second nested domain had a grid size of 160 × 120 and a spacing of 5 km. The *ERA5* data was divided into 39 vertically non-equidistant layers. In this study, simulations were conducted for each month of the year 2019. The simulation period started from 00:00 on the 25th day of the previous month and continued until 00:00 on the first day of the following month. The analysis period covered the entire month, starting from 0:00 on the first day of the month and ending at 23:00 on the last day of the month. The integration time step for the simulations was set as 180 s, and the *WRF* model output was recorded at hourly intervals.

Parameterization Scheme: For microphysics processes, the Single-Moment 6-class scheme was employed in this study. The Betts–Miller–Janjic, RRTM, and Dudhia schemes were used for cumulus convection parameterization, longwave radiation, and

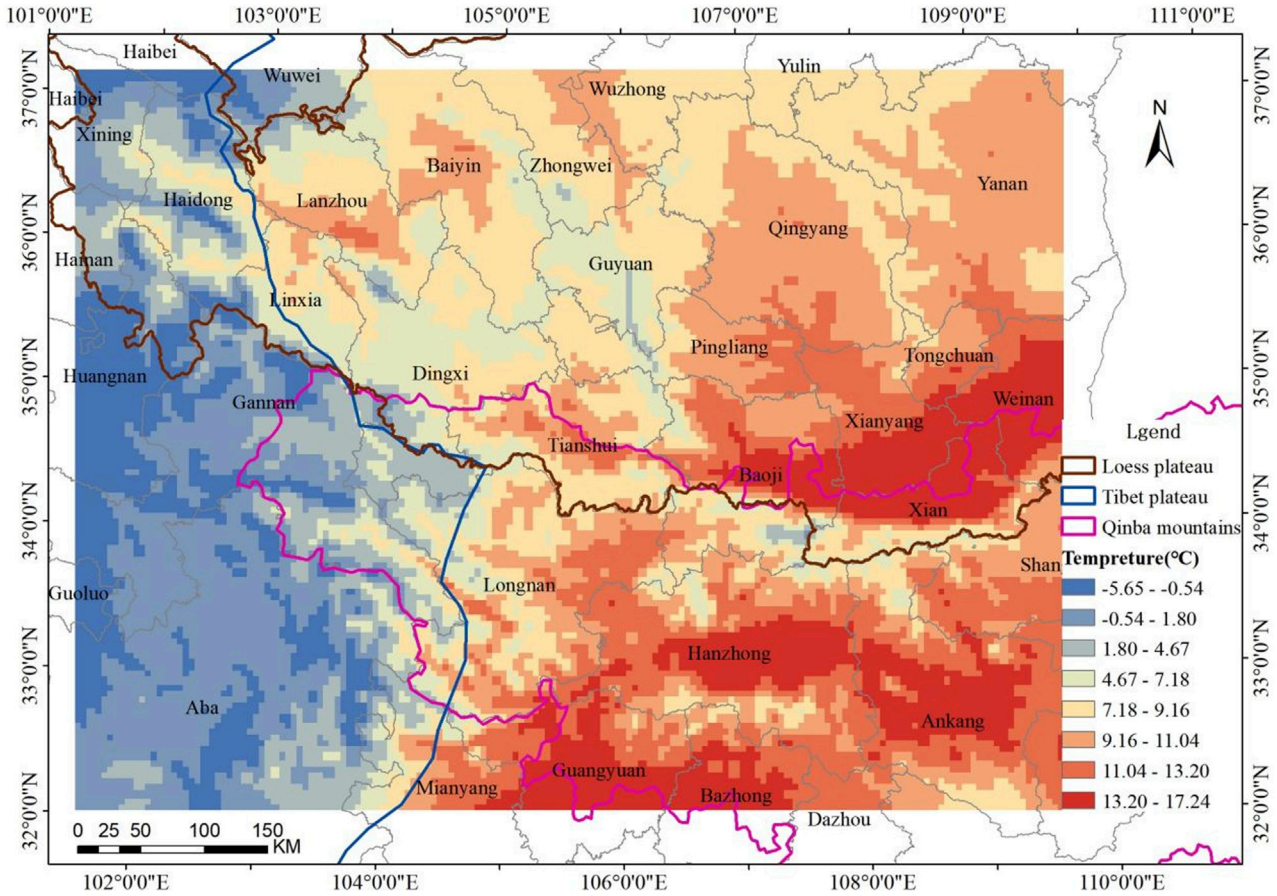

FIGURE 3
5 km × 5 km annual mean ground temperature in the study area in 2019.

shortwave radiation, respectively. The Noah and MYJ schemes were employed for land surface processes and boundary layer parameterization, respectively. Additionally, the Monin–Obukhov scheme was applied for the near-surface layer.

3.1.1.2 *WRF* model correlation validation

To verify the effectiveness of the *ECMWF-ERA5* dataset as the initial boundary conditions for simulating meteorological fields in the study area, several representative stations were selected for validation. These stations included Gannan in the western part of the study area, Baiyin, Haidong, and Xianyang, which recorded relatively greater *FSD* emissions, as well as Hanzhong in the southern part of the study area. Monthly observed data from January to December of 2019 were used to calculate u_i (monthly mean 10-m wind speed), *Ti* (monthly mean ground temperature), and P_j (monthly precipitation), which were required as inputs for the C in the *WEQ* model. The results of the *WRF* model simulations were then compared and validated against the observed data, as presented in Table 1.

As indicated in Table 1, the simulated u_i, T_i, P_i for the five stations in the study area from January to December exhibited desirable correlation with the observed values. The overall correlation followed the order $T_i > P_i > u_i$, suggesting that the *WRF* model's monthly time series simulation results correlate well with the actual data in the context of complex terrains. Concerning *RMSE*, the performance of each station varied across different meteorological factors. Baiyin Station exhibited the highest *RMSE* for u_i. This is mainly because all five stations are located within basin terrains, In which the observed u_i tends to be relatively lower owing to terrain obstruction. But, the simulated u_i tends to be overestimated to varying degrees during most months, with Baiyin Station being overestimated the most. The *RMSE* of T_i followed the order: Qindu > Baiyin > Hezuo > Ping'an > Hanzhong. The simulated T_i was generally overestimated in most months. The *RMSE* of P_i followed the order: Hanzhong > Hezuo > Qindu > Baiyin > Ping'an. This is primarily owing to the relatively larger annual precipitation in Hanzhong, Hezuo, and Qindu compared with Baiyin and Ping'an, and the model's tendency to overestimate precipitation during the flood season. With regard to the *MFB* and *MFE*, aside from the T_i and P_i at Baiyin, the *MFB* of remaining factors are bigger than-30% and smaller than 30%, and the *MFE* of them are lower than 50%, suggesting that the simulation results are acceptable for Baiyin and outstanding for the other stations (Taylor, 2001). Based on the aforementioned evaluation, It is fair to conclude that the *WRF* model's meteorological simulation results for the study area can be used for calculating *C* of the *WEQ* model.

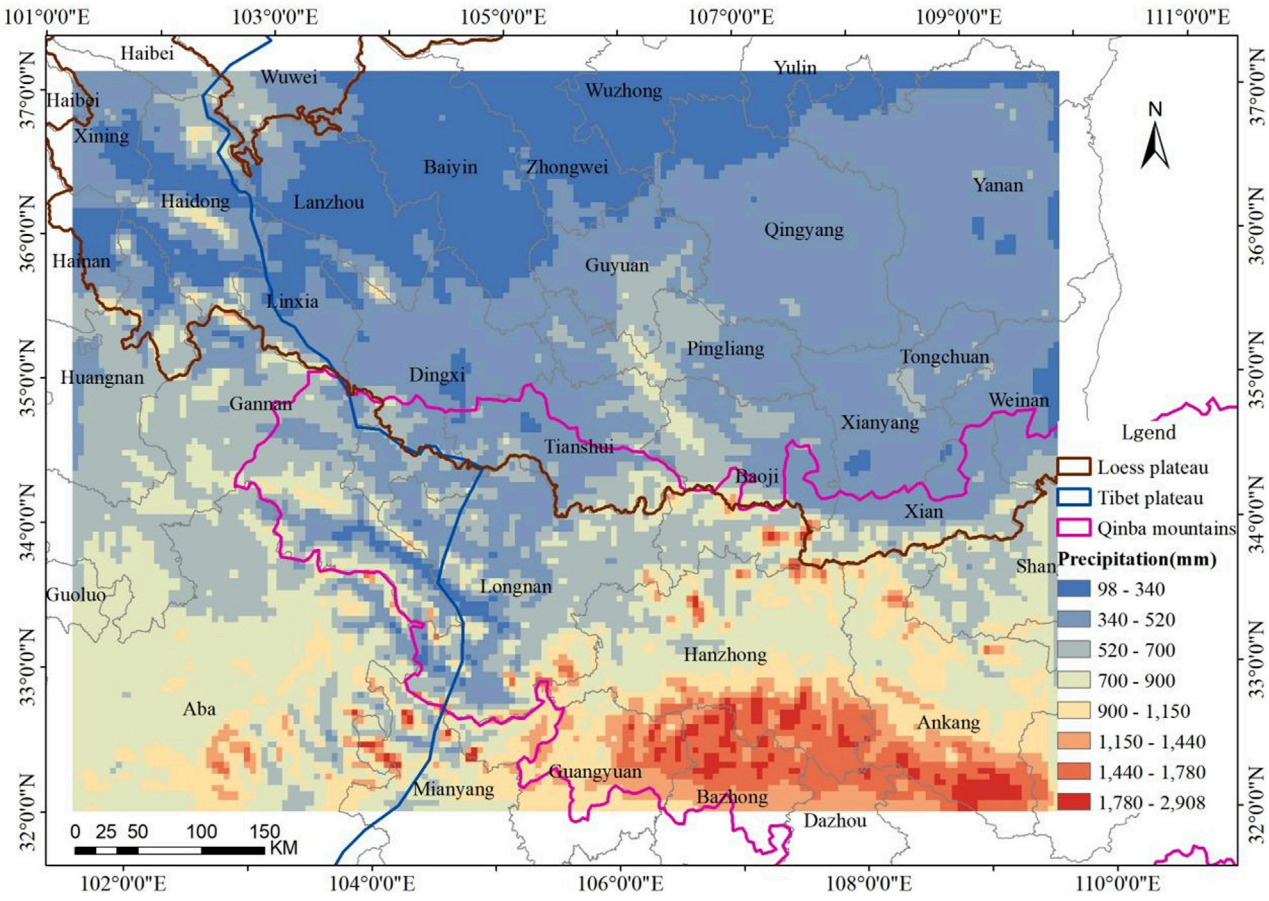

FIGURE 4
5 km × 5 km precipitation in the study area in 2019.

3.1.1.3 Climate factor Calculation

In previous studies, the calculation of *C* in the *WEQ* model has been primarily based on meteorological data from representative weather stations within the cities or counties in the study area. These data include u (annual mean 10-m wind speed), T_i, and P_i (Li et al., 2020; Song et al., 2021). However, because of the complex terrain and significant elevation differences in the study area, along with varying *VC*, most cities are situated in valleys or basins, making it challenging for the observed data from urban meteorological stations to accurately represent the meteorological conditions within the cities, prefectures, and counties (districts). Therefore, in this study, we used the *WRF* simulation results for each month in 2019 to extract the values of u, T_i, and P_i, for each grid cell and each month. We found that the distribution of 10-m wind speed, temperature and precipitation in the study area was extremely uneven, as shown in Figures 2–4.

Figure 2 clearly shows that the Loess Plateau has the highest u, particularly in areas around Baiyin, Zhongwei, and Wuzhong. The u is relatively lower on the Tibet Plateau and lowest on the Qinba Mountains. Figure 3 indicates that the annual mean temperature in the study area has an east-west and south-north gradient, with higher temperatures observed in the eastern and southern regions and lower temperatures in the western and northern areas. Owing to the "heat island effect," the highest temperatures are concentrated in urban built-up areas. As depicted in Figure 4, the annual precipitation gradually decreases from south to north within the study area. The Qinba Mountains receive the most annual precipitation, followed by the Tibet Plateau, while the lowest precipitation is found on the Loess Plateau.

Because the three factors are overestimated to varying degrees, and the *MFB* of monthly precipitation is larger, part of the overestimation will be offset in the calculation of climate factors. The value of *C* for each grid cell in the study area can be calculated by Eqs 2.3, 2.4. Figure 5 illustrates the range of the *C*, which spans from a minimum of 0.0001 to a maximum of 1.227, with a mean value of 0.0586. These findings align closely with that of the magnitudes reported by Li et al. (2020) for different districts across Beijing. The distribution of *C* in the study area is uneven, with the highest values being found for the Loess Plateau, particularly in the northern areas around Baiyin, Zhongwei, and Wuzhong. The Tibet Plateau follows, exhibiting relatively higher *C* values, primarily in areas such as Haidong, Hainan, and Huangnan prefectures. Conversely, the lowest *C* values are observed in the Qinba Mountains. The primary factors contributing to the variation in the distribution of *C* are the 10-m wind speed and precipitation. In the northern part of the Loess Plateau, the terrain is relatively flat, resulting in higher 10-m wind speed. However, this region falls within a semi-arid and arid zone, resulting in relatively lower precipitation. Furthermore,

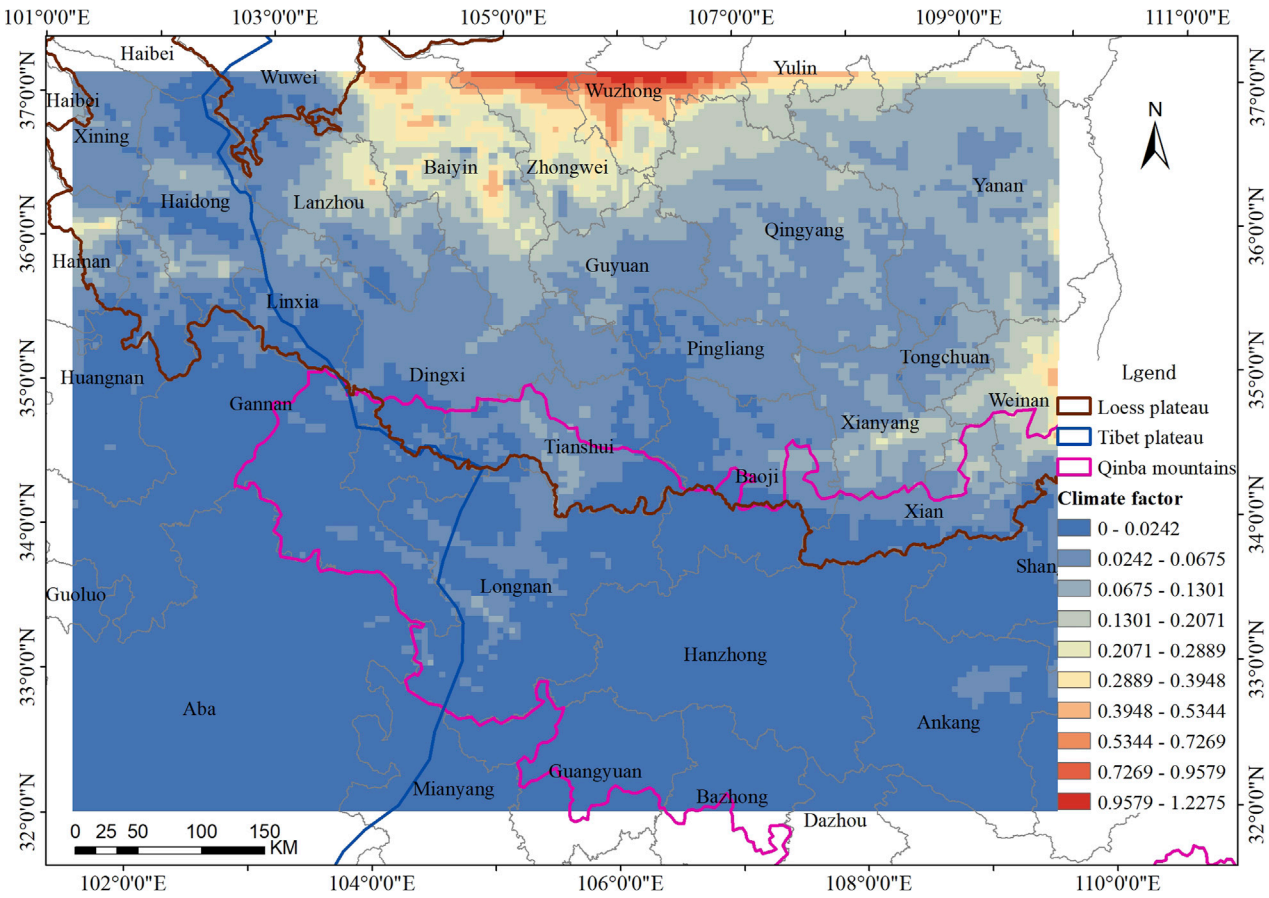

FIGURE 5
5 km × 5 km climate factor of the study area in 2019.

Figure 5 indicates that even within the same city or county-level administrative area, there are certain variations in *C* among grid cells, with high values typically absent in urban built-up areas.

3.1.2 Vegetation cover factor

In this study, we used the 2019 *MODIS MCD12Q1* product to calculate the spatial distribution of *VC* values for each month, as well as the distribution of annual mean *VC* values. Figure 6 illustrates the *VC* values for representative months and the overall year. Different land use types, such as forests, grasslands, deserts, and croplands (including crops), feature diverse vegetation types. Natural vegetation has different growth cycles, and agricultural crops have varying periods for planting, growth, and harvesting. Consequently, the *VC* values vary each month for different land use types. As depicted in Figure 6, the *VC* values exhibit variations across months, regions, and grid points. On the Loess Plateau, the *VC* values are the lowest among the three regions, with the minimum values occurring in July and August. This decline may be primarily attributed to winter wheat harvesting (Qi et al., 2022). The Tibet Plateau exhibits intermediate *VC* values, with the lowest value being observed in March, when grasses wither till April (Zhuo et al., 2018). In contrast, the Qinba Mountains exhibit the highest *VC* values, with the lowest value being observed in June, possibly associated with the harvest of economic crops such as rapeseed (oil crop) and vegetables (Xiao, 2022; Chen et al., 2023).

In areas of urban construction, fugitive dust emissions mainly arise from road and construction activities, while stockpile dust appear around industries and mining facilities, and *FSD* outside urban built-up areas. *FSD* regions are typically located outside urban built-up areas, and water areas and rice paddies are generally considered *non-FSD* regions (Ministry of Environmental Protection, 2014). Therefore, construction areas, water areas, and paddy fields are categorized as non-sources for *FSD* in this study using the *LUCC* data (Xu et al., 2018).

Furthermore, Zhao, (2006) conducted wind tunnel experiments on the Inner Mongolia grassland and reported that on places whose *VC* are above 40%, wind erosion does not occur even when the wind speed arrives at 10 m s^{-1}. Additionally, on high-*VC* grasslands where the *VC* reaches 60%–80%, wind erosion is effectively suppressed even when wind speed increases to 14–18 m s^{-1}. Furthermore, other Chinese researchers have suggested that when the *NDVI* exceeds 0.61, *FSD* emissions are considered negligible (Song et al., 2021). Accordingly, areas with *VC* values greater than 0.61 are also classified as non-sources for *FSD*. Having been optimized by *GIS*, the mean *VC* value in the study region comes to 0.5. Figure 7 provides a visual representation of the *VC* at a resolution of 1 km. Additionally, the mean *V* values, which represents the absence of vegetation, is calculated to be 0.33. As depicted in Figure 8, the distribution of *V* values at a 5-km resolution is opposite to that of

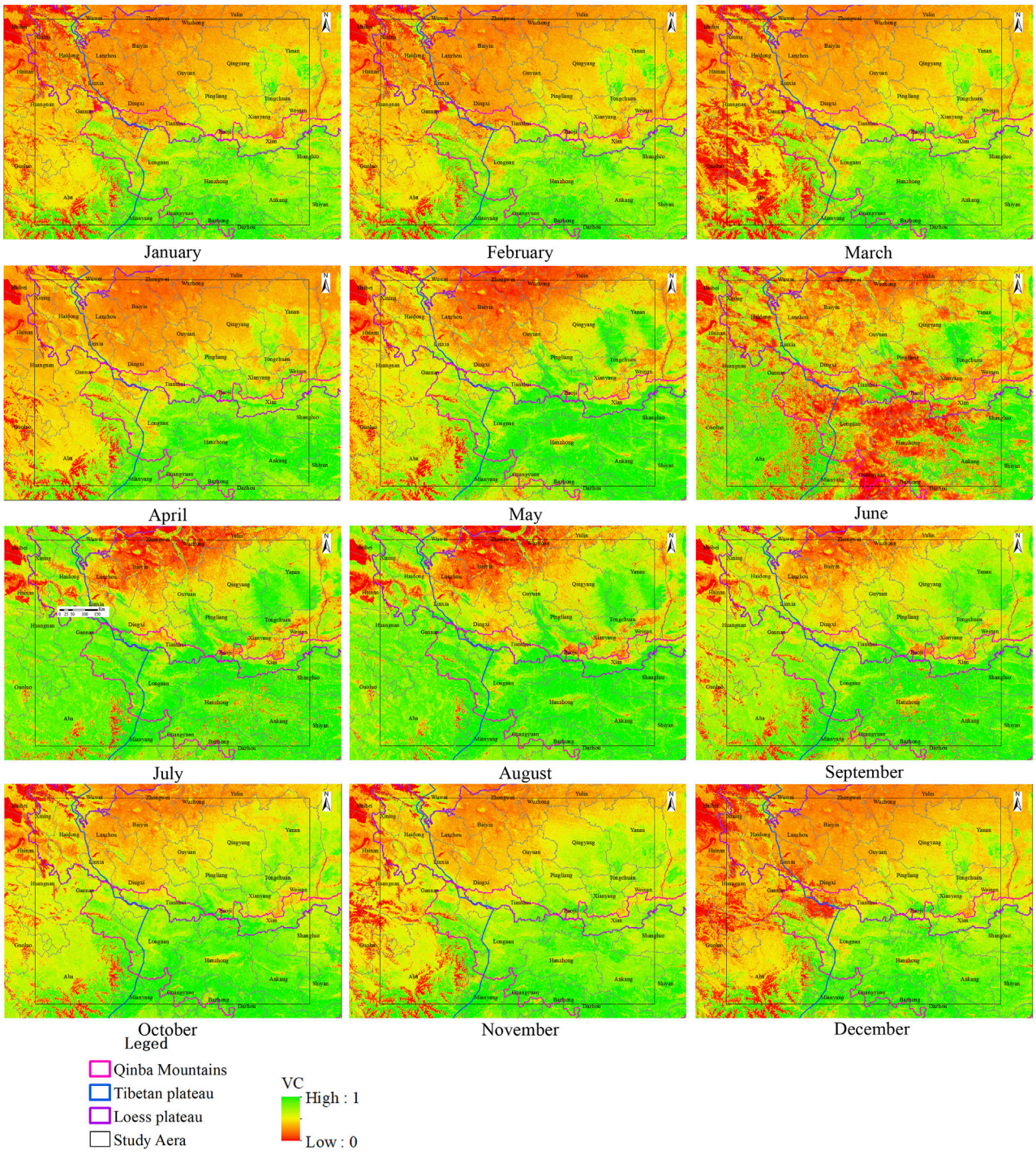

FIGURE 6
Monthly mean *VC* (250 m × 250 m) in the study area of Western China in2019.

VC, indicating areas with lower vegetation cover tend to have higher soil bareness.

3.1.3 Wind erosion index

The Wind Erosion Index hinges on the soil texture type. In this study, we have cited the soil texture from the Chinese soil dataset (V1.1) provided by the Scientific Data Center for Cold and Arid Regions (*http://westdc.Westgis.ac.cn*), and referenced the *I* of many types from the "Technical Guidelines for the Compilation of Fugitive Dust Emission Inventories" (*http://www.zhb.gov.cn/gkml/hbb/qt/201407/t20140714_276127.htm*), thereby eliciting the distribution of soil texture and I in the whole area, as demonstrated in Table 2 and Figure 9.

The study area encompasses nine soil typesl, with loam being the most widely distributed, especially on the Loess Plateau, and exhibiting the highest wind erosion index, accounting for 75.34%

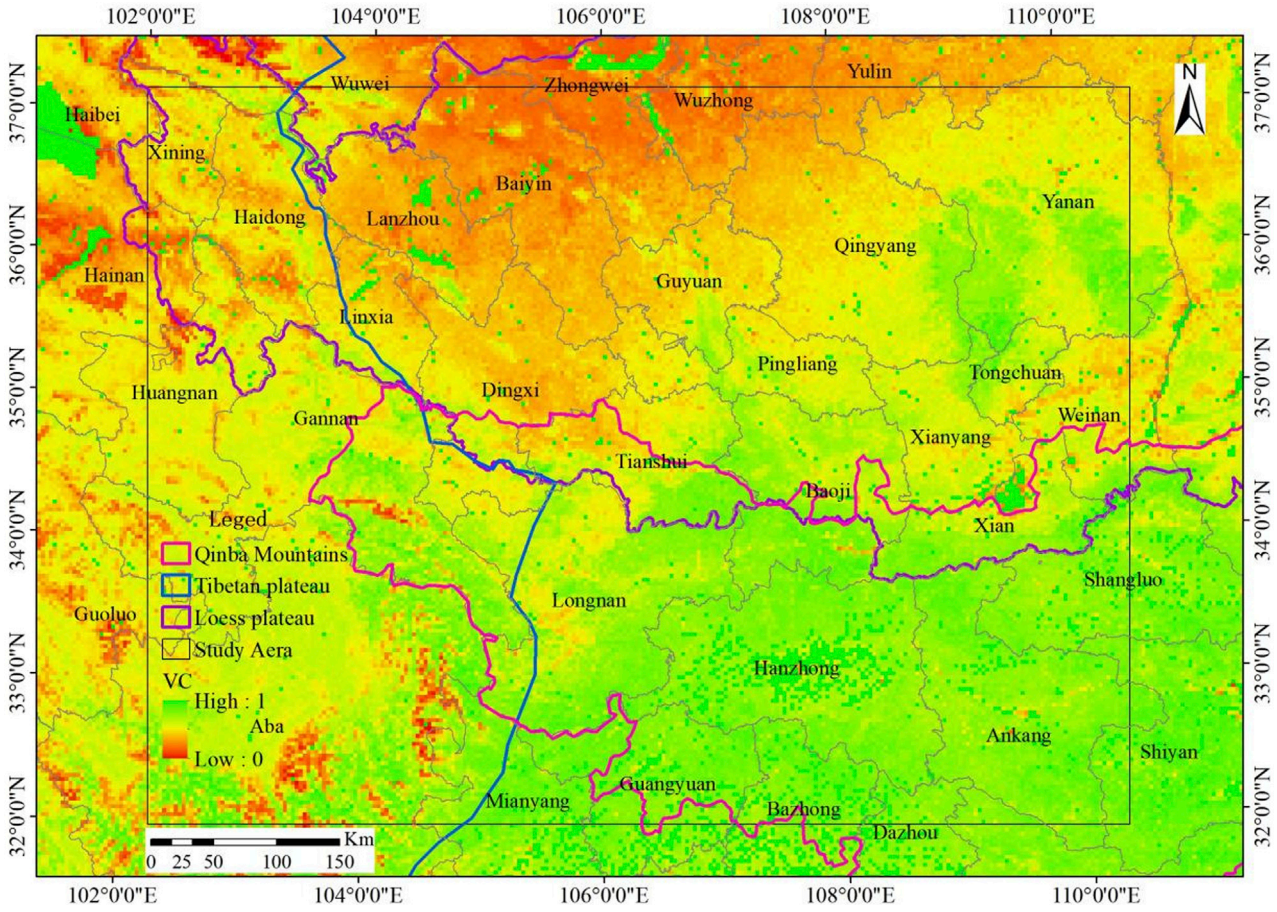

FIGURE 7
Optimized annual mean *VC* (1 km × 1 km) in the study area in 2019.

of the whole. Sandy loam constitutes 9.58% of the study area and is distributed across various regions, notably Wuzhong City in Ningxia Autonomous Region, Qingyang City, and Gannan Prefecture in Gansu Province, as well as Huangnan Prefecture in Qinghai Province. Loamy sandy soil represents 5.74% of the area and is primarily distributed on the Qinba Mountains. Silty loam occupies 3.78% and is primarily concentrated in Xi'an and Weinan cities in Shaanxi Province. Sandy clay loam, characterized by high wind erosion index, is less prevalent and primarily concentrated in the Qinba Mountains. Additionally, small water areas account for 0.09% of the study area, as indicated in Table 2 and Figure 9.

The reference values for wind erosion index provided by the "Technical Guidelines for the Compilation of Fugitive Dust Emission Inventories" show a consistent ratio of 1:0.3:0.05 for TSP, PM10, and PM2.5 across various soil types, respectively. Therefore, the distribution of I value for TSP, PM10, and PM2.5 in the study area is consistent. In this study, the I value is assigned to the 1 km × 1 km resolution soil types, and GIS geometric calculations are conducted to derive the distribution of I for TSP at a resolution of 5 km × 5 km, as detailed in Figure 10. In this study, TSP has been analyzed as an example. The wind erosion index of the Loess Plateau is the highest in the study area, reaching 911t·(hm2•a)−1, primarily found in regions with loam distribution. The Tibet Plateau followed, and the Qinba Mountain has the lowest, as low as 6.4t·(hm2•a)−1.

3.1.4 Remaining parameters setup

In addition to the parameters motioned above, there are two remaining parameters in the *WEQ* model: *K* and *L*. *K* represents the surface roughness factor and has a value of 0.5. However, in coastal, island, lakeside, and desert regions, the value of *K* is set at 1. This adjustment accounts for the different surface characteristics and their influence on wind erosion.

The parameter *L* denotes the unshielded width factor, representing the maximum distance without significant barriers (such as buildings or tall trees). The value of *L* depends on the width of the unshielded area. In the model, three categories are defined based on the unshielded width: (1) When the unshielded width is ≤ 300 m, $L = 0.7$. (2) For unshielded width between 300 m and 600 m, $L = 0.85$. (3) When the unshielded width is ≥ 600 m, $L = 1.0$.

In this study, the croplands in the western region included in this study are primarily dry lands and are predominantly flat. They are surrounded by protective forests; therefore, the *K* value was set at 0.5 and the *L* value at 0.7. For grasslands with medium and low *VC*, the *K* value is also set at 0.5, and the *L* value is considered as the intermediate value of 0.85, indicating a wider unshielded width compared to croplands. In sandy areas, deserts, saline-alkali lands, bare soil, and rocky terrain, both *K* and *L* values are set at 1.0. This reflects the high surface roughness and the absence of significant barriers, as these areas are more prone to wind erosion.

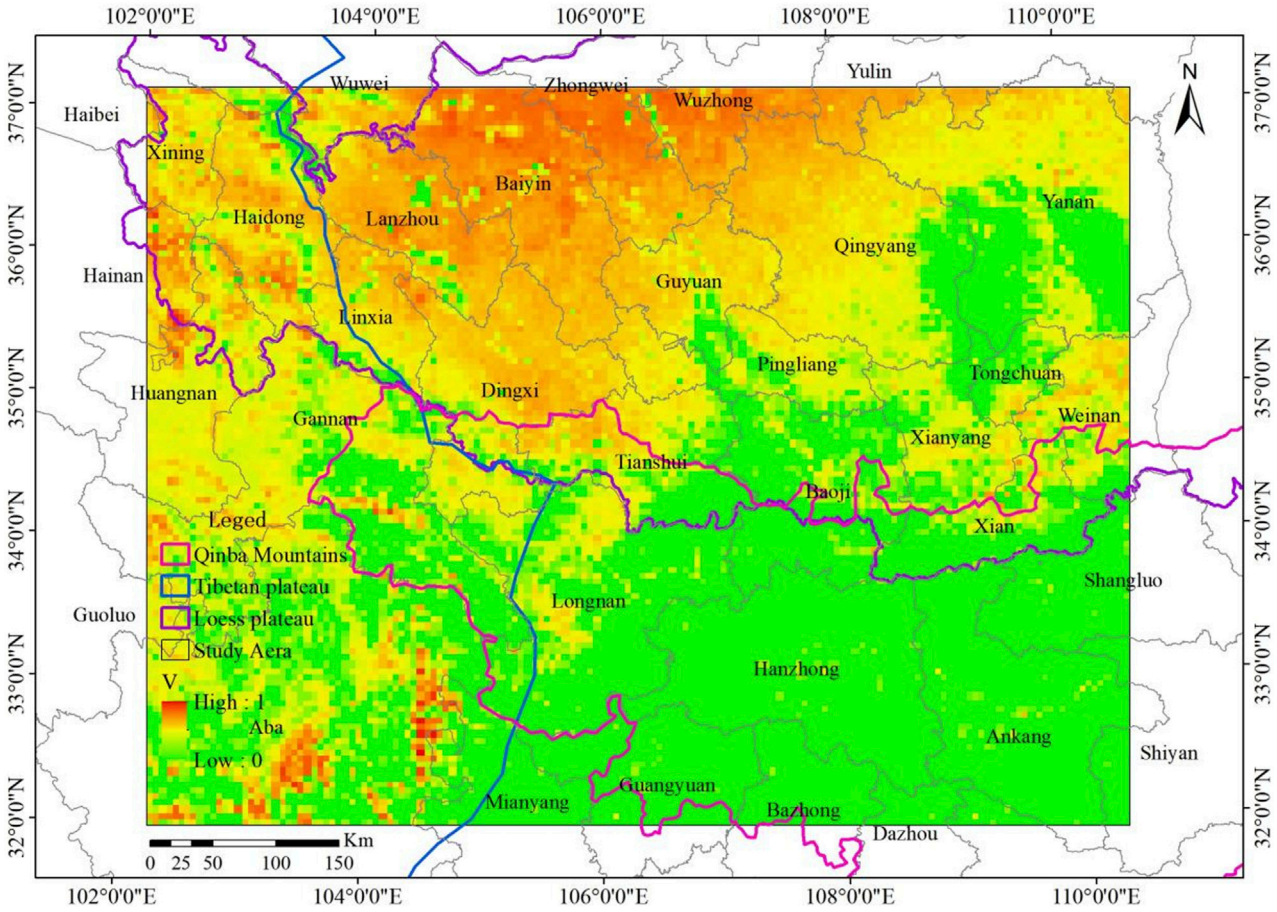

FIGURE 8
Annual mean *V* (5 km × 5 km) in the study area in 2019.

3.2 Spatial distribution

Based on calculations, the annual *TSP* emissions in the study area for the year 2019 amounted to 983.59 kt/a, PM_{10} emissions totaled 2950.8 kt/a, and $PM_{2.5}$ emissions were recorded as 491.8 kt/a. As *TSP*, PM_{10}, and $PM_{2.5}$ have the same scale factor, their spatial distribution patterns in the study area are consistent. For the purpose of spatial distribution analysis, $PM_{2.5}$ has been selected as an example. A 5 km-resolution grid-based *FSD* emission inventory for $PM_{2.5}$ was generated for the year 2019, based on the corresponding parameters, as depicted in Figure 11 and Table 3.

The results reveal that the regions with the highest $PM_{2.5}$ emissions from *FSD* and emission intensity in the study area are primarily located in the Loess Plateau. In 2019, the $PM_{2.5}$ emissions in this area amounted to 474.72 kt, accounting for 96.53% of the entire study area. The *FSD*-source areas covered approximately 191,304.4 km^2, resulting in an emission intensity of 2.48 t/km^2. Notably, the key emission hotspots are concentrated in the northern part of the study area, including Baiyin City of Gansu Province and Zhongwei and Wuzhong cities of Ningxia Autonomous Region. Moreover, the maximum emission in a 5 km × 5 km grid reached 1,182.04 t.

TABLE 2 Proportion of soil types in the study area.

Serial number	Soil type	Area (km^2)	Proportion (%)
1	Water area	392.47	0.09
2	Silty clay	80.59	0.02
3	Clay	11918.41	2.61
4	Clay loam	1633.08	0.36
5	Silty loam	17235.79	3.78
6	Loam	343783.19	75.34
7	Sandy clay loam	9795.83	2.15
8	Sandy loam	43720.27	9.58
9	Loamy sandy soil	26203.15	5.74
10	Sandy soil	1537.22	0.34
	Total	456300.00	100.00

The *FSD* emissions in the Tibet Plateau ranked second, with total $PM_{2.5}$ emissions of 35.75 kt in 2019, constituting 7.27% of the entire study area. The *FSD*-source areas covered approximately

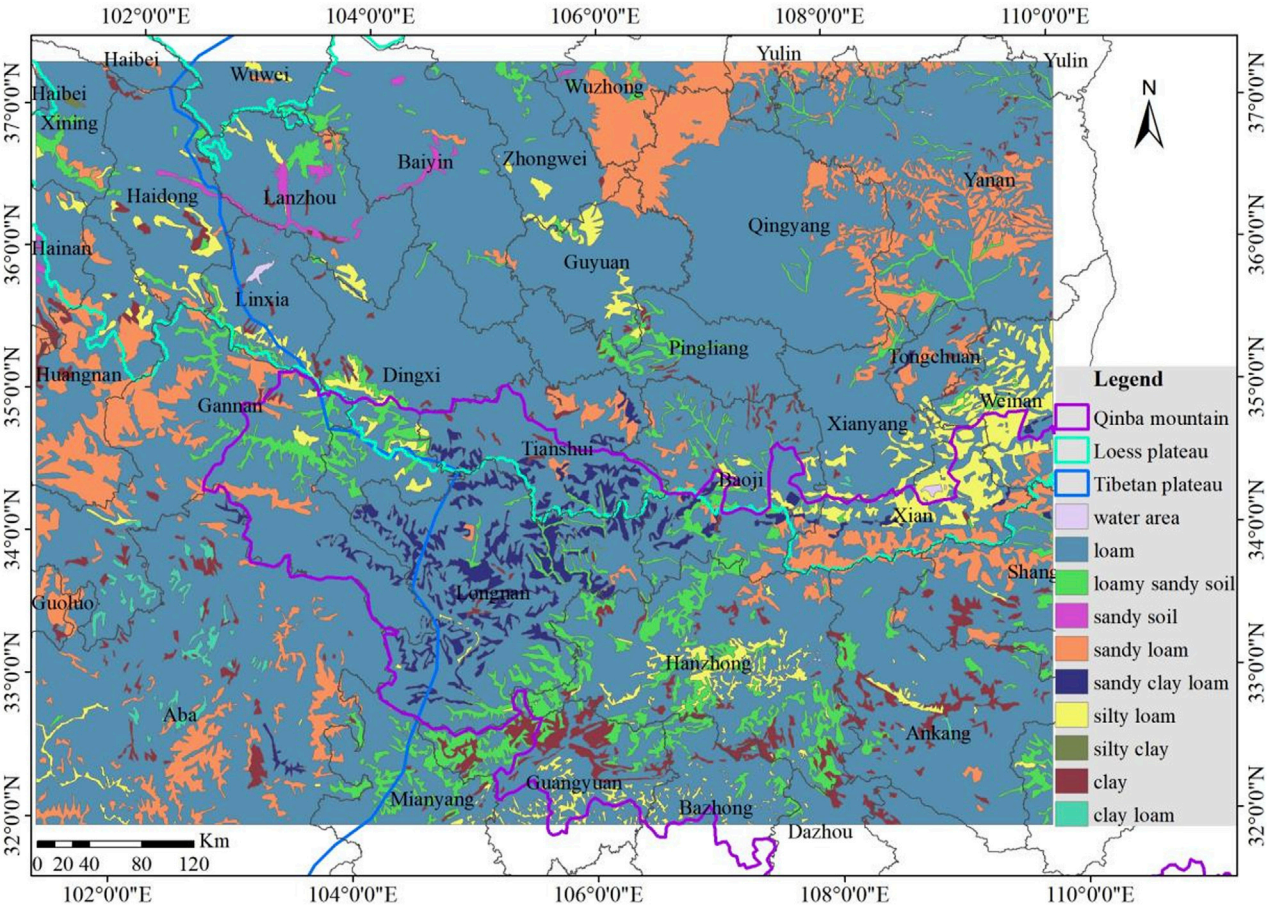

FIGURE 9
Soil types in the study area in Western China.

98,993.1 km^2, resulting in an emission intensity of 0.36 t/km^2. The key emission hotspots were identified in the northwestern part of the study area, specifically in Huangnan and Haidong prefectures of Qinghai Province. In a 5 km × 5 km grid, the maximum emission of Tibet Plateau reached 331.2t.

On the other hand, the *FSD* emissions in the Qinba Mountains were relatively lower than the former two regions, with total $PM_{2.5}$ emissions of 11.94 kt in 2019, accounting for 2.43% of the entire study area. The *FSD*-source areas covered approximately 35,977.51 km^2, resulting in an emission intensity of 0.33 t/km^2. The highest emission intensity was observed in the northeastern part of Xi'an City and the southern part of Weinan City of Shaanxi Province. For Qinba Mountains, its maximum emission in a 5 km × 5 km grid in 2019 was 72.82t. The total emissions from the Tibet Plateau, Loess Plateau, and Qinba Mountains are higher than the total emissions in the study area owing to a few overlapping areas.

Moreover, a comparison was conducted between the soil dust emissions in the study area and other regions in China using $PM_{2.5}$ as a reference. The comparison considered emissions quantity, *FSD*-source areas, and emission intensity, as presented in Table 3. From Table 3, it can be observed that the emission intensity of $PM_{2.5}$ in the Beijing–Tianjin–Hebei region and Hebei Province is relatively consistent. Surprisingly, in the study area, the emission intensity of $PM_{2.5}$ from *FSD* exceeds that of Beijing–Tianjin–Hebei and Hebei Province by three times. This significant difference is primarily attributed to the high emission intensity of 2.48 t/km^2 on the Loess Plateau, which is approximately five times that of the Beijing–Tianjin–Hebei region, resulting in elevated emission intensity levels in the study area. Meanwhile, the Tibet Plateau and Qinba Mountains exhibit lower *FSD* emission intensities of only 0.36 and 0.33 t/km^2, respectively, owing to their higher *VC* and precipitation levels. Both these values are lower than those estimated in the Beijing–Tianjin–Hebei region. The higher *FSD* emission intensity in the study area, particularly on the Loess Plateau, compared with the Beijing–Tianjin–Hebei region, to factors such as lower *VC* and precipitation levels, higher wind speed and wind erosion index, all of which are prevalent in the study area because of its comparable latitude and similar annual mean temperature variations with the Beijing–Tianjin–Hebei region.

3.3 Temporal distribution characteristics

In the *WEQ* model, the estimation of wind erosion is typically based on annual mean statistics, which may not account for variations in wind erosion potential across different months of the year. However, in this study, it was observed that the variations between different months are primarily influenced by

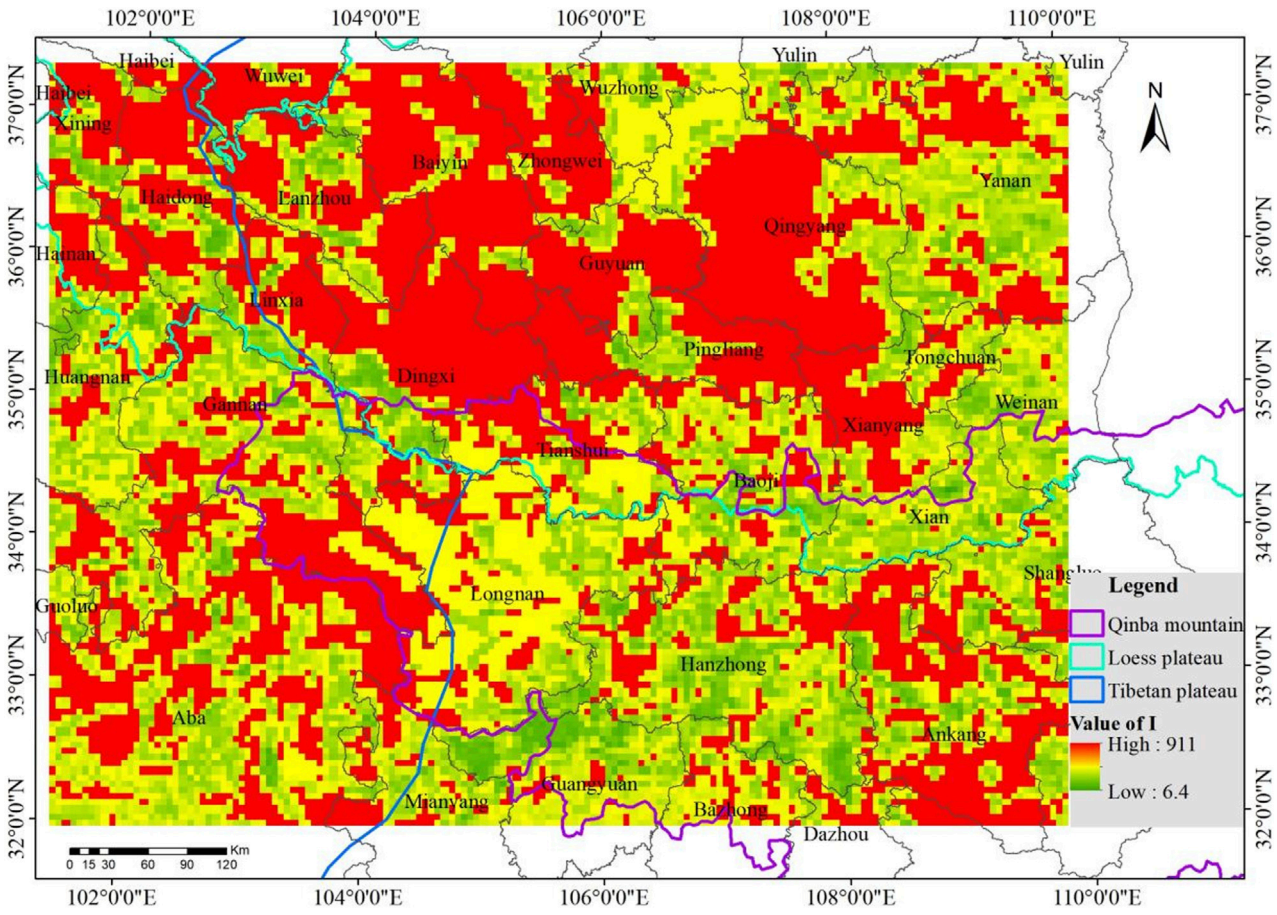

FIGURE 10
Wind erosion index (*TSP*) of the study area in Western China.

climate factors and vegetation cover, which are also the main drivers of fluctuations in *FSD* emissions throughout the year. Additionally, Skidmore and Woodruff (1968) suggested using the annual *PE* to compute monthly climate factor. Therefore, To address this limitation and capture the monthly variations in wind erosion potential, we proposed to calculate the monthly allocation coefficients using the *V* and *C* values for each grid and each month, as presented in Eq. 2.11.

$$k_{ij} = V_{ij} \times u_{ij}^{3} \Big/ \left\{ \left[P_i \Big/ \left(1.8T_{ij} + 22 \right) \right]^{10/9} \right\}^{2} \qquad (2.11)$$

Where, k_{ij} represents the distribution coefficient for grid *i* in month *j*. V_{ij} represents the *V* value for grid *i* in month *j*. u_{ij} is the monthly mean 10-m wind speed for grid *i* in month *j*. P_{ij} is the cumulative precipitation for grid *i* in month *j*. T_{ij} is the monthly mean ground temperature for grid *i* in month *j*.

By using Eq. 2.7 we calculated the allocation coefficients for each grid within the study area for the year 2019. These coefficients were then normalized and combined with the annual emission distribution to determine the monthly emissions of $PM_{2.5}$ from *FSD* in each grid during that year, as shown in Table 6. In our study, we computed the values for each grid separately due to the variations in *C* and *V* across different months. Figure 12 illustrates the monthly distribution of $PM_{2.5}$ emissions from *FSD*, highlighting the variations observed for each grid.

Based on the results presented in Table 4, the $PM_{2.5}$ emissions from *FSD* in the study area exhibits significant non-linear monthly variations. The highest emissions occur in April, accounting for 36.21% of the total annual emissions. The second and third highest emissions are in August and June, respectively. These variations are primarily because the northern region of the study area is part of the Loess Plateau and located in a semi-arid zone. During the summer months, the ground temperature increases without a significant increase in precipitation, leading to higher emissions. On the other hand, the lowest emissions are observed in July.

When considering the seasonal distribution, spring demonstrates the most significant $PM_{2.5}$ emissions from *FSD* in the study area, accounting for 51.32% of the total annual emissions. Summer follows with 22.67%, and autumn with 15.64%. Winter exhibits the lowest emissions, accounting for only 10.37% of the total annual emissions. Overall, the emission pattern exhibits a seasonal trend of spring > summer > autumn > winter. The high emissions observed during spring, summer, and autumn primarily occur on the Loess Plateau, influenced by low precipitation and poor *VC* in the region. Conversely, emissions from the Tibet Plateau increase proportionately during winter.

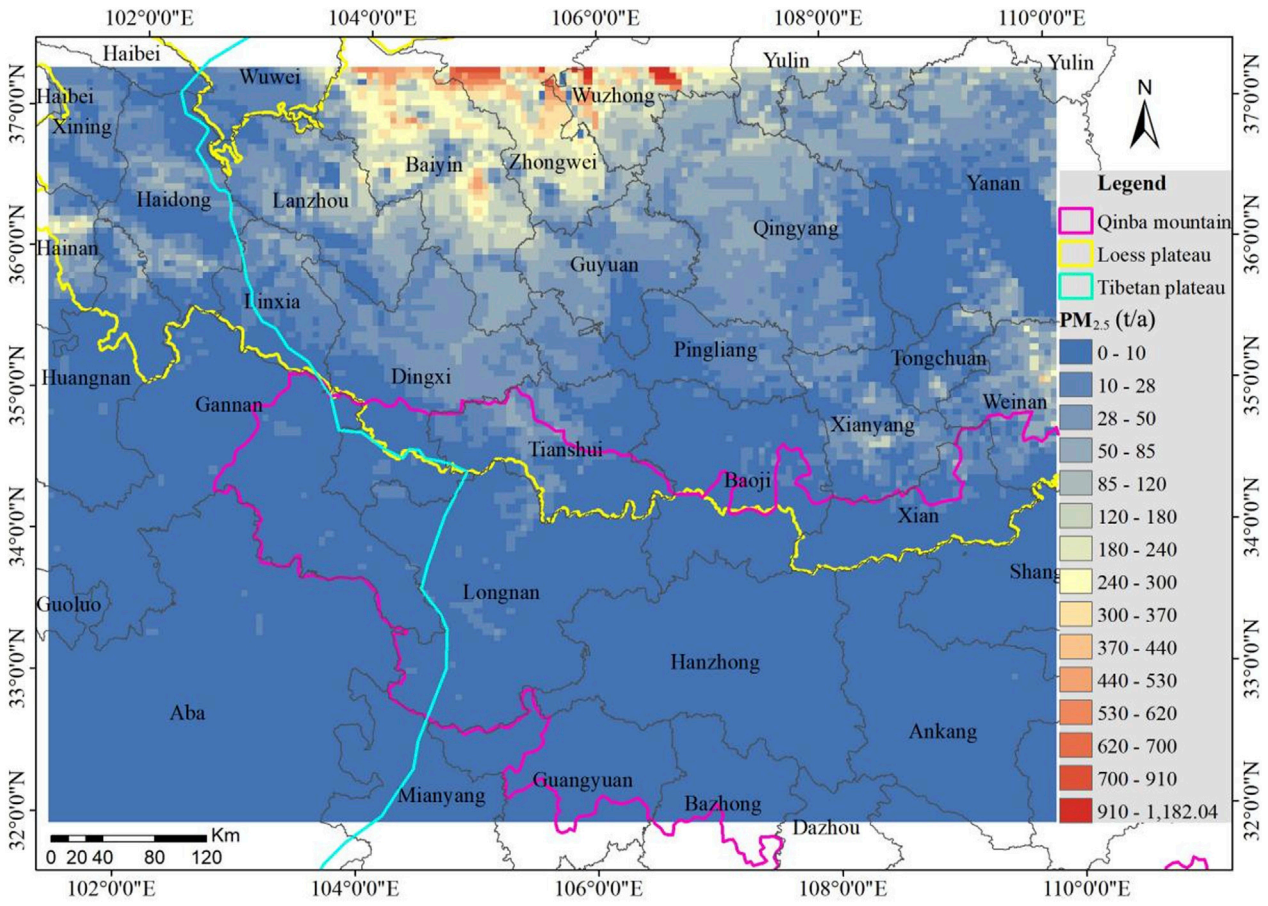

FIGURE 11
$PM_{2.5}$ from *FSD* in the study area in Western China in 2019.

TABLE 3 Comparison of *FSD* emission intensity between the study area and other regions.

Region	Year	$PM_{2.5}$ emission (t)	*FSD*-source area (km^2)	Mean emission intensity (t/km^2)	Literature
Study Area	2019	491796.44	279525	1.76	This study
Specifically Tibet Plateau	2019	35754.61	98993.1	0.36	
Loess Plateau	2019	474722.53	191304.4	2.48	
Qinba Mountains	2019	11941.49	35977.51	0.33	
Beijing–Tianjin–Hebei Region	2017	65000	116630	0.56	Song et al. (2021)
Hebei Province	2015	39699	77627	0.51	Guo et al. (2017)

Based on Figure 12, the primary areas for $PM_{2.5}$ emissions from *FSD* in the study area are identified as Baiyin City in Gansu Province, and Zhongwei and Wuzhong cities in the Ningxia Autonomous Region. These areas consistently exhibit high emissions throughout the months in 2019, primarily due to factors such as high wind speed, poor vegetation coverage, and low precipitation. These conditions contribute to increased wind erosion and subsequent $PM_{2.5}$ emissions from *FSD*.

Xianyang and Weinan cities of Shaanxi Province represent the secondary emission source areas on the Loess Plateau. The $PM_{2.5}$ emissions from *FSD* exhibit a gradually increasing trend from January to April, followed by a fluctuant decrease from April to September, reaching its lowest level in September, and then a subsequent increase from October to December. This pattern aligns with local agricultural activities, as described in Qi et al. (2022).

In parts of the Tibet Plateau, $PM_{2.5}$ emissions from *FSD* remain relatively constant in January and February, decrease in March, increase in April, gradually decline from April to September, and start to rise again from

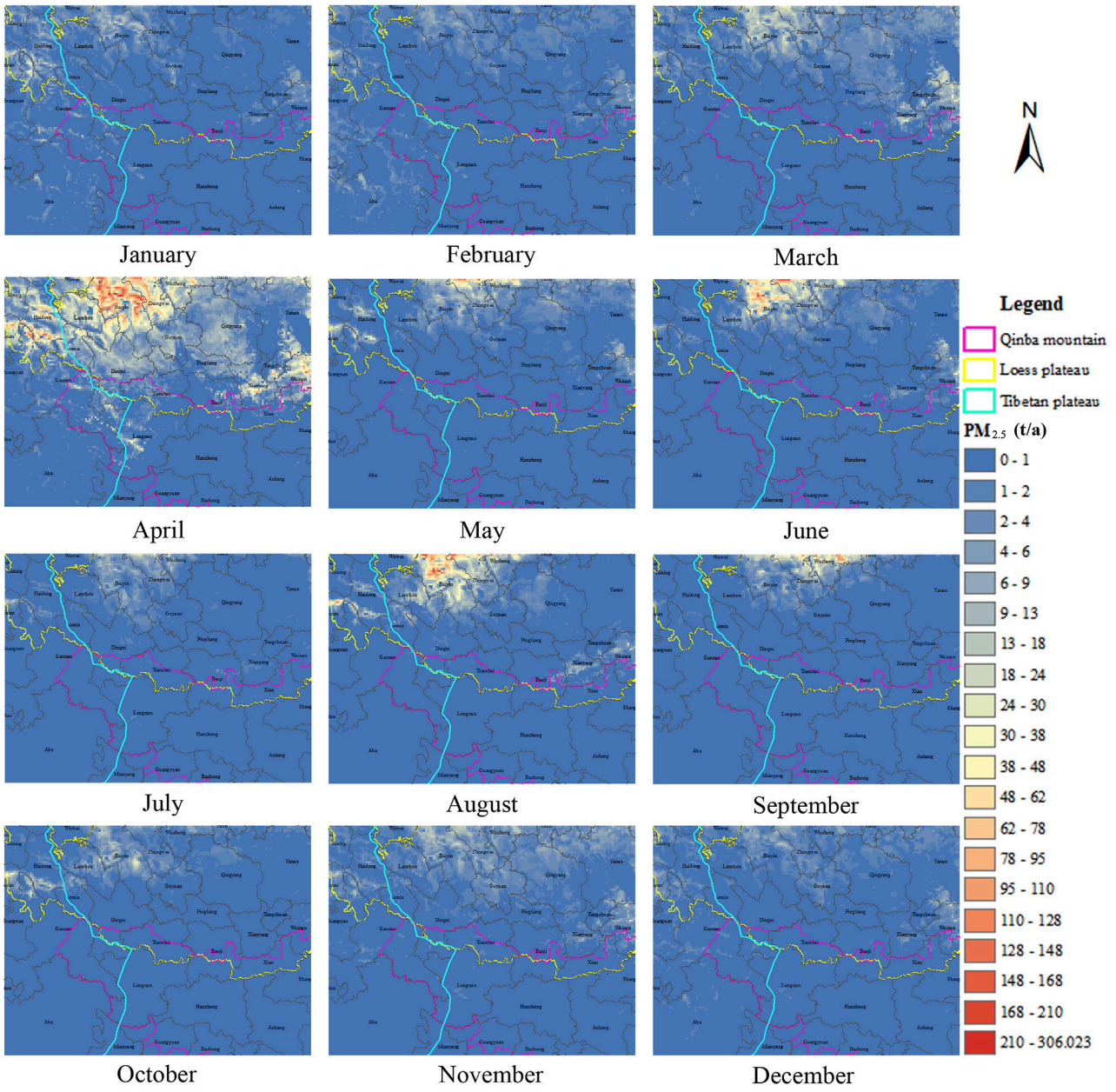

FIGURE 12
Fugitive Soil dust levels in the study area in Western China in 2019.

TABLE 4 Overview of $PM_{2.5}$ emissions from *FSD* in the study area for January to December in 2019 Unit: t.

Month	3	4	5	6	7	8	9	10	11	12	1	2
Season	Spring			Summer			Autumn			Winter		
TSP	71.41	320.63	62.33	82.02	24.36	94.34	54.35	27.02	56.99	29.99	27.20	34.58
PM_{10}	23.80	106.88	20.78	27.34	8.12	31.45	18.12	9.01	19.00	10.00	9.07	11.53
$PM_{2.5}$	3.97	17.81	3.46	4.56	1.35	5.24	3.02	1.50	3.17	1.67	1.51	1.92

October to December These emission patterns are closely associated with agricultural and pastoral practices in the region, as mentioned in Zhuo et al. (2018). The overall emission levels on the Qinba Mountains are low, with the primary emission areas situated in the southern parts of Xi'an and Weinan cities.

3.4 Uncertainty analysis

The uncertainty in the emission inventories for certain atmospheric pollution stems primarily from the calculation and selection of activity levels and emission factors (Zhong et al., 2007). In this study, the uncertainty involved in the *FSD* emission inventory can be attributed primarily to the following factors: 1. The climate factors were simulated using the *WRF* model, and the simulation results may thus deviate from the actual conditions, causing the uncertainty of the estimation results. 2. The *MODIS MOD13Q1* product provides remote sensing image data at 16-day intervals. In this study, the mean *VC* for a specific month was calculated using the 16-day images. However, this approach may introduce discrepancies compared to the actual values. 3. The wind erosion index and particle size multiplier were referenced from the "Technical Guidelines for the Compilation of Fugitive Dust Emission Inventories (Trial)", without conducting specific particle size sampling and analysis for different soil types, thereby introducing certain uncertainties.

4 Conclusion

Compared to existing studies on Wind Erosion Quantity, our research takes the convergent areas of the Loess Plateau, Tibet Plateau, and Qinba Mountains as a case study to estimate *FSD* emissions. We have introduced innovative approaches, such as utilizing *WRF* simulated data to calculate climate factors, optimizing the vegetation cover factor using *NDVI* and *LUCC* data, and establishing improved criteria for calculating the monthly allocation coefficients. The results of our study reveal the following key findings:

1) The study area is located in the convergence areas of the Tibet Plateau, Loess Plateau, and Qinba Mountains. Due to the influence of topography and monsoons, meteorological factors, including wind speed, precipitation, and temperature, exhibit uneven distribution. Using weather station data to calculate *FSD* emissions may introduce deviations from reality. By employing *ERA5* reanalysis data to drive the *WRF* model, our study found that the maximum, minimum, and mean climate factor values in the study area are 0.8601, 0.0000764, and 0.0388, respectively.
2) After the optimization process, which involved excluding construction land, water areas, paddy fields, and regions with *VC* values greater than 0.61 as *FSD* emissions, the mean soil bareness (*V*) in the study area for 2019 was determined to be 0.33. Moreover, *VC* and *V* values for different land use types across different months exhibit non-linear variations due to the influence of regional background and agricultural and pastoral activities.
3) In 2019, the annual TSP, PM10, and PM2.5 from FSD emissions in the study area amounted to 9835.9, 2950.8, and 491.8 kt/a, respectively. The highest FSD emissions and emission intensity were observed on the Loess Plateau, particularly in the northern part of the study area, including Baiyin City of Gansu Province, and Zhongwei and Wuzhong cities of Ningxia Autonomous Region. The Tibet Plateau had the second-highest *FSD* emissions, primarily concentrated in the northwestern part of Qinghai Province, particularly in Huangnan and Haidong prefectures. The Qinba Mountains exhibited the lowest overall *FSD* emissions.
4) The monthly allocation coefficients is mainly influenced by climate factor and vegetation cover factor. Climate factor is determined by meteorological conditions, while vegetation cover factor is associated with agricultural and pastoral activities. The monthly allocation coefficients, climate factor, and vegetation cover factor for each grid demonstrate non-linear patterns. In the study area for 2019, April had the highest *FSD* emissions, accounting for 36.21% of the total annual emissions. Following closely were August and June, ranked as the second and third highest emission months, respectively. These patterns can be attributed to the arid and semi-arid conditions experienced in the primary emission source area, the northern part of the Loess Plateau, during summer. During this season, ground temperatures rise without significant increases in precipitation and vegetation coverage, resulting in elevated *FSD* emissions.

Data availability statement

Publicly available datasets were analyzed in this study. This data can be found here: ERA5: https://cds.climate.copernicus.eu/cdsapp#!/home; NDVI: https://modis.gsfc.nasa.gov/; LUCC: https://www.resdc.cn/Harmonized World Soil Database: http://www.ncdc.ac.cn. Surface meteorological observation data: http://data.cma.cn/data/detail/dataCode/A.0012.0001.html.

Author contributions

PW: Methodology, Writing–original draft, Formal Analysis. MC: Writing–original draft, Writing–review and editing. WA: Data curation, Writing–original draft. YL: Data curation, Writing–original draft. FP: Writing–review and editing.

Funding

The author(s) declare financial support was received for the research, authorship, and/or publication of this article. Supported by Special funds for basic scientific research operations of central universities: Source analysis of $PM_{2.5}$ and formation mechanism of secondary organic aerosol in Lanzhou City (No. lzujbky-2017-66).

Acknowledgments

Supported by Supercomputing Center of Lanzhou University.

Conflict of interest

The authors declare that the research was conducted in the absence of any commercial or financial relationships that could be construed as a potential conflict of interest.

Publisher's note

References

Apte, J. S., Marshall, J. D., Cohen, A. J., and Brauer, M. (2015). Addressing global mortality from ambient $PM_{2.5}$. *Environ. Sci. Technol.* 49, 8057–8066. doi:10.1021/acs.est.5b01236

Asian Clean Air Center (2021). Available at: http://www.allaboutair.cn/a/reports/2021/1027/622.html (Accessed July 12, 2023).

Bi, X., Feng, Y., Wu, J., Wang, Y., and Zhu, T. (2007). Source apportionment of PM_{10} in six cities of northern China. *Atmos. Environ.* 41, 903–912. doi:10.1016/j.atmosenv.2006.09.033

Buschiazzo, D. E., and Zobeck, T. M. (2008). Validation of WEQ, RWEQ and WEPS wind erosion for different arable land management systems in the Argentinean Pampas. *Earth Surf. Process. Landforms* 33, 1839–1850. doi:10.1002/esp.1738

Chen, G. P., Sun, X. M., Li, Y., Xue, Y., Xing, L. H., Xi, G. Q., et al. (2023). Development status and suggestions of rapeseed industry in Hanzhong. *Tillage Cultiv.* 43 (1), 146–148. doi:10.13605/j.cnki.52-1065/s.2023.01.031

Cheng, N., Zhang, D., Li, Y., Xie, X., Chen, Z., Meng, F., et al. (2017). Spatio-temporal variations of $PM_{2.5}$ concentrations and the evaluation of emission reduction measures during two red air pollution alerts in Beijing. *Sci. Rep.* 7, 8220. doi:10.1038/s41598-017-08895-x

Chepil, W. S. (1958). Soil conditions that influence wind erosion. *AgEcon Search*. Technical Bulletins 157333. . doi:10.22004/ag.econ.157333

Countess Environmental, Bonifacio, H. F., Maghirang, R. G., and Trabue, S. L. (2006). *WRAP fugitive dust handbook. Prepared by countess environmental, westlake village. Calif., for western governors' association*. Denver. Colo Sept.7.

Cowherd, C., Jr., Axetell, K., Jr., Guenther, C. M., and Jutze, G. A. (1974). *Development of emission factors for fugitive dust sources*. National Service Center for Environmental Publications (NSCEP). EPA-450/3-74-037.

Craig, D. C., and Turelle, J. W. (1964). *Guide for wind erosion control on cropland in the great plains States, soil conservation service*, 104. Washington, D.C.: U.S. Department of Agriculture, 41.

Fryrear, D. W., Bilbro, J. D., Saleh, A., Schomberg, H., Stout, J. E., and Zobeck, T. M. (2000). RWEQ: improved wind erosion technology. *J. Soil Water Conservation* 55, 183–189.

Fu, X., Wang, S., Zhao, B., Xing, J., Cheng, Z., Liu, H., et al. (2013). Emission inventory of primary pollutants and chemical speciation in 2010 for the Yangtze River Delta region, China. *Atmos. Environ.* 70, 39–50. doi:10.1016/j.atmosenv.2012.12.034

Gitelson, A. A., Kaufman, Y. J., Stark, R., and Rundquist, D. (2002). Novel algorithms for remote estimation of vegetation fraction. *Rem. Sens. Environ.* 80 (1), 76–87. doi:10.1016/S0034-4257(01)00289-9

Gregory, J. M., Wilson, G. R., Singh, U. B., and Darwish, M. M. (2004). TEAM: integrated, process-based wind-erosion model. *Environ. Model. Softw.* 19, 205–215. doi:10.1016/S1364-8152(03)00124-5

Guo, X., Feng, H. B., and Lu, Y. J. (2017). Estimation of emissions of $PM_{2.5}$ from soil dust in Hebei Province. *J. Industrial Sci. Technol.* 34 (6), 477–482. doi:10.7535/hbgykj.2017yx06015

Ji, D., Deng, Z., Sun, X., Ran, L., Xia, X., Fu, D., et al. (2020). Estimation of $PM_{2.5}$ mass concentration from visibility. *Adv. Atmos. Sci.* 37, 671–678. doi:10.1007/s00376-020-0009-7

Jia, K., Yao, Y. J., Wei, X. Q., Gao, S., Jiang, B., and Zhao, X. (2013). A review on fractional vegetation cover estimation using remote sensing. *Adv. Earth Sci.* 28, 774–782. doi:10.11867/j.issn.1001-8166.2013.07.0774

Jutze, G., and Axetell, K. (1974). *Investigation of fugitive dust*, Vol. 1 - Sources. National Service Center for Environmental Publications (NSCEP). EPA-450/3-74-036-a.Emissions and control

Jutze, G., and Axetell, K. (1976). "Factors influencing emissions from fugitive dust," in *Symposium on fugitive emission measurement and control* (Hartford, CT: National Service Center for Environmental Publications (NSCEP)).

Li, B.-B., Huang, Y.-H., Bi, X.-H., Liu, L.-Y., and Qin, J.-P. (2020). Localization of soil wind erosion dust emission factor in beijing. *Environ. Sci.* 41, 2609–2616. doi:10.13227/j.hjkx.201908243

Li, T., Bi, X., Dai, Q., Wu, J., Zhang, Y., and Feng, Y. (2021). Optimized approach for developing soil fugitive dust emission inventory in "2+26" Chinese cities. *Environ. Pollut.* 285, 117521. doi:10.1016/j.envpol.2021.117521

Liu, A. B., Wu, Q. Z., Chen, Y. T., Zhao, T. C., and Cheng, X. (2018). Estimation of dust emissions from bare soil erosion over beijing plain area. *Zhongguo Huanjing Kexue/China Environ. Sci.* 38 (2), 471–477. doi:10.19674/j.cnki.issn1000-6923.2018.0054

Liu, H., Wu, B., Liu, S., Shao, P., Liu, X., Zhu, C., et al. (2018). A regional high-resolution emission inventory of primary air pollutants in 2012 for Beijing and the surrounding five provinces of North China. *Atmos. Environ.* 181, 20–33. doi:10.1016/j.atmosenv.2018.03.013

Liu, J., Han, Y., Tang, X., Zhu, J., and Zhu, T. (2016). Estimating adult mortality attributable to $PM_{2.5}$ exposure in China with assimilated $PM_{2.5}$ concentrations based on a ground monitoring network. *Sci. Total Environ.* 568, 1253–1262. doi:10.1016/j.scitotenv.2016.05.165

Liu, Q., Guo, Z. L., Chang, C. P., Wang, R. D., Li, J. F., Li, Q., et al. (2021). Potential wind erosion simulation in the agro-pastoral ecotone of northern China using RWEQ and WEPS models. *J. Desert Res.* 41, 27–37. doi:10.7522/j.issn.1000-694X.2020.00122

Lu, L., and Liu, C. (2019). Chinese soil data set based on world soil database (hwsd) (v1.1). *National Cryosphere Desert Data Center*. doi:10.12072/ncdc.westdc.db3647.2023

Lyles, L. (1983). Erosive wind energy distributions and climatic factors for the West. *J. Soil Water Conserv.* 38 (2), 106–109.

Mandakh, N., Tsogtbaatar, J., Dash, D., and Khudulmur, S. (2016). Spatial assessment of soil wind erosion using WEQ approach in Mongolia. *J. Geogr. Sci.* 26, 473–483. doi:10.1007/s11442-016-1280-5

Ministry of Environmental Protection, (2014). Available at: https://www.mee.gov.cn/gkml/hbb/bgg/201501/t20150107_293955.htm (Accessed July 12, 2023).

Panebianco, J., and Buschiazzo, D. (2008). Erosion predictions with the Wind Erosion Equation (WEQ) using different climatic factors. *Land Degrad. Dev.* 19, 36–44. doi:10.1002/ldr.813

Qi, J., Zheng, B., Li, M., Yu, F., Chen, C., Liu, F., et al. (2017). A high-resolution air pollutants emission inventory in 2013 for the Beijing-Tianjin-Hebei region, China. *Atmos. Environ.* 170, 156–168. doi:10.1016/j.atmosenv.2017.09.039

Qi, Y., Zhang, Q., Hu, S. J., Cai, D. H., Zhao, F. N., Chen, F., et al. (2022). Climate change and its impact on winter wheat potential productivity of Loess Plateau in China. *Ecol. Environ. Sci.* 31 (8), 1521–1529. doi:10.16258/j.cnki.1674-5906.2022.08.003

Shang, X., Zhang, K., Meng, F., Wang, S., Lee, M., Suh, I., et al. (2018). Characteristics and source apportionment of fine haze aerosol in Beijing during the winter of 2013. *Atmos. Chem. Phys.* 18, 2573–2584. doi:10.5194/acp-18-2573-2018

Shao, Y. P., Raupach, M. R., and Leys, J. F. (1996). A model for predicting aeolian sand drift and dust entrainment on scales from paddock to region. *Soil Res.* 34, 309–342. doi:10.1071/sr9960309

Skidmore, E. L. (1986). *Soil erosion by wind: an Overview*. Dordrecht: Springer.

Skidmore, E. L., and Woodruff, N. P. (1968). *Wind erosion forces in the United States and their use in predicting soil loss*. United States: Agriculture handbook. Department of Agriculture no. 346.

Song, H., Zhang, K., Piao, S., and Wan, S. (2016). Spatial and temporal variations of spring dust emissions in northern China over the last 30 years. *Atmos. Environ.* 126, 117–127. doi:10.1016/j.atmosenv.2015.11.052

Song, L., Li, T., Bi, X., Wang, X., Zhang, W., Zhang, Y., et al. (2021). Construction and dynamic method of soil fugitive dust emission inventory with high spatial resolution in beijing-tianjin-hebei region. *Res. Environ. Sci.* 34 (8), 1771–1781. doi:10.13198/j.issn.1001-6929.2021.05.03

Taylor, K. E. (2001). Summarizing multiple aspects of model performance in a single diagram. *J. Geophys. Res. Atmos.* 106 (D7), 7183–7192. doi:10.1029/2000JD900719

The State Council (2013). Available at: http://www.gov.cn/zwgk/2013-09/12/content_2486773.htm (Accessed July 12, 2023).

The State Council (2018). Available at: http://www.gov.cn/zhengce/content/2018-07/03/content_5303158.htm (Accessed July 12, 2023).

US. Environmental Protection Agency (1977). *Guideline for development of control strategies in areas with fugitive dust problems*. Triangle Park, North Carllina: S. Environmental Protection Agency.

Wang, S., Wang, T., Shi, R., and Tian, J. (2014). Estimation of different fugitive dust emission inventory in Nanjing. *J. Univ. Chin. Acad. Sci.* 31, 351–359. doi:10.7523/j.issn.2095-6134.2014.03.009

Woodruff, N. P., and Siddoway, F. H. (1965). A wind erosion equation. *Soil Sci. Soc. Am. J.* 29, 602–608. doi:10.2136/sssaj1965.03615995002900050035x

Xiao, Y. (2022). *Temporal and spatial changes and prediction of carbon budget in palnting and animal husbandry in Guangyuan during the last 25 years*. Sichuan Normal University. Master's thesis.

Xu, X., Liu, J., Zhang, S., Yan, C., and Wu, s (2018). Data from Remote sensing data set of multi-period land use monitoring in China (CNLUC). Resource and environmental science data registration and publication system. http://www.resdc.cn/DOI/doi.aspx?DOIid=54.

Xu, Y. Q., Jiang, N., Yan, Q., Zhang, R. Q., Chen, L. F., and Li, S. S. (2016). Research on emission inventory of bareness wind erosion dust in zhengzhou. *Environ. Pollut. Control*. doi:10.15985/j.cnki.1001-3865.2016.04.005

Xuan, J., Liu, G., and Du, K. (2000). Dust emission inventory in Northern China. *Atmos. Environ.* 34, 4565–4570. doi:10.1016/S1352-2310(00)00203-X

Zhang, G., Liu, J., Zhang, Z., Zhao, X., and Zhou, Q. (2002). Spatial changes of wind erosion-caused landscapes and their relation with wind field in China. *J. Geogr. Sci.* 12, 153–162. doi:10.1007/BF02837469

Zhang, Z., Gong, D., Mao, R., Kim, S. J., Xu, J., Zhao, X., et al. (2017). Cause and predictability for the severe haze pollution in downtown Beijing in November-December 2015. *Sci. Total Environ.* 592, 627–638. doi:10.1016/j.scitotenv.2017.03.009

Zhao, Y. L. (2006). *Test and evaluation on influences of vegetation coverage on soil wind erosion by means of the movable wind tunnel*. Inner Mongolia Agricultural University. Master's thesis.

Zheng, J., Zhang, L., Che, W., Zheng, Z., and Yin, S. (2009). A highly resolved temporal and spatial air pollutant emission inventory for the Pearl River Delta region, China and its uncertainty assessment. *Atmos. Environ.* 43, 5112–5122. doi:10.1016/j.atmosenv.2009.04.060

Zhong, L. J., Zheng, J. Y., Louie, P., and Chen, J. (2007). Quantitative uncertainty analysis in air pollutant emission inventories: methodology and case study. *Res. Environ. Sci.* 20 (4), 15–20. doi:10.13198/j.res.2007.04.19.zhonglj.004

Zhuo, G., Chen, S. R., and Zhou, B. (2018). Spatio-temporal variation of vegetation coverage over the Tibetan Plateau and its responses to climatic factors. *Acta Ecol. Sin.* 38 (9), 3208–3218. doi:10.5846/stxb201705270985

Zou, X. Y., Zhang, C. L., Cheng, H., Kang, L. Q., Wu, X. X., Chang, C. P., et al. (2014). Classification and representation of factors affecting soil wind erosion in a Model. *Adv. Earth Sci.* 29 (8), 875–889. doi:10.11867/j.issn.10018166.2014.08.0875

frontiers | Frontiers in Earth Science

TYPE Original Research
PUBLISHED 27 December 2023
DOI 10.3389/feart.2023.1249107

OPEN ACCESS

EDITED BY
Zhiyuan Hu,
Sun Yat-Sen University, China

REVIEWED BY
Hong Wang,
Institute of Geographic Sciences and Natural Resources Research, Chinese Academy of Sciences (CAS), China
Leilei Min,
Center for Agricultural Resources Research, Institute of Genetics and Developmental Biology, Chinese Academy of Sciences (CAS), China
Xingcai Liu,
Institute of Geographic Sciences and Natural Resources Research, Chinese Academy of Sciences (CAS), China
Zhiyong Liu,
Sun Yat-Sen University, China

*CORRESPONDENCE
Gonghuan Fang,
fanggh@ms.xjb.ac.cn
Yaning Chen,
chenyn@ms.xjb.ac.cn

RECEIVED 28 June 2023
ACCEPTED 31 October 2023
PUBLISHED 27 December 2023

CITATION
Gao X, Fang G, Chen Y and Zhang X (2023), Analysis of runoff variations in an arid catchment based on multi-model ensemble- a case study in the Tarim River Basin in Central Asia.
Front. Earth Sci. 11:1249107.
doi: 10.3389/feart.2023.1249107

Analysis of runoff variations in an arid catchment based on multi-model ensemble- a case study in the Tarim River Basin in Central Asia

Xiaoyu Gao[1], Gonghuan Fang[2]*, Yaning Chen[2]* and Xueqi Zhang[2]

[1]University of Chinese Academy of Sciences, Beijing, China, [2]State Key Laboratory of Desert and Oasis Ecology, Key Laboratory of Ecological Safety and Sustainable Development in Arid Lands, Xinjiang Institute of Ecology and Geography, Chinese Academy of Sciences, Urumqi, China

Runoff variation is of significant importance to the current and future water availability of a region, particularly in arid regions, and plays a crucial role in economic and social development. The Tarim River Basin, spanning an area of approximately 102 × 10^4 km^2, is the largest inland river basin in China. Due to the basin's extremely dry climate, water shortage is the most critical natural factor restricting socio-economic development in the region. This study focuses on analyzing the historical and future runoff changes of the four headstreams (the Kaidu, Aksu, Yarkand, and Hotan rivers) in the Tarim River Basin with historical observations and multiple-model projections. The results indicate that the runoff of the Tarim's four headstreams showed an increasing trend during 1957–2022, with a remarkable increment of 40.70 × 10^8 m^3, or 18% in percentage. Rising temperatures and precipitation are the main reasons for the runoff's increase. Higher temperature accelerates the melting of glaciers, leading to enhanced recharge of meltwater, while more precipitation also boosts the increase in river runoff. Based on the modelling results from the extended SWAT (Soil and Water Assessment Tool), the runoff in the Kaidu, Aksu, Yarkand, and Hotan rivers will remain at a high level in the near future (–2035), with an average increase of 3.2%–7.55%. In the mid 21st century (2036–2065), the runoff of the Yarkand and Hotan River originated from the Kunlun and Karakoram mountains is expected to continue increasing by around 6.25%–15.2%. Under SSP126, the tipping point of glacier melt runoff in the basin may happen by 2058, while under SSP370 and SSP585 scenarios, it may be around 2080. The timing of peak water aligns with projections in the mountainous Asia, but is later compared to the tropical Andes, Western Canada, and the Swiss Alps, whose peak water has already been reached. The results of this study can provide a scientific basis for the allocation and efficient utilization of water resources in the Tarim River Basin and offer valuable insights into the forthcoming runoff changes in mountainous regions.

KEYWORDS

runoff change, SWAT-glacier, future trend, peak water, Tarim River Basin

1 Introduction

The Tarim River Basin is a typical river basin located in northwestern China. It covers an area of approximately 102 × 10^4 km^2 and is bordered by the Tianshan Mountains to the north, the Karakorum-Kunlun and Altun Mountains to the south, and the Pamir Plateau to the west. The basin consists of nine river systems (the Kaidu-kongque, Dina, Weigan-Kuqa, Aksu, Kashgar, Yarkand, Hotan, Keriya, and Cherchen rivers), along with numerous small rivers. However, due to the combined influence of climate change and human activities, several headwaters of the Tarim River, including the Dina, Weigan-Kuqa, Kashgar, Keriya, and Cherchen, have dried up and separated from the mainstream (Chen, 2015). At present, only four sources–the Kaidu-Kongque, Aksu, Yarkand and Hotan rivers–have surface hydrological connections with the Tarim River. Together, these rivers form the current hydrological pattern of "four sources and one mainstream" that characterizes the Tarim River Basin (Figure 1).

The Tarim River Basin has an extremely dry climate with scarce precipitation (Chen et al., 2009). Water shortage is thus the main natural factor restricting the region's economic and social development and ecological security. The runoff provides the primary water source for the basin's irrigated agriculture and determines the prosperity or declining of this arid region. The runoff is mainly recharged by glacier and snow melt water in the high mountainous area, rainfall in the middle-altitude forest belt, and bedrock fissure water in the low mountain zone (Chen et al., 2009; Chen et al., 2019; Wang et al., 2023). The multiple recharge sources make the hydrological processes very complex. Given its special location and geographical features, the hydrological processes and climate change of the Tarim River Basin attract the attention of numerous scholars (Xu et al., 2004; Duethmann et al., 2015; Duethmann et al., 2016; Shen et al., 2018; Yang et al., 2019; Wang et al., 2021; Bolch et al., 2022; Fang et al., 2022; Wortmann et al., 2022). Their research results show that the climatological and hydrological processes are highly sensitive to climate change (Chen et al., 2006; Wortmann et al., 2022). The climatological and hydrological processes in the basin have altered significantly (Chen et al., 2009; Chen, 2014). Generally, it's basically been agreed that the runoff of the mountainous areas generally showed an increasing trend on the whole (Yao et al., 2022; Chen et al., 2023).

However, the future changes of runoff of the region is hotly debated and inadequately quantified. Some authors suggested that the river runoff may show an increasing trend prior to 2050, but it will likely decrease in the long run (the end of the 21st century) (Liu et al., 2013; Ban et al., 2018). More specifically, river discharge is projected to first increase by about 20% in the Aksu River catchments with subsequent decreases of up to 20%. In contrast, discharge in the Hotan and Yarkand catchments is projected to increase by 15%–60% towards the end of the century (Bolch et al., 2022; Su et al., 2022; Wortmann et al., 2022; Xiang et al., 2022). The increase in runoff is mainly caused by the larger increase in precipitation and glacier runoff than the decrease in winter snow accumulation. For the Kaidu River, runoff will reduce with great uncertainty in precipitation (Zhang et al., 2017; Zhao et al., 2021), but the snowmelt runoff will increase significantly (Xiang et al., 2019). These projections are generally based on GCM outputs and

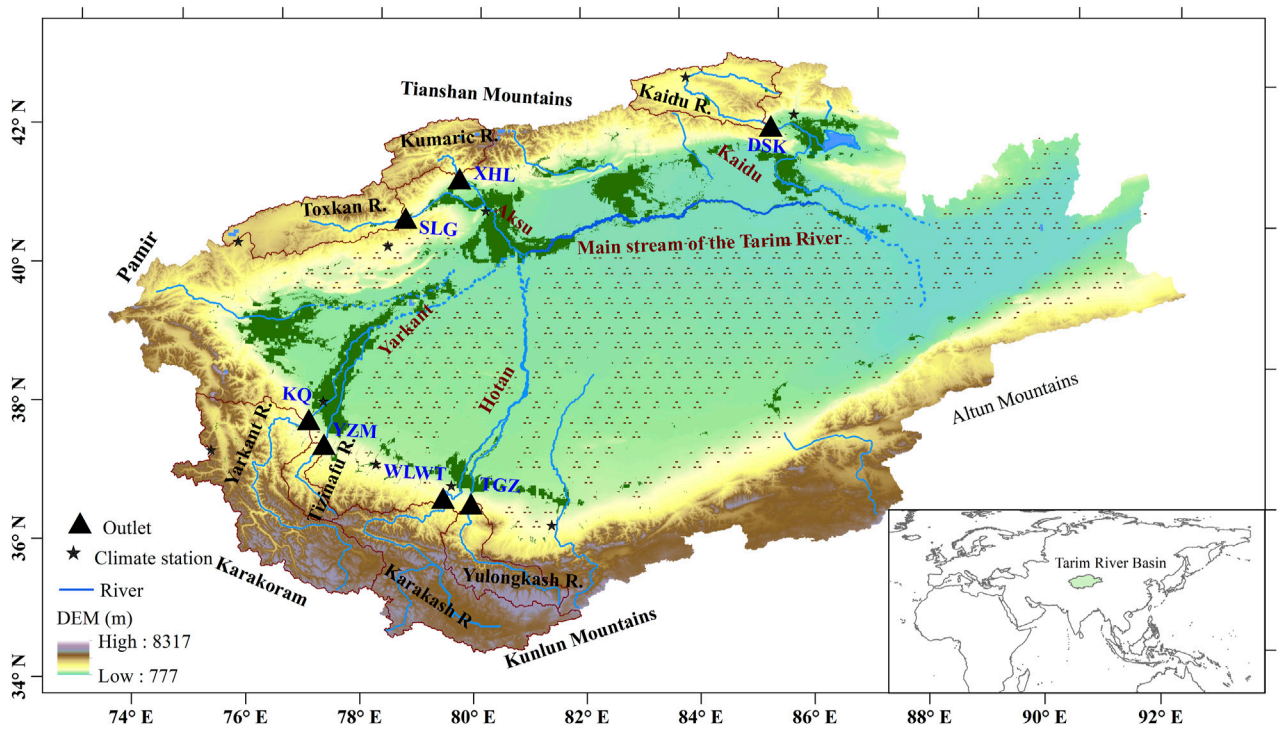

FIGURE 1
Study area of the Tarim River Basin with the spatial location of the headwaters and the corresponding outlets.

catchment-scale hydrological models and most of them focused on one or two headwaters, and few of them validated the model against the glacier melt processes (Bolch et al., 2022; Su et al., 2022; Wang et al., 2022; Fang et al., 2023).

To fill this gap, this study investigates future changes of runoff used multi-model ensemble constructed by a process-based, well-established glacier-hydrology model SWAT-Glacier (Fang et al., 2018; Fang et al., 2023), a global hydrological model H08 (Hanasaki et al., 2008) and glacier evolution model GloGEM (Zhao et al., 2023). The aim is to achieve a comprehensive understanding of the basin's overall water resources, especially changes in glacier melt runoff.

This paper is structured as follows. Section 2 outlines the data and methodology. Section 3 presents findings on historical runoff changes, the sensitivity of runoff to climatic factors, and future runoff predictions using model ensemble. This is followed by discussions and conclusions in Section 4 and Section 5.

2 Data and methods

2.1 Data

In this study, the meteorological data for the Tarim River Basin was obtained from the China Meteorological Data Sharing Network and China Meteorological Administration. These meteorological stations mainly monitor air temperature, precipitation, relative humidity, dew point temperature, water vapor pressure, wind speed, and solar radiation. The monitoring step is daily and the time span is from 1951 to 2022. These data were subjected to rigorous homogeneity tests and used as input for hydrological simulation. The daily meteorological data together with the daily streamflow data were used for analysis of historical runoff changes and for model construction and validation.

For future climate change, the daily precipitation and maximum/minimum temperature from the high spatial resolution regional climate model dataset of the Coordinated Regional Downscaling Experiment (CORDEX) (Giorgi and Gutowski, 2015), an important subprogram of the World Climate Research Program (WCRP) was used. This dataset is used to force the SWAT-Glacier model to project future changes in runoff.

The outputs from the H08 model, forced by four global circulation models (GCM) within the Inter-Sectoral Impact Model Intercomparison Project (ISIMIP2b, www.isimip.org), were also analyzed. The time span is from 1990 to 2100.

Monthly temperature and precipitation data from the ERA5-Land reanalysis dataset were used to force the GloGEM to simulate runoff changes during 1999–2021 and to predict future changes (2022–2100) using ten bias-corrected GCM of from CMIP6.

2.2 Methods and models

For the analysis of historical runoff changes, the Mann-Kendall mutation test method was employed in this study to identify abrupt changes in annual runoff (Kendall, 1975). Initially, the simulation of hydrological processes and runoff was conducted using the SWAT-glacier model (Fang et al., 2018; Fang et al., 2023). The SWAT-glacier model integrates a glacier dynamic module into the original version of the SWAT model (Soil and Water Assessment Tool). In SWAT-Glacier, the glacier melt is calculated using the degree-day method (Neitsch et al., 2002), which is a widely accepted approach for accounting for the glacier melt processes. The theoretical basis of the degree-day method and the extension of the SWAT model have been extensively discussed in previous studies (Hock, 2003; Fang et al., 2018). The model is built for each catchment, and is calibrated against daily streamflow, glacier area changes and glacier melt water contribution. For more details on model configuration and calibration, please refer to Fang et al. (2023).

The sensitivity of runoff to climatic factors was investigated through numerical experiments, wherein only one input variable was altered while keeping the others constant. Firstly, the simple climate change scenario [for temperature, an additive change (Δ) is used: ΔT = −1, 0, 1, 2, 3, 4, and 5°C, etc. For precipitation, a relative change (δ) is used: δP = −20%, −10%, 0, 10%, 20%, 30%, etc) was constructed to represent a wide range of changes in climatic variables. Then these climate data were used to force the SWAT-Glacier to determine the changes in streamflow in response to changes in climatic variables.

Regarding future runoff changes, the bias-corrected outputs of the RCM (Regional Climate Model) were utilized to drive the SWAT-Glacier model and estimate projected changes in streamflow. Other meteorological factors such as solar radiation, wind speed, and relative humidity remained unchanged, as these factors were found to be insensitive and have relatively minor impacts on streamflow based on the Sobols' analysis. In addition, the outputs from the H08 model, forced by four GCMs were also analyzed. Lastly, the outputs of the Global Glacier Evolution Model (GloGEM), driven by ten GCM outputs, were analyzed to understand future changes in glacier melt runoff (Figure 2).

3 Results analysis

Based on the meteorological and hydrological observations of the Tarim River and the multi-model ensemble, the historical and future variations of runoff were analyzed, along with the responses of runoff to climatic factors.

3.1 Historical changes in runoff

3.1.1 Inter-annual variations of runoff

During the study period (1957–2022), the runoff from the mountainous headwaters of the Tarim River showed an obvious increasing trend, with the average runoff of the four sources increased from 230.20 × 10^8 m^3 to 270.90 × 10^8 m^3, accounting for a total increase of 40.70 × 10^8 m^3, or 18%. During the same period, the Kaidu, Aksu, Yarkand and Hotan rivers increased by 9.65 × 10^8 m^3, 11.23 × 10^8 m^3, 10.11 × 10^8 m^3, and 9.71 × 10^8 m^3, respectively (Figure 3; Table 1), with the Kaidu and Hotan rivers experiencing the highest relative change, by 27% and 22%,

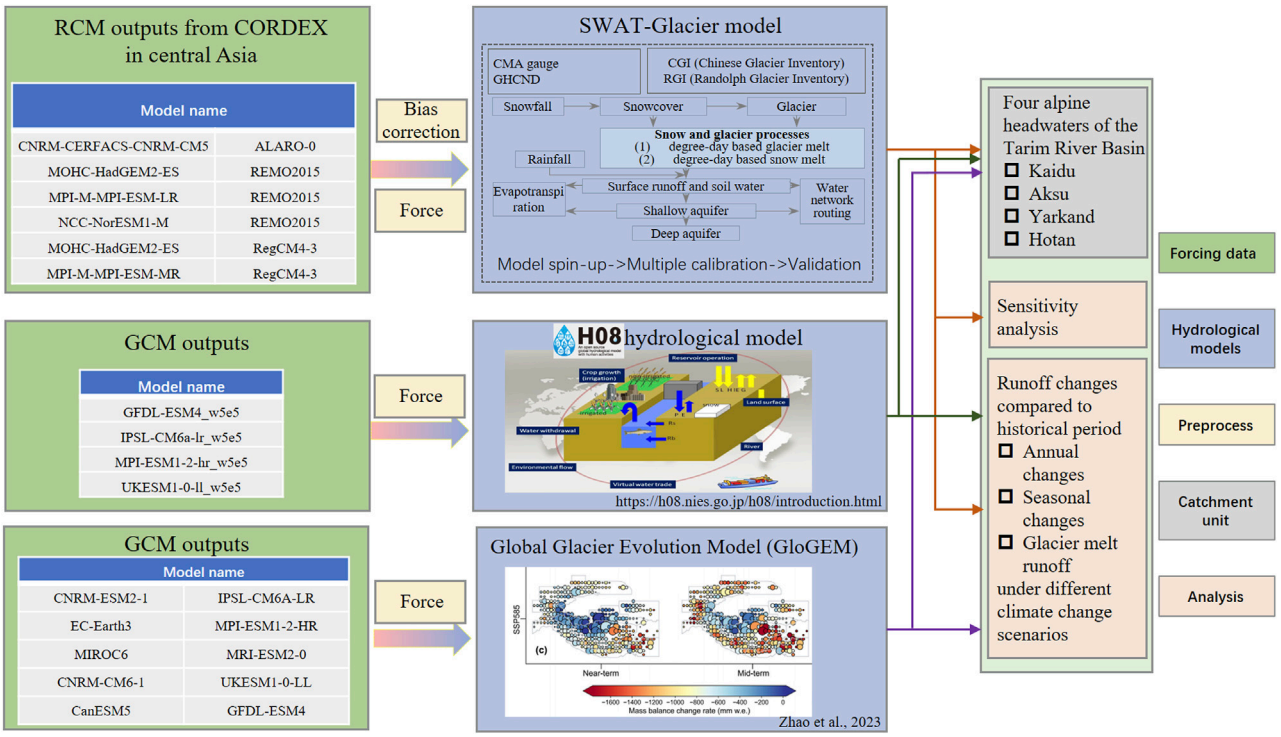

FIGURE 2
Work flow of the multiple model simulation of runoff in the Tarim River Basin. The diagram of H08 is adapted from its and GloGEM are adapted from its official website and the figures of the GloGEM is from Zhao et al. (2023).

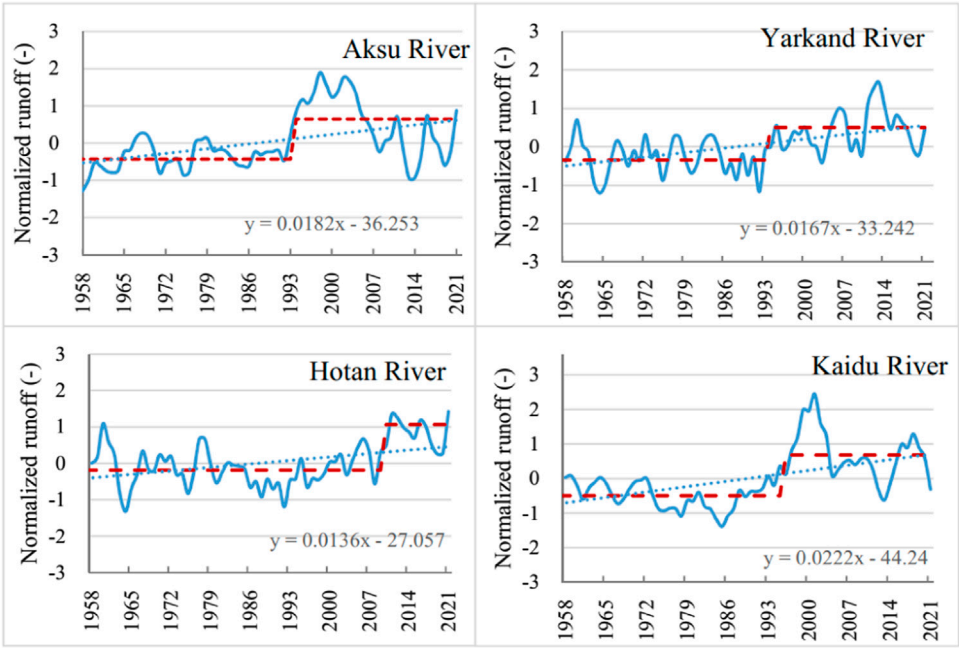

FIGURE 3
Interannual variations of runoffs of the four headwaters in the Tarim River Basin represented by three-year smoothing normalized runoff. Note that the runoff of each source is the sum of runoff from its tributaries and interval flow. The red line indicates the mean runoff during a specific period, while the dotted line represents the linear fitting line.

TABLE 1 Variations of runoff in the "four sources" of the Tarim River Basin (unit: 10^8 m^3).

Headwaters	Mean annual runoff	1950s	1960s	1970s	1980s	1990s	2000s	2010–2022
Kaidu River	39.81	42.51	36.02	34.4	34.34	41.73	45.2	42.66
Aksu River	82.64	68.3	79.45	77.75	78.54	91.47	91.66	80.55
Yarkand River	77.75	72.94	73.12	76.02	72.89	77.92	81.48	86.73
Hotan River	45.63	45.56	43.97	45.84	41.74	41.43	47.89	52.56

respectively. In addition, the runoff from the Kaidu, Aksu, Yarkand, and Hotan rivers exhibited a "jump increase" in 2010, 1993, 1994, and 1996, respectively. This rise in runoff is closely associated with the considerable temperature rise and precipitation increase. Firstly, the higher temperatures accelerated the melting of snow and glaciers, resulting in a substantial increase in runoff, where is primarily recharged by glacial and snowmelt water. Secondly, the warmer atmosphere has a greater capacity to hold water, potentially leading to an elevation in atmospheric precipitable water, which in turn can influence both extreme and average rainfall patterns. The abrupt fluctuations in temperature and precipitation may be attributed to large-scale circulation processes, particularly the Tibetan Plateau Index B (Chen, 2014). However, in the long term, these abrupt changes could be attributed to natural variations in the climate system (Su et al., 2022).

3.1.2 Seasonal changes in runoff

Seasonally, the spring and autumn runoff accounted for about 20%–25%, summer runoff accounted for 40%–65%, and winter runoff accounted for about 10% for the annual runoff in the headwaters of the Tarim River. The Kaidu, Aksu, Yarkand, and Hotan rivers had the smallest proportion of runoff in February (3.20%, 1.29%, 1.85%, and 1.21%, respectively). The maximum runoff of the Aksu, Yarkand, and Hotan rivers for four consecutive months occurred from June to September, accounting for 75.86%, 79.60%, and 82.96% of the entire year, respectively, while that of the Kaidu River occurred from May to August, accounting for only 56.40% of the entire year. The annual distribution of the runoff of the Kaidu River was relatively uniform compared with the other rivers, peaking in July, which accounted for 16.40% of the annual runoff. During the winter, due to scarce precipitation and low temperatures, river runoff was mainly fed by bedrock fissure water and groundwater in the lower mountain zone, and the proportion of runoff was small. This is a common feature in rivers that are mainly fed by glacier and snow meltwater.

During 1957–2022, the Kaidu, Aksu, Yarkand, and Hotan rivers showed an obvious increase in runoff during October to March, with an earlier spring flood. Among these rivers, the runoff increased most significantly in December for the Hotan and Aksu rivers, while the runoff increases most significantly in January for the Yarkand River and in April for the Kaidu River. It is worth noting that although the relative increase was large, the absolute increment of the runoff was small. During April to September, the runoff also showed an increasing trend. Although the relative increase was less than that during October to March, the actual increment was larger, resulting in a greater and more concentrated flooding trend.

3.2 Sensitivity of runoff to climate factors

There is a close relationship between runoff change and climate change in the Tarim River Basin. Throughout the first half of the historical study period (1957–1997), there was a steady rise in both temperature and precipitation. Then, in the late 1990s, the temperature "leaped" (Chen, 2014; Chen et al., 2023), with the mean temperature increasing by 0.93°C after 1998 compared to the period of 1957–1997. Precipitation also showed an obvious rising trend at an increasing rate of 7.47 mm/10a. In one hand, warmer temperatures accelerated the melting of glaciers, leading to more glacial meltwater. On the other hand, warmer temperature boosted evapotranspiration, and resulting in increased water consumption. The increased precipitation had a positive effect on river runoff. Using the Simple Climate Change scenario, this study analyzed the response of runoff to climatic factors of the headwaters (Kaidu River, Aksu River, Yarkand River, and Hotan River). The results revealed notable differences in hydrological changes among different rivers.

(1) Runoff in the Kaidu River increased quasi-linearly with increases in precipitation, while the response of runoff to temperature depending on the range of the temperature change. When the temperature increased by more than 2°C, the runoff decreased significantly, but when the temperature rose less than 2°C, the changes in runoff were almost linear with the changes in precipitation. The elastic coefficient ($\delta Q/\delta P$) was about 1.0, indicating that when average annual precipitation increased by 1%, the average annual runoff will increase by 1%. The runoff depth is 197 mm, and the mean annual precipitation is 378 mm, which suggests a sub-humid condition of the mountainous Kaidu River Catchment. However, it is important to note that this value is not fixed and can be influenced by changes in future climate conditions (Tang et al., 2019). If precipitation decreases or increases in the future, this value may also fluctuate accordingly.
(2) For the Aksu River, the runoff increased almost linearly with the increase in precipitation when the temperature remained unchanged. Precipitation increased by 10% and runoff increased by about 3%. The response of the runoff to temperature was more complex. When the temperature rose by 1°C, the runoff increased by about 5%. However, when the temperature fell by 1°C, the runoff decreased by 14%. The findings indicate that evapotranspiration and glacier melt runoff are sensitive to temperature.
(3) The increase in temperature and precipitation in the Yarkand River Basin boosted the increase in runoff, as the runoff appeared to be very sensitive to temperature. An increase of 1°C in temperature resulted in an increase in runoff by

TABLE 2 Model performance of the SWAT-Glacier in the "four source streams" of the Tarim River Basin.

Headwaters	Tributaries	Hydrological station				Catchment area/km^2	Mean annual runoff/ 10^8 m^3	Monthly NS coefficient of SWAT-Glacier driven by observed climate	Monthly NS coefficient of SWAT-Glacier driven by correct RCM outputs
		Station name	Longitude	Latitude	Elevation				
Kaidu River	Kaidu River	Dashankou	85°44′	42°13′	1,340	19,022	39.81	0.83	[0.68,0.31]
Aksu River	Kumarak River	Xiehela	79°37′	41°34′	1,487	12,816	48.43	0.87	[0.78,0.68]
	Toshgan River	Shaliguilank	78°36′	40°57′	2,000	19,166	28.13	0.69	[0.60,0.50]
Yarkand River	Yarkand River	Kaqun	76°54′	37°59′	1,370	50,248	68.36	0.87	[0.73,0.48]
	Tizinafu River	Yuzimenluoke	77°12′	37°38′	1,620	5,389	9.39	0.72	[0.67,0.56]
Hotan River	Kalakash River	Wuluwati	79°26′	36°52′	1,800	19,983	22.37	0.77	[0.77,0.47]
	YulongKash River	Tongguziluoke	79°55′	36°49′	1,650	14,575	23.26	0.81	[0.75,0.53]

10.2%–16.2%. However, when precipitation rose 10%, runoff increased by only about 3%. When the temperature increased within 2°C, the runoff increased 3.3%–7.7%, and when the temperature increased by 3°C, 4°C, and 5°C, the runoff increased by 17.3%, 24.6%, and 11.8%, respectively.

(4) For the Hotan River, the runoff responds differently to climatic factors for its two tributaries (i.e., Karakash and Yulongkash River). The Karakash River is highly sensitive to the snow related processes, while the Yulongkash River is sensitive to glacier melt processes. Additionally, the runoff of the Kalakash River showed an "increase-decrease" trend with rises in temperature, whereas the runoff of the Yulongkash River presented an increasing trend with rising temperature but low sensitivity to precipitation changes.

3.3 Forecast of future runoff

3.3.1 Runoff prediction based on the SWAT model

This study uses the corrected high-resolution climate dataset CORDEX to force the distributed hydrological model SWAT-Glacier. The model performance is shown in Table 2. The estimation period includes the historical period 1976–2005 and the future periods (i.e., 2006–2035, 2036–2065, and 2066–2095). The temperature of the Tarim River Basin will continue rising under the RCP4.5 and RCP8.5 scenarios. Compared with the historical period (1976–2005), the temperature will rise by 1.22°C ± 0.72°C during the middle of the 21st century (2036–2065), with a greater increase occurring in the southern slopes of the Tianshan Mountains compared with the northern slopes of the Kunlun Mountains. The rise in average temperature in the Kaidu and Aksu catchments is anticipated to be 1.39°C, while that in the Yarkand and Hotan river basins is estimated to be 1.21°C. In the Tarim River Basin, the temperature is expected to increase by 4.27°C ± 2.59°C by the end of the 21st century. It is worth pointing out that the various GCM-RCM models also show different predictions.

In terms of future precipitation, precipitation shows an overall increasing trend compared with 1976–2005. During 2036–2065, the average increase in precipitation in the Tarim River Basin is anticipated to be 3.81 ± 14.72 mm, with the Yarkand catchment expected to have the largest increase, followed by the Kaidu catchment. By the end of the 21st century, the precipitation is expected to increase by 20.52 ± 27.66 mm.

In the future, the runoff will remain at a high level with moderate fluctuations. In the near future (–2035), the runoff of the Kaidu, Aksu, Yarkand, and Hotan rivers will increase slightly, with an average increase of 3.2%–7.55%. The increase is mainly due to the increase in ice/snow melt water and precipitation in the alpine areas caused by global warming. For the mid 21st century (2036–2065), the average increase in runoff in the Yarkand and Hotan rivers will be around 6.25%–15.2% compared with the historical period, while the runoff in the Kaidu River will remain the current level (Table 3).

Seasonally, the runoff in the Tarim River Basin is expected to increase in spring. For the Kaidu River Basin, the runoff tends to shift forward, forming a snowmelt peak from April to May. For the Aksu and Yarkand rivers, due to the influence of summer snow and glacier meltwater, the summer streamflow will increase significantly. For the Hotan River, the runoff from the mountains in summer also shows an increasing trend.

3.3.2 Runoff prediction based on the global distributed hydrological model

Based on the ISIMIP2b protocol, the H08 hydrological model was adopted in this study. We selected gfdl-esm4_w5e5, ipsl-cm6a-lr_w5e5, mpi-esm1-2-hr_w5e5 and ukesm1-0-ll_w5e5 as climate drivers and analyzed future runoff changes in the Tarim River Basin under the SSP126, SSP370, and SSP585 scenarios.

The results showed an increasing trend in the runoff of the Kaidu, Aksu, Yarkand, and Hotan rivers under the SSP126 scenario. We found that during 1990–2100, the increase rate of the runoff in the Kaidu River was 0.02 × 108 m^3 per year, while that of the Aksu River was 0.08 × 108 m^3 per year (among which, increase rates of the Aksu's two major tributaries, the Kumarak and Toshgan rivers, were

10.3389/feart.2023.1249107

TABLE 3 Prediction list of future runoff changes of typical rivers in the Tarim River Basin (10^8 m^3).

Headwaters	Observed value	Estimated value			
	1981–2015	2016–2035 (RCP4.5)	2016–2035 (RCP8.5)	2036–2065 (RCP4.5)	2036–2065 (RCP8.5)
Kaidu River	35.97	37.60	35.60	32.7	31.6
Aksu River	80.41	83.01	82.01	85.4	84.9
Yaokand River	75.50	78.40	78.50	87.0	90.9
Hotan River	44.26	47.60	48.60	49.8	50.5

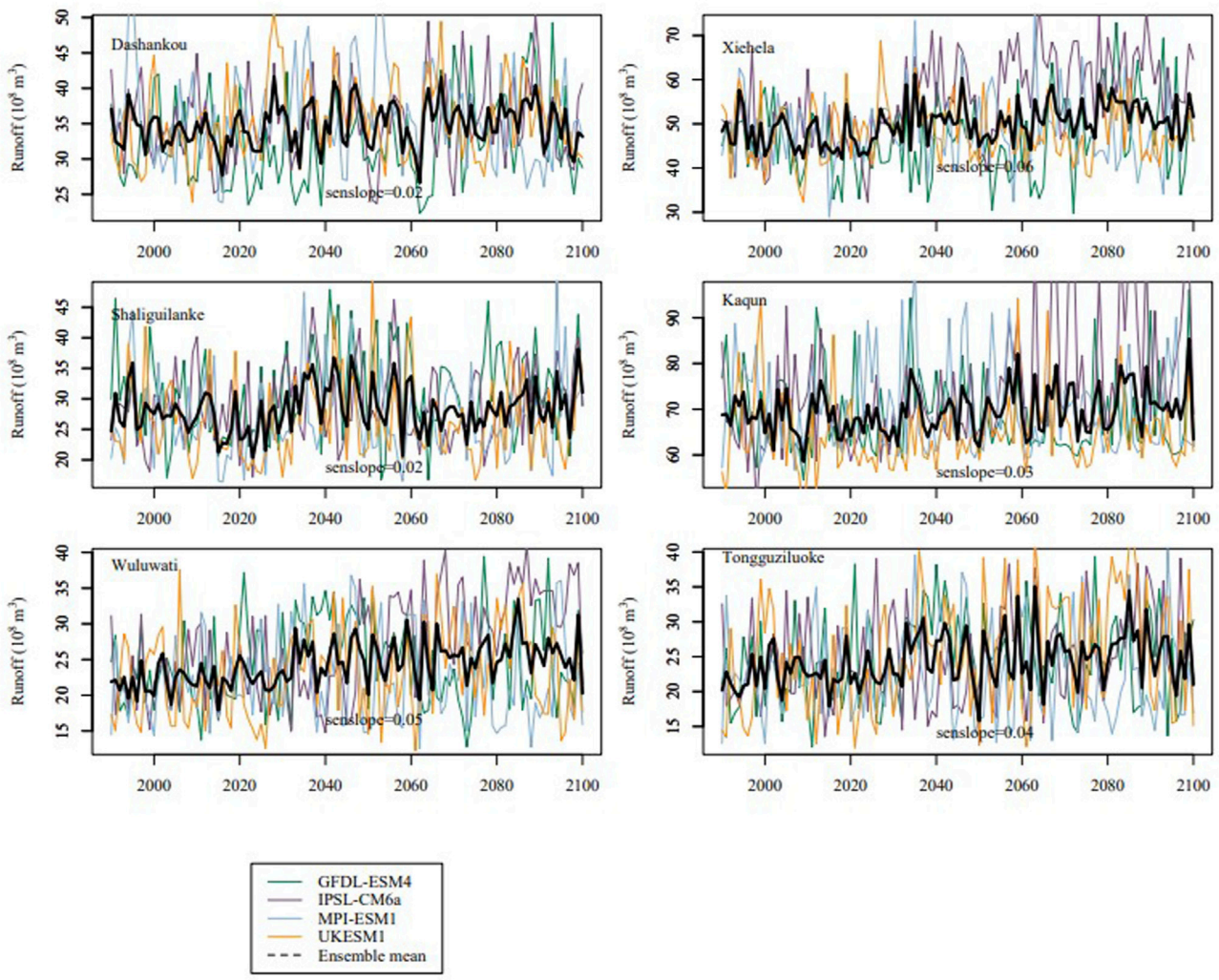

FIGURE 4
Runoff variations of four headstreams of the Tarim River under SSP126 scenario based on ISIMIP datasets. The colored fine lines indicate single model simulations while the black thick line is the ensemble mean.

0.06 × 108 m^3 and 0.02 × 108 m^3 per year, respectively). Increases in the runoff of the Yarkand and Hotan rivers were 0.03 × 108 m^3/year and 0.09 × 108 m^3/year, respectively (Figure 4).

Under the SSP585 scenario, we found that during 1990–2100, runoff in the Aksu River increased by 0.02 × 108 m^3/year (the Kumarak and Toshgan rivers both increased at a rate of 0.01 × 108 m^3/year), while runoff in the Yarkand River and the Hotan River increased at a rate of 0.03 × 108 m^3 and 0.11 × 108 m^3 per year, respectively (Figure 5).

3.3.3 Forecast of future change trends in melt runoff

Based on the GloGEM, this study calculated the changes in glacier melt runoff in the Tarim River Basin (Zhao et al., 2023).

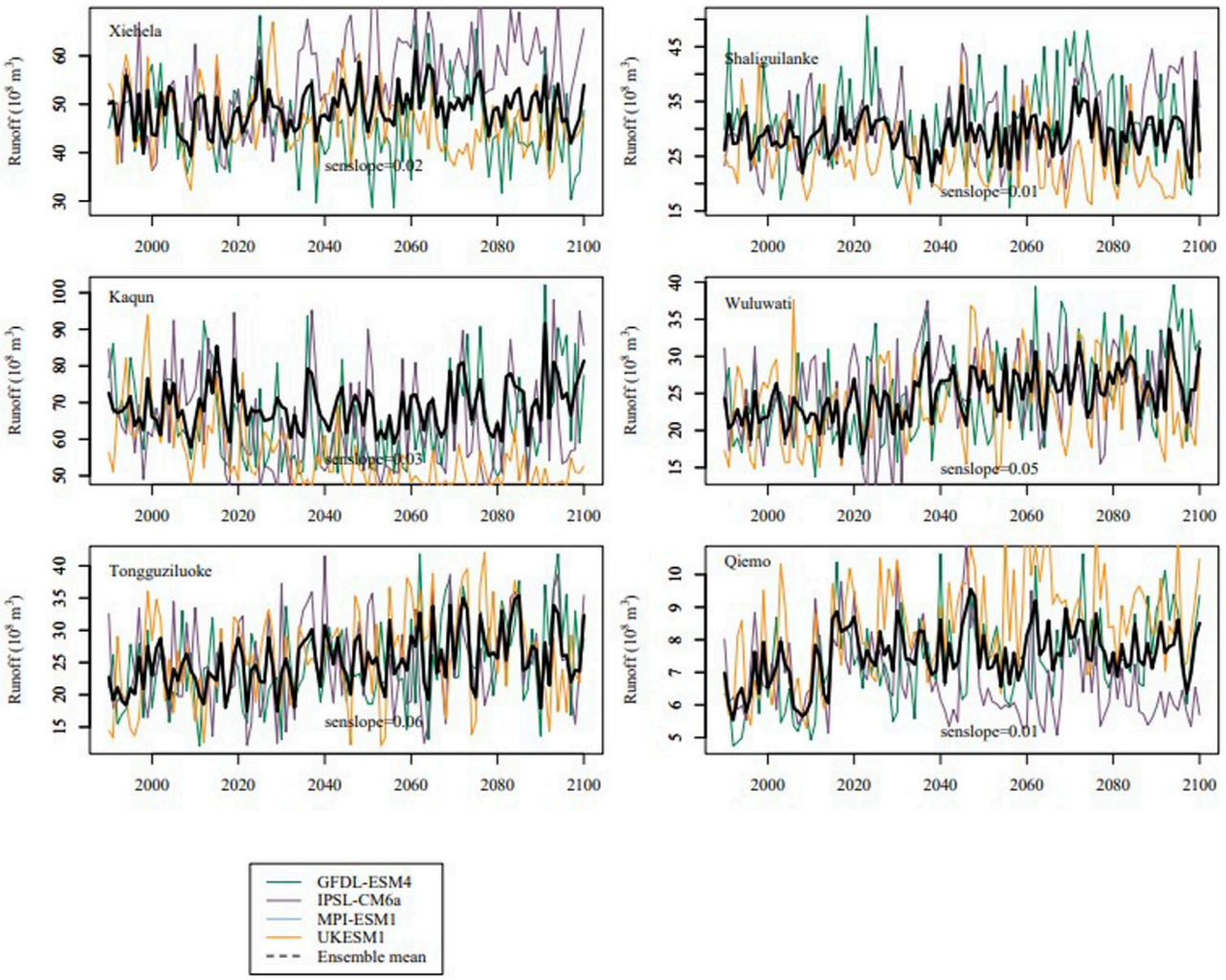

FIGURE 5
Runoff variations of four headstreams of the Tarim River under SSP585 scenario based on ISIMIP datasets. The colored fine lines indicate single model simulations while the black thick line is the ensemble mean.

Under global warming, the increase in temperature significantly influenced the glacier meltwater in the Tarim River Basin. Under the SSP126 scenario, the tipping point of glacier melt in the basin may occur around 2058, while under the SSP370 and SSP585 scenarios, it is anticipated to occur around 2080. For the Aksu River, the tipping point of the glacier melting runoff is around 2040–2050 (Figure 6). Under the SSP126 scenario, the Tarim River runoff may be lower than or equal to the historical period by the end of the 21st century. And the runoff in the Yarkand and Hotan rivers will show a continuous increasing trend. However, compared with the beginning of the 21st century, the runoff presents a slight decrease (7%) only under RCP2.6 scenario, whereas the runoff will increase under other scenarios.

4 Discussion

The Tarim River Basin is China's largest inland basin, and nearly all the water resources come from the mountainous areas. However, climate change is impacting the hydrological processes by affecting the precipitation and runoff generation processes, as well as the melting of glaciers and snow and underlying surface changes (e.g., frozen soil, landuse), thus altering annual and seasonal variations of water resources across the basin. For example, the vegetation in the mountainous watershed of the Kaidu River is lush and expansive. When the temperature rises, vegetation transpiration increases substantially and consumes large amount of water. This may lead to a decreasing trend in the runoff in the middle to late 21st century for the Kaidu river. The simulated increase in runoff is largely caused by increased glacier meltwater in the mountains. However, the glacier retreat in the Tarim River Basin is obvious, which will lead to enhanced hydrological fluctuations considering the intensified climate extremes (Fang et al., 2022; Zhang et al., 2022).

Under the SSP126 and SSP370 scenarios, the runoff in the Aksu River shows an increasing trend, while under the SSP585 scenario, the runoff shows a weak decreasing trend after 2066. Except for the SSP370 scenario, runoff in the Yarkand River basically maintains a high variation and increasing trend.

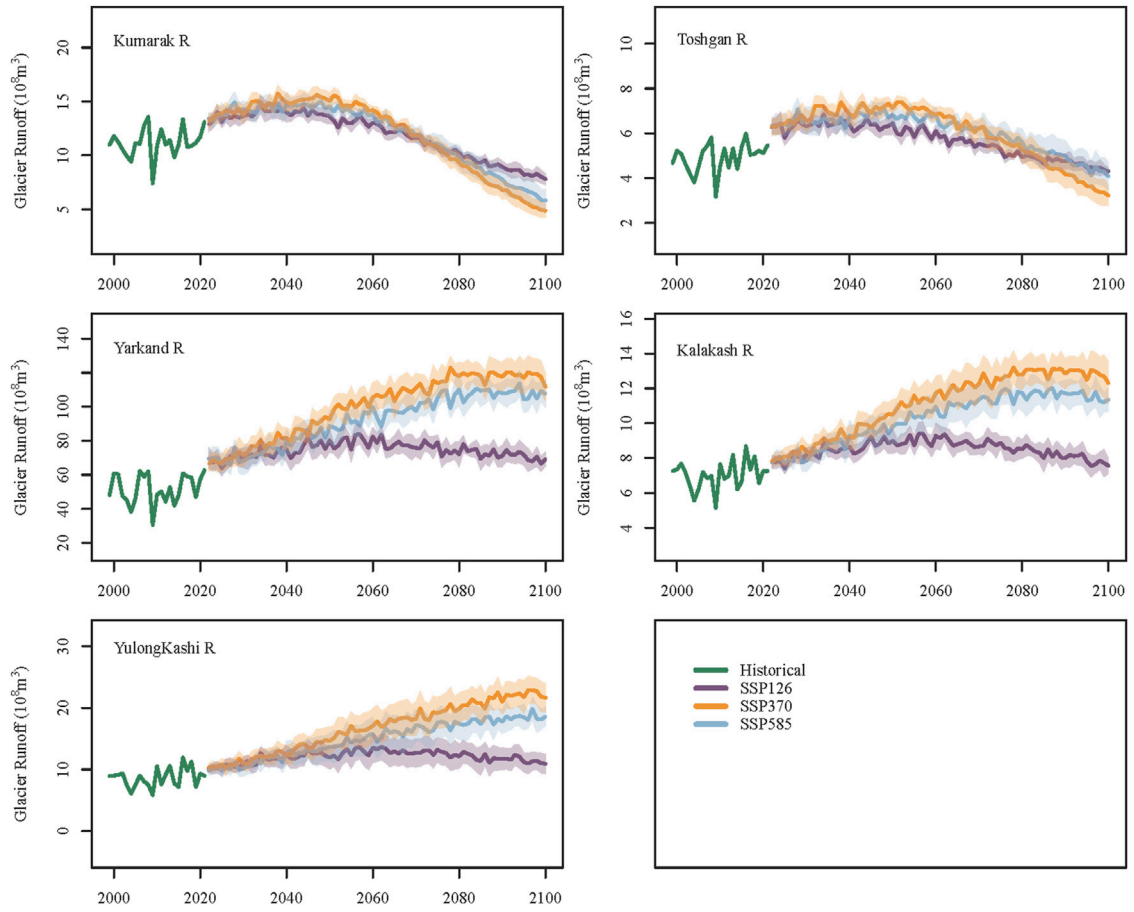

FIGURE 6
Future changes in glacier meltwater runoff in the headwaters of the Tarim River. The shaded area represents the multiple model mean ± standard deviation.

Similarly, the future runoff of the Hotan River, which originates from the northern slope of the Kunlun Mountain, also presents a high variation and increasing trend. Compared with previous study, the results are inconsistent with results projected by two glacio-hydrological models forced by eight GCMs, that river discharge is projected to first increase by about 20% in the Aksu River catchment with subsequent decrease of up to 20%, while the Hotan and Yarkand catchments is projected to increase by 15%–60% towards the end of the century (Wortmann et al., 2022). Some studies also projected a slightly decrease in runoff with increase spring and winter runoff in the end of the 21st century (Liu et al., 2013). Note that the direction of changes in the Kaidu River is debated with both increasing trend (Zhang et al., 2017; Ren et al., 2018; Wang et al., 2018) and decreasing trend (Liu et al., 2011; Xu et al., 2016; Luo et al., 2018; Huang et al., 2020). The future runoff in the Yarkand and Hotan rivers is basically in an increasing trend with different magnitude (Zhang et al., 2012; Luo et al., 2018; Su et al., 2022). The runoff in the Aksu River will increase in the near future but will decrease in the end of the 21st century with the dramatic decrease in glacier area (Duethmann et al., 2016; Wang et al., 2018; Huang, 2019).

From the future projection of glacier melt runoff, the tipping point of glacier meltwater runoff in the Tarim River Basin will likely occur within the next 10–30 years. After that, the runoff will remain at a high level, mainly because of the increase in mountainous precipitation. Under the influence of steady warming, the huge tongues of the glaciers will likely melt and recede, but a certain amount of glacial meltwater will still be generated to maintain the stability of the runoff. The timing of peak water varying globally. For glacier-fed rivers with predominantly smaller glaciers, for example, in the tropical Andes (Frans et al., 2015; Polk et al., 2017), Western Canada (Fleming and Dahlke, 2014) and the Swiss Alps (Huss and Fischer, 2016), the peak water has been reached before 2019. For the High Mountain Asia, the European Alps, and Western Canada and United States , the peak water will generally be reached before or around the middle of the century (IPCC, 2019). We have to admit that the timing of peak water varies for different circulation conditions and glacier characteristics.

Note that there is some uncertainty regarding future runoff in large basins with numerous glaciers. The changing pattern of runoff in the future presents challenges, especially considering potential underestimation of evapotranspiration due to vegetation changes, altered routine processes resulting from glacier retreat, and other factors. To address this challenge, it is strongly recommended to incorporate more physical processes into the modeling approach.

5 Conclusion

Global warming has led to changes in glacier and snow meltwater and therefore changes the runoff in the Tarim River Basin. This paper assessed the future changes in runoff in the Tarim River Basin based on multi-model ensemble including SWAT-Glacier, H08 and GloGEM. The following conclusions can be drawn.

(1) The runoff from the mountains in the Tarim River Basin showed an overall increasing trend. For more than half a century (1957–2022), the runoff in the mountainous area in the Kaidu, Aksu, Yarkand, and Hotan rivers increased at a rate of 2.56×10^8 m^3, 2.06×10^8 m^3, 2.11×10^8 m^3, and 1.12×10^8 m^3 per decade, respectively. The runoff increased by 40.7×10^8 m^3 during 1957–2022.

(2) There is a close relationship between runoff change and climate change in the Tarim River Basin. During the historical period (1957–2022), both the temperature and the precipitation increased. Warmer temperatures accelerated both the evapotranspiration and the glacier melt, leading to changes in runoff. The rise in precipitation had a positive effect on river runoff. Under global warming, the hydrological fluctuations will further increase.

(3) Under the RCP4.5 and RCP8.5 scenarios, future runoff in the Tarim River shows an increasing trend. Up to 2035, the runoff in the Kaidu, Aksu, Yarkand, and Hotan rivers will likely remain at a high level, with an average increase of around 3.2%–7.55%. In the mid 21st century (2036–2065), the runoff of the Yarkand and Hotan rivers originating in the Kunlun and Karakoram mountains is expected to follow an increasing trend of around 6.25%–15.2%. According to the prediction results of the global hydrological model H08, the runoff is expected to increase during the mid 21st century under the SSP126 and SSP585 scenarios. Under the SSP126 scenario, the tipping point of glacier melt runoff in the basin may occur around 2058, while under the SSP370 and SSP585 scenarios, it may occur around 2080. The timing of peak water in the Yarkand and Hotan rivers aligns well with previous projections in mountainous Asia, where the presence of large glaciers is a contributing factor. However, it occurs much later compared to the tropical Andes, Western Canada, and the Swiss Alps, where peak water has been already reached before 2019.

Data availability statement

The datasets presented in this study can be found in online repositories. The names of the repository/repositories and accession number(s) can be found in the article.

Author contributions

XG: Writing–original draft preparation, Visualization, Investigation. GF: Analysis and interpretation of data. YC: Conception and design of the work. XZ: Acquisition and processing of data. GF and YC: Conceptualization, Writing–review and editing. All authors contributed to the article and approved the submitted version.

Funding

The research is supported by the National Natural Science Foundation of China (grant numbers U1903208 and 42071046), the Open Project of Key Laboratory of Xinjiang, China (grant number 2022D04043) and Xinjiang Natural Science Foundation (grant number 2022D01A348).

Conflict of interest

The authors declare that the research was conducted in the absence of any commercial or financial relationships that could be construed as a potential conflict of interest.

The reviewer HW and XL declared a shared affiliation with the author XG to the handling editor at time of review.

Publisher's note

All claims expressed in this article are solely those of the authors and do not necessarily represent those of their affiliated organizations, or those of the publisher, the editors and the reviewers. Any product that may be evaluated in this article, or claim that may be made by its manufacturer, is not guaranteed or endorsed by the publisher.

References

Ban, C., Tao, H., Dong, Y., and Zhao, C. (2018). "Simulation of daily runoff process in the mainstream area of the Tarim River under future climate scenario," in *Arid zone research* (Berlin, Germany: Springer).

Bolch, T., Duethmann, D., Wortmann, M., Liu, S., and Disse, M. (2022). Declining glaciers endanger sustainable development of the oases along the Aksu-Tarim River (Central Asia). *Int. J. Sustain. Dev. World Ecol.* 29, 209–218. doi:10.1080/13504509.2021.1943723

Chen, H., Chen, Y., Li, W., and Li, Z. (2019). Quantifying the contributions of snow/glacier meltwater to river runoff in the Tianshan Mountains, Central Asia. *Glob. Planet. change* 174, 47–57. doi:10.1016/j.gloplacha.2019.01.002

Chen, Y. (2014). *Water resources research in Northwest China*. Berlin, Germany: Springer Science & Business Media.

Chen, Y. (2015). *Ecological protection and sustainable management of the Tarim River Basin*. Beijing: Science press.

Chen, Y., Li, Z., Xu, J., Shen, Y., Xing, X., Xie, T., et al. (2023). Changes and protection suggestions in water resources and ecological environment in arid region of northwest China. *Bull. Chin. Acad. Sci.* 38, 385–393. doi:10.16418/j.issn.1000-3045.20230120005

Chen, Y., Takeuchi, K., Xu, C., Chen, Y., and Xu, Z. (2006). Regional climate change and its effects on river runoff in the Tarim Basin, China. *Hydrol. Process.* 20, 2207–2216. doi:10.1002/hyp.6200

Chen, Y., Xu, C., Hao, X., Li, W., Chen, Y., Zhu, C., et al. (2009). Fifty-year climate change and its effect on annual runoff in the Tarim River Basin, China. *Quat. Int.* 208, 53–61. doi:10.1016/j.quaint.2008.11.011

Duethmann, D., Bolch, T., Farinotti, D., Kriegel, D., Vorogushyn, S., Merz, B., et al. (2015). Attribution of streamflow trends in snow and glacier melt-dominated catchments of the Tarim River, Central Asia. *Water Resour. Res.* 51, 4727–4750. doi:10.1002/2014wr016716

Duethmann, D., Menz, C., Jiang, T., and Vorogushyn, S. (2016). Projections for headwater catchments of the Tarim River reveal glacier retreat and decreasing surface water availability but uncertainties are large. *Environ. Res. Lett.* 11, 054024. doi:10.1088/1748-9326/11/5/054024

Fang, G., Li, Z., Chen, Y., Liang, W., Zhang, X., and Zhang, Q. (2023). Projecting the impact of climate change on runoff in the Tarim River simulated by the soil and water assessment Tool Glacier Model. *Remote Sens.* 15, 3922. doi:10.3390/rs15163922

Fang, G., Li, Z., Yang, J., Chen, Y., Duan, W., Amory, C., et al. (2022). Changes in flooding in the alpine catchments of the Tarim River Basin, central Asia. *J. Flood Risk Manag.* 16, e12869. doi:10.1111/jfr3.12869

Fang, G., Yang, J., Chen, Y., Li, Z., Ji, H., and De Maeyer, P. (2018). How hydrologic processes differ spatially in a large basin: multisite and multiobjective modeling in the Tarim River Basin. *J. Geophys. Res. Atmos.* 123, 7098–7113. doi:10.1029/2018jd028423

Fleming, S. W., and Dahlke, H. E. (2014). Modulation of linear and nonlinear hydroclimatic dynamics by mountain glaciers in Canada and Norway: results from information-theoretic polynomial selection. *Can. Water Resour. Journal/Revue Can. Des. ressources hydriques* 39, 324–341. doi:10.1080/07011784.2014.942164

Frans, C., Istanbulluoglu, E., Lettenmaier, D. P., Naz, B. S., Clarke, G. K., Condom, T., et al. (2015). Predicting glacio-hydrologic change in the headwaters of the Z ongo R iver, C ordillera R eal, B olivia. *Water Resour. Res.* 51, 9029–9052. doi:10.1002/2014wr016728

Giorgi, F., and Gutowski, W. J., Jr (2015). Regional dynamical downscaling and the CORDEX initiative. *Annu. Rev. Environ. Resour.* 40, 467–490. doi:10.1146/annurev-environ-102014-021217

Hanasaki, N., Kanae, S., Oki, T., Masuda, K., Motoya, K., Shirakawa, N., et al. (2008). An integrated model for the assessment of global water resources–Part 1: model description and input meteorological forcing. *Hydrology Earth Syst. Sci.* 12, 1007–1025. doi:10.5194/hess-12-1007-2008

Hock, R. (2003). Temperature index melt modelling in mountain areas. *J. hydrology* 282, 104–115. doi:10.1016/s0022-1694(03)00257-9

Huang, J. (2019). "Analysis of stream flow composition in glacierized inland river basin—case study from Aksu river basin," in *Analysis of stream flow composition in glacierized inland river basin—case study from Aksu river basin*. Editor J. Huang (Beijing: University of Chinese Academy of Sciences).

Huang, Y., Ma, Y., Liu, T., and Luo, M. (2020). Climate change impacts on extreme flows under IPCC RCP scenarios in the mountainous Kaidu watershed, Tarim River basin. *Sustainability* 12, 2090. doi:10.3390/su12052090

Huss, M., and Fischer, M. (2016). Sensitivity of very small glaciers in the Swiss Alps to future climate change. *Front. earth Sci.* 4, 34. doi:10.3389/feart.2016.00034

IPCC (2019). in *IPCC special report on the ocean and cryosphere in a changing climate*. Editors H. Portner, D. C. Roberts, V. Masson-Delmotte, P. Zhai, M. Tignor, E. Poloczanska, et al. (Cambridge, UK and New York, USA: Cambridge University Press).

Kendall, M. G. (1975). *Rank correlation methods*. 4th edition. London: Charles Griffin.

Liu, T., Willems, P., Pan, X. L., Bao, A. M., Chen, X., Veroustraete, F., et al. (2011). Climate change impact on water resource extremes in a headwater region of the Tarim basin in China. *Hydrology Earth Syst. Sci.* 15, 3511–3527. doi:10.5194/hess-15-3511-2011

Liu, Z., Xu, Z., Fu, G., and Yao, Z. (2013). Assessing the hydrological impacts of climate change in the headwater catchment of the Tarim River basin, China. *Hydrology Res.* 44, 834–849. doi:10.2166/nh.2012.237

Luo, Y., Wang, X., Piao, S., Sun, L., Ciais, P., Zhang, Y., et al. (2018). Contrasting streamflow regimes induced by melting glaciers across the Tien Shan – Pamir – North Karakoram. *Sci. Rep.* 8, 16470. doi:10.1038/s41598-018-34829-2

Neitsch, S., Arnold, J., and Kiniry, J. (2002). *Soil and water assessment tool theoretical manual*. Texas: Grassland Soil Water Research Laboratory.

Polk, M. H., Young, K. R., Baraer, M., Mark, B. G., Mckenzie, J. M., Bury, J., et al. (2017). Exploring hydrologic connections between tropical mountain wetlands and glacier recession in Peru's Cordillera Blanca. *Appl. Geogr.* 78, 94–103. doi:10.1016/j.apgeog.2016.11.004

Ren, W., Yang, T., Shi, P., Xu, C.-Y., Zhang, K., Zhou, X., et al. (2018). A probabilistic method for streamflow projection and associated uncertainty analysis in a data sparse alpine region. *Glob. Planet. Change* 165, 100–113. doi:10.1016/j.gloplacha.2018.03.011

Shen, Y.-J., Shen, Y., Fink, M., Kralisch, S., Chen, Y., and Brenning, A. (2018). Trends and variability in streamflow and snowmelt runoff timing in the southern Tianshan Mountains. *J. Hydrology* 557, 173–181. doi:10.1016/j.jhydrol.2017.12.035

Su, F., Pritchard, H. D., Yao, T., Huang, J., Ou, T., Meng, F., et al. (2022). Contrasting fate of western Third Pole's water resources under 21st century climate change. *Earth's Future* 10, e2022EF002776. doi:10.1029/2022ef002776

Tang, Y., Tang, Q., Wang, Z., Chiew, F. H. S., Zhang, X., and Xiao, H. (2019). Different precipitation elasticity of runoff for precipitation increase and decrease at watershed scale. *J. Geophys. Res. Atmos.* 124, 11932–11943. doi:10.1029/2018jd030129

Wang, A., Su, B., Huang, J., Jing, C., Kundzewicz, Z. W., Tao, H., et al. (2023). Runoff components and the contributions of precipitation and temperature in a highly glacierized river basin in Central Asia. *Front. Earth Sci.* 17, 361–377. doi:10.1007/s11707-022-0995-0

Wang, C., Xu, J., Chen, Y., Bai, L., and Chen, Z. (2018). A hybrid model to assess the impact of climate variability on streamflow for an ungauged mountainous basin. *Clim. Dyn.* 50, 2829–2844. doi:10.1007/s00382-017-3775-x

Wang, N., Liu, W., Wang, H., Sun, F., Duan, W., Li, Z., et al. (2021). Improving streamflow and flood simulations in three headwater catchments of the Tarim River based on a coupled glacier-hydrological model. *J. Hydrology* 603, 127048. doi:10.1016/j.jhydrol.2021.127048

Wang, N., Sun, F. B., Wang, H., and Liu, W. B. (2022). Effects of cryospheric hydrological processes on future flood inundation and the subsequent socioeconomic exposures in Central Asia. *Environ. Res. Lett.* 17, 124020. doi:10.1088/1748-9326/aca491

Wortmann, M., Duethmann, D., Menz, C., Bolch, T., Huang, S., Jiang, T., et al. (2022). Projected climate change and its impacts on glaciers and water resources in the headwaters of the Tarim River, NW China/Kyrgyzstan. *Clim. Change* 171, 30. doi:10.1007/s10584-022-03343-w

Xiang, Y., Li, L., Chen, J., Xu, C.-Y., Xia, J., Chen, H., et al. (2019). Parameter uncertainty of a snowmelt runoff model and its impact on future projections of snowmelt runoff in a data-scarce deglaciating River Basin. *Water* 11, 2417. doi:10.3390/w11112417

Xiang, Y., Wang, Y., Chen, Y., and Zhang, Q. (2022). Impact of climate change on the hydrological regime of the yarkant River Basin, China: an assessment using three SSP scenarios of CMIP6 GCMs. *Remote Sens.* 14, 115. doi:10.3390/rs14010115

Xu, C., Zhao, J., Deng, H., Fang, G., Tan, J., He, D., et al. (2016). Scenario-based runoff prediction for the Kaidu River basin of the tianshan mountains, northwest China. *Environ. Earth Sci.* 75, 1126. doi:10.1007/s12665-016-5930-9

Xu, Z. X., Chen, Y. N., and Li, J. Y. (2004). Impact of climate change on water resources in the Tarim River basin. *Water Resour. Manag.* 18, 439–458. doi:10.1023/b:warm.0000049142.95583.98

Yang, P., Xia, J., Zhang, Y., Zhan, C., and Sun, S. (2019). How is the risk of hydrological drought in the Tarim River Basin, northwest China? *Sci. Total Environ.* 693, 133555. doi:10.1016/j.scitotenv.2019.07.361

Yao, J., Chen, Y., Guan, X., Zhao, Y., Chen, J., and Mao, W. (2022). Recent climate and hydrological changes in a mountain–basin system in Xinjiang, China. *Earth-Science Rev.* 226, 103957. doi:10.1016/j.earscirev.2022.103957

Zhang, F., Li, L., and Ahmad, S. (2017). "Streamflow pattern variations resulting from future climate change in middle Tianshan Mountains region in China," in *World environmental and water resources congress 2017* (Reston, VA: American Society of Civil Engineers), 437–446.

Zhang, S., Gao, X., Zhang, X., and Hagemann, S. (2012). Projection of glacier runoff in yarkant River basin and beida River basin, western China. *Hydrol. Process.* 26, 2773–2781. doi:10.1002/hyp.8373

Zhang, X., Chen, Y., Fang, G., Xia, Z., Yang, Y., Duan, W., et al. (2022). Future changes in extreme precipitation from 1.0 °C more warming in the Tienshan Mountains, Central Asia. *J. Hydrology* 612, 128269. doi:10.1016/j.jhydrol.2022.128269

Zhao, B., Sun, H., Yan, D., Wei, G., Tuo, Y., and Zhang, W. (2021). Quantifying changes and drivers of runoff in the Kaidu River Basin associated with plausible climate scenarios. *J. Hydrology Regional Stud.* 38, 100968. doi:10.1016/j.ejrh.2021.100968

Zhao, H., Su, B., Lei, H., Zhang, T., and Xiao, C. (2023). A new projection for glacier mass and runoff changes over High Mountain Asia. *Sci. Bull.* 68, 43–47. doi:10.1016/j.scib.2022.12.004

frontiers | Frontiers in Environmental Science

TYPE Original Research
PUBLISHED 22 January 2024
DOI 10.3389/fenvs.2023.1294456

OPEN ACCESS

EDITED BY
Hainan Gong,
Chinese Academy of Sciences (CAS), China

REVIEWED BY
Debashis Nath,
Sun Yat-sen University, Zhuhai Campus, China
Gorica Stanojević,
Geographical Institute Jovan Cvijić, Serbian Academy of Sciences and Arts, Serbia

*CORRESPONDENCE
Md Adilur Rahim,
mrahim6@lsu.edu

RECEIVED 14 September 2023
ACCEPTED 15 December 2023
PUBLISHED 22 January 2024

CITATION
Rahim MA, Rohli RV, Mostafiz RB, Bushra N and Friedland CJ (2024), Historical global and regional spatiotemporal patterns in daily temperature.
Front. Environ. Sci. 11:1294456.
doi: 10.3389/fenvs.2023.1294456

Historical global and regional spatiotemporal patterns in daily temperature

Md Adilur Rahim[1,2,3]*, Robert V. Rohli[4,3], Rubayet Bin Mostafiz[2,4,3], Nazla Bushra[4,5] and Carol J. Friedland[2,3]

[1]Engineering Science Program, Louisiana State University, Baton Rouge, LA, United States, [2]LaHouse Research and Education Center, Department of Biological and Agricultural Engineering, Louisiana State University Agricultural Center, Baton Rouge, LA, United States, [3]Coastal Studies Institute, Louisiana State University, Baton Rouge, LA, United States, [4]Department of Oceanography and Coastal Sciences, Louisiana State University, Baton Rouge, LA, United States, [5]Department of Geoscience, University of North Alabama, Florence, AL, United States

The abrupt increase in surface air temperature over the last few decades has received abundant scholarly and popular attention. However, less attention has focused on the specific nature of the warming spatially and seasonally, using high-resolution reanalysis output based on historical temperature observations. This research uses the European Centre for Medium-range Weather Forecasts (ECMWF) Reanalysis Version 5 (ERA5) output to identify spatiotemporal features of daily mean surface air temperature, defined both as the mean of the maximum and minimum temperatures over the calendar day ("meanmaxmin") and as the mean of the 24 hourly observations per day ("meanhourly"), across the terrestrial Earth. Results suggest temporal warming throughout the year, with several "hot spots" of significantly increasing temperature, including in the Arctic transition seasons, Northern Hemisphere mid-latitudes in July, Eurasia in spring, Europe and the lower latitudes in summer, and tropical autumn. Cooling is also observed, but generally at rates more likely to be statistically insignificant than warming rates. These trends are nearly identical regardless of whether calculated as "meanmaxmin" or "meanhourly." These results may assist scientists and citizens to understand more fully observed agricultural, commercial, ecological, economic, and recreational trends in light of climate change considerations.

KEYWORDS

global climate change, global warming, ERA5 land skin temperature, regional climate anomalies, seasonal temperature change

1 Introduction

Many lines of evidence suggest that globally-averaged surface air temperature has increased over the last several decades. However, many details about the spatio-seasonal properties of these trends remain unknown, either because recent such studies focus on the local to regional scale, such as for China (Yiqi et al., 2023) and Latvia (Kalvāns et al., 2023), or even the hemispheric scale (Deng and Fu, 2023), or because global-scale studies tend to examine annual trends (e.g., Lindsey and Dahlma, 2020). Distribution within the day-night cycle of that long-term temperature trend has remained uncharacterized holistically using long-term, high-resolution data collected within the Satellite Era.

The objective of this manuscript is to examine the global trend using a current reanalysis data set and then to elucidate the regionality of the daily temperature trends by month across

the terrestrial Earth. To identify whether the method of calculating the daily trend influences the results, we calculate daily means by averaging the daily maximum and minimum values, and also by considering "daily" as the mean of the 24 hourly values. This approach will strengthen our knowledge of the extent to which nuances in the calculation method influence the regionality and monthly distribution of the temperature trends.

Four hypotheses regarding the daily mean surface air temperature over the terrestrial Earth are tested. The first is that the method of calculating daily mean temperature (i.e., "meanmaxmin" vs. "meanhourly") produces statistically significantly different temperatures. Testing this hypothesis is important because it has long been recognized that maximum and minimum temperatures change asymmetrically, with minimum temperature often changing more substantially than the maximum (Karl et al., 1993). The next two are that a linear temporal trend exists in the global annual mean temperature, and in the global monthly mean temperatures for each of the 12 months, for the Earth as a whole. These hypotheses are important to test again for the post-Satellite Era, now that more updated data and data sets are available. The fourth hypothesis is inspired by the comments of Michaels and Stooksbury (1992) about the importance of the regionality and seasonality of the warming; we hypothesize that the temporal trend is not uniform spatially by month.

2 Background

A rapid increase in research on the globally increasing trend in observed surface air temperature had begun by the latter part of the 20th century. For example, after correcting for inconsistencies in the temperature record due to instrumental inaccuracies, non-uniform measurement techniques, changes in spatial coverage, and irregularity in time and location of the measurements, Jones et al. (1986) detected a long-term warming trend at a monthly scale from 1861 to 1984, with the three warmest years in the 1980s. In an analysis of annual time series from 1854 to 1988, Ghil and Vautard (1991) found an insignificant surface air temperature trend until 1910 and an increase of 0.4C° afterwards, with some inter-annual and inter-decadal oscillations due to the El Niño-Southern Oscillation (ENSO) phenomenon (Rasmusson et al., 1990) and extratropical ocean circulation (Bjerknes, 1964). Liebmann et al. (2010) identified a similar trend over the 1850 to 2009 time series.

With the availability of 30 years of air temperature data measured during the Satellite Era came more robust and precise global temperature climatologies. For example, in examining global temperature data from 1979 to 2010 from surface and satellite records, Foster and Rahmstorf (2011) found steady statistically significant warming trends ranging from 0.014 to 0.018°C per year for five global data sets, after discarding short-term variability, with the warmest 2 years at the end of the data series. Several studies during this era offered suggestions for attribution, including predominantly anthropogenic (Lean and Rind, 2008), anthropogenic with some impact of solar forcing (Wild et al., 2007), multidecadal variability associated with strengthening of the global thermohaline circulation and some impact from greenhouse gas accumulation (Wu et al., 2007; Wu et al., 2011), sea surface temperatures associated particularly with the Pacific decadal variability pattern (Wang et al., 2009), the Atlantic meridional overturning circulation (Keenlyside et al., 2008; Semenov et al., 2010; DelSole et al., 2011), and a combination of the above effects (Swanson et al., 2009).

The increasing availability of high-resolution observational and proxy and climate model output further enhanced global air temperature trend analysis spatially and temporally. For example, Marcott et al. (2013) quantified the global temperature trends since the last deglaciation, including the relatively warm mid-Holocene, subsequent cooling of approximately 0.7°C over the next 5,000 years into the Little Ice Age, and abrupt and steady warming since that time, with a global mean temperature today exceeding that during 90 percent of the Holocene. Marotzke and Forster (2015) identified discrepancies between the climate model output, which showed a significant long-term temperature increase from 1900 to 2012, and the observational data, which includes a hiatus in the increasing trend. Using a combination of observations, global climate model simulations, and proxy evidence, Hawkins et al. (2017) found that 1986–2005 was likely 0.55–0.80°C warmer globally than preindustrial times. Variability of temperature about the long-term warming trend has also been a focus area in recent years. Climate model ensembles suggest that equilibrium climate sensitivity (ECS), defined as the change in temperature after atmospheric CO_2 instantly doubles and equilibrium is reached (Meraner et al., 2013), is between 2.3 and 4.7°C at a 95% confidence interval (Sherwood et al., 2020), with a central estimate at 2.8°C (Cox et al., 2018), but possibly even greater (Zelinka et al., 2020), though Scafetta (2022) suggested that it could be lower. In addition to evaluating the increasing global temperature trend, climate modeling has projected future air temperature trends under different climate scenarios (Collins et al., 2013). Similarly, many analyses of terrestrial surface air temperature have been conducted in the last few years (e.g., Toreti and Desiato, 2008; You et al., 2010; Jain & Kumar, 2012; Saboohi et al., 2012; Ji et al., 2014; Sato and Robeson, 2014; Deniz and Gönençgil, 2015; Dong et al., 2015; Gonzalez-Hidalgo et al., 2015; Mondal et al., 2015; Chattopadhyay and Edwards, 2016; Ahmadi et al., 2018; Asfaw et al., 2018; Ghasemifar et al., 2020; Matewos and Tefera, 2020; Miheretu, 2021), but of these, only Ji et al. (2014) worked at the global scale. While many other studies (e.g., Intergovernmental Panel on Climate Change, (2021) and the many references contained within it) assert that the near-surface atmosphere is warming, few recent studies consider the details of the spatial distribution of that warming globally, at fine spatio-temporal resolution.

Models have generated data sets that have been used to analyze temperature and other variables globally. Much of this work has used the first-generation National Center for Atmospheric Research Reanalysis product (Kalnay et al., 1996). More recent efforts have used the second generation products (Kanamitsu et al., 2002), which improved the spatial resolution from 5° to 2.5° for results since the Satellite Era began in 1979. Data sets with much greater spatial resolution have also been developed based on interpolation techniques. Hijmans et al. (2005) produced an impressive early data set available at 1-km resolution, for the terrestrial Earth. The National Centers for Environmental Prediction (NCEP) developed the NCEP Climate Forecast System Reanalysis (CFSR) to emphasize the coupled atmosphere-ocean-land surface-sea ice system, at 38-km spatial resolution and 64 atm levels, with 40 levels at resolution of 0.5° or finer (Saha et al., 2010). NASA's Famine Early Warning Systems Network (FEWS NET) Land Data Assimilation System (FLDAS; McNally et al., 2017) is available at a spatial resolution of 0.1 × 0.1 from 1982 to present. Other highly respected data sets include ECOCLIMAP-V1 (Masson et al., 2003), Global Precipitation

Climatology Centre (Schneider et al., 2017), WorldClim 2.0 (Fick and Hijmans, 2017), and ENACTS (International Research Institute for Climate and Society, 2017). The Japanese 55-year Reanalysis Project (JRA-55; Japan Meteorological Agency, 2014) has also been important for understanding historical temperature trends globally. Rohli et al. (2019) summarized several key features of JRA-55, as described by Kobayashi (2016), including: 1) length and completeness of the time series for full observing system reanalysis using the most advanced data assimilation scheme, 2) incorporation of several new observational data sets, 3) introduction of a new radiation scheme, 4) improvements offered by variational bias correction over the previous iteration (JRA-25), and 5) availability of companion data sets that permit the assessment of the impact of data assimilation.

A recent addition to the global reanalysis data sets is the European Centre for Medium-range Weather Forecasts (ECMWF) Reanalysis Version 5 (ERA5; Copernicus Climate Change Service (C3S), 2019). ERA5 provides benefits that originated in its predecessor (ERA-Interim reanalysis; Dee et al., 2011) which include improved model physics, core dynamics, and data assimilation (Hersbach et al., 2020). This data set has already been used in a wide range of atmospheric and environmental research. Recent studies have reported that ERA5 generally corresponds well to surface temperature observations in East Africa (Gleixner et al., 2020) and Antarctica (Zhu et al., 2021). Yang et al. (2022) found overall improved performance for ERA5 and 20th Century Reanalysis version 3 (20CRv3; Slivinski et al., 2019) over other reanalysis data sets. Of course, it should be remembered that these reanalysis data sets, including the ERA5, are indeed model output themselves, drawn from a wide array of input data.

3 Materials and methods

Hourly air temperature at 2 m above the terrestrial surface is collected from the ERA5 output for the period 1 January 1981 to 31 December 2020, at a resolution of 0.1 × 0.1 (or approximately 11.1 km at the equator). This data set is compiled from NetCDF files, resulting in an array of 365.25 × 24 × 40 temperature values for each of the 2,212,863 grid points located over land. The mean daily temperature is then calculated, by grid point, in two separate ways: first, as the mean of the maximum and minimum values on a calendar day ("meanmaxmin"), and second, as the mean of the 24 hourly observations ("meanhourly"). The time series of monthly mean global temperatures, calculated from the daily means, is then computed using both the meanmaxmin and meanhourly approaches. A statistically significant difference in the temperature distributions indicates that both approaches should be used in testing the hypotheses.

Differences in local time infer that the daily temperature value for a given calendar day at a given grid point is actually based partially on values for the calendar day before or after the reported value, except for grid points within the Greenwich mean time zone. Increasing offset from Greenwich mean time corresponds to less overlap of the hourly, and therefore daily, meanmaxmin, and meanhourly values with that of the calendar day. No adjustment is made for this inconsistency, as it creates no complication for the hypothesis testing.

Testing of each hypothesis requires investigation of linear temporal trends. To avoid relying on assumptions of normality of the distribution, serial independence, and long time series, non-parametric tests of serial randomness in the form of rank correlation methods are appropriate and robust (Mitchell et al., 1966). The Mann-Kendall test (Mann, 1945; Kendall, 1948; Kendall, 1995) and the synonymous (Qian et al., 2015) Şen's estimator method (P.K. Şen, 1968; Z. Şen, 2012; 2014) have been useful for identifying the statistical significance of a linear trend in similar research (e.g., Mondal et al., 2012; Mahmood et al., 2019; Panda and Sahu, 2019; Sayyad et al., 2019; Yacoub and Tayfur, 2019; Alemu and Dioha, 2020; Bojago and YaYa, 2021; Chand et al., 2021). Likewise, Spearman's rank-order test for trend (Mitchell et al., 1966) is also widely used in similar work (Rahman et al., 2017), including on temperature trends (e.g., Yücel et al., 2019; Singh et al., 2021). Serra et al. (2001) noted that Spearman is generally more appropriate for large sample sizes with few tied ranks (although Mitchell et al. (1966) suggested that Spearman is more appropriate for handling tied ranks), and for data sets with non-monotonic trends (i.e., with multiple inflection points) in which the focus is on long-term trends rather than abrupt changes. Thus, the Spearman test is selected here over the Mann-Kendall test, but several time-series analyses in geophysical data sets (e.g., Yue et al., 2002; Kahya and Kalaycı, 2004; Rahman et al., 2017) have shown little difference in the results and power, defined as the probability of correctly rejecting a false null hypothesis (Villarini et al., 2009) in the two tests. Levels of significance of 0.05 and 0.10 are used to represent statistical significance for all trends.

In testing the first two hypotheses, if daily temperature from the 2,212,863 terrestrial grid points were simply averaged into a single global value for each calendar day, the convergence of meridians of longitude poleward would cause the 0.1°-spaced meridians to oversample the polar areas relative to the low latitudes. Thus, calculation of the global mean temperature annually and for each month (using both the meanmaxmin and meanhourly methods, separately) contains an extra step. Specifically, the mean terrestrial latitudinal temperature ($\bar{T}_i$), where i represents the latitude at 0.1° increments over the terrestrial Earth (i.e., from the South Pole (90°S) to 83.5°N), is multiplied by the cosine of its latitude, at each of the 0.1°-spaced parallels (separately). Then, these values are divided by the sum of the cosines of the latitudes to compute the global mean terrestrial temperature for that Julian day ($\bar{T}_G$) adjusted for the convergence of longitudes at the poles. Thus,

$$\bar{T}_G = \frac{\sum_{-90}^{83.5} (\bar{T}_i \cos i)}{\sum_{-90}^{83.5} (\cos i)}$$

Monthly aggregated maps comprised of averages of each of the $\bar{T}_G$ maps from that month, across the time series are shown here. In other work not shown here, the set of daily maps can be used to identify trends in finer detail.

The daily meanmaxmin- and meanhourly-adjusted $\bar{T}_G$ values are compared statistically (Hypothesis 1). The annual (Hypothesis 2) and monthly (Hypothesis 3) global terrestrial temperatures are then calculated for the two approaches. Thus, all 365 of the $\bar{T}_G$ values for a given calendar year (discarding leap days) are aggregated for a single annual global temperature (Hypothesis 2), and all 28, 30, or 31 $\bar{T}_G$ values for that month in a given calendar year are aggregated for a single monthly global temperature, for each of the 12 months (Hypothesis 3). Spearman tests for trend are run on the 40 data points (i.e., one data point per year) (Hypothesis 2), and for each of the 12 months of the year (Hypothesis 3).

For addressing the "regionality" component of Hypothesis 4, global terrestrial maps—one for each calendar month using the

TABLE 1 Globally-weighted mean daily temperature difference (°C), and absolute maximum and minimum temperature difference by gridpoint, by temperature-calculating algorithm (i.e., "meanmaxmin" minus "meanhourly") by month, 1981–2020.

	Average	Maximum	Minimum
Overall	0.20	1.56	−1.41
January	0.24	1.71	−1.40
February	0.24	1.71	−1.76
March	0.21	1.57	−1.94
April	0.18	1.65	−2.11
May	0.15	1.57	−2.02
June	0.16	1.60	−2.33
July	0.18	1.73	−2.10
August	0.20	1.97	−2.05
September	0.21	1.89	−1.66
October	0.21	1.85	−1.54
November	0.21	1.83	−1.63
December	0.23	1.73	−1.47

meanmaxmin and/or meanhourly approach—are produced. Maps for January, April, July, and October are shown here to represent the four meteorological seasons (Trenberth, 1983). Maps showing the Theil-Sen slope (°C yr^{-1}), areas with *p*-values surpassing the significance threshold, and temperature (°C) difference (2011–2020 mean minus 1981–1990 mean) are shown. For each grid point, the values are calculated based on the 365 × 40 daily mean values compiled from the hourly values. No temperature correction is necessary for these collections of point-specific calculations. The "seasonality" component of Hypothesis 4 is also assessed cartographically.

4 Results and discussion

Testing Hypothesis 1—that the meanmaxmin and meanhourly calculations yield different results—requires the non-parametric Wilcoxon signed rank test, because the time series of mean monthly temperatures compiled from both approaches are found to be distributed non-normally. Wilcoxon testing reveals that globally, the meanmaxmin temperature significantly exceeds the meanhourly temperature (*p*-value <<0.05), with a mean difference of 0.20°C. This result aligns with those of Weiss and Hays (2005), who found similar differences between means produced by these two methods. Global mean differences between the two algorithms by month are shown in Table 1.

Moreover, the temperature differences as calculated by the two algorithms vary spatially, as was also found by Weiss and Hays. In most of the world, particularly the Americas and equatorial Africa, the meanmaxmin approach yields the higher temperatures, while in most of northern Africa, the Arabian Peninsula, and central Asia, the opposite is true. Nevertheless, the most extreme difference in the mean temperature calculation at individual places is less than 0.2°C (Figure 1).

Figure 2 shows these differences using January, April, July, and October as representative of the four seasons, and Supplementary Figure S1 shows the differences for the remaining 8 months. The meanmaxmin-calculated temperature exceeds meanhourly by the greatest amounts in the Americas in April (Figure 2B), and equatorial Africa in April and July (Figures 2B,C), while meanhourly exceeds meanmaxmin in much of northern Africa and Eurasia throughout the year (Figure 2 and Supplementary Figure S1).

Testing of Hypothesis 2 reveals that regardless of whether the meanmaxmin or meanhourly approach is used a linearly increasing trend (Spearman r of 0.861 (p << 0.001) and 0.866 (p << 0.001)) exists

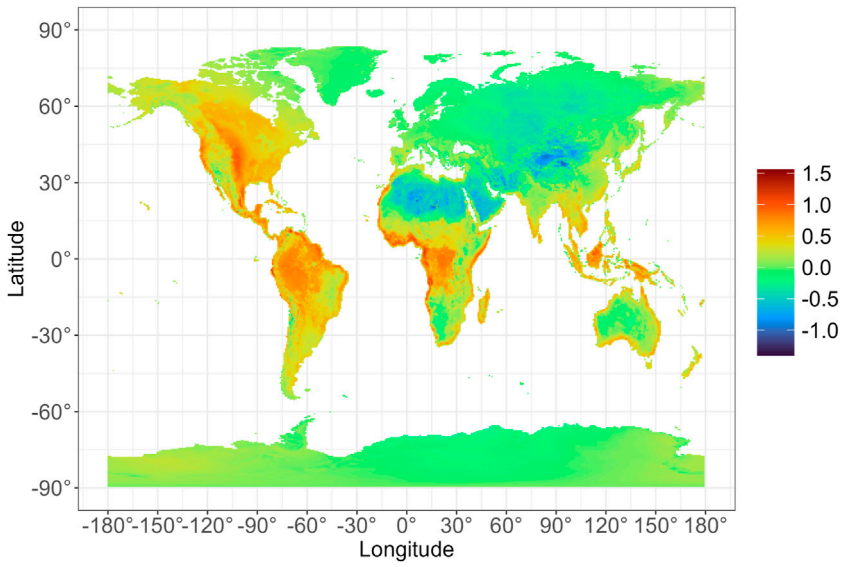

FIGURE 1
Spatial distribution of the daily mean temperature (°C) difference (meanmaxmin minus meanhourly), 1981–2020.

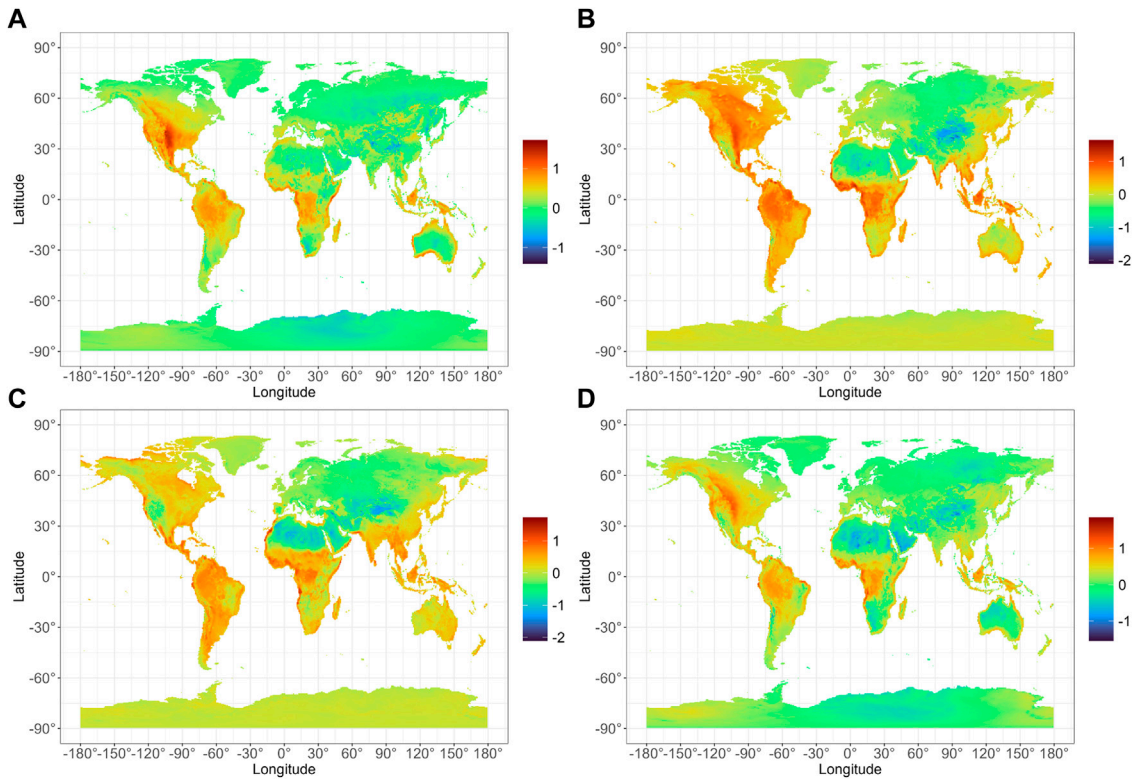

FIGURE 2
As in Figure 1, except for January **(A)**, April **(B)**, July **(C)**, and October **(D)**, over the 1981–2020 period.

TABLE 2 Spearman correlations and corresponding Theil-Şen slopes for each of the methods of calculating global temporal trends in surface air temperature, 1981–2020.

	Meanmaxmin		Meanhourly	
	Spearman r	Theil-Şen estimator (i.e., slope) (°C yr^{-1})	Spearman r	Theil-Şen estimator (i.e., slope) (°C yr^{-1})
Overall	0.861	0.026	0.866	0.027
January	0.730	0.023	0.729	0.023
February	0.607	0.025	0.613	0.025
March	0.734	0.027	0.743	0.028
April	0.781	0.025	0.792	0.026
May	0.779	0.023	0.798	0.024
June	0.807	0.025	0.805	0.025
July	0.758	0.024	0.766	0.024
August	0.808	0.022	0.818	0.023
September	0.880	0.029	0.889	0.030
October	0.893	0.032	0.897	0.033
November	0.805	0.030	0.809	0.030
December	0.704	0.023	0.700	0.023

*All Spearman correlations are statistically significant at $p < 0.001$.

in the air temperatures. Hypothesis 3 is confirmed, with the Spearman tests revealing statistically significantly increasing trends ($p << 0.001$) in each of the 12 months, regardless of whether the meanmaxmin or meanhourly approach is used. The Theil-Şen slope (Akritas et al., 1995) suggests that the rate of temperature increase ranges from 0.022°C yr^{-1} (August) to 0.033°C yr^{-1} (October), as shown in (Table 2).

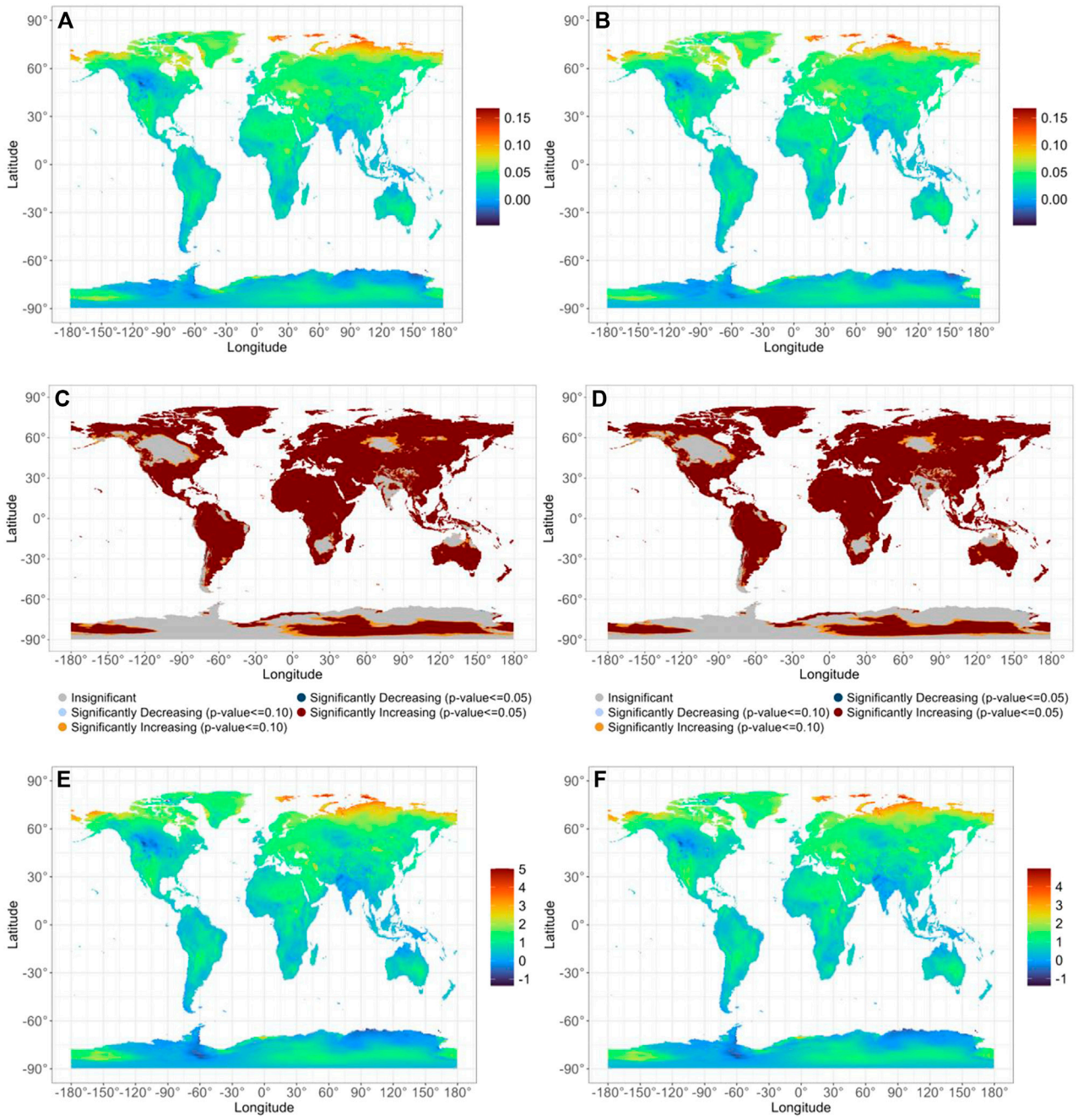

FIGURE 3
Surface air temperature trends **(A,B)** using the Theil-Şen slope (°C yr^{-1}), statistical significance at $p \leq 0.05$ **(C,D)**, and temperature (°C) difference (2011–2020 mean minus 1981–1990 mean **(E,F)**), for meanmaxmin **(A,C,E)** and meanhourly (b, d, and **(F)** approaches.

Regarding the "regionality" aspect of Hypothesis 4, spatial distributions of the rate of annual temperature increase (°C yr^{-1}), as evidenced by the Theil-Şen slope, level of significance, and the absolute temperature increase from the 1981–1990 mean to 2011–2020 mean, are shown in Figure 3, for the meanmaxmin and meanhourly calculations in a side-by-side comparison. Nearly identical results appear for the two approaches, despite previous evidence for the influence of air mass type on the shape of the daily temperature curve (Bernhardt, 2020). Most of the terrestrial Earth is warming at a rate exceeding 0.05°C yr^{-1} with the steepest rates approaching 0.15°C yr^{-1} in the Arctic (Figures 3A,B). Some areas, such as Antarctica, the Indian Subcontinent, inland northern North America, and northern Australia, are cooling, but mostly at rates of 0.05°C yr^{-1} or less (Figures 3A,B). Most of the warming is statistically significant, while nearly all cooling is statistically insignificant (Figures 3C,D). Regardless, however, the absolute value of the temperature change from the 1981–1990 mean to the 2011–2020 mean is less than 2°C (Figures 3E,F).

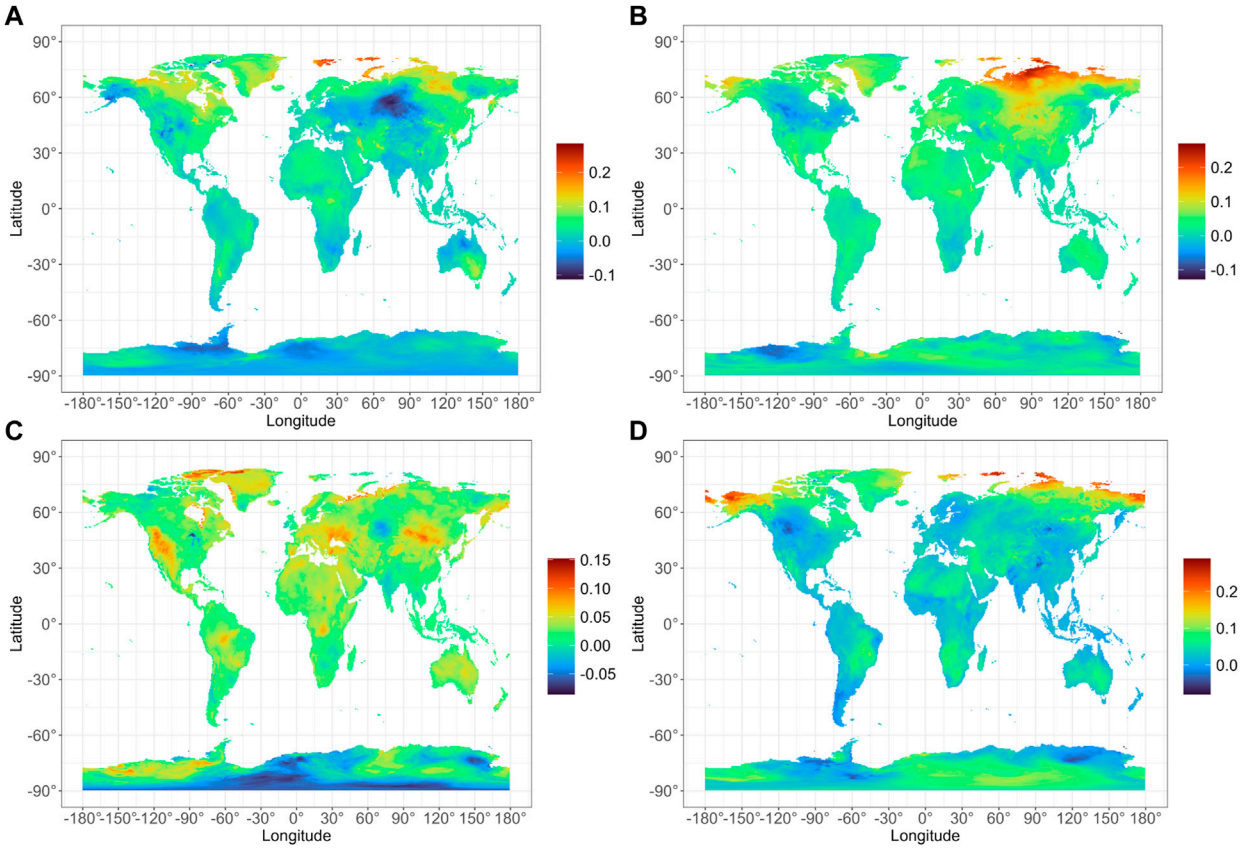

FIGURE 4
Rate of surface air temperature increase using the Theil-Şen slope (°C yr^{-1}), for January **(A)**, April **(B)**, July **(C)**, and October **(D)**, over the 1981–2020 period, using the "meanhourly" approach.

Because the spatial patterns shown in Figure 3 are virtually identical for the two methods, results for the "seasonality" component of Hypothesis 4 are shown only for the "meanhourly" approach. Figures 4A–D shows the spatial distribution of the Theil-Şen slope (°C yr^{-1}) for January, April, July, and October, respectively, and those for the remaining months are shown in Supplementary Figure S2. The spatial distribution of statistical significance for those same 4 months across space is shown in Figures 5A–D, with that for the other 8 months shown in Supplementary Figure S3.

The spatial pattern of the temperature rate increase and significance of the temperature trends are similar to the overall patterns shown in Figures 3A–D, but with some additional, notable, monthly features. For instance, the Arctic warming rate is most prominently significant in the transition seasons (Figures 4B,D; Figures 5B,D, and Supplementary Figures S2B–D, F,G, Supplementary Figures S3B–D, F,G), with Arctic cooling prominent in eastern Siberia in February (Supplementary Figure S2A) though not as significant (Supplementary Figure S3A), and in northern North America in February and March (Supplementary Figures S2A,B) though again largely insignificant (Supplementary Figures S3A,B). In the Northern Hemisphere mid-latitudes, warming is most intense in July (Figure 4C and 5C) but not as prominent in the rest of summer (Supplementary Figures S2D,E, S3D,E). Other large, contiguous areas of statistically significant warming trends are in Eurasia in spring, Europe and the lower latitudes in summer, and the tropics in autumn (Figure 4, 5 and Supplementary Figures S2, S3). While data are sparse over the oceans, evidence from island stations indicates that significantly increasing trends also appear in the major ocean basins (Figure 4, 5).

The region of greatest decreasing temperatures is in Antarctica in summer and winter, by approximately 0.1°C yr^{-1} (Figures 4A,C, and Supplementary Figure S2) but these trends are largely statistically insignificant (Figures 5A,C and Supplementary Figure S3). Other largely statistically insignificant areas of cooling are concentrated over Eurasia in December and January, with some areas of cooling in southwest Asia in November.

The temperature change between the 1981–1990 and 2011–2020 means for January, April, July, and October is shown in Figure 6, with that for the other 8 months shown in Supplementary Figure S4. Again, the strongest warming appears over Arctic Asia, particularly in boreal spring, but with warming in extensive parts of Eurasia, Africa, and the Americas in boreal summer. Cooling appears most substantially in boreal spring in North America and Antarctica, and in boreal autumn in the

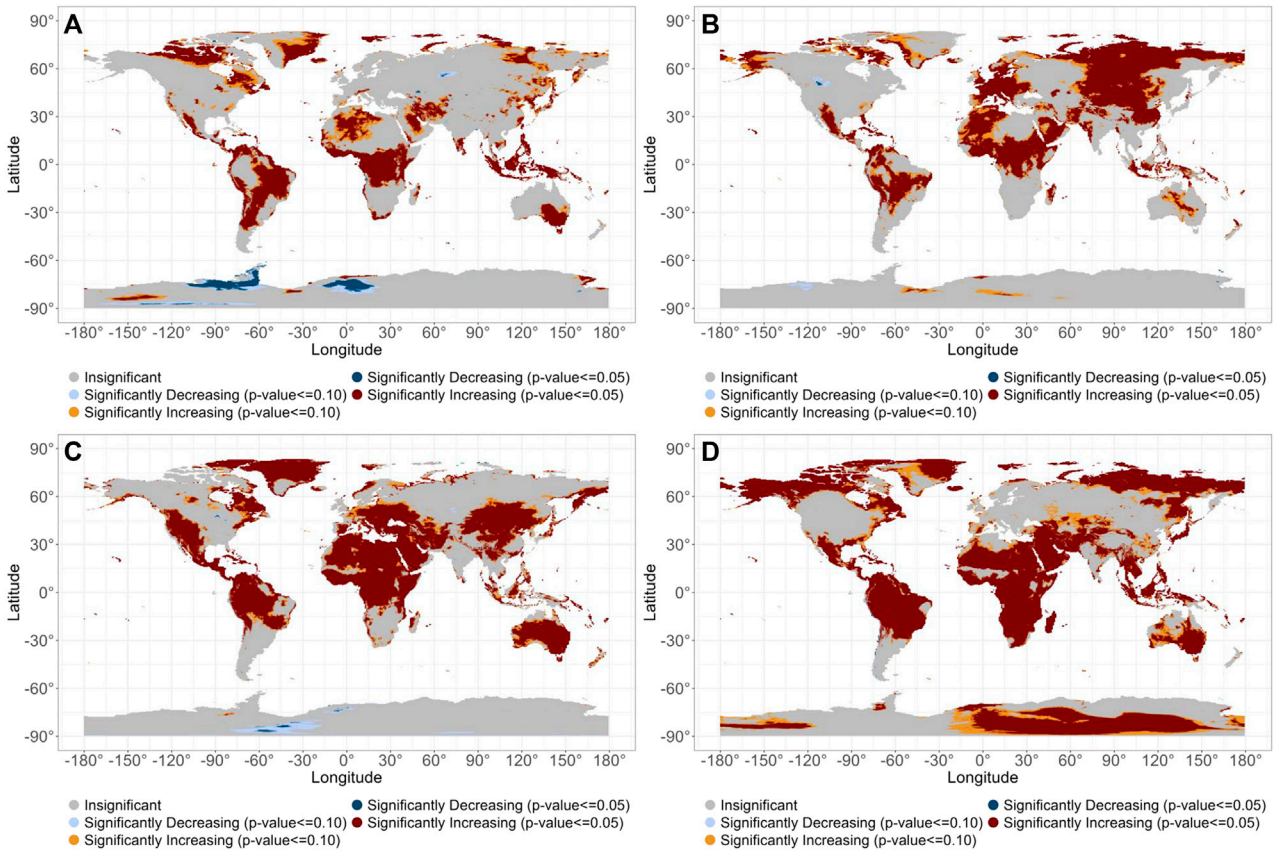

FIGURE 5
Statistical significance ($p < 0.05$) of Theil-Şen slope shown in Figure 2, for January **(A)**, April **(B)**, July **(C)**, and October **(D)**, over the 1981–2020 period, using the "meanhourly" approach.

Americas and much of Eurasia, Africa, and Antarctica, but again, these cooling trends are less substantial than the warming trends.

The globally-weighted terrestrial air temperature increases between the two averaging periods (1981–1990 vs. 2011–2020) for the meanhourly algorithm is 0.72°C by month. Scafetta (2022) found a 0.58°C increase globally (including oceans) for the 1980–1990 vs. 2011–2021 averaging periods using ERA5 data and reported similar differences using other datasets. For instance, use of UK Met Office Hadley Centre/Climatic Research Unit version 5.0.1.0 (HadCRUT5; Morice et al., 2021) revealed a difference of 0.58°C, and differences of 0.57°C, 0.52°C, 0.52°C, 0.59°C, and 0.56°C were observed using GISTEMP v4 (Lenssen et al., 2019), NOAAGlobalTemp v5 (Huang et al., 2020), HadCRUT4 (Morice et al., 2012), Berkeley Earth group (Rohde and Hausfather, 2020), and Japanese Meteorological Agency (Ishihara, 2006), respectively. A comparison of these results with ours suggests that the terrestrial Earth warmed more than the marine world.

Table 3 shows that the 2011–2020 period is warmer than the 1981–1990 decade in every month, on a globally-weighted average basis, with the greatest warming globally between the two averaging periods in October, followed by September and November, and the smallest increases in December and January. The reduced amount of warming in boreal winter is likely influenced by the lack of ice-albedo effect in the low latitudes, which occupies a large component of Earth's surface area.

5 Summary and conclusion

All too often, scientists and the lay public are more concerned with how much the world will warm rather than how it will warm. This research characterized the warming in terms of the geographical distribution and its seasonality, using recently-available, high-resolution ERA5 temperatures, synthesized from a wide array of data sources, and with the daily mean temperature calculated as the mean of the daily maximum and minimum temperature and as the mean of the 24 hourly observations throughout the day.

The first hypothesis—that the two methods of calculating daily mean temperature yield different temperature records—was partially confirmed. The meanmaxmin approach yields statistically significantly higher daily temperatures than the meanhourly, on a global basis, but with significant regionality. Northern Africa and central Eurasia actually show higher temperatures from the meanhourly calculation, with most of the rest of the world showing the opposite. However, the spatial distribution of statistical significance in spatiotemporal temperature trends resulting from the two approaches is similar. This result is important because the instrumental and modeling

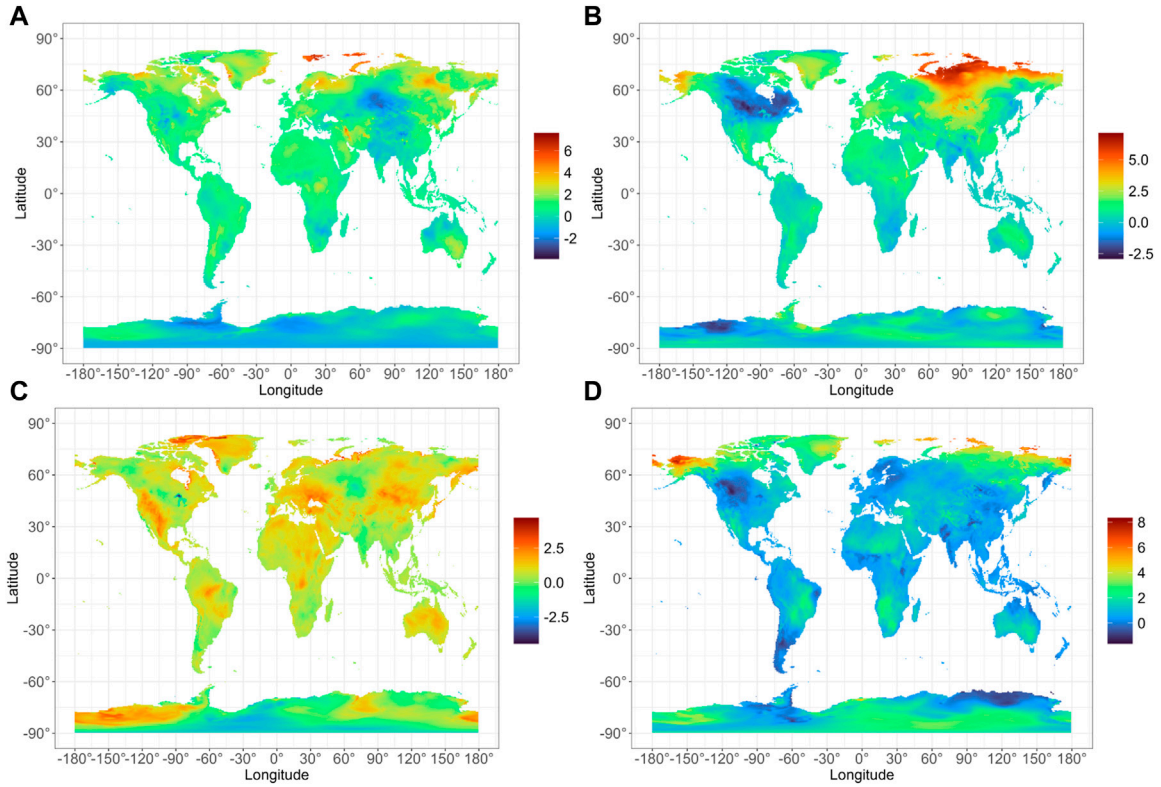

FIGURE 6
Temperature (°C) difference (2011–2020 mean minus 1981–1990 mean), for January **(A)**, April **(B)**, July **(C)**, and October **(D)**), using the "meanhourly" approach.

TABLE 3 Globally-weighted difference of means (°C) between the daily mean temperature for the 1981–1990 vs. 2011–2020 averaging periods, using the "meanhourly" algorithm, by month, with absolute maximum and minimum differences at individual grid points.

	Average	Maximum	Minimum
Overall	0.72	4.98	−1.38
January	0.64	7.62	−3.89
February	0.67	9.01	−4.63
March	0.74	8.94	−3.29
April	0.70	7.13	−2.91
May	0.66	4.11	−2.90
June	0.72	6.12	−4.96
July	0.67	4.70	−4.45
August	0.66	6.07	−4.20
September	0.82	5.90	−3.54
October	0.90	8.35	−1.64
November	0.78	9.71	−3.61
December	0.63	9.34	−4.12

capabilities that now permit the computation of the mean daily temperature based on data collected throughout the day may not create as much of a step change in apparent spatial distribution of the warming signal as might be assumed, despite the fact that the terrestrial temperatures tend to be higher when daily mean temperatures are calculated as the mean of the daily maximum and minimum values, except in northern Africa and central Eurasia. While the meanmaxmin or meanhourly approach yield the same spatial patterns, the meanhourly method might be considered to be more accurate because of its additional number of hours in the calculation. However, researchers selecting this method should acknowledge that its use yields higher temperatures in northern Africa and central Eurasia and lower temperatures elsewhere across the terrestrial Earth. Regardless, it is cautioned that all of the results herein may occur at least in part because of the processing algorithms in the ERA5 output.

The second and third hypotheses—that spatially-weighted global terrestrial mean daily temperature values display significantly increasing trends in the annual cycle and in each month of the year—was also confirmed. Global terrestrial temperatures have increased from 1981 to 2020, by approximately 0.026°C yr^{-1}, with a range of approximately 0.022°C yr^{-1} in August to about 0.033°C yr^{-1} in October. These terrestrial trends are likely dominating the global temperature trend that are frequently reported.

The fourth hypothesis—that the warming is uneven geographically—was also confirmed. Several "hot spots" of particularly high concentrations of grid points reported significantly increasing temperature trends. The strongest concentrations of warming are in the transition seasons in the Arctic, in July in the Northern Hemisphere mid-latitudes, and in Eurasia in spring, Europe and the lower latitudes in summer, and the tropics in autumn. Cooling has occurred in some places at some times of the year, but in general, cooling rates are more likely to be statistically insignificant than warming rates.

Future research should be conducted to attribute causes to the observed concentrations of changing temperatures based on atmospheric and oceanic circulation-based forcing. Continuing research using the most current and updated data will shed new light on an environmental situation that is of keen and urgent interest not only to many natural scientists and social scientists, but also to stakeholders in the government and private sectors, and to the general public. It is hoped that future work would also address another limitation of this study by examining non-linear and cyclical temperature trends.

Furthermore, future research is needed to identify spatiotemporal trends in the third category of warming as described by Michaels and Stooksbury (1992)—the distribution of the warming in the day-night cycle. Such results would assist in identifying the main implications of the historical warming. Specifically, temporal increases to daily extreme minimum temperatures, typically observed in early morning hours, would have major implications on sectors such as agriculture (e.g., growing season length), entomology (e.g., insect proliferations), epidemiology (e.g., vector-borne illness), energy consumption (e.g., heating of buildings), and transportation (e.g., road and bridge closures due to ice). Likewise, any observed temporal increases to daily afternoon/maximum temperatures would likely impact human health (e.g., heat stroke), energy consumption (e.g., air conditioning), and agriculture (e.g., increased water demand and drought). Improved understanding of these primary weather/climate impacts will assist in planning for future impacts of extreme weather and climate.

Data availability statement

The original contributions presented in the study are included in the article/Supplementary Material, further inquiries can be directed to the corresponding author.

Author contributions

MR: Conceptualization, Data curation, Formal Analysis, Methodology, Supervision, Visualization, Writing–review and editing. RR: Conceptualization, Data curation, Methodology, Supervision, Validation, Writing–original draft. RM: Conceptualization, Data curation, Methodology, Supervision, Visualization, Writing–review and editing. NB: Conceptualization, Data curation, Investigation, Supervision, Writing–review and editing. CF: Project administration, Supervision, Writing–review and editing.

Funding

The author(s) declare financial support was received for the research, authorship, and/or publication of this article. The publication of this article was supported by the LSU AgCenter LaHouse Research and Education Center and subsidized by the LSU Libraries Open Access Author Fund.

Conflict of interest

The authors declare that the research was conducted in the absence of any commercial or financial relationships that could be construed as a potential conflict of interest.

Publisher's note

Supplementary material

The Supplementary Material for this article can be found online at: https://www.frontiersin.org/articles/10.3389/fenvs.2023.1294456/full#supplementary-material

References

Ahmadi, F., Nazeri Tahroudi, M., Mirabbasi, R., Khalili, K., and Jhajharia, D. (2018). Spatiotemporal trend and abrupt change analysis of temperature in Iran. *Meteorol. Appl.* 25 (2), 314–321. doi:10.1002/met.1694

Alemu, Z. A., and Dioha, M. O. (2020). Climate change and trend analysis of temperature: the case of Addis Ababa, Ethiopia. *Environ. Syst. Res.* 9 (1), 27–15. doi:10.1186/s40068-020-00190-5

Asfaw, A., Simane, B., Hassen, A., and Bantider, A. (2018). Variability and time series trend analysis of rainfall and temperature in northcentral Ethiopia: a case study in Woleka sub-basin. *Weather Clim. Extrem.* 19, 29–41. doi:10.1016/j.wace.2017.12.002

Bernhardt, J. (2020). Comparing daily temperature averaging methods: the role of synoptic climatology in determining spatial and seasonal variability. *Phys. Geogr.* 41 (3), 272–288. doi:10.1080/02723646.2019.1657332

Bjerknes, J. (1964). Atlantic air-sea interaction. *Adv. Geophys.* 10, 1–82. Elsevier. doi:10.1016/s0065-2687(08)60005-9

Bojago, E., and YaYa, D. (2021). Trend analysis of seasonal rainfall and temperature pattern in Damota Gale districts of Wolaita Zone, Ethiopia. *Res. Square* 2021, 454366. doi:10.21203/rs.3.rs-454366/v1

Chand, M. B., Bhattarai, B. C., Pradhananga, N. S., and Baral, P. (2021). Trend analysis of temperature data for the narayani river basin, Nepal. *Sci* 3 (1), 1. doi:10.3390/sci3010001

Chattopadhyay, S., and Edwards, D. R. (2016). Long-term trend analysis of precipitation and air temperature for Kentucky, United States. *Climate* 4 (1), 10. doi:10.3390/cli4010010

Collins, M., Knutti, R., Arblaster, J., Dufresne, J. L., Fichefet, T., Friedlingstein, P., et al. (2013). "Long-term climate change: projections, commitments and irreversibility," in *Climate change 2013-the physical science basis: contribution of working group I to the fifth assessment report of the intergovernmental panel on climate change* (Cambridge: Cambridge University Press), 1029–1136. Available at: https://researchmgt.monash.edu/ws/portalfiles/portal/154950020/153843133_oa.pdf.Last (Accessed September 6, 2022).

Copernicus Climate Change Service (C3S) (2019). C3S ERA5-land reanalysis. Available at: https://cds.climate.copernicus.eu/cdsapp#!/dataset/10.24381/cds.e2161bac.Last (Accessed September 6, 2022).

Cox, P. M., Huntingford, C., and Williamson, M. S. (2018). Emergent constraint on equilibrium climate sensitivity from global temperature variability. *Nature* 553 (7688), 319–322. doi:10.1038/nature25450

Dee, D. P., Uppala, S. M., Simmons, A. J., Berrisford, P., Poli, P., Kobayashi, S., et al. (2011). The ERA-Interim reanalysis: configuration and performance of the data assimilation system. *Q. J. R. Meteorological Soc.* 137 (656), 553–597. doi:10.1002/qj.828

DelSole, T., Tippett, M. K., and Shukla, J. (2011). A significant component of unforced multidecadal variability in the recent acceleration of global warming. *J. Clim.* 24 (3), 909–926. doi:10.1175/2010JCLI3659.1

Deng, Q., and Fu, Z. (2023). Regional changes of surface air temperature annual cycle in the Northern Hemisphere land areas. *Int. J. Climatol.* 43 (5), 2238–2249. doi:10.1002/joc.7972

Deniz, Z. A., and Gönençgil, B. (2015). Trends of summer daily maximum temperature extremes in Turkey. *Phys. Geogr.* 36 (4), 268–281. doi:10.1080/02723646.2015.1045285

Dong, D., Huang, G., Qu, X., Tao, W., and Fan, G. (2015). Temperature trend–altitude relationship in China during 1963–2012. *Theor. Appl. Climatol.* 122 (1–2), 285–294. doi:10.1007/s00704-014-1286-9

Fick, S. E., and Hijmans, R. J. (2017). WorldClim 2: new 1-km spatial resolution climate surfaces for global land areas. *Int. J. Climatol.* 37 (12), 4302–4315. doi:10.1002/joc.5086

Foster, G., and Rahmstorf, S. (2011). Global temperature evolution 1979–2010. *Environ. Res. Lett.* 6 (4), 044022. doi:10.1088/1748-9326/6/4/044022

Ghasemifar, E., Farajzadeh, M., Mohammadi, C., and Alipoor, E. (2020). Long-term change of surface temperature in water bodies around Iran–Caspian Sea, Gulf of Oman, and Persian Gulf–using 2001–2015 MODIS data. *Phys. Geogr.* 41 (1), 21–35. doi:10.1080/02723646.2019.1618231

Ghil, M., and Vautard, R. (1991). Interdecadal oscillations and the warming trend in global temperature time series. *Nature* 350 (6316), 324–327. doi:10.1038/350324a0

Gleixner, S., Demissie, T., and Diro, G. T. (2020). Did ERA5 improve temperature and precipitation reanalysis over East Africa? *Atmosphere* 11 (9), 996. doi:10.3390/atmos11090996

Gonzalez-Hidalgo, J. C., Peña-Angulo, D., Brunetti, M., and Cortesi, N. (2015). MOTEDAS: a new monthly temperature database for mainland Spain and the trend in temperature (1951–2010). *Int. J. Climatol.* 35 (15), 4444–4463. doi:10.1002/joc.4298

Hawkins, E., Ortega, P., Suckling, E., Schurer, A., Hegerl, G., Jones, P., et al. (2017). Estimating changes in global temperature since the preindustrial period. *Bull. Am. Meteorological Soc.* 98 (9), 1841–1856. doi:10.1175/BAMS-D-16-0007.1

Hersbach, H., Bell, B., Berrisford, P., Hirahara, S., Horányi, A., Muñoz-Sabater, J., et al. (2020). The ERA5 global reanalysis. *Q. J. R. Meteorological Soc.* 146 (730), 1999–2049. doi:10.1002/qj.3803

Hijmans, R. J., Cameron, S. E., Parra, J. L., Jones, P. G., and Jarvis, A. (2005). Very high resolution interpolated climate surfaces for global land areas. *Int. J. Climatol.* 25 (15), 1965–1978. doi:10.1002/joc.1276

Huang, B., Menne, M. J., Boyer, T., Freeman, E., Gleason, B. E., Lawrimore, J. H., et al. (2020). Uncertainty estimates for sea surface temperature and land surface air temperature in NOAAGlobalTemp version 5. *J. Clim.* 33 (4), 1351–1379. doi:10.1175/JCLI-D-19-0395.1

Intergovernmental Panel on Climate Change (2021). in *Climate change 2021:* the physical science basis. Contribution of working group I to the sixth assessment Report of the intergovernmental Panel on climate change. Editors V. Masson-Delmotte, P. Zhai, A. Pirani, S. L. Connors, C. Péan, S. Berger, et al. (Cambridge, United Kingdom and New York, NY, USA: Cambridge University Press). doi:10.1017/978100915789623 91

International Research Institute for Climate and Society (2017). Enhancing national climate services initiative. Available at: http://iri.columbia.edu/resources/enacts (Accessed September 6, 2022).

Ishihara, K. (2006). Calculation of global surface temperature anomalies with COBE-SST. *Weather Serv. Bull.* 73, S19–S25.

Jain, S. K., and Kumar, V. (2012). Trend analysis of rainfall and temperature data for India. *Curr. Sci.* 102 (1), 37–49.

Japan Meteorological Agency (2014). JRA-55: Japanese 55-year reanalysis, monthly means and variances. Research data archive at the national center for atmospheric research, computational and information systems laboratory. Available at: https://doi.org/10.5065/D60G3H5B (Accessed September 6, 2022).

Ji, F., Wu, Z., Huang, J., and Chassignet, E. P. (2014). Evolution of land surface air temperature trend. *Nat. Clim. Change* 4 (6), 462–466. doi:10.1038/NCLIMATE2223

Jones, P., Wigley, T., and Wright, P. (1986). Global temperature variations between 1861 and 1984. *Nature* 322 (6078), 430–434. doi:10.1038/322430a0

Kahya, E., and Kalaycı, S. (2004). Trend analysis of streamflow in Turkey. *J. Hydrology* 289 (1–4), 128–144. doi:10.1016/j.jhydrol.2003.11.006

Kalnay, E., Kanamitsu, M., Kistler, R., Collins, W., Deaven, D., Gandin, L., et al. (1996). The NCEP/NCAR 40-year reanalysis project. *Bull. Am. Meteorological Soc.* 77 (3), 437–471. doi:10.1175/1520-0477(1996)077<0437:TNYRP>2.0.CO;2

Kalvāns, A., Kalvāne, G., Zandersons, V., Gaile, D., and Briede, A. (2023). Recent seasonally contrasting and persistent warming trends in Latvia. *Theor. Appl. Climatol.* 2023, 1–15. doi:10.1007/s00704-023-04540-y

Kanamitsu, M., Ebisuzaki, W., Woollen, J., Yang, S. K., Hnilo, J. J., Fiorino, M., et al. (2002). NCEP-DOE AMIP-II reanalysis (R-2). *Bull. Am. Meteorological Soc.* 83 (11), 1631–1644. doi:10.1175/BAMS-83-11-1631

Karl, T. R., Jones, P. D., Knight, R. W., Kukla, G., Plummer, N., Razuvayev, V., et al. (1993). A new perspective on recent global warming: asymmetric trends of daily maximum and minimum temperature. *Bull. Am. Meteorological Soc.* 74 (6), 1007–1023. doi:10.1175/1520-0477(1993)074<1007:ANPORG>2.0.CO;2

Keenlyside, N. S., Latif, M., Jungclaus, J., Kornblueh, L., and Roeckner, E. (2008). Advancing decadal-scale climate prediction in the North Atlantic sector. *Nature* 453 (7191), 84–88. doi:10.1038/nature06921

Kendall, M. G. (1948). *Rank correlation methods*. New York: Hafner.

Kendall, M. G. (1995). *Rank correlation methods*. 4th edition. London: Charles Griffin.

Kobayashi, S. (2016). The climate data guide: JRA-55. Available at: https://climatedataguide.ucar.edu/climate-data/jra-55 (Accessed August 18, 2016).

Lean, J. L., and Rind, D. H. (2008). How natural and anthropogenic influences alter global and regional surface temperatures: 1889 to 2006. *Geophys. Res. Lett.* 35 (18), L18701. doi:10.1029/2008GL034864

Lenssen, N. J., Schmidt, G. A., Hansen, J. E., Menne, M. J., Persin, A., Ruedy, R., et al. (2019). Improvements in the GISTEMP uncertainty model. *J. Geophys. Res. Atmos.* 124 (12), 6307–6326. doi:10.1029/2018JD029522

Liebmann, B., Dole, R. M., Jones, C., Bladé, I., and Allured, D. (2010). Influence of choice of time period on global surface temperature trend estimates. *Bull. Am. Meteorological Soc.* 91 (11), 1485–1492. doi:10.1175/2010BAMS3030.1

Lindsey, R., and Dahlma, L. (2020). Climate change: global temperature. Climate.gov 16. Available at: https://www.climate.gov/news-features/understanding-climate/climate-change-global-temperature.

Mahmood, G. G., Rashid, H., Anwar, S., and Nasir, A. (2019). Evaluation of climate change impacts on rainfall patterns in Pothohar region of Pakistan. *Water Conservation Manag.* 3 (1), 01–06. doi:10.26480/wcm.01.2019.01.06

Mann, H. B. (1945). Nonparametric tests against trend. *Econometrica* 13 (3), 245–259. doi:10.2307/1907187

Marcott, S. A., Shakun, J. D., Clark, P. U., and Mix, A. C. (2013). A reconstruction of regional and global temperature for the past 11,300 years. *Science* 339 (6124), 1198–1201. doi:10.1126/science.1228026

Marotzke, J., and Forster, P. M. (2015). Forcing, feedback and internal variability in global temperature trends. *Nature* 517 (7536), 565–570. doi:10.1038/nature14117

Masson, V., Champeaux, J.-L., Chauvin, F., Meriguet, C., and Lacaze, R. (2003). A global database of land surface parameters at 1-km resolution in meteorological and climate models. *J. Clim.* 16 (9), 1261–1282. doi:10.1175/1520–0442–16.9.1261

Matewos, T., and Tefera, T. (2020). Local level rainfall and temperature variability in drought-prone districts of rural Sidama, central rift valley region of Ethiopia. *Phys. Geogr.* 41 (1), 36–53. doi:10.1080/02723646.2019.1625850

McNally, A., Arsenault, K., Kumar, S., Shukla, S., Peterson, P., Wang, S., et al. (2017). Data Descriptor: a land data assimilation system for sub-Saharan Africa food and water security applications. *Sci. Data* 4, 170012. doi:10.1038/sdata.2017.12

Meraner, K., Mauritsen, T., and Voigt, A. (2013). Robust increase in equilibrium climate sensitivity under global warming. *Geophys. Res. Lett.* 40 (22), 5944–5948. doi:10.1002/2013GL058118

Michaels, P. J., and Stooksbury, D. E. (1992). Global warming: a reduced threat? *Bull. Am. Meteorological Soc.* 73 (10), 1563–1577. doi:10.1175/1520-0477(1992)073<1563:GWART>2.0.CO;2

Miheretu, B. A. (2021). Temporal variability and trend analysis of temperature and rainfall in the Northern highlands of Ethiopia. *Phys. Geogr.* 42 (5), 434–451. doi:10.1080/02723646.2020.1806674

Mitchell, J. M., Dzerdzeevskii, B., Flohn, H., Hofmeyr, W. L., Lamb, H. H., Rao, K. N., et al. (1966). *Climatic change. Technical note No. 79*. Geneva: World Meteorological Organization. Available at: https://library.wmo.int/doc_num.php?explnum_id=865.Last (Accessed September 6, 2022).

Mondal, A., Khare, D., and Kundu, S. (2015). Spatial and temporal analysis of rainfall and temperature trend of India. *Theor. Appl. Climatol.* 122 (1), 143–158. doi:10.1007/s00704-014-1283-z

Mondal, A., Kundu, S., and Mukhopadhyay, A. (2012). Rainfall trend analysis by Mann-Kendall test: a case study of north-eastern part of Cuttack district, Orissa. *Int. J. Geol. Earth Environ. Sci.* 2 (1), 70–78. Available at: https://www.cibtech.org/jgee.htm.Last (Accessed September 6, 2022).

Morice, C. P., Kennedy, J. J., Rayner, N. A., and Jones, P. D. (2012). Quantifying uncertainties in global and regional temperature change using an ensemble of observational estimates: the HadCRUT4 data set. *J. Geophys. Res. Atmos.* 117 (D8), D08101. doi:10.1029/2011JD017187

Morice, C. P., Kennedy, J. J., Rayner, N. A., Winn, J. P., Hogan, E., Killick, R. E., et al. (2021). An updated assessment of near-surface temperature change from 1850: the HadCRUT5 data set. *J. Geophys. Res. Atmos.* 126 (3), e2019JD032361. doi:10.1029/2019JD032361

Panda, A., and Sahu, N. (2019). Trend analysis of seasonal rainfall and temperature pattern in Kalahandi, Bolangir and Koraput districts of Odisha, India. *Atmos. Sci. Lett.* 20 (10), e932. doi:10.1002/asl.932

Qian, C., Zhou, W., Fong, S. K., and Leong, K. C. (2015). Two approaches for statistical prediction of non-Gaussian climate extremes: a case study of Macao hot extremes during 1912–2012. *J. Clim.* 28 (2), 623–636. doi:10.1175/JCLI-D-14-00159.1

Rahim, M. A. (2023). Adilurrahim/GlobalTemperatureTrend_ERA5: historical global and regional spatiotemporal patterns in daily temperature (v1.0). Zenodo. Available at: https://doi.org/10.5281/zenodo.7753968.

Rahman, M. A., Yunsheng, L., and Sultana, N. (2017). Analysis and prediction of rainfall trends over Bangladesh using Mann–Kendall, Spearman's rho tests and ARIMA model. *Meteorology Atmos. Phys.* 129 (4), 409–424. doi:10.1007/s00703-016-0479-4

Rasmusson, E. M., Wang, X., and Ropelewski, C. F. (1990). The biennial component of ENSO variability. *J. Mar. Syst.* 1 (1–2), 71–96. doi:10.1016/0924-7963(90)90153-2

Rohde, R. A., and Hausfather, Z. (2020). The Berkeley earth land/ocean temperature record. *Earth Syst. Sci. Data* 12 (4), 3469–3479. doi:10.5194/essd-12-3469-2020

Rohli, R. V., Ates, S. A., Rivera-Monroy, V. H., Polito, M. J., Midway, S. R., Castañeda-Moya, E., et al. (2019). Inter-annual hydroclimatic variability in coastal Tanzania. *Int. J. Climatol.* 39 (12), 4736–4750. doi:10.1002/joc.6103

Saboohi, R., Soltani, S., and Khodagholi, M. (2012). Trend analysis of temperature parameters in Iran. *Theor. Appl. Climatol.* 109 (3–4), 529–547. doi:10.1007/s00704-012-0590-5

Saha, S., Moorthi, S., Pan, H.-L., Wu, X., Wang, J., Nadiga, S., et al. (2010). The NCEP climate forecast system reanalysis. *Bull. Am. Meteorological Soc.* 91 (8), 1015–1058. doi:10.1175/2010BAMS3001.1

Sato, N., and Robeson, S. M. (2014). Trends in the near-zero range of the minimum air-temperature distribution. *Phys. Geogr.* 35 (5), 429–442. doi:10.1080/02723646.2014.927321

Sayyad, R. S., Dakhore, K. K., and Phad, S. V. (2019). Analysis of rainfall trend of parbhani, maharshtra using mann–kendall test. *J. Agrometeorology* 21 (2), 239–240. doi:10.54386/jam.v21i2.244

Scafetta, N. (2022). CMIP6 GCM ensemble members versus global surface temperatures. *Clim. Dyn.* 60, 3091–3120. doi:10.1007/s00382-022-06493-w

Schneider, U., Finger, P., Meyer-Christoffer, A., Rustemeier, E., Ziese, M., and Becker, A. (2017). Evaluating the hydrological cycle over land using the newly-corrected precipitation climatology from the Global Precipitation Climatology Centre (GPCC). *Atmosphere* 8 (3), 52. doi:10.3390/atmos8030052

Semenov, V. A., Latif, M., Dommenget, D., Keenlyside, N. S., Strehz, A., Martin, T., et al. (2010). The impact of North Atlantic–Arctic multidecadal variability on Northern Hemisphere surface air temperature. *J. Clim.* 23 (21), 5668–5677. doi:10.1175/2010JCLI3347.1

Şen, P. K. (1968). Estimates of the regression coefficient based on Kendall's tau. *J. Am. Stat. Assoc.* 63 (324), 1379–1389. doi:10.1080/01621459.1968.10480934

Şen, Z. (2012). Innovative trend analysis methodology. *J. Hydrologic Eng.* 17 (9), 1042–1046. doi:10.1061/(ASCE)HE.1943-5584.0000556

Şen, Z. (2014). Trend identification simulation and application. *J. Hydrologic Eng.* 19 (3), 635–642. doi:10.1061/(ASCE)HE.1943-5584.0000811

Serra, C., Burgueno, A., and Lana, X. (2001). Analysis of maximum and minimum daily temperatures recorded at Fabra Observatory (Barcelona, NE Spain) in the period 1917–1998. *Int. J. Climatol.* 21 (5), 617–636. doi:10.1002/joc.633

Sherwood, S. C., Webb, M. J., Annan, J. D., Armour, K. C., Forster, P. M., Hargreaves, J. C., et al. (2020). An assessment of Earth's climate sensitivity using multiple lines of evidence. *Rev. Geophys.* 58 (4), 2019RG000678. doi:10.1029/2019RG000678

Singh, R. N., Sah, S., Das, B., Chaturvedi, G., Kumar, M., Rane, J., et al. (2021). Long-term spatiotemporal trends of temperature associated with sugarcane in west India. *Arabian J. Geosciences* 14 (19), 1955. doi:10.1007/s12517-021-08315-5

Slivinski, L. C., Compo, G. P., Whitaker, J. S., Sardeshmukh, P. D., Giese, B. S., McColl, C., et al. (2019). Towards a more reliable historical reanalysis: improvements for version 3 of the Twentieth Century Reanalysis system. *Q. J. R. Meteorological Soc.* 145 (724), 2876–2908. doi:10.1002/qj.3598

Swanson, K. L., Sugihara, G., and Tsonis, A. A. (2009). Long-term natural variability and 20th century climate change. *Proc. Natl. Acad. Sci.* 106 (38), 16120–16123. doi:10.1073/pnas.0908699106

Toreti, A., and Desiato, F. (2008). Temperature trend over Italy from 1961 to 2004. *Theor. Appl. Climatol.* 91 (1–4), 51–58. doi:10.1007/s00704-006-0289-6

Trenberth, K. E. (1983). What are the seasons? *Bull. Am. Meteorological Soc.* 64 (11), 1276–1282. doi:10.1175/1520-0477(1983)064<1276:WATS>2.0.CO;2

Villarini, G., Serinaldi, F., Smith, J. A., and Krajewski, W. F. (2009). On the stationarity of annual flood peaks in the continental United States during the 20th century. *Water Resour. Res.* 45 (8), W08417. doi:10.1029/2008WR007645

Wang, H., Schubert, S., Suarez, M., Chen, J., Hoerling, M., Kumar, A., et al. (2009). Attribution of the seasonality and regionality in climate trends over the United States during 1950–2000. *J. Clim.* 22 (10), 2571–2590. doi:10.1175/2008JCLI2359.1

Weiss, A., and Hays, C. J. (2005). Calculating daily mean air temperatures by different methods: implications from a non-linear algorithm. *Agric. For. Meteorology* 128 (1–2), 57–65. doi:10.1016/j.agrformet.2004.08.008

Wild, M., Ohmura, A., and Makowski, K. (2007). Impact of global dimming and brightening on global warming. *Geophys. Res. Lett.* 34 (4), L04702. doi:10.1029/2006GL028031

Wu, Z., Huang, N. E., Long, S. R., and Peng, C. K. (2007). On the trend, detrending, and variability of nonlinear and nonstationary time series. *Proc. Natl. Acad. Sci.* 104 (38), 14889–14894. doi:10.1073/pnas.0701020104

Wu, Z., Huang, N. E., Wallace, J. M., Smoliak, B. V., and Chen, X. (2011). On the time-varying trend in global-mean surface temperature. *Clim. Dyn.* 37, 759. doi:10.1007/s00382-011-1128-8

Yacoub, E., and Tayfur, G. (2019). Trend analysis of temperature and precipitation in Trarza region of Mauritania. *J. Water Clim. Change* 10 (3), 484–493. doi:10.2166/wcc.2018.007

Yang, Y., Li, Q. X., Song, Z. Y., Sun, W. B., and Dong, W. J. (2022). A comparison of global surface temperature variability, extremes and warming trend using reanalysis datasets and CMST-Interim. *Int. J. Climatol.* 42, 5609–5628. doi:10.1002/joc.7551

Yiqi, C., Yuanjie, Z., Yubin, L., and Shugang, S. (2023). Changes in lengths of the four seasons in China and the relationship with changing climate during 1961–2020. *Int. J. Climatol.* 43 (3), 1349–1366. doi:10.1002/joc.7919

You, Q., Kang, S., Pepin, N., Flügel, W. A., Yan, Y., Behrawan, H., et al. (2010). Relationship between temperature trend magnitude, elevation and mean temperature in the Tibetan Plateau from homogenized surface stations and reanalysis data. *Glob. Planet. Change* 71 (1–2), 124–133. doi:10.1016/j.gloplacha.2010.01.020

Yücel, A., Atilgan, A., and Öz, H. (2019). Trend analysis in temperature, precipitation and humidity: the case of Mediterranean region. *Sci. Pap. Ser. E-Land Reclam. Earth Observations Surv. Environ. Eng.* 8, 91–98.

Yue, S., Pilon, P., and Cavadias, G. (2002). Power of the Mann–Kendall and Spearman's rho tests for detecting monotonic trends in hydrological series. *J. Hydrology* 259 (1–4), 254–271. doi:10.1016/S0022-1694(01)00594-7

Zelinka, M. D., Myers, T. A., McCoy, D. T., Po-Chedley, S., Caldwell, P. M., Ceppi, P., et al. (2020). Causes of higher climate sensitivity in CMIP6 models. *Geophys. Res. Lett.* 47 (1), e2019GL085782. doi:10.1029/2019GL085782

Zhu, J. P., Xie, A. H., Qin, X., Wang, Y. T., Xu, B., and Wang, Y. C. (2021). An assessment of ERA5 Reanalysis for Antarctic near-surface air temperature. *Atmosphere* 12 (2), 217. doi:10.3390/atmos12020217

frontiers | Frontiers in Environmental Science

TYPE Review
PUBLISHED 28 February 2024
DOI 10.3389/fenvs.2024.1307840

OPEN ACCESS

EDITED BY
Haipeng Yu,
Chinese Academy of Sciences (CAS), China

REVIEWED BY
Nadeem Tahir,
Henan Agricultural University, China
Manoj Kumar Jhariya,
Sant Gahira Guru Vishwavidyalaya, India

*CORRESPONDENCE
Hesham S. Ghazzawy,
hghazzawy@kfu.edu.sa
Mohamed Ashour,
microalgae_egypt@yahoo.com

RECEIVED 05 October 2023
ACCEPTED 12 February 2024
PUBLISHED 28 February 2024

CITATION
Ghazzawy HS, Bakr A, Mansour AT and Ashour M (2024), Paulownia trees as a sustainable solution for CO_2 mitigation: assessing progress toward 2050 climate goals. *Front. Environ. Sci.* 12:1307840. doi: 10.3389/fenvs.2024.1307840

Paulownia trees as a sustainable solution for CO_2 mitigation: assessing progress toward 2050 climate goals

Hesham S. Ghazzawy[1,2]*, Ahmed Bakr[3], Abdallah Tageldein Mansour[4,5] and Mohamed Ashour[6]*

[1]Date Palm Research Center of Excellence, King Faisal University, Al-Hasa, Saudi Arabia, [2]Central Laboratory for Date Palm Research and Development, Agriculture Research Center, Giza, Egypt, [3]Environment and Bio-agriculture Department, Faculty of Agriculture, Al-Azhar University, Cairo, Egypt, [4]Animal and Fish Production Department, College of Agricultural and Food Sciences, King Faisal University, Al-Hasa, Saudi Arabia, [5]Fish and Animal Production Department, Faculty of Agriculture (Saba Basha), Alexandria University, Alexandria, Egypt, [6]National Institute of Oceanography and Fisheries (NIOF), Cairo, Egypt

Due to the progressive climate change on our planet, scientists are interested in solving this issue since it threatens not only certain regions or countries but also the world's ecosystems and economies. Therefore, minimizing carbon dioxide (CO_2) emissions and reducing atmospheric levels are global priorities. Thus, it is necessary at this moment to develop an appropriate approach to reduce or stabilize CO_2 levels in the atmosphere. However, CO_2 capture projects are long-term, low-profitable, and high-risk environmental projects. Consequently, it is necessary to find an appropriate and sustainable CO_2 capture approach that is efficient in reducing atmospheric CO_2 levels while having a safe impact on the environment. Although carbon (C) is the key basic component used to produce biological compounds by photosynthetic organisms in terrestrial plants, the C pathway is a key factor affecting the capture of CO_2 by photosynthetic organisms. Among photosynthetic organisms, *Paulownia*, a multipurpose tree, is popular around the world for its timber and its potential role in CO_2 sequestration. *Paulownia spp*. belongs to the Paulowniaceae family and comprises a group of trees. These trees are primarily found in southeastern Asia, particularly in China, and have been intentionally grown for more than two millennia due to their ornamental, cultural, and medicinal value. The number of Paulownia species varies depending on taxonomic classification, ranging from 6 to 17. Among them, *Paulownia tomentosa, Paulownia elongata, Paulownia fortunei,* and *Paulownia catalpifolia* are the most widely recognized and favored species. The present review provides a comprehensive technical-economic scenario for the capture of one million tons of CO_2 by Paulownia trees (as a terrestrial plant model, grown on 2,400 ha^{-1}). *P. tomentosa* can be utilized in agroforestry systems to mitigate greenhouse gas (GHG) emissions within urban cities and emphasize the carbon storage potential of agroforestry. In conclusion, Paulownia trees as an environmental mass project showed great encouragement to investors and governments to expand these types of projects to achieve global climate goals by 2050.

KEYWORDS

global warming, carbon concentrating mechanism, carbon pathways, Paulownia tree, Rubisco, PEPCase, carbon dioxide biofixation

1 Introduction

The climate change challenge is a global issue affecting many species of plants and animals, as well as human civilization and the health of the earth. The continued increase in greenhouse gas (GHG) emissions, such as CO_2, CH_4, N_2O, and fluorinated gases, has only served to worsen this situation (Adams and Engel, 2021). Among greenhouse gases, carbon dioxide (CO_2) is the most important and essential for photosynthesis, which sustains the life of plants. However, the concentration of CO_2 can vary, with natural gas power plants emitting CO_2 at a rate of 3%–4%, while coal power plants release it at a rate of 10%–13%. Conversely, bio-refineries can have a CO_2 concentration of up to 80%. Generally, the amount of atmospheric CO_2 globally has risen significantly, from 313 ppm in 1960 to 411 ppm in 2020, and is projected to reach 450 ppm by 2035 (Santori et al., 2018). This could result in a 2°C increase in global warming and have a major impact on the global economy, with a 99% chance of this outcome (Santori et al., 2018; Bushing, 2021). However, increased atmospheric CO_2 is considered the predominant cause of global climate change (Shreyash et al., 2021).

The reduction of CO_2 emissions is a pressing global concern, and a strategy must be put in place to lower or maintain CO_2 levels in the atmosphere. Despite extensive research on reducing CO_2 emissions by physical and chemical methods, there are several environmental, technical, and economic challenges. Therefore, it is crucial to find a sustainable, profitable, and effective approach for capturing CO_2 that reduces atmospheric CO_2 levels better than physical and chemical methods (Kadlec et al., 2021). A study conducted by Prasad et al. (2021) found that there are two crucial approaches for reducing CO_2 emissions: 1) reducing dependence on fossil fuels and increasing the use of renewable energy sources and 2) capturing and storing CO_2 through biological, chemical, or physical methods (Shreyash et al., 2021). Osman et al. (2021) have identified three primary methods for CO_2 capture, storage, and utilization: pre-combustion, post-combustion, and oxyfuel combustion.

Among CO_2 capture and storage (CCS) technologies, biological CCS is the most cost-efficient and environmentally sound option, relying primarily on photosynthetic organisms such as terrestrial and aquatic plants (Chu and Majumdar, 2012; Benedetti et al., 2018). Through photosynthesis, photoautotrophic organisms, including terrestrial and aquatic plants, can convert CO_2 into carbon-based products such as sugars, proteins, and lipids. Globally, these organisms can store solar energy at a rate of 120 TW y^{-1} (Zhu et al., 2010). This means that photoautotrophic organisms can cover the global energy demand by 800%. Therefore, the widespread cultivation of these organisms is a promising solution for meeting a significant portion of the world's energy needs (Stephenson et al., 2011).

Several published studies have reported that urban green areas can play a crucial role in reducing the carbon footprint of cities. These areas include trees, parks, gardens, and canals and provide several benefits, such as improved air quality, reduced noise, preservation of biodiversity, mitigation of urban heat islands, management of microclimate, soil stability, groundwater recharge, avoidance of soil erosion, and CO_2 capture (Strohbach et al., 2012; Singh et al., 2018). Such urban green spaces, along with vegetation, green areas, and soils, have the potential to lower atmospheric CO_2 levels and influence the CO_2 cycle (Chang et al., 2017; Roeland et al., 2019). In another work, Chia et al. (2016) reported that forests are seen as a way to mitigate the effects of climate change, given that it is a global issue.

Forests play a critical role in carbon sequestration, storing carbon in trees and soils. They also provide numerous other ecosystem services that are essential for human wellbeing and the functioning of the planet. Forests provide a habitat for countless species of plants and animals, many of which are essential for pollination, pest control, and nutrient cycling. They also play a critical role in regulating the water cycle, helping prevent erosion and flooding, and providing clean drinking water to downstream communities (Martínez Pastur et al., 2018; Chaudhry et al., 2021). For a long time, forest CO_2 capture projects were considered high-risk investments due to the long time frames involved. Thus, they have been adopted relatively slowly or excluded from international carbon markets, such as those established by the Kyoto Protocol and the EU Emissions Trading Scheme (ETS). Recently, over 25 public funds have provided incentives for forest operations related to carbon rather than relying on carbon markets. This helps governments better manage their forests (van der Gaast et al., 2018). The findings of Chia et al. (2016) align with those of Osman et al. (2021), who stated that carbon pricing is an effective approach to encourage investment in the carbon sequestration and storage industries. Regarding this point, terrestrial plants have attractive CO_2 capture potential and high biomass productivity. Trees have an average CO_2 capture potential of 1.78 tons CO_2 tons biomass^{-1} y^{-1} and an average biomass productivity of 2.6–3.9 tons ha^{-1} y^{-1} (Fuhrer and Molnar, 2003; Khan and Ansari, 2005).

Investigating the C pathways in terrestrial plants is crucial to assessing their ability to absorb atmospheric CO_2 and produce oxygen (O_2) through photosynthesis, as well as their contribution to the ecosystem. The exchange of CO_2 and O_2 by photosynthetic cells through their cell walls plays a crucial role in this process. However, understanding the unique carbon pathways in terrestrial plants can provide valuable information about their potential as a tool for CO_2 capture (Kheyrodin and Kheyrodin, 2017). When the stomata of a plant are open, CO_2 enters and is utilized in the photosynthesis process. At the same time, O_2, a byproduct of photosynthesis, can escape. However, in hot and dry conditions, this problem is amplified because, while the stomata are open, the plant also loses water through transpiration. As a result, the efficiency of a plant's CO_2 fixation can vary. Plants fix CO_2 in the atmosphere through one of three pathways: the C3, C4, and Crassulacean acid metabolism (CAM) pathways (Winter and Holtum, 2017).

C3 plants, which make up more than 85% of plants on Earth (Kheyrodin and Kheyrodin, 2017), are referred to as the "C3 pathway" because the first molecule created in the cycle is a 3-carbon molecule called 3-phosphoglyceric acid. Although C3 plants are the most common on the planet, C4 plants are estimated to be twice as efficient at photosynthesizing as C3 plants, although this difference becomes less noticeable in high CO_2 environments (Mondal et al., 2017). This increased efficiency is because C4 plants concentrate carbon and reduce carbon loss during the fixation process. In contrast, C3 plants fix CO_2 through the Calvin cycle, where the RuBisCO enzyme causes an

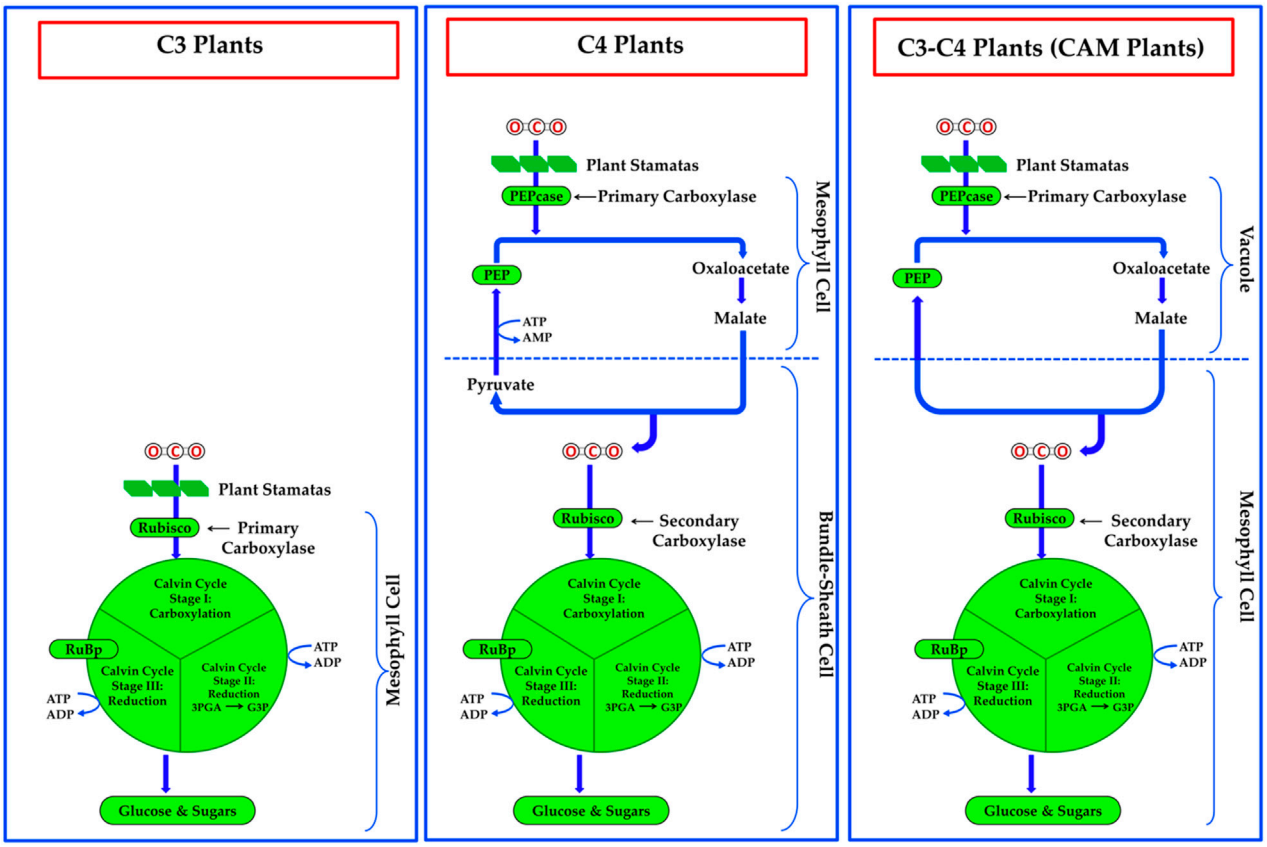

FIGURE 1
Carbon pathways (C3, C4, and CAM) in plants.

oxidation reaction that accounts for part of the energy utilized in photosynthesis being lost through photorespiration. As a result, the amount of carbon that the plant fixes and releases back into the environment as CO_2 has decreased by approximately 25%. In C3 plants, the main carboxylase is RuBisCO, and the main product of RuBP's carboxylation is a three-carbon sugar. Additionally, RuBP's oxygenation, which is the first stage of photorespiration, is catalyzed by RuBisCO in C3 plants (Zhu et al., 2010). Figure 1 shows the carbon pathways in plant cells. The C4 pathway was unknown until the 1960s, when scientists discovered the C4 pathway in sugarcane. The C4 pathway, also known as the Hatch–Slack cycle, is named for the 4-carbon intermediate molecules that were generated (malic or aspartic acid).

In C4 plants, the PEPCase enzyme is the main carboxylase, a 4-carbon molecule is the main carboxylation product in light, and a secondary carboxylase is RuBisCO, which works under high CO_2 conditions to limit oxygenation and photorespiration. C4 plants have an additional step in their pathway before starting the Calvin cycle, which decreases the amount of carbon lost in the CO_2 fixation process (Santos et al., 2022; Silva Araújo et al., 2022). In C4 plants, CO_2 reacts with phosphoenolpyruvate to produce 4-carbon acids (malate), which are transported to bundle sheath cells where CO_2 is liberated and used in the Calvin cycle. The typical carbon isotope composition in C4 plants ranges from 10% to 14%. In CAM plants, which are found in deserts and shallow bodies of water, the stomata close during the day to conserve water and open at night to absorb CO_2, which is stored as malate. During daylight, photosynthesis starts through the Calvin cycle. Table 1 summarizes the differences between the three pathways, as described in various studies (Hatfield et al., 2009; Carvajal, 2010; Kheyrodin and Kheyrodin, 2017; Guidi et al., 2019).

Paulownia trees, also known as the "princess tree," are part of the Paulowniaceae family and have attracted attention for their potential to capture CO_2 from the atmosphere. These trees have a fast growth rate and are known for their exceptional carbon sequestration abilities. When grown in large quantities, they can absorb substantial amounts of CO_2, making them a promising solution for combating the impacts of climate change (Janjić and Janjić, 2019).

Several studies have indicated that Paulownia trees can absorb up to twice as much CO_2 compared to other tree species. The CO_2 absorbed by Paulownia trees is stored in their wood and soil, making them effective long-term carbon sinks. In addition, these trees are resistant to pests and require minimal input of water, fertilizer, and pesticides (Magar et al., 2018; Jakubowski, 2022; Testa et al., 2022). The popularity of Paulownia trees has skyrocketed due to their remarkable CO_2 capture and storage capabilities (Icka et al., 2016b; Magar et al., 2018). They are known for their high productivity and carbon sequestration potential and are widely considered valuable assets in the fight against climate change (Dong et al., 2014). Furthermore, they are versatile and can be utilized for a range of purposes, such as lumber, construction materials, and musical

TABLE 1 Most important differences between C3, C4, and CAM pathways.

Item	C3	C4	CAM
Plant distributions on Earth	85% (approximately 250,000 species)	3% (approximately 7,600 species)	8% (approximately 16,000 species)
Optimum temperature	15–25 (°C)	30–40 (°C)	More than 40 (°C)
Habitat	Ample and luxurious areas (all photosynthetic plants)	Warm and grassland areas (tropical plants)	Humid and tropics areas (semi-arid conditions)
Photorespiration rate	High	Not seen	Seen in the noon time
Photosynthetic efficiency	Low	High	High
Photosynthetic performance	Only when the stomatal condition is open	Even stomatal condition is open or closed	Even stomatal condition is open or closed
Movement of stomata	Open during the daytime and close at night	Open during the daytime and close at night	Inverted (open at night and close at daytime)
Number of stomata	2000–3000	10,000–160,000	100–800
Involved cells	Mesophyll cells (C3)	Mesophyll cells (C3), followed by bundle sheath cells (C4)	Both C3 and C4 (mesophyll cells)
Secondary CO_2 fixation carboxylase enzyme	–	RuBisCO	RuBisCO
Carbon pathway (cycle)	C3 cycle (Calvin cycle)	Hatch–Slack cycle (C4) assists the Calvin cycle (C3)	Hatch–Slack cycle (C4) assists the Calvin cycle (C3) using the Crassulacean acid metabolism
First product from CO_2 fixation	PGA	Malate (day and night)	Malate (night only)
CO_2 assimilation efficiency	Low	High	High
CO_2 assimilation rate	Low	High	High
(NADPH: ATP, respectively) required number to produce glucose molecule	12: 18	12: 30	12: 39
Ratio of (CO_2: ATP: NADPH), respectively	1: 3: 2	1: 5: 2	1: 6: 5
Plant types	Hydrophytic, mesophytic, and xerophytic plants	Mesophytic plants	Xerophytic plants
Species examples of terrestrial plants	Most grasses and trees, spinach, peanuts, cotton, wheat, rice *etc.*	Paulownia, corn, sugarcane, maize, sorghum, millet, sorghum, pineapple, daisies, cabbage *etc.*	Cacti, orchids, jade, sedum, agave *etc.*

instruments. With their ability to absorb and store significant amounts of CO_2, Paulownia trees have become a popular choice for reforestation and carbon offset projects. The effectiveness of these trees in capturing CO_2 is contingent upon various factors, such as location, growth conditions, and management practices (Jakubowski, 2022).

A comprehensive evaluation of the entire life cycle of Paulownia trees, including their harvesting and processing, is crucial to determining their actual carbon footprint. The potential of Paulownia trees to capture CO_2 from the atmosphere is substantial, but more research and analysis are required to understand its effectiveness and limitations regarding C sequestration value and information about *P. tomentosa* and its implementation for CO_2 mitigation. This work offers a review of carbon pathways in terrestrial photosynthetic plants as well as an in-depth assessment of the ability of terrestrial plants, particularly the Paulownia genus, to capture CO_2 from the atmosphere. The study also contains a detailed techno-economic scenario aimed at capturing one million tons of CO_2 using the Paulownia species. The expected results from using the Paulownia are carefully evaluated and discussed. Finally, the work gives a comprehensive overview of ongoing carbon credit projects and assesses the prospects of achieving global climate objectives by 2050.

2 Role of terrestrial plants in CO_2 capture for biomass production

During biophysical processes, trees absorb and release CO_2 into the atmosphere. In the process of photosynthesis, leaves capture CO_2 through their stomata and utilize the energy from the sun to transform it into O_2, carbohydrates, and water. These substances are then used to create the structures of wood, as well as the vitamins, resins, and hormones required for tree development, growth, and health. Trees get their energy from the carbohydrates that are produced during photosynthesis. The net storage of CO_2 by the tree is the result of the interaction between photosynthesis and respiration (Aguaron and McPherson, 2012). Indeed, urban green

areas, especially those with trees, have a great potential to capture CO_2 from the atmosphere and reduce the effects of climate change in urban areas. However, several studies have reported that urban green areas can be critical to reducing carbon footprints (Strohbach et al., 2012; Nouri et al., 2019; Sharma et al., 2020). As previously reported by Sharma et al. (2020), there are three ways to reduce CO_2 levels naturally in the atmosphere: (I) increase atmospheric CO_2 capture rates through tree planting; (II) reduce energy demand; and (III) increase bioenergy demand and utilization of bioenergy.

The expression "atmospheric CO_2 storage" describes the accumulation of woody biomass that accumulates over time as plants grow. The annual rate of CO_2 uptake in biomass for one growing season is called "atmospheric CO_2 sequestration." Sequestration relies on tree growth and death, which is strongly dependent on species diversity and demographic factors such as the age of the urban forest. Carbon stored in one location at a specific moment is referred to as "carbon stock." Carbon stocks in forests include live and standing dead plants, wood waste and litter, organic matter present in the soil, and harvested stocks like timber for wood products and fuel (Robards, 2008). According to the Intergovernmental Panel on Climate Change (IPCC) report (Pedersen et al., 2022), the plant ecosystem involves five major carbon pools, namely, 1) above-ground biomass (AGB), 2) below-ground biomass (BGB), 3) dead wood, 4) detritus, and 5) soil organic matter. When trees die, the biomass becomes part of the food chain or becomes soil carbon (Suryawanshi et al., 2014).

However, the average rate of CO_2 sequestration in trees is mainly influenced by factors such as the size of the tree at maturity, the lifespan, and the growth rate (Nowak and Crane, 2002). To determine the amount of CO_2 stored in trees, Aguaron and McPherson (2012) used allometric formulas that consider several characteristics, including diameter at breast height (DBH), site index, height, moisture content, wood density, and overall tree conditions. These characteristics can vary between species and even within individual trees, making it difficult to determine an accurate average. The allometric biomass equations used for this calculation come in two forms: volumetric and direct. The volumetric equation calculates the above-ground volume of a tree using DBH and height, while the direct equation determines the above-ground dry weight using the same variables (Domec and Gartner, 2002). The study conducted by MacDicken (1997) concluded that tree biomass, including AGB, BGB, total biomass (TB), carbon content (CC), and equivalent CO_2 ($CO_{2\text{-Eq.}}$), can be estimated by measuring the diameter at breast height (DBH, cm) of the tree using morphometric equations. These equations were designed specifically for a dry climate with an average seasonal rainfall of up to 1,500 mm.

$$\mathrm{AGB\ (kg)} = 34.4703 - (8.0671 \times \mathrm{DTBH}) + (0.6589 \times \mathrm{DTBH2}),$$

$$\mathrm{BGB\ (kg)} = \mathrm{AGB} \times (15/100),$$

$$\mathrm{TB\ (kg)} = \mathrm{AGB} + \mathrm{BGB},$$

$$\mathrm{CC\ (kg)} = 0.5 \times \mathrm{TB},$$

$$\mathrm{CO_{2\text{-Eq.}}\ (kg)} = (\mathrm{CC} \times 44)/12.$$

As described in the study by Sharma et al. (2020), AGB, BGB, TB, CC, and $CO_{2\text{-Eq.}}$ were calculated for several trees commonly used in the construction of landscapes and green belts. Table 2 presents the mean values (based on 10 trees) of AGB, BGB, TB, CC, and $CO_{2\text{-Eq.}}$ found in the Godavari Botanical Garden in Nepal (Magar et al., 2018) and at the Amity University Campus in India (Sharma et al., 2020).

The IPCC report demonstrated that urban green areas (green belts) may reduce atmospheric carbon in three primary ways (Pörtner et al., 2022). First, atmospheric CO_2 is absorbed by the leaves, and a portion of this adsorbed CO_2 is then released into the atmosphere. The remaining portion is stored in the plant tissues, both AGB and BGB (total biomass), leading to plant growth in the form of biomass. Second, soils are considered one of the major contributors to carbon stocks because they make up only a small portion of the overall carbon stocks; litter and dead wood are not significant sources of carbon. Third, urban areas minimize the need for heating by lowering wind speed and the need to cool infrastructure by offering shade and evaporation. This significantly lowers the need to use fossil fuels to generate energy, which balances out carbon emissions (Jo, 2002).

Most published studies on carbon have focused on AGB because BGB assessments are inherently more expensive and time-consuming. There is still a demand for reliable BGB equations, although very few studies have concentrated on creating equations to predict BGB based on straightforward tree variables (Hertel et al., 2009; Ziegler et al., 2012; Yuen et al., 2013; Kralicek et al., 2017). The amount of CO_2 captured per hectare using the formula based on plant photosynthesis and wood chemical composition can be estimated by calculating the average yearly increase of the trees, and this value was estimated to be 981 kg m^{-3} (Fuhrer and Molnar, 2003).

Intelligent selection of effective and suitable species, as well as their proper management in urban spaces, are vital in increasing the potential and success of these areas (Bhalla and Bhattacharya, 2015; Ram et al., 2015). Therefore, to guarantee the success of any green belt project, the specific tree species must be identified before starting the project planning. The study by Alotaibi et al. (2020) investigated which specific, effective, and tolerant tree species must be planted and used within the frame of the "Green Riyadh Project," one of the limited greening-belt projects. This study aimed to assess the air pollution tolerance index (APTI) associated with the anticipated performance index (API) for five tree species (*Ficus altissima*, *Eucalyptus camaldulensis*, *Ziziphus spina-christi*, *Albizia lebbeck*, and *Prosopis juliflora*), which are usually planted and used along roadsides and around industrial and residential spaces. Four different Riyadh sites were used to collect leaf samples: a residential area, a busy intersection, an industrial area, and a reference site that was approximately 20 km outside the city. Based on the APTI and API performance data, they concluded that the green belt planning in the "Green Riyadh Project" must include growing *Ficus altissima* on roadsides and heavy industrial locations, followed by *Z. spina-christi* and *A. lebbeck*.

3 Current carbon credit industries and projects

To reach the goal of reducing global CO_2 emissions by 2050, there is a growing need for projects that capture CO_2. Various strategies have been proposed and implemented throughout the

TABLE 2 CO_2 equivalent content of some tree species used in the construction of CO_2 capture, landscape, and green belts.

Common name	Scientific name	AGB (kg)	BGB (kg)	TB (kg)	CC (kg)	$CO_{2\text{-Eq.}}$ (kg)
Paulownia tree*	*Paulownia tomentosa*	6.92	1.38	8.3	4.15	15.21
Paulownia tree**	*Paulownia tomentosa*	361.47	72.29	433.76	203.86	747.48
Paulownia tree***	*Paulownia tomentosa*	472.20	115.43	587.63	293.81	1,077.32
Weeping fig	*Ficus benjamina*	332.1	49.8	382.0	191.0	700.3
Indian laburnum	*Cassia fistula*	335.3	50.3	385.6	192.8	706.9
White Frangipani	*Plumeria obtusa*	334.3	50.1	384.4	192.2	704.8
Flame tree	*Delonix regia*	326.2	48.9	375.2	187.6	687.8
Kadam	*Neolamarckia cadamba*	327.5	49.1	376.6	188.3	690.4
Laurel fig	*Ficus microcarpa*	331.3	49.7	381.0	190.5	698.6
Indian mahogany	*Chukrasia tabularis*	330.5	49.6	380.1	190.0	696.8
Drumstick tree	*Moringa oleifera*	326.3	48.9	375.2	187.6	687.9
Silver oak	*Grevillea robusta*	328.4	49.3	377.7	188.9	692.5
Royal palm	*Roystonea regia*	329.4	49.4	378.8	189.4	694.5
Bottlebrush tree	*Callistemon viminalis*	334.3	50.2	384.5	192.3	704.9
Eucalyptus	Eucalyptus sp.	321.1	48.2	369.3	184.6	677.0
Banana	Musa sp.	334.2	50.1	384.4	192.2	704.7
Spanish cherry	*Mimusops elengi*	329.9	49.5	379.4	189.7	695.6
Neem	*Azadirachta indica*	327.0	49.1	376.0	188.0	689.4
Pride of India	*Lagerstroemia speciosa*	332.2	49.8	382.1	191.0	700.4
Dwarf white orchid	*Bauhinia acuminata*	332.0	49.8	381.8	190.9	699.9
Indian rosewood	*Dalbergia sissoo*	329.0	49.4	378.4	189.2	693.7
White fig	*Ficus virens*	327.4	49.1	376.5	188.2	690.2
Indian gooseberry	*Phyllanthus emblica*	324.0	48.6	372.5	186.3	683.0
White mulberry	*Morus alba*	326.1	48.9	375.0	187.5	687.4
Date palm	*Phoenix dactylifera*	318.4	47.8	366.2	183.1	671.3
Sacred fig	*Ficus religiosa*	310.9	46.6	357.5	178.8	655.5
Bamboo	*Bambusa vulgaris*	255.0	38.2	293.2	146.6	537.5
Scholar's tree	*Alstonia scholaris*	252.2	37.8	290.1	145.0	531.8
Copper pod	*Peltophorum pterocarpum*	201.6	30.2	231.9	115.9	425.1

(*), (**), and (***): average values of 100, 30, and 30 trees of Paulownia (Paulownia *tomentosa*), cultured at Godavari Botanical Garden, Nepal), under the age of 4 months (*), 4 years (**), and 5 years (***), respectively (Magar et al., 2018).

world, including improving energy efficiency, implementing a carbon tax, increasing the production of renewable energy, planting trees, and capturing CO_2 from the atmosphere in power plants (Nunez, 2019). Carbon capture and storage (CCS) and carbon capture, utilization, and storage (CCUS) are considered effective solutions for addressing climate change. As the climate change crisis intensifies, CCS/CCUS projects are becoming increasingly common. In a comprehensive study of CCUS systems, Hong (2022) reviewed technologies for CO_2 capture, separation, transport, utilization, and storage. The study indicated various methods for CO_2 capture, such as industrial separation, pre- and post-combustion, oxyfuel combustion, chemical looping combustion, and direct air capture (DAC).

Therefore, the current study specifically focuses on DAC technology using biological adsorption through trees and microalgae. Studies by Deutz and Bardow (2021), Keith et al. (2018), and Abanades et al. (2020) have shown that the efficiency of CO_2 removal, energy consumption, and cost for the DAC technology are 85%–93% vol, 5.25 GJ $tons^{-1}$ CO_2, and USD 140–USD 340 $tons^{-1}$ CO_2, respectively. Carbon credit pricing is a crucial aspect in promoting the development and growth of CO_2 capture technologies (Lefvert et al., 2022). To make these

technologies commercially viable, it is important to have attractive carbon pricing mechanisms, such as carbon taxes or allowances. The value of carbon taxes varies among countries, ranging from a few US $ to 100 US $ per ton of CO_2. In 2017, the carbon allowance equivalent was valued at 5.17 dollars per ton of CO_2, and it is projected to increase to 47.25 USD per ton of CO_2 by 2023 (Chen et al., 2020; Osman et al., 2021). In 2020, there were 22 demo CO_2 capture projects around the world, with the United States and China being the main contributors with seven and five projects, respectively (Vega et al., 2020). The number of commercial CO_2 capture projects has been steadily increasing, with a reported increase from 51 projects in 2019 to 135 projects in 2021 (Turan et al., 2021). In September 2021, the global CO_2 capture capacity was estimated at 49.4 million tons per year.

The Americas region had the highest CO_2 capture capacity, contributing 58.5% of all global projects. Europe ranked second with a total of 38 projects and 28.1% of global projects (E Silva and Costa, 2021), while the Asia–Pacific region ranked third with 14 projects (Steyn and Havercroft, 2021). The Middle East has the lowest number of commercial CCS/CCUS projects, representing only 10% of the global CO_2 captured (Turan et al., 2021), with a total CO_2 capture capacity reached in September 2021 of 3.8 million tons CO_2 y^{-1}. In the Middle East region, the total number of CCS/CCUS commercial projects was four, coming from three countries (one in Qatar, one in Saudi Arabia, and two in the United Arab Emirates) (Steyn and Havercroft, 2021). The European Union aims to achieve net-zero CO_2 emissions by 2050, leading to an increase in CCS/CCUS projects and facilities in the region. The United Kingdom government has invested 1 billion GBP in CCS/CCUS facilities to establish four industrial clusters that will be able to capture 10 million metric tons of CO_2 per year by 2030 (Turner et al., 2021). This investment has contributed to the growth of CCS/CCUS projects and facilities in the EU, leading to a 32% increase in the maximum CO_2 capture capacity. This capacity increased to 37.4 million tons of CO_2 per year in September 2021, up from 28.4 million metric tons of CO_2 in 2020 (Turan et al., 2021; E Silva and Costa, 2021).

In response to the global increase in carbon emissions and the decline in the carbon budget, the use of CCS technology has become increasingly critical in addressing climate change. Therefore, the use of CCS technology has become increasingly crucial in mitigating the impact of rising global carbon emissions. The IEA has outlined a Sustainable Development Scenario (IEA-SDS) that calls for CCS to reduce global emissions by 9%. The IEA-SDS aims to reduce the world's annual CO_2 emissions from 33 to 10 gigatons by 2050, which requires the development of 2,000 commercial CO_2 capture projects. This means that an estimated 70 to 100 new projects need to be built each year, requiring a total capital investment of between 655 and 1,280 billion USD (Rassool, 2021; Yan et al., 2021). On the other hand, scientists are incorporating CCS into their scenario models as a means of effectively capturing and storing CO_2 in geological formations. This aligns with the goals outlined in the Paris Agreement and is reflected in the Sustainable Development Scenario (IEA-SDS) (Newell et al., 2021; Berrada et al., 2022).

Due to the high cost of implementation, private sector investment is crucial to financing CCS projects. The majority of funding is expected to come from debt, financial markets, and sovereign wealth funds, as governments may not be able to provide the necessary capital within the required time frame. According to the Global CCS Institute Report 2021 (Rassool, 2021), the prices of CCS systems are projected to decrease as more projects are implemented, but the rate of decrease depends on several variables, such as geography and industry. The CCS learning rate predicts a cost reduction of 10%–25% for every doubling of installed capacity, leading to an estimated total capital need of 655–1,280 billion US $.

Developing nations still lack sufficient government-led programs that recognize the value of CO_2. However, programs that incentivize CO_2 capture investment have been implemented successfully in developed countries in the form of carbon credits. These credits are used to offset emissions and finance mitigation projects in less developed countries. The most well-known example of a crediting system is the Clean Development Mechanism (CDM) under the Kyoto Protocol (Bajaj, 2022). The report by Doda et al. (2021) found that the voluntary carbon market (VCM) is rapidly growing in the carbon credit industry, but they also noted that these credits alone will not be enough to address all climate risks. They concluded that investment in CO_2 capture through both natural and technical means, including CCS, is necessary. Additionally, investment in CO_2 capture can be made through VCMs as the need for compensation becomes increasingly important. More than 612 million USD of carbon credits were granted through VCM programs between 2007 and 2019, including 142 million USD in 2019 (Doda et al., 2021).

4 Taxonomy, characteristics, and cultivation of Paulownia

4.1 Paulownia classification and botanical description

In the past, Paulownia was classified as a member of the Scrophulariaceae family before its current classification as a member of the Paulowniaceae family (Schneiderová and Šmejkal, 2015). There is a lack of consensus on the exact number of Paulownia species, as taxonomical classifications vary. Depending on the classification, the number of species ranges from 6 to 17 (Kadlec et al., 2021). In the study conducted by Li et al. (2020), eight species of Paulownia have been defined, namely, *P. catalpifolia*, *P. tomentosa*, *P. australis*, *P. kawakamii*, *P. coreana*, *P. fortune*, *P. fargesii*, and *P. elongata*. However, the Chinese Flora Editorial Committee differs in its classification, as it does not recognize *P. coreana* but instead includes two additional variations of *P. tomentosa: P. tomentosa* var. *tomentosa* and *P. tomentosa* var. *tsinlingensis* (Cheng et al., 2019). In addition, other studies have recognized *P. albiflora*, *P. taiwaniana*, and *P. glabrata* (Yadav et al., 2013; He et al., 2016).

Typically, a mature Paulownia tree reaches a height ranging from 20 to 30 m; the tallest registered specimen was 50 m (Icka et al., 2016a; Yi et al., 2020). The trunk is typically approximately 1 m thick but can reach 2 m under suitable environmental conditions. Under normal environmental conditions, the trunk of a mature Paulownia tree generally has a diameter of approximately 1 m. However, under favorable environmental conditions, the trunk can grow even thicker, reaching up to 2 m in diameter (Kadlec et al., 2021).

Paulownia trees possess extensive and well-developed root systems that can extend up to a depth of 8 m in the soil. The upper part of the roots is densely packed, exhibiting branching and dichotomous growth patterns. The bark of the tree is typically brown or black. In young Paulownia trees, lenticels begin to form, and as the tree matures, these lenticels expand, eventually developing into vertical cracks on the bark's surface (Jakubowski et al., 2018).

Mature Paulownia trees have umbrella-shaped leaves that measure approximately 10–12 cm in width and 15–30 cm in length. The leaves have smooth, undulating edges. It is worth noting that younger trees have even larger leaves, with a width that can reach up to 80 cm (Woods, 2008b). The flowering period for Paulownia occurs in May and June, with flowers displaying five petals that range in color from white to light purple. The fruits of the Paulownia tree are approximately 4 cm long and 2.5 cm wide. They mature in the autumn season, and each fruit can release up to 2,000 winged seeds (Šmejkal et al., 2007). Many different substances are secreted by glandular trichomes covering the surfaces of leaves, fruits, and flowers (Asai et al., 2008; Kobayashi et al., 2008).

4.2 Cultivation and growth conditions of Paulownia

Paulownia trees have the ability to reproduce both generatively and vegetatively, although vegetative reproduction is predominantly employed in industrial settings. Traditional methods of reproduction, such as root-splitting, which is also utilized for natural species, have been historically employed (Yi et al., 2020). Additionally, techniques like mini-cuttings at an early developmental stage (Stuepp et al., 2015) or stimulating rooting in green cuttings (Temirov et al., 2021) have been utilized. However, *in vitro* propagation serves as the primary means of propagation for many clones (Gyuleva, 2010; Magar et al., 2016). The production of a robust and well-developed root system is a critical aspect of the reproduction phase, leading to extensive research focused on addressing this matter (Pożoga et al., 2019; Mohamad et al., 2022).

Among the most commonly cultivated species of paulownias are *P. tomentosa*, *P. catalpifolia*, *P. elongata*, *P. taiwaniana*, *P. fortunei*, *P. glabrata*, and *P. fargesii* (Woods, 2008b). During the initial global introduction of paulownias, pure botanical species were used predominantly. The United States was one of the early adopters, importing Paulownias (specifically *P. tomentosa*) around 1840. Due to its rapid growth, it earned the nickname "the tree of the future." Over the past 150 years, it has spread across various states, causing significant problems and sparking heated debates concerning all species of Paulownia. *P. tomentosa* has been officially recognized as an invasive species, leading to its eradication in many states. In the United States, Paulownia has garnered both opponents and proponents, and discussions surrounding the genus are contentious due to the substantial profits generated by existing crops (Snow, 2015).

Recent research indicates that *P. tomentosa* has the ability to spread in various areas where forests have been damaged by several disturbances (Chongpinitchai and Williams, 2021). In certain countries, specific Paulownia species like *P. tomentosa* have been identified as hazardous and recognized as invasive, as seen in Austria (Franz, 2007). Although natural Paulownia species are still cultivated in Asia, including Turkey, there is a growing shift toward hybrid varieties. In Bulgaria, for instance, hybrids have gained importance after unsuccessful attempts to cultivate pure species (Gyuleva, 2010).

4.3 Paulownia as a sustainable model for CO_2 mitigation

The study by Sage and Sultmanis (2016) highlighted an important issue to consider: why are C3 trees more suitable for forests and carbon sequestration than C4 trees? Most C4 species are associated with harsh habitats, such as deserts and salty areas, where arborescence is not feasible. Most C4 species are grasses and sedges that lack the meristems required for tree growth. Only seven species of Hawaiian Euphorbia and a few desert plants that become arborescent with age exhibit C4 photosynthesis. Therefore, wherever C3 trees can grow, they have a competitive advantage over C4 plants due to their height (Sage and Sultmanis, 2016). Recently, published research in the field of reducing climate change has increased rapidly, particularly in the area of biomass production as a renewable energy resource (Jamil et al., 2021; Sikkema et al., 2021; Kirikkaleli et al., 2022). Numerous reports predict that the demand for wood and wood-based products will continue to increase until at least 2050 (Haldar and Sethi, 2021; Kircher, 2022). The production of trees and timber species for biomass use is also increasing worldwide (Ols and Bontemps, 2021; Hamdan and Houri, 2022). They are also considered one of the most promising C4 trees, known for their air-purifying properties (Magar et al., 2018; Jakubowski, 2022; Testa et al., 2022).

One notable characteristic of Paulownia is its remarkable ability to grow to enormous sizes within a remarkably short period. In China, it is often said that Paulownia "shoots up like a pole in 1 year, transforms into an umbrella in 3 years, and can be harvested for boards in 5 years" (Zhu et al., 1986). China has witnessed the existence of extraordinary specimens, such as an 80-year-old *P. fortunei* tree in Kweichow Province, which soared to a towering height of 49.5 m, possessed a DBH of 202 cm, and yielded a wood volume of 34 m^3. Another striking example was a 90-year-old Paulownia with a DBH of 224 cm and a wood volume of 44 m^3. Even younger trees demonstrated impressive dimensions, such as an 11-year-old *P. fortunei* tree in the Guangxi Zhuang Autonomous Region of southern China, which was 22 m tall, had a DBH of 75.1 cm and produced a wood volume of 3.69 m^3. *P. elongata* also achieved similar sizes. In their native habitats in China, Paulownia typically attains a DBH of 30–40 cm within a decade and produces approximately 0.3–0.5 m^3 of wood. However, under ideal conditions, valuable timber can be obtained in just 5–6 years (Zhu et al., 1986; Yi et al., 2020).

As reported in the study conducted by Kozakiewicz et al. (2020), the environmental and growth conditions of Paulownia vary between different species, such as *P. tomentosa, P. fortunei,* and *P. elongata*, which consequentially contribute to the variation in the density of Paulownia wood. The density of Paulownia wood ranges from 220 to 400 kg m^{-3}, with an average of approximately 270 kg m^{-3} (Akyildiz and Kol Sahin, 2010; Madhoushi and Boskabadi, 2019; Lachowicz and Giedrowicz, 2020a). Paulownia trees have a high growth rate and low wood density, but they do not

efficiently produce biofuel (Jakubowski, 2022). Recently, using Paulownia for the production of biomass has gained popularity, especially as a way to mitigate the harmful effects of CO_2 (Magar et al., 2018). These trees can produce more biomass per year than other trees can produce in several seasons. However, the region in which trees are grown can limit biomass production (Zuazo et al., 2013). In a study by Magar et al. (2018), *P. tomentosa* trees were planted in the Godavari Botanical Garden in Nepal at a density of 2000 plants ha^{-1}. The researchers assessed the carbon content of the total biomass of 5-year-old, 1-year-old, and newly planted 4-month-old *P. tomentosa* trees. They found that the 5-year-old trees had a carbon content of 4.52 kg C y^{-1} $tree^{-1}$, yielding 9 tons of C ha^{-1} y^{-1}. The 1-year-old trees had a carbon content of 18.21 kg C y^{-1} $tree^{-1}$, resulting in 0.36 tons of C y^{-1} ha^{-1}. The newly planted 4-month-old *P. tomentosa* trees in a remote village in Nepal had a carbon content of 6.07 kg of C $tree^{-1}$.

In a study conducted by Gyuleva et al. (2021), they estimated the productivity (dried biomass content) of two cultivated Paulownia species (*P. tomentosa* and the hybrid species *P. elongata* × *P. fortunei*) after 2 and 4 years of planting in southwestern Bulgaria. They found that after 2 or 4 years, *P. tomentosa* showed higher productivity (3.47 and 36.99 tons ha^{-1}, respectively) than the hybrid species (2.73 and 19.96 tons ha^{-1}, respectively). The carbon content of *P. tomentosa* was also higher after 2 or 4 years (1.73 and 18.49 tons ha^{-1}, respectively) than that of the hybrid species (1.15 and 9.98 tons ha^{-1}, respectively). Similarly, the equivalent capture of CO_2 ($CO_{2\text{-Eq}}$.) of *P. tomentosa* was also higher after 2 or 4 years (6.34 and 67.79 tons ha^{-1}, respectively) than that of the hybrid species (4.21 and 36.59 tons ha^{-1}, respectively).

In another study, Joshi (2015) reported that a 16-year-old trial of *P. tomentosa* in Asia yielded 38.8 tons of C y^{-1} ha^{-1}, while a 21-year-old trial yielded more than 105 tons C y^{-1} ha^{-1}. Paulownia can have reduced growth rates when grown in poor soil conditions. In a study by Madejón et al. (2016), the biomass of *P. fortune* cultivated in Spain for 3 years was 3.34 tons ha^{-1} (Madejón et al., 2016), compared to the symmetrically grown Eucalyptus globules, which had a biomass of 40.4 tons ha^{-1}. In a related study, Stankova et al. (2019) used a model to demonstrate how the crop species had an impact on the differences in biomass production, which ranged from 0.3 to 4.5 tons ha^{-1} of dry matter. Although modeling is continually improving, it still has several issues because of how complicated the factors that might affect prediction are, such as different areas and their local conditions. This is particularly true for the prediction of wood characteristics and biomass production (Abbasi et al., 2020; Lachowicz and Giedrowicz, 2020b; Palma et al., 2021). Therefore, globally, using Paulownia as a significant component of biomass production requires special attention in nations where the growth of hybrids that could compete with native species is encouraged. In recent reports, Iran, due to its field experience, has reported its ability to plant Paulownia in an area of approximately 16×10^4 km^2 (Galán-Martín et al., 2015; Abbasi et al., 2020). More importantly, several nations are beginning to advance in this area, such as Portugal (Abreu et al., 2020), Iran (Abbasi et al., 2020), Spain (Parra-Lopez et al., 2015; Pleguezuelo et al., 2015), Romania (BUZAN et al., 2018), Italy (Testa et al., 2022), Serbia (Janjić and Janjić, 2019), Ukraine (Morozova et al., 2020; Kaletnik et al., 2021), Northern Ireland (Woods, 2008a; Olave et al., 2015), and Kyrgyzstan (Thevs et al., 2021).

Compared to the production and utilization of fossil fuels, the production and utilization of bioenergy are considered more environmentally benign (Pieratti, 2020). Globally, concerned parties are increasingly understanding that implementing strategies to combat climate change reduces environmental risks, increases production efficiency, and increases profits (Hiloidhari et al., 2019; Secinaro et al., 2020). According to the literature, numerous studies have shown that farmers, especially in the EU, are motivated by their position toward adopting cleaner production methods that can reduce the harmful effects of climate change (Sacchelli et al., 2017; Boyer and Touzard, 2021). Globally, Paulownia culture is a trend that has been pervasive in recent years, in addition to their environmental tasks, such as fighting climate change. As a primary key to the sustainable production of biomass crops, Paulownia farms powerfully achieve economic sustainability for farmers (Magar et al., 2018).

A recent study conducted by Testa et al. (2022) evaluated the economic profitability of the Paulownia farming that replaced a vineyard. The study was conducted on a farm located in southern Italy. They reported that Paulownia farming for wood and woodchip production generated an annual overall margin of approximately 357.91 € ha^{-1}, compared to the annual overall margin of wine grapes of approximately 237.41 € ha^{-1}, yielding 150% annual profit ha^{-1}, whereas Paulownia farming for biomass production only has roughly zero profitability (4.22 € ha^{-1}). Finally, they concluded that profitability relies not only on the product type but also on future price variations, public funding, rewards, and the appropriate decisions made by entrepreneurs for the sustainable development of supply chains from an environmental and social perspective.

5 Investment opportunities and risks in Paulownia and other carbon sequestration-based projects

Forestry-based projects have struggled to take off in compliance and voluntary carbon markets due to various reasons, including investment risks related to non-permanence and leakage (Verma and Ghosh, 2023). Non-permanence refers to the risk that carbon stored in forests will be released back into the atmosphere before the end of the project's crediting period, while leakage refers to the risk that emission reductions achieved in one area are offset by increased emissions in another area. These risks have led to uncertainty in the carbon market and a lack of investor confidence in forestry-based projects (Henry, 2023; Wang et al., 2023). Additionally, there have been challenges in accurately measuring carbon sequestration in forests and ensuring the permanence of carbon storage over time. As a result, there have been relatively few forestry-based projects in the compliance market, with most focused on afforestation and reforestation. In the voluntary market, forestry projects have also faced challenges in attracting buyers due to the perception that they are less credible than other types of carbon credits (Chen et al., 2023).

These challenges have been exacerbated by the limited availability of funding for forest projects and a lack of standardized methodologies for measuring and verifying carbon sequestration. However, recent developments in measurement and verification technologies, as well as the emergence of new voluntary

carbon markets and standards, may provide opportunities for forestry-based projects to overcome these challenges and play a more significant role in global efforts to mitigate climate change (Ince, 2022).

On the other hand, Paulownia, also known as the "empress tree," is a fast-growing hardwood species that has become increasingly popular as an investment opportunity in recent years. The tree's ability to grow rapidly, even on poor soils, makes it an attractive option for timber production as well as for carbon sequestration and ecosystem restoration projects. However, as with any investment opportunity, there are both potential rewards and risks associated with investing in Paulownia projects (Yadav et al., 2013). One of the primary benefits of investing in Paulownia projects is the fast growth rate, which allows for relatively quick returns on investment. Additionally, the high-quality wood of the tree is in demand for a variety of uses, including furniture, flooring, and musical instruments, further increasing the potential for profitability (Fos et al., 2023).

Another potential benefit of Paulownia projects is their ability to sequester carbon. As trees grow, they absorb CO_2 from the atmosphere, helping mitigate climate change. In addition, Paulownia can be planted on degraded or marginal land, helping restore ecosystems and providing a variety of additional benefits, such as improved soil health and increased biodiversity (Marana, 2018). In addition to the importance of Paulownia culture in the fields of CO_2 mitigation, biomass, and wood production, this tree has great commercial potential due to the bioproducts it could produce. Paulownia wood can be used in the production of wood plastics and their composites (Khanjanzadeh et al., 2012; Ebrahimi et al., 2021), blackboards (Nelis et al., 2019), low-density woods (Li et al., 2018; Yu et al., 2018), lightweight particleboards (Nelis et al., 2018; Nelis and Mai, 2021), biopolymers (Rodríguez-Seoane et al., 2020), as well as energy sources (Zhang et al., 2017) such as bioethanol (Zhang et al., 2017; Kirikkaleli et al., 2022), biomethane (Janjić and Janjić, 2019), and biohydrogen (Zhang et al., 2022). In addition to the applications of Paulownia wood, the Paulownia flowers, leaves, and their remains can be utilized for medicinal (Yang et al., 2019; Adach et al., 2021; Dżugan et al., 2021; Huang et al., 2021; Nowak et al., 2022), animal feed (Al-Sagheer et al., 2019; Ganchev et al., 2019; Alagawany et al., 2022), and bioremediation applications (Tzvetkova et al., 2015; Miladinova-Georgieva et al., 2018a; Miladinova-Georgieva et al., 2018b). Despite these potential benefits, there are also several risks associated with investing in Paulownia projects (Ferguson et al., 2010).

One of the main risks is the potential for crop failure. Although Paulownia is known for its fast growth, it is also susceptible to disease, pests, and other environmental factors that can impact growth rates and yield. Additionally, the tree's rapid growth can make it more vulnerable to wind damage, which can result in significant losses. In addition to these risks, there are also several regulatory and legal considerations that investors in Paulownia projects should be aware of. Depending on the location of the plantation, there may be specific regulations related to forest management practices, land use, and environmental impacts that must be complied with. Failure to comply with these regulations can result in fines or legal action, which can have a significant impact on the profitability of the project (de Deus Ribeiro et al., 2021). Despite these risks, several strategies can be employed to minimize potential losses and maximize returns on investment in Paulownia projects. One approach is to diversify investments across multiple projects or regions, reducing the impact of any individual crop failure or market downturn. Additionally, investors can work with experienced plantation management teams that have a proven track record of success in Paulownia projects. This can help ensure that best practices are followed and that risks are minimized (Zhao et al., 2019; Oliveira et al., 2020).

6 Techno-economic scenario for Paulownia CO_2 capture

To achieve global climate targets by 2050, there will be greater demand for approximately 2000 commercial CO_2 capture projects and a rate of 70–100 commercial CO_2 capture projects y^{-1}, with a total capital investment ranging from 655 to 1,280 billion USD. This number clearly shows that these projects required large investments, which governments (Alprol et al., 2021; Ashour and Omran, 2022) have not been prepared to make in the required time (Bajaj, 2022). Biological CO_2 capture projects are the most sustainable, safe, and attractive solution that can overcome and mitigate high levels of atmospheric CO_2. Although the Paulownia tree, a terrestrial C4 plant, differs in its nature and habitats, they are both photosynthetic organisms and have a greater potential for biological CO_2 fixation than other terrestrial and aquatic plants (Mansour et al., 2022). Although biological CO_2 capture projects are seen as long-term, low-profitability, and high-risk environmental projects, recent microalgae-based CO_2 capture projects have proven otherwise. They are commercial, short-term, highly profitable, and low-risk. Additionally, these types of projects have a significant environmental impact by reducing high levels of atmospheric CO_2. However, to capture 1 million tons of atmospheric CO_2 over 10 years as a part of a megaproject, a technical and economic scenario for Paulownia trees is presented below. The cost of the used land is not included.

For wood production, Paulownia hybrid trees (Wu et al., 2014; Huseinovic et al., 2017) are mainly planted primarily at a distance of 4 m^2 × 4 m^2 (Zhao et al., 2019), with approximately 625 trees ha-^{1} (Icka et al., 2016b; Berdón Berdón et al., 2017). As reported by several studies (Newman et al., 1997; Popescu and Sabau, 2016; Zhao et al., 2019), the standard cycle duration for Paulownia trees' roundwood is 10 years. Based on this fact, the current study has selected 10 years as the ideal cycle duration for Paulownia trees. The study conducted by Jakubowski (Zhao et al., 2019) reported that there are ideal growing conditions for Paulownia trees for wood production in southern Europe and the Middle East. However, the crop yield of Paulownia trees varies based on several parameters, such as climate change, soil type, culture conditions, age, species, and cultivation regions. In Asia, at 16 and 21 years of age, *P. tomentosa* yields approximately 382.6 and 223 tons y^{-1} ha^{-1}, respectively (Joshi, 2015). In Bulgaria, after 2 and 4 years, *P. tomentosa* showed higher productivity (3.47 and 36.99 tons ha^{-1}, respectively) than the hybrid species (*P. elongata* × *P. fortunei*), (2.73 and 19.96 tons ha^{-1}, respectively) (Gyuleva et al., 2021). In China, at 80 and 90 years of age, Paulownia trees reached a wood volume of 34 m^3 and 44 m^3, respectively. In Spain, after 3 years, the total biomass of *P. fortune* was 3.34 tons ha^{-1} (Madejón et al., 2016).

TABLE 3 Technical and economic comparison of Paulownia trees, concerning the capture of 1 million tons of CO_2 over 10 years.

Technical comparison	Paulownia trees
Land use	Very high (4200 ha^{-1} 10-$year^{-1}$)
Produced biomass (tons)	568,301
CO_2 capture (million tons)	1.04
Biomass production	Fixed
Climate change impact	Impacted
Culture conditions	Natural
CO_2 sources	Atmospheric CO_2
CO_2 capture capacity	Little
CO_2 removal/fixation ability	Limited
Chemical hazards	Fertilizers remain in the soil
Diseases potential	Moderate
Sensitive to contaminants	Moderate
Risk	Moderate
CO_2-final-converted forms	Manly wood and leaves
Commercial applications (final products and coproducts)	Wood, leaves, medicinal, animal feed, and bioremediation applications
Time of return on investment (ROI)	Long (not less than 5 years)
Economical comparison	Million USD
Total cost of the investment	1,121
Total marketing values (return)	1,136
Net profit	8.56
Carbon credit	49.7

In Nepal, the average total biomass of *P. tomentosa* after 5 years was 19.50 tons ha^{-1} y^{-1} (Magar et al., 2018).

Based on the literature, proposed model, and calculations, in the best-case scenario to capture 1 million tons of CO_2 over 10 years using Paulownia trees, 1.5 million trees will be planted in approximately 2,400 ha^{-1} with a planting density of 625 trees ha^{-1} (the distance needed for each tree is approximately 4 m^2 × 4 m^2). Based on the literature, proposed model, calculations, and the best-case scenario, each Paulownia tree will gradually capture CO_2 ($CO_{2\text{-Eq.}}$) in the 1st, 2nd, 3rd, 4th, 5th, 6th, 7th, 8th, 9th, and 10th years as follows: 6.25, 12.50, 25.00, 27.50, 33.00, 42.90, 60.06, 93.09, 144.29, and 250 kg CO_2 $tree^{-1}$, respectively. For 1.5 million trees in 10 years, it will be calculated that all 1.5 M trees will gradually capture CO_2 as follows: 9,375; 18,750; 37,500; 41,250; 49,500; 64,350; 90,090; 139,635; 216,435; and 375,000 tons CO_2 1.5 million trees at 2,400 ha^{-1}.

After 10 years, the CO_2 captured by 1.5 million trees on 2,400 ha^{-1} is approximately 1.04 million tons of CO_2. According to Equations 6 and 5, to convert $CO_{2\text{-Eq.}}$ to CC (eq. 6) and then to TB (eq. 5), the constant factors 0.27273 and 0.5, respectively, should be used. Therefore, the total biomass of Paulownia trees yearly was calculated as follows: 5,114; 10,227; 20,455; 22,500; 27,000; 35,100; 49,140; 76,165; 118,055; and 204,545 tons, respectively. As a result, after 10 years, the total crop biomass (wood) of 1.5 million trees is approximately 568,301 tons (Sharma et al., 2020).

To establish a mass project over 10 years to capture 1.04 million tons of atmospheric CO_2 using Paulownia trees, 1.5 million trees will be planted on 2,400 ha^{-1} to produce 568,301 tons of total crop biomass (wood). The total cost (capital and operating costs) of the investment required for the planting of 1.5 million tons in 2,400 ha^{-1} over 10 years is approximately 1,128 billion USD. The total marketing value of Paulownia's wood (568,301 tons) is estimated at 1,136.6 billion USD (based on 2,000 USD ton^{-1} wood).

Our proposed scenario is based on the study by Testa et al. (2022), who evaluated the economic profitability of Paulownia and concluded that the highest profit of Paulownia is approximately USD 358 ha^{-1} y^{-1}, while the lowest profit is approximately USD 5 ha^{-1} y^{-1}. Furthermore, as described previously (Chen et al., 2020; Osman et al., 2021), the carbon allowance in 2023 is equivalent to approximately USD 47.25 tons of CO_2, which means that the equivalent carbon allowance of 1.04 million tons of CO_2 (captured by 1.5 million trees on 2,400 ha^{-1} 10-$year^{-1}$) is approximately 49.7 billion USD (based on the lowest estimated value reported for 2023). In conclusion, Table 3 shows a technical and economical comparison between Paulownia trees with respect to the capture of 1 million tons of atmospheric CO_2 over 10 years.

7 Conclusion and future perspectives

Reducing CO_2 emissions is a global priority. Thus, it is necessary to develop an appropriate approach to reduce or stabilize CO_2 levels in the atmosphere. First, CO_2 capture projects are long-term, low-profitable, and high-risk environmental projects. To achieve global climate goals by 2050, there is a greater demand for approximately 2000 commercial CO_2 capture projects, with an average of 70–100 commercial CO_2 capture projects per year, with a total capital investment ranging from 655 to 1,280 billion USD (Rassool, 2021). This figure clearly shows that the majority of CO_2 capture project funding will come from debt, financial markets, and sovereign wealth funds. Therefore, it is necessary to provide direct support for CO_2 capture projects on a large scale, especially in developing countries. In addition, this number clearly shows that these projects require high investments that governments were not prepared to spend in the required time. Therefore, the private sector should be encouraged to participate in this type of investment. Carbon credit pricing is the most effective way to encourage investors to expand and develop CO_2 capture technologies. It is essential to have enough attractive carbon pricing for CO_2 capture technology to become commercially viable, such as a carbon tax or carbon allowances, especially for investors. Private sector encouragement may include tax exemption and providing technologies with low facility prices. On the other hand, requiring flue and power plants to participate in financing such projects increases the carbon tax on the companies and factories that emit high CO_2 levels into the atmosphere, as well as on transport, shipping, and aviation companies (Rassool, 2021). These challenges make investors, as well as governments, not prefer this type of project. Therefore, it is necessary to find appropriate, sustainable, and profitable CO_2 capture projects that are efficient in reducing atmospheric CO_2 levels. Previously, many scientists focused on capturing atmospheric CO_2.

Today, scientists around the world are proposing a completely different new strategy. Scientists try not only to capture atmospheric CO_2 but also to use it straightaway for energy generation alongside other vital commercial applications by converting atmospheric CO_2 into several biologically bioactive carbonic compounds such as proteins, carbohydrates, and lipids. Therefore, the regeneration of bioenergy alongside the capture of atmospheric CO_2, in addition to the benefit of other carbonic bioactive compounds, is a wonderful concept and a likely solution to the global warming issue (Doda et al., 2021).

Based on the literature, recommended calculations, and equations, this review presents the latest developments in the use of Paulownia trees as a biological solution for capturing CO_2, with a focus on technical and economic aspects. The study provides a scenario for the implementation of a million ton CO_2 capture project using C4 Paulownia trees grown on 2,400 ha. The results demonstrate the profitability and feasibility of Paulownia trees as a large-scale CO_2 capture project and provide insights into the potential for investment and government support toward achieving global climate goals by 2050.

Author contributions

HG: conceptualization, funding acquisition, investigation, methodology, writing–original draft, and writing–review and editing. AB: investigation, writing–original draft, and writing–review and editing. ATM: investigation and writing–original draft. MA: investigation, writing–original draft, conceptualization, methodology, and writing–review and editing.

Funding

The author(s) declare that financial support was received for the research, authorship, and/or publication of this article. The authors extend their appreciation to the Deputyship for Research and Innovation, Ministry of Education in Saudi Arabia for funding this research work through the project number INSTV007.

Acknowledgments

The authors would like to acknowledge the Deanship of Scientific Research, Vice Presidency for Graduate Studies and Scientific Research, King Faisal University, Saudi Arabia.

Conflict of interest

The authors declare that the research was conducted in the absence of any commercial or financial relationships that could be construed as a potential conflict of interest.

The author(s) declared that they were an editorial board member of Frontiers, at the time of submission. This had no impact on the peer review process and the final decision.

Publisher's note

References

Abanades, J. C., Criado, Y. A., and Fernández, J. R. (2020). An air CO 2 capture system based on the passive carbonation of large Ca (OH) 2 structures. *Sustain. Energy and Fuels* 4, 3409–3417. doi:10.1039/d0se00094a

Abbasi, M., Pishvaee, M. S., and Bairamzadeh, S. (2020). Land suitability assessment for Paulownia cultivation using combined GIS and Z-number DEA: a case study. *Comput. Electron. Agric.* 176, 105666. doi:10.1016/j.compag.2020.105666

Abreu, M., Reis, A., Moura, P., Fernando, A. L., Luís, A., Quental, L., et al. (2020). Evaluation of the potential of biomass to energy in Portugal—conclusions from the CONVERTE project. *Energies* 13, 937. doi:10.3390/en13040937

Adach, W., Żuchowski, J., Moniuszko-Szajwaj, B., Szumacher-Strabel, M., Stochmal, A., Olas, B., et al. (2021). *In vitro* antiplatelet activity of extract and its fractions of Paulownia Clone *in vitro* 112 leaves. *Biomed. Pharmacother.* 137, 111301. doi:10.1016/j.biopha.2021.111301

Adams, J. C., and Engel, J. (2021). "Human-made risks and climate change with global heating," in *Life and its future* (Springer).

Aguaron, E., and Mcpherson, E. G. (2012). "Comparison of methods for estimating carbon dioxide storage by Sacramento's urban forest," in *Carbon sequestration in urban ecosystems* (Springer).

Akyildiz, M. H., and Kol Sahin, H. (2010). *Some technological properties and uses of paulownia*. wood: Paulownia tomentosa Steud.

Alagawany, M., Farag, M. R., Sahfi, M. E., Elnesr, S. S., Alqaisi, O., El-Kassas, S., et al. (2022). Phytochemical characteristics of Paulownia trees wastes and its use as unconventional feedstuff in animal feed. *Anim. Biotechnol.* 33, 586–593. doi:10.1080/10495398.2020.1806074

Alotaibi, M. D., Alharbi, B. H., Al-Shamsi, M. A., Alshahrani, T. S., Al-Namazi, A. A., Alharbi, S. F., et al. (2020). Assessing the response of five tree species to air pollution in Riyadh City, Saudi Arabia, for potential green belt application. *Environ. Sci. Pollut. Res.* 27, 29156–29170. doi:10.1007/s11356-020-09226-w

Alprol, A. E., Ashour, M., Mansour, A. T., Alzahrani, O. M., Mahmoud, S. F., and Gharib, S. M. (2021). Assessment of water quality and phytoplankton structure of eight alexandria beaches, southeastern mediterranean sea, Egypt. *J. Mar. Sci. Eng.* 9, 1328. doi:10.3390/jmse9121328

Al-Sagheer, A. A., Abd El-Hack, M. E., Alagawany, M., Naiel, M. A., Mahgoub, S. A., Badr, M. M., et al. (2019). Paulownia leaves as a new feed resource: chemical composition and effects on growth, carcasses, digestibility, blood biochemistry, and intestinal bacterial populations of growing rabbits. *Animals* 9, 95. doi:10.3390/ani9030095

Asai, T., Hara, N., Kobayashi, S., Kohshima, S., and Fujimoto, Y. (2008). Geranylated flavanones from the secretion on the surface of the immature fruits of Paulownia tomentosa. *Phytochemistry* 69, 1234–1241. doi:10.1016/j.phytochem.2007.11.011

Ashour, M., and Omran, A. M. (2022). Recent advances in marine microalgae production: highlighting human health products from microalgae in view of the coronavirus pandemic (COVID-19). *Fermentation* 8, 466. doi:10.3390/fermentation8090466

Bajaj, J. S. (2022). *Carbon credit and climate change nexus*. Climate change. Springer.

Benedetti, M., Vecchi, V., Barera, S., and Dall'osto, L. (2018). Biomass from microalgae: the potential of domestication towards sustainable biofactories. *Microb. Cell Factories* 17, 173–218. doi:10.1186/s12934-018-1019-3

Berdón Berdón, J., Montero Calvo, A., Royano Barroso, L., Parralejo Alcobendas, A., and González Cortés, J. (2017). Study of Paulownia's biomass production in mérida (badajoz), southwestern Spain. *Environ. Ecol. Res.* 5, 521–527. doi:10.13189/eer.2017.050709

Berrada, T., Engelhardt, L., Gibson, R., and Krueger, P. (2022). *The economics of sustainability linked bonds*. Swiss Finance Institute Research Paper.

Bhalla, P., and Bhattacharya, P. (2015). Urban biodiversity and green spaces in Delhi: a case study of new settlement and lutyens' Delhi. *J. Hum. Ecol.* 52, 83–96. doi:10.1080/09709274.2015.11906933

Boyer, J., and Touzard, J.-M. (2021). To what extent do an innovation system and cleaner technological regime affect the decision-making process of climate change adaptation? Evidence from wine producers in three wine clusters in France. *J. Clean. Prod.* 315, 128218. doi:10.1016/j.jclepro.2021.128218

Bushing, L. H. (2021). The Australian paradox: politics of an energy transition.

Buzan, R. L., Maxim, A., Odagiu, A., Balint, C., and Hartagan, R. M. (2018). Paulownia sp. used as an energetic plant, for the phytoremediation of soils and in agroforestry systems. *ProEnvironment Promediu* 11.

Carvajal, M. (2010). *Investigation into CO2 absorption of the most representative agricultural crops of the region of murcia*. Madrid: CSIC (Consejo Superior de Investigaciones Cientificas.

Chang, J., Qu, Z., Xu, R., Pan, K., Xu, B., Min, Y., et al. (2017). Assessing the ecosystem services provided by urban green spaces along urban center-edge gradients. *Sci. Rep.* 7, 11226–11229. doi:10.1038/s41598-017-11559-5

Chaudhry, S., Sidhu, G. P. S., and Paliwal, R. (2021). Restoring ecosystem services of degraded forests in a changing climate. *Handb. Ecol. Ecosyst. Eng.*, 353–375. doi:10.1002/9781119678595.ch19

Chen, D., Cheng, Y., Zhou, N., Chen, P., Wang, Y., Li, K., et al. (2020). Photocatalytic degradation of organic pollutants using TiO2-based photocatalysts: a review. *J. Clean. Prod.* 268, 121725. doi:10.1016/j.jclepro.2020.121725

Chen, J., Hu, S., Chen, L., Gu, J., Ge, F., and Wang, S. (2023). Optimal forest rotation from the viewpoint of carbon sequestration efficiency based on the gilpin-ayala model. *IAENG Int. J. Appl. Math.* 53.

Cheng, C.-l., Jia, X.-h., Xiao, C.-m., and Tang, W.-z. (2019). Paulownia C-geranylated flavonoids: their structural variety, biological activity and application prospects. *Phytochem. Rev.* 18, 549–570. doi:10.1007/s11101-019-09614-2

Chia, E. L., Fobissie, K., and Kanninen, M. (2016). Exploring opportunities for promoting synergies between climate change adaptation and mitigation in forest carbon initiatives. *Forests* 7, 24. doi:10.3390/f7010024

Chongpinitchai, A. R., and Williams, R. A. (2021). The response of the invasive princess tree (Paulownia *tomentosa*) to wildland fire and other disturbances in an Appalachian hardwood forest. *Glob. Ecol. Conservation* 29, e01734. doi:10.1016/j.gecco.2021.e01734

Chu, S., and Majumdar, A. (2012). Opportunities and challenges for a sustainable energy future. *nature* 488, 294–303. doi:10.1038/nature11475

De Deus Ribeiro, G. B., Batista, F. R. S., De Magalhães, M. A., Valverde, S. R., Carneiro, A. d. C. O., and Amaral, D. H. (2021). Techno-economic feasibility analysis of a eucalyptus-based power plant using woodchips. *Biomass Bioenergy* 153, 106218. doi:10.1016/j.biombioe.2021.106218

Deutz, S., and Bardow, A. (2021). Life-cycle assessment of an industrial direct air capture process based on temperature–vacuum swing adsorption. *Nat. Energy* 6, 203–213. doi:10.1038/s41560-020-00771-9

Doda, B., Theuer, S. L. H., Cames, M., Healy, S., and Schneider, L. (2021). Voluntary offsetting: credits and allowances. *Clim. Change* 4, 2021.

Domec, J. C., and Gartner, B. L. (2002). How do water transport and water storage differ in coniferous earlywood and latewood? *J. Exp. Bot.* 53, 2369–2379. doi:10.1093/jxb/erf100

Dong, Y., Fan, G., Zhao, Z., and Deng, M. (2014). Compatible solute, transporter protein, transcription factor, and hormone-related gene expression provides an indicator of drought stress in Paulownia fortunei. *Funct. Integr. genomics* 14, 479–491. doi:10.1007/s10142-014-0373-4

Dżugan, M., Miłek, M., Grabek-Lejko, D., Hęclik, J., Jacek, B., and Litwińczuk, W. (2021). Antioxidant activity, polyphenolic profiles and antibacterial properties of leaf extract of various paulownia spp. clones. *Agronomy* 11, 2001. doi:10.3390/agronomy11102001

Ebrahimi, H., Vaziri, V., Faraji, F., Aminian, H., and Jamalirad, L. (2021). The effect of using PET to Paulownia strands on physical and mechanical properties of OSB. *For. Wood Prod.* 74, 371–382.

E Silva, I. M. M., and Costa, H. K. M. (2021). The United Kingdom's experience in Carbon Capture and Storage projects: the current regulatory framework and related challenges. *Carbon Capture Storage Int. Energy Policy Law*, 141–153. doi:10.1016/B978-0-323-85250-0.00001-3

Ferguson, I., Bull, L., and Gorrie, G. (2010). Improving the investment climate for Australian forest industries. Growing green assets: Removing constraints to private sector investment in forestry in Asia and the Pacific, 27.

Fos, M., Oliver-Villanueva, J.-V., and Vazquez, M. (2023). Radial variation in anatomical wood characteristics and physical properties of Paulownia elongata x Paulownia fortunei hybrid Cotevisa 2 from fast-growing plantations. *Eur. J. Wood Wood Prod.* 81, 819–831. doi:10.1007/s00107-023-01941-8

Franz, E. (2007). From ornamental to detrimental? The incipient invasion of Central Europe by Paulownia tomentosa. *Preslia* 79, 377–389.

Fuhrer, E., and Molnar, S. (2003). *The amount of carbon stored in the live matter in Hungarian forests*. Faipar (Hungary).

Galán-Martín, Á., Pozo, C., Guillén-Gosálbez, G., Vallejo, A. A., and Esteller, L. J. (2015). Multi-stage linear programming model for optimizing cropping plan decisions under the new Common Agricultural Policy. *Land use policy* 48, 515–524. doi:10.1016/j.landusepol.2015.06.022

Ganchev, G., Ilchev, A., and Koleva, A. (2019). Digestibility and energy content of Paulownia (Paulownia elongata SY Hu) leaves. *Agric. Sci. Technol.* (1313-8820), 11.

Guidi, L., Lo Piccolo, E., and Landi, M. (2019). Chlorophyll fluorescence, photoinhibition and abiotic stress: does it make any difference the fact to be a C3 or C4 species? *Front. plant Sci.* 10, 174. doi:10.3389/fpls.2019.00174

Gyuleva, V. (2010). Micropropagation of hybryd paulownia from long-term preserved seeds. *Silva Balcan* 11, 45–58.

Gyuleva, V., Stankova, T., Zhiyanski, M., and Andonova, E. (2021). Five years growth of paulownia on two sites in Bulgaria. *For. Sci* 1, 11–22.

Haldar, A., and Sethi, N. (2021). Effect of institutional quality and renewable energy consumption on CO2 emissions– an empirical investigation for developing countries. *Environ. Sci. Pollut. Res.* 28, 15485–15503. doi:10.1007/s11356-020-11532-2

Hamdan, H. Z., and Houri, A. F. (2022). CO2 sequestration by propagation of the fast-growing Azolla spp. *Environ. Sci. Pollut. Res.* 29, 16912–16924. doi:10.1007/s11356-021-16986-6

Hatfield, R. D., Marita, J. M., Frost, K., Grabber, J., Ralph, J., Lu, F., et al. (2009). Grass lignin acylation: p-coumaroyl transferase activity and cell wall characteristics of C3 and C4 grasses. *Planta* 229, 1253–1267. doi:10.1007/s00425-009-0900-z

He, T., Vaidya, B., Perry, Z., Parajuli, P., and Joshee, N. (2016). Paulownia as a medicinal tree: traditional uses and current advances. *Eur. J. Med. plants* 14, 1–15. doi:10.9734/ejmp/2016/25170

Henry, B. (2023). Potential for soil carbon sequestration in Northern Australian grazing lands: a review of the evidence.

Hertel, D., Moser, G., Culmsee, H., Erasmi, S., Horna, V., Schuldt, B., et al. (2009). Below-and above-ground biomass and net primary production in a paleotropical natural forest (Sulawesi, Indonesia) as compared to neotropical forests. *For. Ecol. Manag.* 258, 1904–1912. doi:10.1016/j.foreco.2009.07.019

Hiloidhari, M., Baruah, D., Kumari, M., Kumari, S., and Thakur, I. (2019). Prospect and potential of biomass power to mitigate climate change: a case study in India. *J. Clean. Prod.* 220, 931–944. doi:10.1016/j.jclepro.2019.02.194

Hong, W. Y. (2022). A techno-economic review on carbon capture, utilisation and storage systems for achieving a net-zero CO2 emissions future. *Carbon Capture Sci. Technol.* 3, 100044. doi:10.1016/j.ccst.2022.100044

Huang, H., Szumacher-Strabel, M., Patra, A. K., Ślusarczyk, S., Lechniak, D., Vazirigohar, M., et al. (2021). Chemical and phytochemical composition, *in vitro* ruminal fermentation, methane production, and nutrient degradability of fresh and ensiled Paulownia hybrid leaves. *Animal Feed Sci. Technol.* 279, 115038. doi:10.1016/j.anifeedsci.2021.115038

Huseinovic, S., Osmanović, Z., Bektić, S., and Ahmetbegović, S. (2017). Paulownia elongata sy hu in function of improving the quality of the environment. *Periodicals Eng. Nat. Sci. (PEN)* 5. doi:10.21533/pen.v5i2.83

Icka, P., Damo, R., and Icka, E. (2016a). Paulownia tomentosa, a fast growing timber. *Ann. Valahia Univ. Targoviste Agric.* 10, 14–19. doi:10.1515/agr-2016-0003

Icka, P., Damo, R., and Icka, E. (2016b). Paulownia *tomentosa,* a fast growing timber. *Ann. Valahia Univ. Targoviste, Agric.* 10, 14–19. doi:10.1515/agr-2016-0003

Ince, O. F. (2022). *Economic and environmental effects of improved forest management and loblolly pine genotypes on carbon sequestration in the southeast US.* University of Georgia.

Jakubowski, M. (2022). Cultivation potential and uses of paulownia wood: a review. *Forests* 13, 668. doi:10.3390/f13050668

Jakubowski, M., Tomczak, A., Jelonek, T., and Grzywiński, W. (2018). Wykorzystanie drewna i możliwości uprawy drzew z rodzaju paulownia. *Acta Sci. Polonorum Silvarum Colendarum Ratio Industria Lignaria* 17.

Jamil, K., Liu, D., Gul, R. F., Hussain, Z., Mohsin, M., Qin, G., et al. (2021). Do remittance and renewable energy affect CO2 emissions? An empirical evidence from selected G-20 countries. *Energy and Environ.*, 0958305X211029636.

Janjić, Z., and Janjić, M. (2019). Paulownia, characteristics and perspectives of its exploitation. *Innovation Woodwork. Industry Eng. Des.*, 34–41.

Jo, H.-K. (2002). Impacts of urban greenspace on offsetting carbon emissions for middle Korea. *J. Environ. Manag.* 64, 115–126. doi:10.1006/jema.2001.0491

Joshi, N. R. (2015). Development of allometric equations for Paulownia tomentosa (Thunb.) to estimate biomass and carbon stocks: an assessment from the ICIMOD Knowledge Park, Godavari, Nepal. *Int. Centre Integr. Mt. Dev*.

Kadlec, J., Novosadová, K., and Pokorný, R. (2021). Preliminary results from a plantation of semi-arid hybrid of Paulownia Clone *in vitro* 112® under conditions of the Czech Republic from the first two years. *Balt.* 27, 18–25. doi:10.46490/bf477

Kaletnik, G., Pryshliak, N., and Tokarchuk, D. (2021). Potential of production of energy crops in Ukraine and their processing on solid biofuels. *Ecol. Engeneering Environ. Technol.* 22. 3, 59–70. doi:10.12912/27197050/135447

Keith, D. W., Holmes, G., Angelo, D. S., and Heidel, K. (2018). A process for capturing CO2 from the atmosphere. *Joule* 2, 1573–1594. doi:10.1016/j.joule.2018.05.006

Khan, F. A., and Ansari, A. A. (2005). Eutrophication: an ecological vision. *botanical Rev.* 71, 449–482. doi:10.1663/0006-8101(2005)071[0449:eaev]2.0.co;2

Khanjanzadeh, H., Bahmani, A. A., Rafighi, A., and Tabarsa, T. (2012). Utilization of bio-waste cotton (Gossypium hirsutum L.) stalks and underutilized paulownia (paulownia fortunie) in wood-based composite particleboard. *Afr. J. Biotechnol.* 11, 8045–8050. doi:10.5897/ajb12.288

Kheyrodin, H., and Kheyrodin, S. (2017). CO2 gas exchange in Crassulacean acid metabolism and C3 and C4 plants. *Int. J. Adv. Res. Biol. Sci.* 4, 36–43.

Kircher, M. (2022). Economic trends in the transition into a circular bioeconomy. *J. Risk Financial Manag.* 15, 44. doi:10.3390/jrfm15020044

Kirikkaleli, D., Güngör, H., and Adebayo, T. S. (2022). Consumption-based carbon emissions, renewable energy consumption, financial development and economic growth in Chile. *Bus. Strategy Environ.* 31, 1123–1137. doi:10.1002/bse.2945

Kobayashi, S., Asai, T., Fujimoto, Y., and Kohshima, S. (2008). Anti-herbivore structures of Paulownia tomentosa: morphology, distribution, chemical constituents and changes during shoot and leaf development. *Ann. Bot.* 101, 1035–1047. doi:10.1093/aob/mcn033

Kozakiewicz, P., Laskowka, A., and Ciołek, S. (2020). A study of selected features of Shan Tong variety of plantation paulownia and its wood properties. *Ann. Wars. Univ. Life Sci. SGGW For. Wood Technol* 111, 116–123. doi:10.5604/01.3001.0014.6904

Kralicek, K., Huy, B., Poudel, K. P., Temesgen, H., and Salas, C. (2017). Simultaneous estimation of above-and below-ground biomass in tropical forests of Viet Nam. *For. Ecol. Manag.* 390, 147–156. doi:10.1016/j.foreco.2017.01.030

Lachowicz, H., and Giedrowicz, A. (2020a). Characteristics of the technical properties of Paulownia COTE-2 wood. *Sylwan* 164, 414–423.

Lachowicz, H., and Giedrowicz, A. (2020b). Charakterystyka jakości technicznej drewna paulowni COTE– 2. *Sylwan* 164, 414–423.

Lefvert, A., Rodriguez, E., Fridahl, M., Grönkvist, S., Haikola, S., and Hansson, A. (2022). What are the potential paths for carbon capture and storage in Sweden? A multi-level assessment of historical and current developments. *Energy Res. Soc. Sci.* 87, 102452. doi:10.1016/j.erss.2021.102452

Li, H., Jiang, X., Ramaswamy, H. S., Zhu, S., and Yu, Y. (2018). High-pressure treatment effects on density profile, surface roughness, hardness, and abrasion resistance of paulownia wood boards. *Trans. ASABE* 61, 1181–1188. doi:10.13031/trans.12718

Li, P., Lou, G., Cai, X., Zhang, B., Cheng, Y., and Wang, H. (2020). Comparison of the complete plastomes and the phylogenetic analysis of Paulownia species. *Sci. Rep.* 10, 2225. doi:10.1038/s41598-020-59204-y

Macdicken, K. G. (1997). A guide to monitoring carbon storage in forestry and agroforestry projects.

Madejón, P., Alaejos, J., García-Álbala, J., Fernández, M., and Madejón, E. (2016). Three-year study of fast-growing trees in degraded soils amended with composts: effects on soil fertility and productivity. *J. Environ. Manag.* 169, 18–26. doi:10.1016/j.jenvman.2015.11.050

Madhoushi, M., and Boskabadi, Z. (2019). Relationship between the dynamic and static modulus of elasticity in standing trees and sawn lumbers of Paulownia fortune planted in Iran. *Maderas. Cienc. Tecnol.* 21, 35–44.

Magar, L. B., Khadka, S., Joshi, J. R. R., Pokharel, U., Rana, N., Thapa, P., et al. (2018). Total biomass carbon sequestration ability under the changing climatic condition by Paulownia *tomentosa* Steud. *Int. J. Appl. Sci. Biotechnol.* 6, 220–226. doi:10.3126/ijasbt.v6i3.20772

Magar, L. B., Shrestha, N., Khadka, S., Joshi, J. R., Acharya, J., Gyanwali, G. C., et al. (2016). Challenges and opportunity of *in vitro* propagation of Paulownia tomentosa Steud for commercial production in Nepal. *Int. J. Appl. Sci. Biotechnol.* 4, 155–160. doi:10.3126/ijasbt.v4i2.14752

Mansour, A. T., Ashour, M., Alprol, A. E., and Alsaqufi, A. S. (2022). Aquatic plants and aquatic animals in the context of sustainability: cultivation techniques, integration, and blue revolution. *Sustainability* 14, 3257. doi:10.3390/su14063257

Marana, B. (2018). A green GIS solution against air pollution in the Province of bergamo: the paulownia tree. *J. Geogr. Inf. Syst.* 10, 193–218. doi:10.4236/jgis.2018.102010

Martínez Pastur, G., Perera, A. H., Peterson, U., and Iverson, L. R. (2018). Ecosystem services from forest landscapes: an overview. *Ecosyst. Serv. For. landscapes broadscale considerations*, 1–10.

Miladinova-Georgieva, K., Geneva, M., and Markovska, Y. (2018a). Effects of EDTA and citrate addition to the soil on C4 photosynthetic enzymes and biochemical indicators for heavy metal tolerance in two paulownia hybrids. *Plant Physiol.* 8, 68–81.

Miladinova-Georgieva, K., Ivanova, K., Georgieva, T., Geneva, M., Petrov, P., Stancheva, I., et al. (2018b). EDTA and citrate impact on heavy metals phytoremediation using paulownia hybrids. *Int. J. Environ. Pollut.* 63, 31–46. doi:10.1504/ijep.2018.092985

Mohamad, M. E., Awad, A., Majrashi, A., Abd Esadek, O., El-Saadony, M. T., Saad, A. M., et al. (2022). *In vitro* study on the effect of cytokines and auxins addition to growth medium on the micropropagation and rooting of Paulownia species (Paulownia hybrid and Paulownia tomentosa). *Saudi J. Biol. Sci.* 29, 1598–1603. doi:10.1016/j.sjbs.2021.11.003

Mondal, M., Goswami, S., Ghosh, A., Oinam, G., Tiwari, O., Das, P., et al. (2017). Production of biodiesel from microalgae through biological carbon capture: a review. *3 Biotech.* 7, 99–21. doi:10.1007/s13205-017-0727-4

Morozova, I., Oechsner, H., Roik, M., Hülsemann, B., and Lemmer, A. (2020). Assessment of areal methane yields from energy crops in Ukraine, best practices. *Appl. Sci.* 10, 4431. doi:10.3390/app10134431

Nelis, P. A., Henke, O., and Mai, C. (2019). Comparison of blockboards with core layers made of kiri (Paulownia spp.) and of spruce (Picea abies) regarding mechanical properties. *Eur. J. Wood Wood Prod.* 77, 323–326. doi:10.1007/s00107-019-01381-3

Nelis, P. A., and Mai, C. (2021). The influence of low-density (Paulownia spp.) and high-density (Fagus sylvatica L.) wood species on various characteristics of light and medium-density three-layered particleboards. *Wood Material Sci. Eng.* 16, 21–26. doi:10.1080/17480272.2019.1659850

Nelis, P. A., Michaelis, F., Krause, K. C., and Mai, C. (2018). Kiri wood (Paulownia tomentosa): can it improve the performance of particleboards? *Eur. J. wood wood Prod.* 76, 445–453. doi:10.1007/s00107-017-1222-7

Newell, R., Raimi, D., Villanueva, S., and Prest, B. (2021). Global energy outlook 2021: pathways from Paris. *Resour. Future* 8.

Newman, S., Bennett, K., and Wu, Y. (1997). Performance of maize, beans and ginger as intercrops in Paulownia plantations in China. *Agrofor. Syst.* 39, 23–30. doi:10.1023/a:1005938310106

Nouri, H., Borujeni, S. C., and Hoekstra, A. Y. (2019). The blue water footprint of urban green spaces: an example for Adelaide, Australia. *Landsc. urban Plan.* 190, 103613. doi:10.1016/j.landurbplan.2019.103613

Nowak, B., Moniuszko-Szajwaj, B., Skorupka, M., Puchalska, J., Kozłowska, M., Bocianowski, J., et al. (2022). Effect of paulownia leaves extract levels on *in vitro* ruminal fermentation, microbial population, methane production, and fatty acid biohydrogenation. *Molecules* 27, 4288. doi:10.3390/molecules27134288

Nowak, D. J., and Crane, D. E. (2002). Carbon storage and sequestration by urban trees in the USA. *Environ. Pollut.* 116, 381–389. doi:10.1016/s0269-7491(01)00214-7

Nunez, C. (2019). *Carbon dioxide levels are at a record high*. National geographic, 13. Here's what you need to know.

Olave, R., Forbes, G., Muñoz, F., and Lyons, G. (2015). Survival, early growth and chemical characteristics of Paulownia trees for potential biomass production in a cool temperate climate. *Ir. For*.

Oliveira, N., Pérez-Cruzado, C., Cañellas, I., Rodríguez-Soalleiro, R., and Sixto, H. (2020). Poplar short rotation coppice plantations under Mediterranean conditions: the case of Spain. *Forests* 11, 1352. doi:10.3390/f11121352

Ols, C., and Bontemps, J.-D. (2021). Pure and even-aged forestry of fast-growing conifers under climate change: on the need for a silvicultural paradigm shift. *Environ. Res. Lett.* 16, 024030. doi:10.1088/1748-9326/abd6a7

Osman, A. I., Hefny, M., Abdel Maksoud, M., Elgarahy, A. M., and Rooney, D. W. (2021). Recent advances in carbon capture storage and utilisation technologies: a review. *Environ. Chem. Lett.* 19, 797–849. doi:10.1007/s10311-020-01133-3

Palma, A., Loaiza, J. M., Díaz, M. J., García, J. C., Giráldez, I., and López, F. (2021). Tagasaste, leucaena and paulownia: three industrial crops for energy and hemicelluloses production. *Biotechnol. Biofuels* 14, 89–14. doi:10.1186/s13068-021-01930-0

Parra-Lopez, C., Sayadi-Gmada, S., and Duran-Zuazo, V. H. (2015). Production and use of biomass from short-rotation plantations in Andalusia, southern Spain: limitations and opportunities. *New Medit.* 14, 40–49.

Pedersen, J. T. S., Van Vuuren, D., Gupta, J., Santos, F. D., Edmonds, J., and Swart, R. (2022). IPCC emission scenarios: how did critiques affect their quality and relevance 1990–2022? *Glob. Environ. Change* 75, 102538. doi:10.1016/j.gloenvcha.2022.102538

Pieratti, D. (2020). *Published. Writing like a reader: the power of imitation in writing instruction*. MLA Annual Convention. MLA.

Pleguezuelo, C. R. R., Zuazo, V. H. D., Bielders, C., Bocanegra, J. A. J., Pereatorres, F., and Martínez, J. R. F. (2015). Bioenergy farming using woody crops. A review. *Agron. Sustain. Dev.* 35, 95–119. doi:10.1007/s13593-014-0262-1

Popescu, A., and Sabau, L. (2016). "Paulownia Species" growing for saplings in pots in Romania: technological aspects and comparative expenses, incomes and profit. *Sci. Pap. Ser. Manag. Econ. Eng. Agric. Rural. Dev.* 16, 255–265.

Pörtner, H.-O., Roberts, D. C., Adams, H., Adler, C., Aldunce, P., Ali, E., et al. (2022). *Climate change 2022: impacts, adaptation and vulnerability*. IPCC Sixth Assessment Report.

Pożoga, M., Olewnicki, D., and Jabłońska, L. (2019). *In vitro* propagation protocols and variable cost comparison in commercial production for paulownia tomentosa × paulownia fortunei hybrid as a renewable energy source. *Appl. Sci.* 9, 2272. doi:10.3390/app9112272

Prasad, R., Gupta, S. K., Shabnam, N., Oliveira, C. Y. B., Nema, A. K., Ansari, F. A., et al. (2021). Role of microalgae in global CO2 sequestration: physiological mechanism, recent development, challenges, and future prospective. *Sustainability* 13, 13061. doi:10.3390/su132313061

Ram, S., Majumder, S., Chaudhuri, P., Chanda, S., Santra, S., Chakraborty, A., et al. (2015). A review on air pollution monitoring and management using plants with special reference to foliar dust adsorption and physiological stress responses. *Crit. Rev. Environ. Sci. Technol.* 45, 2489–2522. doi:10.1080/10643389.2015.1046775

Rassool, D. (2021). *Unlocking private finance to support CCS investments*. Global CCS Institute.

Robards, T. (2008). A review of the accuracy of urban forestry biomass functions: utility for the California Climate Action Registry Protocol.

Rodríguez-Seoane, P., Domínguez, H., and Torres, M. D. (2020). Mechanical characterization of biopolymer-based hydrogels enriched with Paulownia extracts recovered using a green technique. *Appl. Sci.* 10, 8439. doi:10.3390/app10238439

Roeland, S., Moretti, M., Amorim, J. H., Branquinho, C., Fares, S., Morelli, F., et al. (2019). Towards an integrative approach to evaluate the environmental ecosystem services provided by urban forest. *J. For. Res.* 30, 1981–1996. doi:10.1007/s11676-019-00916-x

Sacchelli, S., Fabbrizzi, S., Bertocci, M., Marone, E., Menghini, S., and Bernetti, I. (2017). A mix-method model for adaptation to climate change in the agricultural sector: a case study for Italian wine farms. *J. Clean. Prod.* 166, 891–900. doi:10.1016/j.jclepro.2017.08.095

Sage, R. F., and Sultmanis, S. (2016). Why are there no C4 forests? *J. plant physiology* 203, 55–68. doi:10.1016/j.jplph.2016.06.009

Santori, G., Charalambous, C., Ferrari, M.-C., and Brandani, S. (2018). Adsorption artificial tree for atmospheric carbon dioxide capture, purification and compression. *Energy* 162, 1158–1168. doi:10.1016/j.energy.2018.08.090

Santos, M. G., Davey, P. A., Hofmann, T. A., Borland, A., Hartwell, J., and Lawson, T. (2022). Stomatal and mesophyll responses tissue to in light, Vicia faba CO2, and kalanchoë fedtschenkoi. *Stomatal Biol. Beyond*.

Schneiderová, K., and Šmejkal, K. (2015). Phytochemical profile of paulownia tomentosa (thunb). Steud. *Phytochem. Rev.* 14, 799–833. doi:10.1007/s11101-014-9376-y

Secinaro, S., Brescia, V., Calandra, D., and Biancone, P. (2020). Employing bibliometric analysis to identify suitable business models for electric cars. *J. Clean. Prod.* 264, 121503. doi:10.1016/j.jclepro.2020.121503

Sharma, R., Pradhan, L., Kumari, M., and Bhattacharya, P. (2020). Assessment of carbon sequestration potential of tree species in amity university campus Noida. *Environ. Sci. Proc.* 3, 52.

Shreyash, N., Sonker, M., Bajpai, S., Tiwary, S. K., Khan, M. A., Raj, S., et al. (2021). The review of carbon capture-storage technologies and developing fuel cells for enhancing utilization. *Energies* 14, 4978. doi:10.3390/en14164978

Sikkema, R., Proskurina, S., Banja, M., and Vakkilainen, E. (2021). How can solid biomass contribute to the EU's renewable energy targets in 2020, 2030 and what are the GHG drivers and safeguards in energy-and forestry sectors? *Renew. Energy* 165, 758–772. doi:10.1016/j.renene.2020.11.047

Silva Araújo, J., Aires Souza, J. T., Dos Santos Félix, E., De Cássia Alves, R., De Oliveira Filho, T. J., and Cunha De Lira, E. (2022). Gas exchange in genotypes of Nopalea cochenillifera in different seasons and evaluations times. *Acta Bot. Croat.* 81, 177–184. doi:10.37427/botcro-2022-015

Singh, S., Bhattacharya, P., and Gupta, N. (2018). Dust particles characterization and innate resistance for Thevetia peruviana in different land-use pattern of urban area. *Int. J. Environ. Sci. Technol.* 15, 1061–1072. doi:10.1007/s13762-017-1461-5

Šmejkal, K., Grycová, L., Marek, R., Lemiere, F., Jankovská, D., Forejtníková, H., et al. (2007). C-geranyl compounds from Paulownia tomentosa fruits. *J. Nat. Prod.* 70, 1244–1248. doi:10.1021/np070063w

Snow, W. A. (2015). Ornamental, crop, or invasive? The history of the Empress tree (Paulownia) in the USA. *For. Trees Livelihoods* 24, 85–96. doi:10.1080/14728028.2014.952353

Stankova, T., Gyuleva, V., Dimitrov, D., and Popov, E. (2019). Allometric relationships for estimation of aboveground woody biomass of two clones Paulownia at juvenile age. *Nauka za gorata* 55, 43–54.

Stephenson, P. G., Moore, C. M., Terry, M. J., Zubkov, M. V., and Bibby, T. S. (2011). Improving photosynthesis for algal biofuels: toward a green revolution. *Trends Biotechnol.* 29, 615–623. doi:10.1016/j.tibtech.2011.06.005

Steyn, M., and Havercroft, I. (2021). Brief: inclusion of a CCS method under the emissions reduction fund.

Strohbach, M. W., Arnold, E., and Haase, D. (2012). The carbon footprint of urban green space—a life cycle approach. *Landsc. Urban Plan.* 104, 220–229. doi:10.1016/j.landurbplan.2011.10.013

Stuepp, C. A., Zuffellato-Ribas, K. C., Koehler, H. S., and Wendling, I. (2015). Rooting mini-cuttings of Paulownia fortunei var. mikado derived from clonal mini-garden. *Rev. Árvore* 39, 497–504. doi:10.1590/0100-67622015000300010

Suryawanshi, M., Patel, A., Kale, T., and Patil, P. (2014). Carbon sequestration potential of tree species in the environment of North Maharashtra University Campus, Jalgaon (MS) India. *Biosci. Discov.* 5, 175–179.

Temirov, J., Shukurova, G., and Klichov, I. (2021). "Published. Study on the influence of stimulants on the rooting of the paulownia (paulownia) and tulip (liriodendron tulipifera) trees during the propagation by cuttings," in IOP Conference Series: Earth and Environmental Science (IOP Publishing).

Testa, R., Schifani, G., Rizzo, G., and Migliore, G. (2022). Assessing the economic profitability of Paulownia as a biomass crop in Southern Mediterranean area. *J. Clean. Prod.* 336, 130426. doi:10.1016/j.jclepro.2022.130426

Thevs, N., Baier, C., and Aliev, K. (2021). Water productivity of poplar and paulownia on two sites in Kyrgyzstan, central Asia. *J. Water Resour. Prot.* 13, 293–308. doi:10.4236/jwarp.2021.134018

Turan, G., Zapantis, A., Kearns, D., Tamme, E., Staib, C., Zhang, T., et al. (2021). *Global status of CCS 2021*. CCS Accelerating to net zero.

Turner, K., Race, J., Alabi, O., Katris, A., and Swales, J. K. (2021). Policy options for funding carbon capture in regional industrial clusters: what are the impacts and trade-offs involved in compensating industry competitiveness loss? *Ecol. Econ.* 184, 106978. doi:10.1016/j.ecolecon.2021.106978

Tzvetkova, N., Miladinova, K., Ivanova, K., Georgieva, T., Geneva, M., and Markovska, Y. (2015). Possibility for using of two Paulownia lines as a tool for remediation of heavy metal contaminated soil. *J. Environ. Biol.* 36, 145–151.

Van Der Gaast, W., Sikkema, R., and Vohrer, M. (2018). The contribution of forest carbon credit projects to addressing the climate change challenge. *Clim. Policy* 18, 42–48. doi:10.1080/14693062.2016.1242056

Vega, F., Baena-Moreno, F., Fernandez, L. M. G., Portillo, E., Navarrete, B., and Zhang, Z. (2020). Current status of CO2 chemical absorption research applied to CCS: towards full deployment at industrial scale. *Appl. Energy* 260, 114313. doi:10.1016/j.apenergy.2019.114313

Verma, P., and Ghosh, P. K. (2023). The economics of Forest carbon sequestration: a bibliometric analysis. *Environ. Dev. Sustain.* 26, 2989–3019. doi:10.1007/s10668-023-02922-w

Wang, T., Zhang, X., Ma, Y., and Wang, Y. (2023). Risk contagion and decision-making evolution of carbon market enterprises: comparisons with China, the United States, and the European Union. *Environ. Impact Assess. Rev.* 99, 107036. doi:10.1016/j.eiar.2023.107036

Winter, K., and Holtum, J. A. (2017). Facultative crassulacean acid metabolism (CAM) in four small C3 and C4 leaf-succulents. *Aust. J. Bot.* 65, 103–108. doi:10.1071/bt16015

Woods, V. (2008a). *Paulownia as a novel biomass crop for northern Ireland? Agri-food and bioscience Institute*. Occasional publication.

Woods, V. (2008b). "Paulownia as a novel biomass crop for Northern Ireland? a review of current knowledge," in *Hillsborough, Co. Down: agri-food and biosciences Institute, global research unit* (Occasional Publication).

Wu, L., Wang, B., Qiao, J., Zhou, H., Wen, R., Xue, J., et al. (2014). Effects of trunk-extension pruning at different intensities on the growth and trunk form of Paulownia fortunei. *For. Ecol. Manag.* 327, 128–135. doi:10.1016/j.foreco.2014.05.008

Yadav, N. K., Vaidya, B. N., Henderson, K., Lee, J. F., Stewart, W. M., Dhekney, S. A., et al. (2013). A review of Paulownia biotechnology: a short rotation, fast growing multipurpose bioenergy tree. *Am. J. Plant Sci.* 4, 2070–2082. doi:10.4236/ajps.2013.411259

Yan, Y. H., Borhani, T., Subraveti, G., Pai, N., Prasad, V., Rajendran, A., et al. (2021). Harnessing the power of machine learning for carbon capture, utilisation, and storage (CCUS)–a state-of-the-art review. *Energy and Environ. Sci.* 14, 6122–6157. doi:10.1039/d1ee02395k

Yang, H., Zhang, P., Xu, X., Chen, X., Liu, Q., and Jiang, C. (2019). The enhanced immunological activity of Paulownia tomentosa flower polysaccharide on Newcastle disease vaccine in chicken. *Biosci. Rep.* 39. doi:10.1042/bsr20190224

Yi, W., Nadeem, F., Xu, G., Zhang, Q., Joshee, N., and Tahir, N. (2020). Modifying crystallinity, and thermo-optical characteristics of Paulownia biomass through ultrafine grinding and evaluation of biohydrogen production potential. *J. Clean. Prod.* 269, 122386. doi:10.1016/j.jclepro.2020.122386

Yu, Y., Jiang, X., Ramaswamy, H. S., Zhu, S., and Li, H. (2018). Effect of high-pressure densification on moisture sorption properties of Paulownia wood. *BioResources* 13, 2473–2486. doi:10.15376/biores.13.2.2473-2486

Yuen, J. Q., Ziegler, A. D., Webb, E. L., and Ryan, C. M. (2013). Uncertainty in below-ground carbon biomass for major land covers in Southeast Asia. *For. Ecol. Manag.* 310, 915–926. doi:10.1016/j.foreco.2013.09.042

Zhang, C., Chen, X., Wang, J., and Tan, L. (2017). Toxic effects of microplastic on marine microalgae *Skeletonema costatum*: interactions between microplastic and algae. *Environ. Pollut.* 220, 1282–1288. doi:10.1016/j.envpol.2016.11.005

Zhang, Q., Jin, P., Li, Y., Zhang, Z., Zhang, H., Ru, G., et al. (2022). Analysis of the characteristics of paulownia lignocellulose and hydrogen production potential via photo fermentation. *Bioresour. Technol.* 344, 126361. doi:10.1016/j.biortech.2021.126361

Zhao, Y., Qiao, J., Feng, Y., Wang, B., Duan, W., Zhou, H., et al. (2019). The optimal size of a Paulownia-crop agroforestry system for maximal economic return in North China Plain. *Agric. For. Meteorology* 269, 1–9. doi:10.1016/j.agrformet.2019.01.043

Zhu, X.-G., Long, S. P., and Ort, D. R. (2010). Improving photosynthetic efficiency for greater yield. *Annu. Rev. plant Biol.* 61, 235–261. doi:10.1146/annurev-arplant-042809-112206

Zhu, Z.-H., Chao, C.-J., Lu, X.-Y., and Xiong, Y. G. (1986). *Paulownia* in China: cultivation and utilization. International Development Research Centre.

Ziegler, A. D., Phelps, J., Yuen, J. Q., Webb, E. L., Lawrence, D., Fox, J. M., et al. (2012). Carbon outcomes of major land-cover transitions in SE Asia: great uncertainties and REDD+ policy implications. *Glob. change Biol.* 18, 3087–3099. doi:10.1111/j.1365-2486.2012.02747.x

Zuazo, V. H. D., Bocanegra, J. A. J., Torres, F. P., Pleguezuelo, C. R. R., and Martínez, J. R. F. (2013). Biomass yield potential of paulownia trees in a semi-arid Mediterranean environment (S Spain). *Int. J. Renew. Energy Res.* 3, 789–793.

frontiers | Frontiers in Environmental Science

TYPE Review
PUBLISHED 12 March 2024
DOI 10.3389/fenvs.2024.1363837

OPEN ACCESS

EDITED BY
Zhiyuan Hu,
Sun Yat-sen University, China

REVIEWED BY
Yuanjian Yang,
Nanjing University of Information Science and Technology, China
Xuelin Zhang,
Sun Yat-sen University, China

*CORRESPONDENCE
Ping Qi,
qiping929@tlu.edu.cn

RECEIVED 31 December 2023
ACCEPTED 28 February 2024
PUBLISHED 12 March 2024

CITATION
Shi T, Liu L, Wen X and Qi P (2024), Research progress on the synergies between heat waves and canopy urban heat island and their driving factors.
Front. Environ. Sci. 12:1363837.
doi: 10.3389/fenvs.2024.1363837

Research progress on the synergies between heat waves and canopy urban heat island and their driving factors

Tao Shi[1,2,3], Lei Liu[2], XiangCheng Wen[2] and Ping Qi[1,3]*

[1]School of Mathematics and Computer Science, Tongling University, Tongling, Anhui, China, [2]Wuhu Meteorological Bureau, Wuhu, Anhui, China, [3]Anhui Engineering Research Center of Intelligent Manufacturing of Copper-based Materials, Tongling, Anhui, China

Under the background of global warming and accelerating urbanization, the interaction between heat waves (HWs) and canopy urban heat island (CUHI) has become one of the focuses in the field of global climate change research. This paper comprehensively reviewed and summarized the research process on the synergies of HWs and CUHI and their influencing mechanism. The coupling effect between HWs and CUHI remains debated, which may be related to the use of different standards to define heat wave events. The spatiotemporal differences in the synergies between HWs and CUHI was also influenced by climate background and local circulation. For instance, scholars have reached different conclusions regarding the stronger synergistic effect between daytime and nighttime in cities with different climate backgrounds. In addition, the modulation of urban morphological structure to the synergies between HWs and CUHI cannot be ignored. In the future, it is necessary to adopt different definitions of HWs to systematically study the formation mechanism of urban excess warming from different climatic backgrounds, local circulation conditions, and urban morphologies.

KEYWORDS

heat wave, canopy urban heat island, synergies, climatic background, local circulation, urban morphologies

1 Introduction

HWs sually refer to the situation that the daily maximum temperature reaches or exceeds a certain threshold for several days (Tan et al., 2010; Perkins, 2015; Sun et al., 2017; Su and Dong, 2019; Zong et al., 2021). HWs are one of the important causes of diseases such as cardiovascular, respiratory, and digestive systems in the human body, and in extreme cases, they can directly lead to death (Fouillet et al., 2006; Zhang et al., 2018; He et al., 2021). Even in the period of global warming hiatus, the frequency and duration of HWs show an increasing trend, which poses a huge challenge to the health of people and the stable development of society (IPCC, 2021). In addition, urbanization has become an important driving force of regional and global warming (Seto et al., 2012; Shi et al., 2021). Canopy urban heat island is a phenomenon that the canopy urban temperature is higher than that in suburban and rural areas due to the change in the nature of the urban underlying surface and anthropogenic heat emission (Li et al., 2015; Shi et al., 2015; Yang et al., 2023). CUHI effect has become one of the most significant characteristics of urban climate, which has an

important impact on human health and socio-economic development (Gershunov et al., 2009; Ren et al., 2011; Luo and Lau, 2019; Yang et al., 2019).

The interaction between climate change and urbanization and its possible synergistic effects have become the focus of global climate change research (Seto et al., 2012). Urbanization has an impact on the indicators of HWs (Zong et al., 2021), and changes the distribution and intensity of high temperature fields in summer (Founda et al., 2015; Xue et al., 2023). The HWs and CUHI may also have a superimposed effect, even more than the sum of the effects of the two on the urban area (Basara et al., 2010). The frequency of HWs in urban stations increases significantly, the increasing degree of the number of HWs and the duration of HWs is also larger than that in non-urban stations (Mishra et al., 2015; Khan et al., 2020; Mughal et al., 2020; Zinzi et al., 2020). However, some scholars have observed completely different results (Basara et al., 2008; Basara et al., 2010; Ramamurthy and Bou-Zeid, 2017; Chew et al., 2020). Scholar have found that under the HWs condition, the CUHI intensity (CUHII) at nighttime in Melbourne and Adelaide is stronger than that at daytime, while the CUHII at nighttime in Perth is weaker than that at daytime (Rogers et al., 2019). Currently, there is no consensus on whether CUHI will intensify or weaken during heat waves periods.

With the acceleration of urbanization and aggregation of population, the CUHI effect is significant (Liu et al., 2007; Zheng et al., 2018; Yang et al., 2020), which intensifies the occurrence of regional excess warming (Li et al., 2015; Yoon et al., 2018; Zong et al., 2021) and seriously affects the health of residents (Gao et al., 2015; Jiang et al., 2019). The research on HWs and CUHI has been carried out for decades. Especially in recent years, the research results are very rich. This paper comprehensively reviewed the progress on the synergies of HWs and CUHI and their driving factors, in order to provide important theoretical basis and technical support for the construction of high temperature monitoring, prediction, and early warning systems, the improvement of living environment and urban planning management.

2 Difference in the research on the synergies between HWs and CUHI

Over the past few decades, major cities around the world have witnessed rapid expansion of construction land. The CUHI effect caused by urbanization is one of the typical urban climate characteristics (Ren et al., 2015; Yang et al., 2019). In parallel, climate change has led to a significant increase in the frequency of high temperature and heat wave events in most parts of the world (Su and Dong, 2019; Yang et al., 2023). The interaction between CUHI and regional extreme high temperatures cannot be overlooked.

Many scholars have carried out research on the synergies of HWs and CUHI. Some studies have demonstrated a synergistic effect between HWs and CUHI, further compounding the heat risk in urban (Jiang et al., 2019; Yang et al., 2023). Compared with the non-heat waves periods, the maximum CUHII of Beijing at nighttime during the heat waves periods increased by 1.26°C (Jiang et al., 2019), the average CUHII in Shanghai during the heat waves periods increased by 0.9°C (Yang et al., 2023), and the maximum CUHII in Seoul during the heat waves periods increased by 4.5°C (Ngarambe et al., 2020). During the heat waves periods, the average CUHII of 50 cities in the United States was 0.4°C–0.6°C higher than that during the non-heat waves periods (Zhao et al., 2018). During the heat waves periods in the northeast of the United States in 2016, the CUHII of New York City, Washington, and Baltimore was amplified by 1°C–2°C (Ramamurthy and Bou-Zeid, 2017). During the heat waves periods from 2013 to 2018, the CUHII of Shanghai increased by about 0.8°C (Ao et al., 2019). Also during the heat waves periods from 2013 to 2018, Jiang et al. (2019) found that the CUHII of Shanghai increased by 1.0°C, which was close to the research results of Ao et al. (2019), and 1.2°C and 0.9°C were observed in Beijing and Guangzhou. Zong et al. (2021) concluded that the increase of CUHII usually reached a minimum at 0900 and 1800 LST, and the peak often occurred at noon or at midnight (as shown in Figure 1).

Some studies showed that the synergies between HWs and CUHI are not obvious, and even the CUHII may decrease during heat waves periods (Richard et al., 2021). Rogers et al. (2019) found in their study on CUHI during heat waves periods and non-heat waves periods in Australian that the CUHI of nighttime in Perth weakened during heat waves periods. Compared with the non-heat waves periods, there was no CUHI enhancement in Philadelphia during the heat waves periods (Ramamurthy and Bou-Zeid, 2017). Scott et al. (2018) took 15 HWs in Baltimore from 2000 to 2015 as a composite event and found that there were no synergies between HWs and CUHI. After expanding the research scope to 54 cities, even the average CUHII tended to decrease during the heat waves periods. Richard et al. (2021) discovered that the maximum CUHII in Dijon (France) frequently occurs prior to or within the first few days of HWs, and subsequently diminishes during heat waves periods (As shown in Figure 2). Using ground observation data, Chew et al. (2020) discovered that, in contrast to non-heatwave periods, the CUHII does not intensify during heat waves periods. Specifically, the CUHII remains approximately 2.5°C during both heat waves periods and non-heat waves periods, and the results from the WRF simulation are consistent with the observation results. The above findings suggest that there are significant differences in the coupling effect between CUHI and HWs across different regions, necessitating in-depth research that takes into account specific research methods, the geographical location of the research subjects, and other influencing factors.

3 The influence of definition of HWs on the synergies of HWs and CUHI

HWs usually refer to sustained high-temperature weather processes. Most studies only utilize a single variable to identify heat waves, such as the highest daily temperature occurring during the afternoon or the lowest daily temperature occurring in the early morning hours (Bador et al., 2017; You et al., 2017; Oswald, 2018; Ren et al., 2020). Due to the diverse geographical environments, there are differences in the definition of HWs among different countries and regions. For instance, the World Meteorological Organization (WMO) recommends a heat wave event with a daily maximum temperature exceeding 32°C and lasting for more than 3 days. When the daytime heat wave index exceeds 40.5°C for

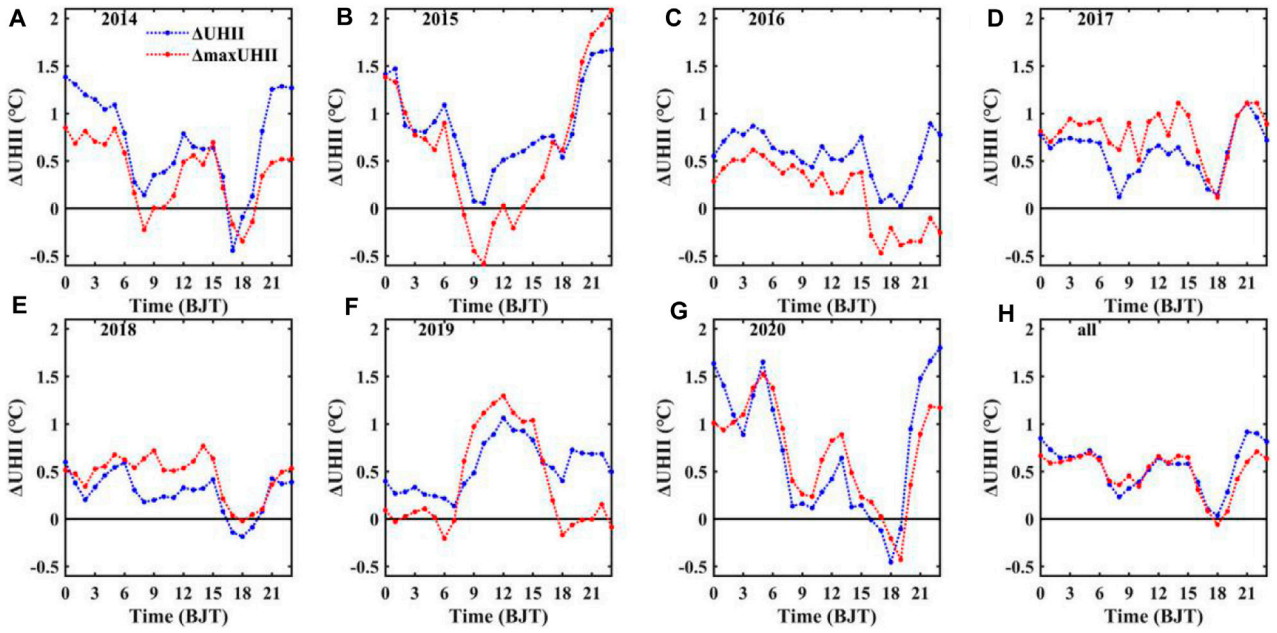

FIGURE 1
Diurnal variation of UHII between HW and NHW periods during summertime (June–August) 2014–2020 **(A–G)** and averaged value **(H)**. HW and NHW periods are indicated by red and blue, respectively. Lines denote average UHII values and shaded areas present the standard deviation of the average UHII values according to all urban reference stations (Zong et al., 2021).

three consecutive hours or is expected to exceed 46.5°C at any given time, the National Oceanic and Atmospheric Administration (NOAA) of the United States issues a high temperature warning. The Royal Netherlands Meteorological Institute (KNMI) defines a heatwave event as a daily maximum temperature exceeding 25°C and lasting for more than 5 days, with at least 3 days of maximum temperature exceeding 30°C. The heatwave standard set by the China Meteorological Administration (CMA) is that the maximum temperature exceeds 35°C for three consecutive days. Fenner et al. (2019a) noted that if hot weather episodes are defined as the ten percent hottest days or nights during May–September, and identified based on daytime conditions or nighttime conditions at inner-city sites, the nighttime CUHI is exacerbated. However, if hot weather episodes are identified based on nighttime conditions at rural sites, the night-time CUHII is reduced. Fenner et al. (2019b) provided an overview of all identified HWs by any of the ten definitions, illustrating the number of definitions that identify a certain calendar day as a HW day. As shown in Figure 3, different methods to identify and define the HWs could affect the occurrence time, duration, and frequency of HWs to a certain extent.

Some scholars have attempted to use bivariate identification of heat waves, such as a method that considers both the maximum and minimum daily temperatures to be above a threshold for multiple consecutive days (Kuglitsch et al., 2010; Chen and Li, 2017; Freychet et al., 2017). Additionally, there are studies that require the occurrence of extreme daytime high temperatures and extreme nighttime high temperatures to follow a specific order (Cowan et al., 2014; Oswald and Rood, 2014). As exemplified by Cowan et al. (2014), who specified that extreme daytime high temperatures must persist continuously for more than 3 days, with extreme nighttime high temperatures occurring on the second and third days. An and Zuo (2021) conducted a study on the HWs observed by meteorological stations in China. Taking Beijing as an example, they found that some HWs only involve extreme daytime high temperatures (Figure 4A), while others are limited to extreme nighttime high temperatures (Figure 4B). Additionally, there are instances where both daytime and nighttime high temperatures are part of the HWs. Furthermore, there is a specific temporal sequence in the occurrence of daytime and nighttime high temperatures (Figures 4C, D). Currently, there is no unified standard for the definition of heat waves, which can introduce some uncertainty in the attempt to gain a deeper understanding of the interaction between HWs and CUHI.

4 The influence of climate background and local circulation on the synergies between HWs and CUHI

In addition to the definition of HWs, the difference in the synergies between HWs and CUHI is also related to the climate background and local circulation (meteorological elements in the boundary layer such as solar radiation, wind speed, wind direction, humidity). HWs are usually caused by synoptic scale high-pressure systems (Matsumura et al., 2015), which severely inhibit the formation of convective clouds (He et al., 2015). Therefore, the synoptic background during heat waves periods is usually breezy and cloudless. Although the synergies of HWs and CUHI has been confirmed in different regions, different results have also been observed in cities under different climate backgrounds (Xie and Zhou, 2023). Liao et al. (2018) studied the HWs in China from 1961 to 2014 and believed that the increasing trends of HWs in

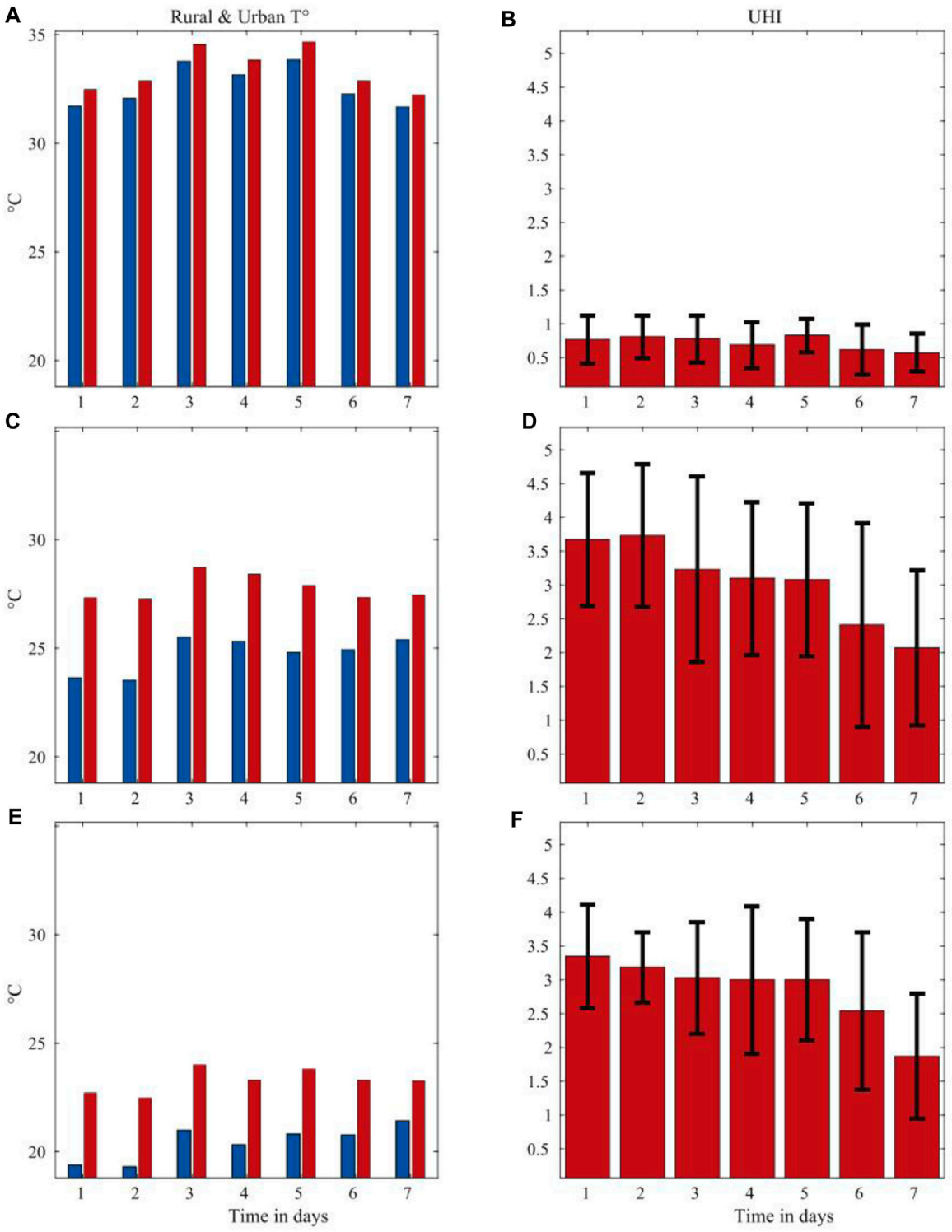

FIGURE 2
Mean rural temperature, urban temperature, and UHI intensity for the first 7 days during long HS&HW. **(A,B)**: Afternoon (1300–1700 UTC). **(C,D)** Evening (1900–2300 UTC). **(E,F)** Night (0000–0400 UTC). **(A)**, **(C)**, and **(E)**: T◦C (rural in blue, urban in red). **(B)**, **(D)**, and **(F)** UHI intensity in K (mean±SD indicated by black error bars) (Rogers et al., 2019).

urban areas are greater than those in rural areas in wet climates, suggesting a positive contribution of urbanization to HW trends. However, the urbanization contribution to HW trends is smaller and even negative in wet climates. Zhao et al. (2018) found that the synergistic effect of HWs and CUHI is more significant in temperate climate regions of the United States, but not in arid regions. Basara et al. (2010) studied the HWs in Oklahoma in 2008 and observed that the HW at nighttime was stronger than that at daytime. Jiang

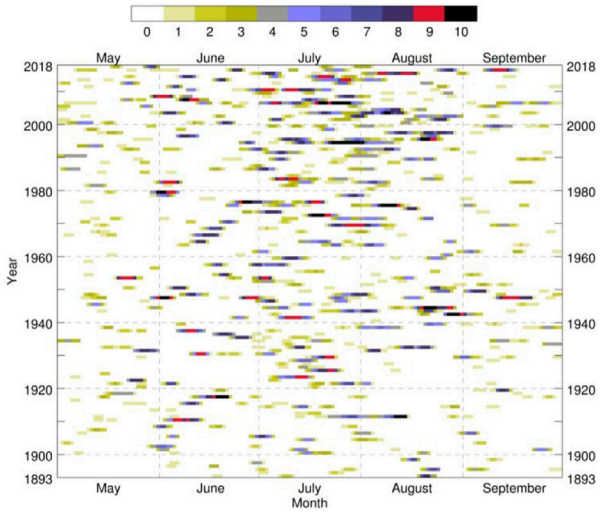

FIGURE 3
The occurrences of HWs at site Potsdam from 1893 to 2017 during the warm season (May–September) for ten different HW definitions. Each colour corresponds to the number of definitions agreeing for each day to be a HWs day and not to an individual HWs definition.

et al. (2019) studied the excess warming of megacities with different climate backgrounds and found that during the heat waves periods, the CUHII of Beijing (temperate semi humid monsoon climate) and Guangzhou (Marine subtropical monsoon climate) at nighttime was higher than that at daytime, while the diurnal variation of Shanghai (subtropical humid monsoon climate) heat island was completely opposite when selecting coastal stations as rural stations.

In addition to the climate background, the local circulation caused by different geographical environments has a significant impact on the temporal and spatial distribution of extreme high temperature in cities (Zhang et al., 2011; Zhou et al., 2020; Chen et al., 2022). Sea land breeze circulation is a secondary atmospheric circulation caused by uneven heating of the underlying surface, and is one of the most prominent mesoscale characteristics in coastal areas (Wagner et al., 2012; He et al., 2020). Yang et al. (2023) selected a day with sea–land breeze (24 September 2013) and a day without sea–land breeze (25 September 2013) and analyzed the diurnal variation of the wind vectors and the CUHII on these 2 days. The daytime CUHII was lower at the coastal sites on days with a sea–land breeze than on days without a sea–land breeze as a result of the influence of the transport of cold and wet air from the sea. The daytime CUHII at downwind urban sites was affected by heat transport and was stronger on days with a sea-land breeze (As shown in Figure 5).

The results confirm that sea breezes reduce the CUHII in coastal site of Shanghai. The formation principle of mountain-valley wind is similar to that of land and sea wind, which is caused by temperature and pressure (Xue et al., 2023). Due to the thermal difference between the valley and its surrounding air, the wind blows from the valley to the hillside at daytime and from the hillside to the valley at nighttime. Taking Lanzhou as an example, during HW periods, the WS increased at almost all moments (Figure 6A). The weather

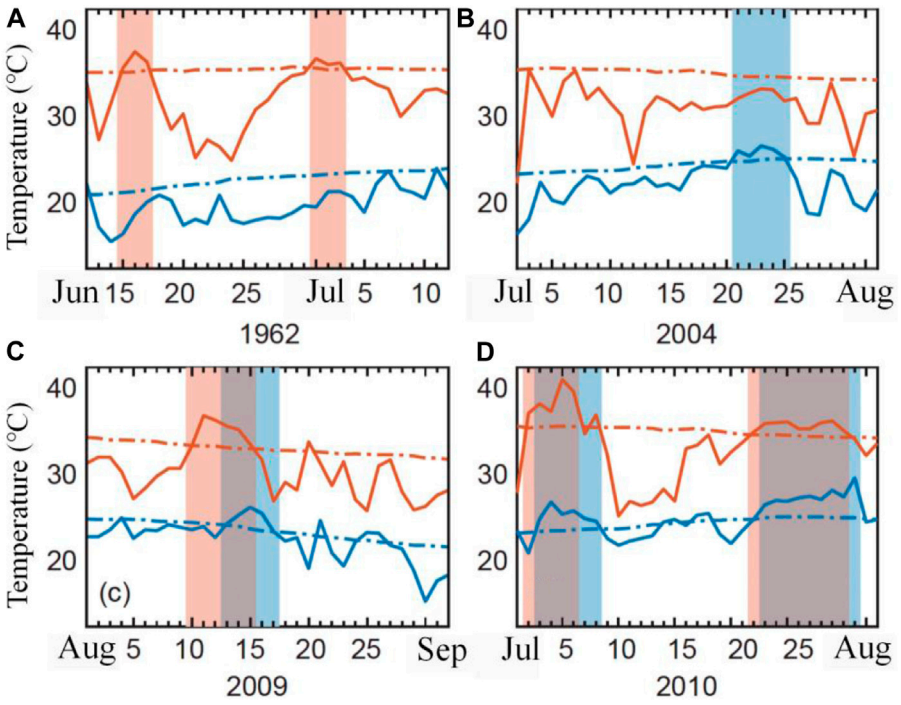

FIGURE 4
Observation cases of HWs in the Beijing Area. **(A–D)** are different heat waves periodss. The red solid line and dotted line are the time series of the daily maximum temperature and its 90th quantile, while the blue solid line and dotted line are the time series of the daily minimum temperature and its 90th quantile, respectively. The heat wave process is indicated by shadows (An and Zuo, 2021).

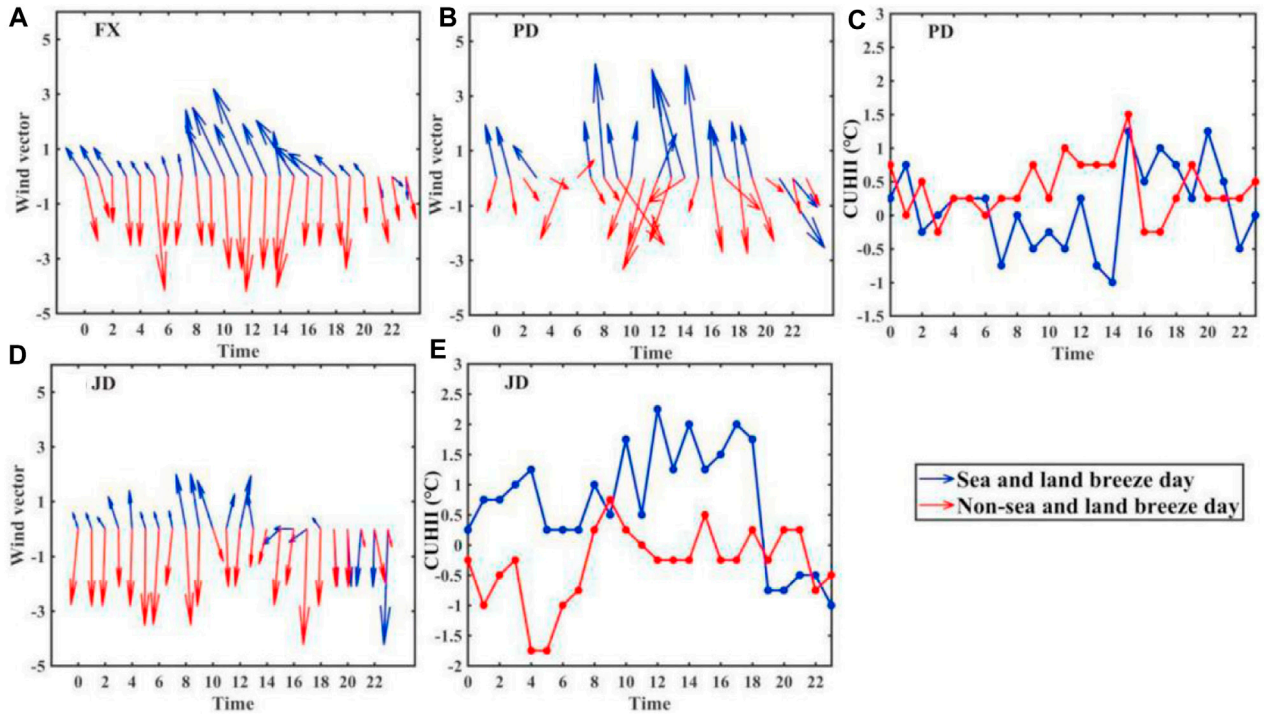

FIGURE 5
Diurnal variation of the **(A,B and D)** wind direction at sites FX, PD and JD and **(C,E)** the CUHII at sites PD and JD on a day with a sea–land breeze (24 September 2013) and a day without a sea–land breeze (25 September 2013) (Yang et al., 2023).

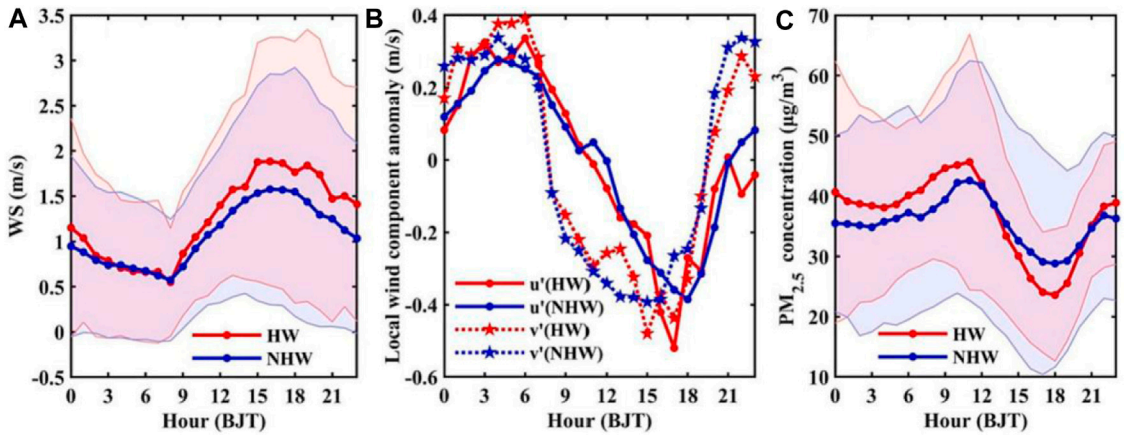

FIGURE 6
Diurnal variation of WS **(A)** and the local wind component anomaly **(B)** in the summertime (July–August) of 2013–2018. Diurnal variation of PM2.5 concentration **(C)** in the summertime (July–August) of 2014–2018. HW and NHW periods are indicated by red and blue, respectively. Shaded areas denote the standard deviation (Xue et al., 2023).

stations were all located in the southern part of the main urban area, so the valley wind circulation of these stations in summer was mainly regulated by the southern mountains. It can be seen from Figure 6B that the local wind circulation had obvious diurnal variations, with negative anomalies during the day (northeast wind) in the u and v directions, and positive anomalies (southwest wind) at night. The anomaly amplitudes of the local wind components in the u and v directions during HW periods were larger than those in NHW periods (Figure 6B), indicating that the local wind had a greater influence in HW periods. During the heat wave, the mountain-valley wind circulation increases the wind speed, which is not conducive to the occurrence of HWs and strong CUHII (Ngarambe et al., 2020; Zong et al., 2021). But it also enhances the surface heat flux and offsets the increased advection cooling (Li and Bou-Zeid, 2013). In addition, the foehn wind is a local airflow movement caused by the mountains, that is, a

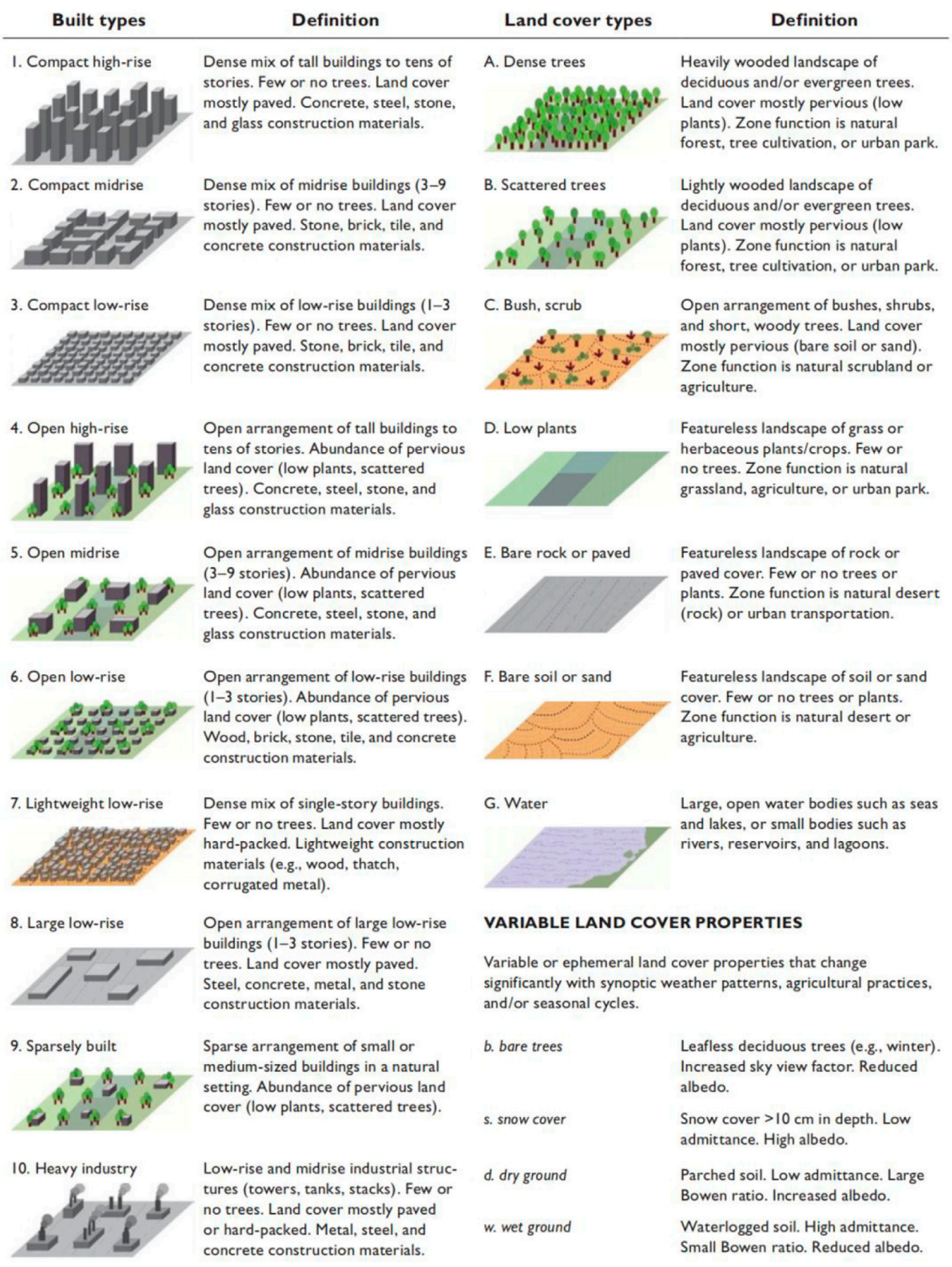

FIGURE 7
Schematic diagram of local climate zoning (Stewart and Oke, 2012).

local wind in which the airflow over the mountains sinks on the leeward slope and becomes dry and hot (McGowan, 1997). Wang et al. (2012) used the observation of multi-element auto weather stations (AWSs) to analyze the foehn effect that occurred on the east slope of Taihang Mountains. The results showed that there are two foehn centers in the northern and southern parts of Taihang Mountains, causing the rapid rising temperature in Hebei Plain. On the whole, the formation mechanism of urban excess warming under different climate backgrounds and local circulation still lacks complete understanding.

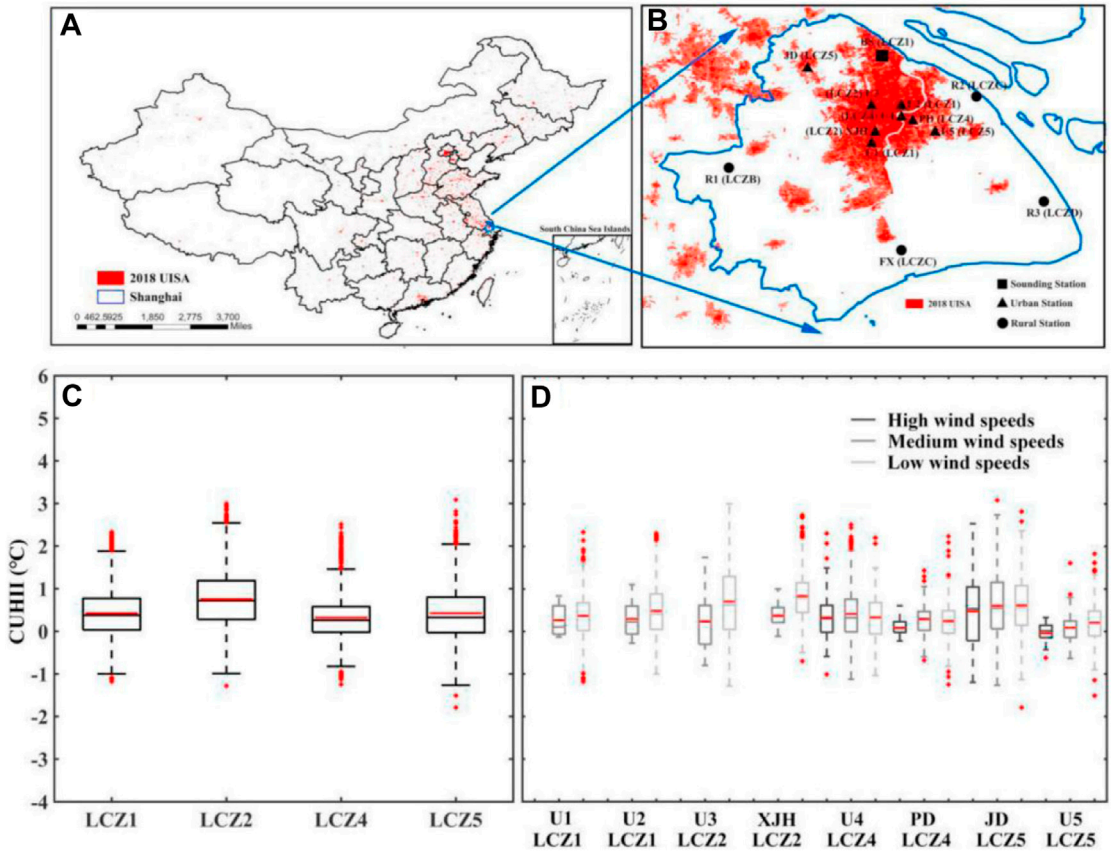

FIGURE 8
Overview of the study area **(A)** and spatial distribution of Shanghai automatic weather stations **(B)**. Box-whisker plots for the CUHII values **(C)** in each LCZ and **(D)** at different wind speeds for each urban station during 2013–2018. The black solid lines are the maximum, upper quartile, median, lower quartile and minimum values from top to bottom, the central red solid line represents the average and the red plus symbols represent outliers (Yang et al., 2023).

5 The influence of urban morphologies on the synergies between HWs and CUHI

At present, a broad consensus has been reached that the spatial heterogeneity of urban areas (such as land cover, roughness of urban underlying surface, height of buildings, and sky view factor) can directly lead to the spatial non-uniform distribution of near surface air temperature (Fenner et al., 2017). Compared with rural areas, the urban land surface albedo is lower, which can amplify the CUHI by absorbing more solar radiation (Oke, 1982), and the reduction of evaporation in urban areas further aggravates the CUHI effect (Taha, 1997; Zhao et al., 2018). In addition, urban buildings increase surface roughness, and reduce wind speed, and urban heat is not easy to dissipate (Fujibe, 2003). In the traditional researches on the CUHI effect, the study areas were simply divided into urban and suburban types, that is, the CUHII was calculated by the average temperature difference between urban stations and reference stations. However, this single division calculation ignored the differences of meteorological elements within the city, thus affecting the accurate assessment of CUHI (Ren and Ren, 2011; Yang et al., 2013; Li et al., 2015; Shi et al., 2022).

Stewart&oke (2012) proposed a set of local climate zones (LCZs), which divides the urban underlying surface into 17 basic types according to the characteristics of the urban surface and differences in human activities (Figure 7). Using the temperature calculation of different types of LCZs can more accurately carry out the comparative study of CUHI at regional and global scales. A few scholars used LCZs to study urban excess warming and promoted the quantitative study of the synergies of HWs and CUHI from the perspective of urban morphologies (Ngarambe et al., 2020; Zheng et al., 2022; Xue et al., 2023; Yang et al., 2023). The CUHII under different LCZs was significantly different and was jointly determined by HWs, wind speed and the location of LCZs from the city center (Xue et al., 2023). For example, in LCZs with a high density of buildings that favor CUHII growth, HWs may last longer. The spatial characteristics of extreme high temperatures of different LCZs in Shanghai show that (Figure 8), the CUHII, the number and duration of HWs of high-density LCZ1 and LCZ2 are significantly higher than those of low-density LCZ4, but the average CUHII of low-density LCZ5 is similar to that of high-density LCZ1 (Yang et al., 2023). High-density buildings reduce wind speed, prolong the duration of HWs, and enhance the synergies between HWs and CUHI (Gemechu, 2022). The CUHII is also affected by anthropogenic heat flux, especially in high-density and high-rise building areas (Zhang et al., 2015). In addition, when the wind speed reaches the threshold of horizontal heat transfer (He, 2018), the CUHII of low-density LCZ5 in the downwind direction increases for

TABLE 1 The difference of research results on the synergies between heat wave and canopy heat island in recent years (self-drawing).

Research area	Direction of synergies	Strength of synergies	References
China/Guangzhou	Enhance	0.8°C–0.9°C	Jiang et al., 2019; Luo and Lau, (2019)
China/Beijing	Enhance	0.9°C	Jiang et al. (2019)
China/Shanghai	Enhance	0.9°C–1.26°C	Ao et al., 2019; Jiang et al., 2019; Yang et al., 2023
China/Lanzhou	Enhance	1.2°C	Xue et al. (2023)
Greece/Athens	Enhance	3.5°C–8.0°C	Founda et al. (2015)
United States/50 cities	Enhance	0.4°C–0.6°C	Zhao et al. (2018)
South Korea/Seoul	Enhance	4.5°C	Ngarambe et al. (2020)
United States/New York City, Washington D.C., and Baltimore	Enhance	1.0°C–2.0°C	Ramamurthy and Bou-Zeid (2017)
United States/Philadelphia	No effect	—	Ramamurthy and Bou-Zeid (2017)
United States/Baltimore	No effect	—	Scott et al. (2018)
Singapore	No effect	—	Chew et al. (2020)
France/Dijon	Weaken from the 5th to 7th day of the heatwave	−0.3–1.0°C	Richard et al. (2021)
Australia/Perth	Weaken in nighttime	−1.3°C	Rogers et al. (2019)

urban areas with a large number of heat emissions (Yang et al., 2023). It is worth noting that few studies have focused on the thermal differences between regions located in different directions within the urban area. Therefore, it is necessary to expand the research focus from a single suburb to the interior of cities, and analyze the impact of different urban morphologies indicators on the local thermal environment, so as to carry out the research on the synergies of HWs and CUHI in megacities.

6 Conclusion

This paper reviewed the research on the difference in the research on the synergies between HWs and CUHI and analysed their formation mechanism from the aspects of definition of HWs, climate backgrounds, local circulations, urban morphologies. In general, the interaction between HWs and CUHI is affected by natural factors (such as humidity, wind speed, and geographical location) and human factors (such as anthropogenic heat emissions, land use change and the definitions of HWs). Different methods to identify and define the HWs could affect the occurrence time, duration, and frequency of HWs to a certain extent. The synergies between HWs and CUHI is also related to the climate background and local circulation. The difference in urbanization degree (such as urban morphologies, urban scale, land cover, and anthropogenic heat flux) also affect the synergies between HWs and CUHI. In summary, influenced by different geographical locations, climate backgrounds, local circulations and urban morphologies, the spatiotemporal distribution of urban excess warming is uneven, and its influencing factors also show complexity, diversity, and variability.

In the context of global warming and rapid urbanization, the synergies between HWs and CUHI poses a significant challenge to human health, production safety, environmental protection, and sustainable urban development. The urgent need is to gain a more comprehensive understanding of the mechanisms and regulatory factors responsible for urban excessive warming caused by HWs and CUHI, which will enable better prediction and assessment of future extreme high temperature events. Table 1.

Author contributions

TS: Writing–original draft, writing–review and editing. LL: Software, methodology, writing–review and editing. XW: Data curation, writing–review and editing. PQ: Writing–review and editing, methodology, funding acquisition, formal analysis.

Funding

The author(s) declare that financial support was received for the research, authorship, and/or publication of this article. This study was supported by National Natural Science Foundation of China (42105147), the Joint Research Project for Meteorological Capacity Improvement (22NLTSQ013), and the Collaborative Innovation Fund of Education Department of Anhui Province (GXXT-2023-050). The data that support the findings of this study are openly available.

Conflict of interest

The authors declare that the research was conducted in the absence of any commercial or financial relationships that could be construed as a potential conflict of interest.

Publisher's note

References

An, N., and Zuo, Z. (2021). Changing structures of summertime heatwaves over China during 1961–2017. *Scientia Sinica (Terrae)*, 51 (8), 1214–1226. doi:10.1360/N072020-0380

Ao, X., Wang, L., Zhi, X., Gu, W., and Yang, H. (2019). Observed synergies between urban heat islands and heat waves and their controlling factors in Shanghai, China. *J. Appl. Meteorology Climatol.* 58, 1955–1972. doi:10.1175/jamc-d-19-0073.1

Bador, M., Terray, L., Boé, J., Somot, S., Alias, A., Gibelin, A. L., et al. (2017). Future summer mega-heatwave and record-breaking temperatures in a warmer France climate. *Environ. Res. Lett.* 12, 074025. doi:10.1088/1748-9326/aa751c

Basara, J. B., Basara, H. G., Illston, B. G., and Crawford, K. C. (2010). The impact of the urban heat island during an intense heat wave in Oklahoma City. *Adv. Meteorology* 2010, 1–10. doi:10.1155/2010/230365

Basara, J. B., Hall, P. K., Jr, Schroeder, A. J., Illston, B. G., and Nemunaitis, K. L. (2008). Diurnal cycle of the Oklahoma city urban heat island. *J. Geophys. Res. Atmos.* 113. doi:10.1029/2008JD010311

Chen, S., Yang, Y., Deng, F., Zhang, Y., Liu, D., Liu, C., et al. (2022). A high-resolution monitoring approach of canopy urban heat island using a random forest model and multi-platform observations. *Atmos. Meas. Tech.* 15, 735–756. doi:10.5194/amt-15-735-2022

Chen, Y., and Li, Y. (2017). An inter-comparison of three heat wave types in China during 1961–2010: observed basic features and linear trends. *Sci. Rep.* 7 (1), 45619. doi:10.1038/srep45619

Chew, L. W., Liu, X., Li, X. X., and Norford, L. K. (2020). Interaction between heat wave and urban heat island: a case study in a tropical coastal city, Singapore. *Atmos. Res.* 247, 105134. doi:10.1016/j.atmosres.2020.105134

Cowan, T., Purich, A., Perkins, S., Pezza, A., Boschat, G., and Sadler, K. (2014). More frequent, longer, and hotter heat waves for Australia in the twenty-first century. *J. Clim.* 27 (15), 5851–5871. doi:10.1175/JCLI-D-14-00092.1

Fenner, D., Holtmann, A., Krug, A., and Scherer, D. (2019b). Heat waves in Berlin and Potsdam, Germany–Long-term trends and comparison of heat wave definitions from 1893 to 2017. *Int. J. Climatol.* 39, 2422–2437. doi:10.1002/joc.5962

Fenner, D., Holtmann, A., Meier, F., Langer, I., and Scherer, D. (2019a). Contrasting changes of urban heat island intensity during hot weather episodes. *Environ. Res. Lett.* 14, 124013. doi:10.1088/1748-9326/ab506b

Fenner, D., Meier, F., Bechtel, B., Otto, M., and Scherer, D. (2017). Intra and inter 'local climate zone' variability of air temperature as observed by crowdsourced citizen weather stations in Berlin, Germany. *Meteorol. Z.* 26 (5), 525–547. doi:10.1127/metz/2017/0861

Fouillet, A., Rey, G., Laurent, F., Pavillon, G., Bellec, S., Guihenneuc-Jouyaux, C., et al. (2006). Excess mortality related to the August 2003 heat wave in France. *Int. Archives Occup. Environ. Health* 80 (1), 16–24. doi:10.1007/s00420-006-0089-4

Founda, D., Pierros, F., Petrakis, M., and Zerefos, C. (2015). Interdecadal variations and trends of the urban heat island in Athens (Greece) and its response to heat waves. *Atmos. Res.* 161-162, 1–13. doi:10.1016/j.atmosres.2015.03.016

Freychet, N., Tett, S., Wang, J., and Hegerl, G. (2017). Summer heat waves over Eastern China: dynamical processes and trend attribution. *Environ. Res. Lett.* 12 (2), 024015. doi:10.1088/1748-9326/aa5ba3

Fujibe, F. (2003). Long-term surface wind changes in the Tokyo metropolitan area in the afternoon of sunny days in the warm season. *J. Meteorological Soc. Jpn.* 81 (1), 141–149. doi:10.2151/jmsj.81.141

Gao, J., Sun, Y., Liu, Q., Zhou, M., Lu, Y., and Li, L. (2015). Impact of extreme high temperature on mortality and regional level definition of heat wave: a multi-city study in China. *Sci. Total Environ.* 505, 535–544. doi:10.1016/j.scitotenv.2014.10.028

Gemechu, F. G. (2022). How the interaction of heatwaves and urban heat islands amplify urban warming. *Adv. Environ. Eng. Res.* 3, 2. doi:10.21926/aeer.2202022

Gershunov, A., Cayan, D. R., and Iacobellis, S. F. (2009). The great 2006 heat wave over California and Nevada: signal of an increasing trend. *J. Clim.* 22, 6181–6203. doi:10.1175/2009JCLI2465.1

He, B. J. (2018). Potentials of meteorological characteristics and synoptic conditions to mitigate urban heat island effects. *Urban Clim.* 24, 26–33. doi:10.1016/j.uclim.2018.01.004

He, B. J., Ding, L., and Prasad, D. (2020). Outdoor thermal environment of an open space under sea breeze: a mobile experience in a coastal city of Sydney, Australia. *Urban Clim.* 31, 100567. doi:10.1016/j.uclim.2019.100567

He, B. J., Wang, J., Liu, H., and Ulpiani, G. (2021). Localized synergies between heat waves and urban heat islands: implications on human thermal comfort and urban heat management. *Environ. Res.* 193, 110584. doi:10.1016/j.envres.2020.110584

He, C., Zhou, T., Lin, A., Wu, B., Gu, D., Li, C., et al. (2015). Enhanced or weakened western north pacific subtropical high under global warming? *Sci. Rep.* 5 (1), 16771. doi:10.1038/srep16771

IPCC (2021). *Climate Change 2021: the physical science basis. Contribution of working group I to the sixth assessment report of the intergovernmental panel on climate change*. New York: Cambridge University Press.

Jiang, S., Lee, X., Wang, J., and Wang, K. (2019). Amplified urban heat islands during heat wave periods. *J. Geophys. Res. Atmos.* 124, 7797–7812. doi:10.1029/2018jd030230

Khan, H. S., Paolini, R., Santamouris, M., and Caccetta, P. (2020). Exploring the synergies between urban overheating and heatwaves (HWs) in Western Sydney. *Energies* 13 (2), 470. doi:10.3390/en13020470

Kuglitsch, F. G., Toreti, A., Xoplaki, E., Della-Marta, P. M., Zerefos, C. S., Türkeş, M., et al. (2010). Heat wave changes in the eastern Mediterranean since 1960. *Geophys. Res. Lett.* 37, 4. 2009GL041841. doi:10.1029/2009GL041841

Li, D., and Bou-Zeid, E. (2013). Synergistic interactions between urban heat islands and heat waves: the impact in cities is larger than the sum of its parts. *J. Appl. Meteorology Climatol.* 52 (9), 2051–2064. doi:10.1175/JAMC-D-13-02.1

Li, Y., Shi, T., Yang, Y., Wu, B. W., Wang, L. B., Shi, C. E., et al. (2015). Satellite-based investigation and evaluation of the observational environment of meteorological stations in anhui province, China. *Pure Appl. Geophys.* 172 (6), 1735–1749. doi:10.1007/s00024-014-1011-8

Liao, W., Liu, X., Li, D., Luo, M., Wang, D., Wang, S., et al. (2018). Stronger contributions of urbanization to heat wave trends in wet climates. *Geophys. Res. Lett.* 45 (11), 310–311. doi:10.1029/2018GL079679

Liu, W., Ji, C., Zhong, J., Jiang, X., and Zheng, Z. (2007). Temporal characteristics of the Beijing urban heat island. *Theor. Appl. Climatol.* 87, 213–221. doi:10.1007/s00704-005-0192-6

Luo, M., and Lau, N. C. (2019). Urban expansion and drying climate in an urban agglomeration of east China. *Geophys. Res. Lett.* 46 (2), 6868–6877. doi:10.1029/2019GL082736

Matsumura, S., Sugimoto, S., and Sato, T. (2015). Recent intensifi-cation of the western Pacific subtropical high associated with the East Asian summer monsoon. *J. Clim.* 28 (7), 2873–2883. doi:10.1175/JCLI-D-14-00569.1

Mcgowan, H. A. (1997). Meteorological controls on wind erosion during foehn wind events in the eastern Southern Alps, New Zealand. *Can. J. Earth Sci.* 34 (11), 1477–1485. doi:10.1139/e17-120

Mishra, V., Ganguly, A. R., Nijssen, B., and Lettenmaier, D. P. (2015). Changes in observed climate extremes in global urban areas. *Environ. Res. Lett.* 10, 024005. doi:10.1088/1748-9326/10/2/024005

Mughal, M. O., Li, X., and Norford, L. K. (2020). Urban heat island mitigation in Singapore: Evaluation using WRF/multilayer urban canopy model and local climate zones. *Urban Clim.* 34, 100714. doi:10.1016/j.uclim.2020.100714

Ngarambe, J., Nganyiyimana, J., Kim, I., Santamouris, M., and Yun, G. Y. (2020). Synergies between urban heat island and heat waves in Seoul: the role of wind speed and land use characteristics. *PLoS ONE* 15, e0243571. doi:10.1371/journal.pone.0243571

Oke, T. R. (1982). The energetic basis of the urban heat island. *Q. J. R. Meteorological Soc.* 108, 1–24. doi:10.1002/qj.49710845502

Oswald, E. M. (2018). An analysis of the prevalence of heat waves in the United States between 1948 and 2015. *J. Appl. Meteorology Climatol.* 57, 1535–1549. doi:10.1175/JAMC-D-17-0274.1

Oswald, E. M., and Rood, R. B. (2014). A trend analysis of the 1930–2010 extreme heat events in the continental United States. *J. Appl. Meteorology Climatol.* 53 (3), 565–582. doi:10.1175/jamc-d-13-071.1

Perkins, S. E. (2015). A review on the scientific understanding of heatwaves-their measurement, driving mechanisms, and changes at the global scale. *Atmos. Res.* 164, 242–267. oct.-no. doi:10.1016/j.atmosres.2015.05.014

Ramamurthy, P., and Bou-Zeid, E. (2017). Heatwaves and urban heat islands: a comparative analysis of multiple cities. *J. Geophys. Res. Atmos.* 122, 168–178. doi:10.1002/2016JD025357

Ren, G., Li, J., Ren, Y., Chu, Z., Zhang, A., Zhou, Y., et al. (2015). An integrated procedure to determine a reference station network for evaluating and adjusting urban

bias in surface air temperature data. *J. Appl. Meteorology Climatol.* 54, 1248–1266. doi:10.1175/JAMC-D-14-0295.1

Ren, L., Wang, D., An, N., Ding, S., Yang, K., Freychet, N., et al. (2020). Anthropogenic influences on the persistent nighttime heat wave in summer 2018 over northeast China. *Bull. Am. Meteorological Soc.* 101, S83–S88. doi:10.1175/BAMS-D-19-0152.1

Ren, Y., and Ren, G. (2011). A remote-sensing method of selecting reference stations for evaluating urbanization effect on surface air temperature trends. *J. Clim.* 24, 3179–3189. doi:10.1175/2010JCLI3658.1

Richard, Y., Pohl, B., Rega, M., Pergaud, J., Thevenin, T., Emery, J., et al. (2021). Is Urban Heat Island intensity higher during hot spells and heat waves (Dijon, France, 2014–2019)? *Urban Clim.* 35, 100747. doi:10.1016/j.uclim.2020.100747

Rogers, C. D., Gallant, A. J., and Tapper, N. J. (2019). Is the urban heat island exacerbated during heatwaves in southern Australian cities? *Theor. Appl. Climatol.* 137, 441–457. doi:10.1007/s00704-018-2599-x

Scott, A. A., Waugh, D. W., and Zaitchik, B. F. (2018). Reduced urban heat island intensity under warmer conditions. *Environ. Res. Lett.* 13, 064003. doi:10.1088/1748-9326/aabd6c

Seto, K. C., Guneralp, B., and Hutyra, L. R. (2012). Global forecasts of urban expansion to 2030 and direct impacts on biodiversity and carbon pools. *Proc. Natl. Acad. Sci.* 109 (40), 16083–16088. doi:10.1073/pnas.1211658109

Shi, T., Huang, Y., Shi, C., and Yang, Y. (2015). Influence of urbanization on the thermal environment of meteorological stations: satellite-observational evidence. *Adv. Clim. Change Res.* 1, 7–15. doi:10.1016/j.accre.2015.07.001

Shi, T., Sun, D., Huang, Y., Lu, G., and Yang, Y. (2021). A new method for correcting urbanization-induced bias in surface air temperature observations: insights from comparative site-relocation data. *Front. Environ. Sci.* 9. doi:10.3389/fenvs.2021.625418

Shi, T., Yang, Y., Sun, D., Huang, Y., and Shi, C. (2022). Influence of changes in meteorological observational environment on urbanization bias in surface air temperature: a review. *Front. Clim.* 3. doi:10.3389/fclim.2021.781999

Stewart, I. D., and Oke, T. R. (2012). Local climate zones for urban temperature studies. *Bull. Am. Meteorological Soc.* 93 (12), 1879–1900. doi:10.1175/BAMS-D-11-00019.1

Su, Q., and Dong, B. (2019). Recent decadal changes in heat waves over China: drivers and mechanisms. *J. Clim.* 32, 4215–4234. doi:10.1175/JCLI-D-18-0479.1

Sun, X., Ren, G., Ren, Y., Fang, Y., Liu, Y., Xue, X., et al. (2017). A remarkable climate warming hiatus over Northeast China since 1998. *Theor. Appl. Climatol.* 133, 579–594. doi:10.1007/s00704-017-2205-7

Taha, H. (1997). Urban climates and heat islands: albedo, evapotranspiration, and anthropogenic heat. *Energy Build.* 25 (2), 99–103. doi:10.1016/S0378-7788(96)00999-1

Tan, J., Zheng, Y., Tang, X., Guo, C., Li, L., Song, G., et al. (2010). The urban heat island and its impact on heat waves and human health in Shanghai. *Int. J. Biometeorology* 54 (1), 75–84. doi:10.1007/s00484-009-0256-x

Wagner, N. L., Riedel, T. P., Roberts, J. M., Thornton, J. A., Angevine, W. M., Williams, E. J., et al. (2012). The sea breeze/land breeze circulation in Los Angeles and its influence on nitryl chloride production in this region. *J. Geophys. Res. Atmos.* 117. doi:10.1029/2012JD017810

Wang, Z., Ding, Y., Zhang, Y., et al. (2012). Feature and mechanism of the foehn weather on east slope Taihang mountains?:statistic feature. *Plateau Meteorol.* 31 (2), 555–561. doi:10.1007/s11783-011-0280-z

Xie, W., and Zhou, B. (2023). On the atmospheric background for the occurrence of three heat wave types in East China. *Weather Clim. Extrem.* 39, 100539. doi:10.1016/j.wace.2022.100539

Xue, J., Zong, L., Yang, Y., Bi, X., Zhang, Y., and Zhao, M. (2023). Diurnal and interannual variations of canopy urban heat island (CUHI) effects over a mountain–valley city with a semi-arid climate. *Urban Clim.* 48, 101425. doi:10.1016/j.uclim.2023.101425

Yang, J., Hu, L., and Wang, C. (2019). Population dynamics modify urban residents' exposure to extreme temperatures across the United States. *Sci. Adv.* 5, eaay3452. doi:10.1126/sciadv.aay3452

Yang, Y., Guo, M., Wang, L., Zong, L., Liu, D., Zhang, W., et al. (2023). Unevenly spatiotemporal distribution of urban excess warming in coastal Shanghai megacity, China: roles of geophysical environment, ventilation and sea breezes. *Build. Environ.* 235, 110180. doi:10.1016/j.buildenv.2023.110180

Yang, Y., Wu, B., Shi, C., Zhang, J. H., Li, Y. B., Tang, W. A., et al. (2013). Impacts of urbanization and station-relocation on surface air temperature series in Anhui province, China. *Pure Appl. Geophys.* 170 (11), 1969–1983. doi:10.1007/s00024-012-0619-9

Yang, Y., Zheng, Z., Yim, S. Y. L., Roth, M., Ren, G., Gao, Z., et al. (2020). PM 2.5 pollution modulates wintertime urban heat island intensity in the BeijingTianjin-hebei megalopolis, China. *Geophys. Res. Lett.* 47 (1), 1–12. doi:10.1029/2019GL084288

Yoon, D., Cha, D. H., Lee, G., Park, C., Lee, M., and Min, K. (2018). Impacts of synoptic and local factors on heat wave events over southeastern region of Korea in 2015. *J. Geophys. Res. Atmos.* 123. doi:10.1029/2018JD029247

You, Q., Jiang, Z., Kong, L., Wu, Z., Bao, Y., Kang, S., et al. (2017). A comparison of heat wave climatologies and trends in China based on multiple definitions. *Clim. Dyn.* 48, 3975–3989. doi:10.1007/s00382-016-3315-0

Zhang, N., Wang, X., Chen, Y., and Dai, W. (2015). Numerical simulations on influence of urban land cover expansion and anthropogenic heat release on urban meteorological environment in Pearl River Delta. *Theor. Appl. Climatol.* 126, 469–479. doi:10.1007/s00704-015-1601-0

Zhang, N., Zhu, L., and Zhu, Y. (2011). Urban heat island and boundary layer structures under hot weather synoptic conditions: a case study of Suzhou City, China. *Adv. Atmos. Sci.* 28 (4), 855–865. doi:10.1007/s00376-010-0040-1

Zhang, Y., Peng, M., Wang, L., and Yu, C. (2018). Association of diurnal temperature range with daily mortality in England and Wales: a nationwide time-series study. *Sci. Total Environ.* 621, 291–300. doi:10.1016/j.scitotenv.2017.11.056

Zhao, L., Oppenheimer, M., Zhu, Q., Baldwin, J. W., Ebi, K. L., Bou-Zeid, E., et al. (2018). Interactions between urban heat islands and heat waves. *Environ. Res. Lett.* 13 (3), 034003. doi:10.1088/1748-9326/aa9f73

Zheng, Z., Ren, G., Gao, H., and Yang, Y. (2022). Urban ventilation planning and its associated benefits based on numerical experiments: a case study in beijing, China. *Build. Environ.* 222, 109383. doi:10.1016/j.buildenv.2022.109383

Zheng, Z., Ren, G., Wang, H., Dou, J., Gao, Z., Duan, C., et al. (2018). Relationship between fine-particle pollution and the urban heat island in Beijing, China: observational evidence. *Boundary-layer Meteorol.* 169, 93–113. doi:10.1007/s10546-018-0362-6

Zhou, X., Okaze, T., Ren, C., Cai, M., Ishida, Y., Watanabe, H., et al. (2020). Evaluation of urban heat islands using local climate zones and the influence of sea-land breeze. *Sustain. Cities Soc.* 55, 102060. doi:10.1016/j.scs.2020.102060

Zinzi, M., Agnoli, S., Burattini, C., and Mattoni, B. (2020). On the thermal response of buildings under the synergic effect of heat waves and urban heat island. *Sol. Energy* 211 (10), 1270–1282. doi:10.1016/j.solener.2020.10.050

Zong, L., Liu, S., Yang, Y., Ren, G., Yu, M., Zhang, Y., et al. (2021). Synergistic influence of local climate zones and wind speeds on the urban heat island and heat waves in the megacity of Beijing, China. *Front. Earth Sci.* 9, 458. doi:10.3389/feart.2021.673786

frontiers | Frontiers in Environmental Science

TYPE Original Research
PUBLISHED 03 April 2024
DOI 10.3389/fenvs.2024.1338678

OPEN ACCESS

EDITED BY
Zhiyuan Hu,
Sun Yat-sen University, China

REVIEWED BY
Jayanarayanan Kuttippurath,
Indian Institute of Technology Kharagpur, India
Radhakrishna Basivi,
National Atmospheric Research Laboratory, India

*CORRESPONDENCE
Sara E. A. Johnson,
johnson.8995@osu.edu

RECEIVED 15 November 2023
ACCEPTED 15 March 2024
PUBLISHED 03 April 2024

CITATION
Johnson SEA, Ye H, Fetzer EJ and Li J (2024), Satellite-observed precipitation and total column water vapor.
Front. Environ. Sci. 12:1338678.
doi: 10.3389/fenvs.2024.1338678

Satellite-observed precipitation and total column water vapor

Sara E. A. Johnson[1]*, Hengchun Ye[2], Eric J. Fetzer[3] and Jingjing Li[4]

[1]Department of Geography, The Ohio State University, Columbus, OH, United States, [2]Office of Graduate Studies and Research, California State University Stanislaus, Turlock, CA, United States, [3]Jet Propulsion Laboratory, California Institute of Technology, Pasadena, CA, United States, [4]Department of Geography, Geology, and Environment, California State University, Los Angeles, CA, United States

This study explores the relationship between water vapor and rainfall intensities over three tropical lands (Amazon Basin, Sahel, southern South America) and three tropical ocean regions (Atlantic Ocean, Indian Ocean, Niño 4). We utilized daily total column water vapor (TCWV) data from the Atmospheric Infrared Sounder (AIRS) and daily precipitation records from the Tropical Rainfall Measuring Mission (TRMM) Multi-satellite Precipitation. Over tropical land, precipitation shows higher sensitivity to changes in water vapor, with a well-sorted pattern of an increased occurrence of higher daily precipitation as TCWV increases. Precipitation intensity over the Sahel, in particular, is extremely responsive to TCWV change. Over tropical oceans, the precipitation intensity is less sensitive to water vapor, particularly in the Indian Ocean and Niño 4 where precipitation intensities above the 40th percentile are no longer responding to the increasing TCWV. Quantifying water vapor and precipitation intensity aids in forecasting the occurrence of precipitation between tropical land and oceans.

KEYWORDS

water vapor, precipitation intensity, AIRS, TRMM, tropics

1 Introduction

An increase in atmospheric water vapor content accompanying a warming climate will affect hydrological cycles on regional and global scales (Trenberth et al., 2003; Sun et al., 2007; O'Gorman and Schneider, 2009; Trenberth, 2011; Donat et al., 2016). Previous studies indicate that the precipitation intensity is closely controlled by the amount of atmospheric water vapor content over the middle and higher latitude lands (Sun et al., 2007; O'Gorman and Schneider, 2009; Muller, 2013; Ye et al., 2014; Ye et al., 2015). An increase in water vapor can also impact precipitation frequency, and duration (Trenberth et al., 2003; Sun et al., 2007; O'Gorman and Schneider, 2009; Trenberth, 2011).

In observational studies, water vapor plays a predominant role in precipitation intensity (Bevis et al., 1992; Troller et al., 2006; Holloway and Neelin, 2009; Van Baelen et al., 2011; Chen et al., 2017a; Zhang et al., 2018). Using historical observational records, Ye et al. (2014); Ye et al. (2015); Ye et al. (2017) found that higher atmospheric water vapor leads to more frequent higher precipitation intensity in all seasons over northern Eurasia. Liang et al. (2020) find that precipitation increases with water vapor, and water vapor stimulates precipitation occurrences over the Tibetan Plateau. The role of water vapor at different levels of the atmosphere on precipitation intensity and areal extent is, also, well studied using observations in Chen et al. (2017a); Chen et al. (2017b) and Radhakrishna and Rao (2021). Furthermore, increases in water vapor are key to the development of severe weather and heavy precipitation events (Van Baelen et al., 2011; Chen et al., 2017a; Zhang et al.,

2018; Liang et al., 2020). These *in situ* studies detail the relationship between water vapor and precipitation intensity.

Studies utilizing satellite data also illustrate the relationship between water vapor and precipitation intensity (Bretherton et al., 2004; Ahmed and Schumacher, 2015; Schiro et al., 2016; Ahmed and Schumacher, 2017; Rushley et al., 2018; Roderick et al., 2019). Few studies have utilized Atmospheric Infrared Sounder (AIRS) to investigate the relationship between precipitation intensity and column water vapor (Roderick et al., 2019; Wang et al., 2021). Roderick et al. (2019) utilizes AIRS's Integrated Water Vapor (IWV) and Surface Air Temperature (SAT) profiles along with rain gauge observations to investigate the rainfall-temperature scaling over Australia. They find that rainfall intensity increases with IWV (Bao et al., 2017; Roderick et al., 2019). Wang et al. (2021) utilize AIRS, Tropical Rainfall Measuring Mission (TRMM), and other satellite products to understand the spatial and temporal variations of water vapor, temperature, and precipitation in the Tibetan Plateau, finding a relationship of water vapor content with precipitation and temperature in most mountainous areas (Wang et al., 2021). Over the continental United States (CONUS) region, Radhakrishna et al. (2015) explored the role of water vapor in generating convection using the Global Navigation Satellite System (GNSS) and radar networking. Ahmed and Schumacher (2015), Ahmed and Schumacher (2017) utilized reanalysis water vapor and TRMM Precipitation Radar observations to investigate the moisture-precipitation relationship. Overall, satellite-derived measurements are valuable in identifying the precipitation-moisture relationship.

Geographic difference have been highlighted in studies of water vapor and precipitation relationships (Bretherton et al., 2004; Schiro et al., 2016; Ahmed and Schumacher, 2017). Bretherton et al. (2004) found that rainfall increases rapidly with water vapor in all tropical ocean regions. Higher mean tropospheric temperature influences precipitation over the West Pacific and Indian Ocean regions. Temperature, particularly daytime heating (Schiro et al., 2016; Ahmed and Schumacher, 2017), influences the precipitation-column water vapor (CWV) relationship differently over tropical ocean and land (Ahmed and Schumacher, 2017; Kuo et al., 2017; Schiro et al., 2018; Neelin et al., 2022). Due to environmental controls, tropical land regions tend to have a less steep precipitation-column water vapor moisture curve than ocean regions (Schiro et al., 2016; Ahmed and Schumacher, 2017). Therefore, it is essential to understand the water vapor and precipitation relationship considering the geographical difference between tropical land and ocean region.

Building on previous usage of satellite products, the first goal of this study is to determine if AIRS water vapor data and TRMM daily and monthly precipitation data can reproduce the moisture-precipitation relationship established in previous studies. There is still a need to understand geographic effects of tropical precipitation intensity response to moisture. Given their global coverage, satellite remote sensing products provide an opportunity to evaluate the role of water vapor on the precipitation intensity and occurrence throughout the Tropics. The second goal of this study is to exploit global, long-term AIRS and TRMM data sets to extend the moisture-precipitation relationships to unstudied regions and time periods. Thus far, the usage of AIRS data to analyze the precipitation-moisture relationship is limited. Here, we describe the water vapor-precipitation relationship using AIRS total column water vapor (TCWV) and TRMM precipitation at daily and monthly scales. Utilizing longer temporal scales will assist in understanding deep convection and the geographic variation in precipitation-moisture relationship. We highlight the geographical difference in the precipitation-moisture relationship and the occurrence of different precipitation intensity over tropical land and ocean. Providing knowledge on the precipitation-water vapor relationship at smaller local scales can also give more information on the local climate effects than a generalized large regional scale study. This is important because long-term precipitation can change rapidly over small scales, especially over varying topography.

2 Materials and methods

2.1 Location of study area

This study considers three tropical ocean locations (Atlantic Ocean, Niño 4, and Indian Ocean), two tropical land regions (Sahel, Amazon Basin), and one subtropical land region (southern South America) (Figure 1). The coordinate extents of these six regions are listed in Table 1.

The Atlantic Ocean, Indian Ocean, and the Pacific Ocean surrounding Kwajalein Island (Niño 4) were selected due to Bretherton et al. (2004) study on the relationship between relative humidity and precipitation averaged over four tropical ocean areas within 20°S-20°N. By selecting smaller areas, we would like to understand variations among different parts of the tropical ocean. For example, we selected Kwajalein Island, within the Niño 4 region, a well-researched area in the equatorial Pacific (Bretherton et al., 2004; Powell, 2019).

An Amazon location is selected based on Schiro et al. (2016) observations between precipitation and water vapor on shorter time scales, including 15-min, 30-min, and hourly intervals. We want to complement their studies by examining longer time scales of daily and monthly relationships. Including the southern part of South America (Chile, Argentina, Paraguay, Uruguay) assists us in understanding the relationship between water vapor and precipitation in a subtropical land region where little research was done.

2.2 Data

2.2.1 Water vapor

We use Atmospheric Infrared Sounder (AIRS)/Advanced Microwave Sounding Unit (AMSU) Aqua Daily and Monthly Standard Physical Retrieval Version 6 Level 3 data (AIRX3STD/AIRX3STM) for TCWV (AIRS project, 2019). AIRS/AMSU is a part of the Aqua satellite, launched on 4 May 2002, by the National Aeronautics and Space Administration (NASA) (Chahine et al., 2006; AIRS project, 2019). At 705 km height in a sun-synchronous orbit, the satellite collects temperature and water vapor profiles to observe the global water and energy cycles, climate variation and trends, and the climate system's response to increasing greenhouse gases (Tian et al., 2017). Measurements are collected once or twice daily for each location; descending (southward moving) orbits

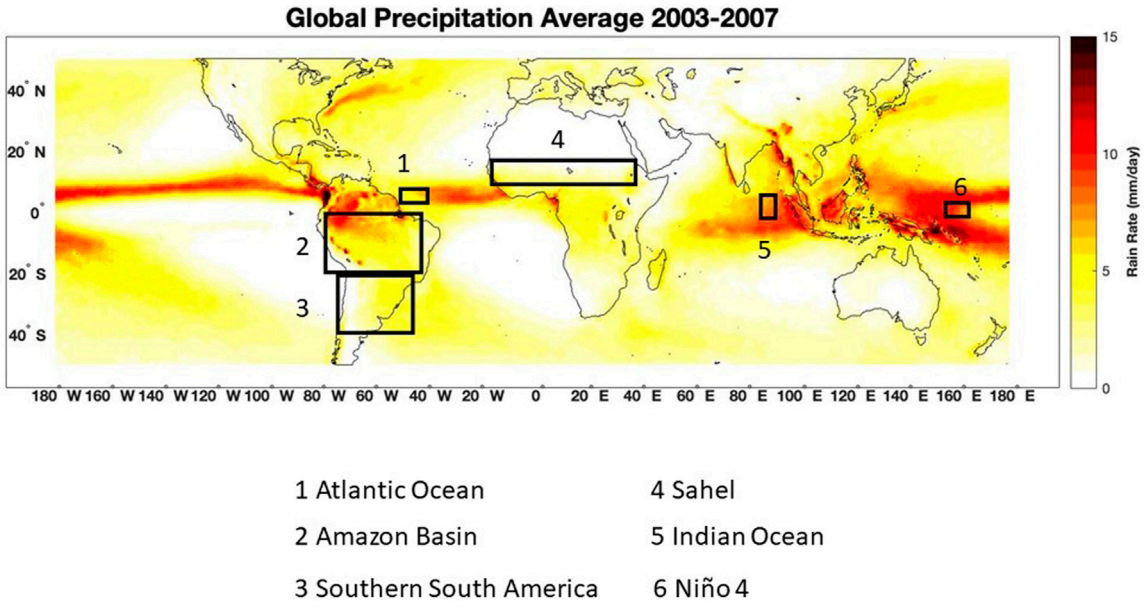

FIGURE 1
Study areas.

TABLE 1 The coordinates extents for six study locations.

Locations	Sahel	Amazon Basin	Southern South America	Atlantic ocean	Niño 4	Indian ocean
Coordinates	20°N –20°S, 160°E –180°E	3° N –20° S, 45° W –85° W	20° S –40° S, 50° W –73° W	0°–10° S, 40° W –50° W	2.5° N –2.5° S, 50° W –73° W	5° N –5° S, 85° E – 95° E

overpass any location at 1:30 a.m. local time and ascending orbit at 1: 30 PM. The spatial coverage is global. AIRS retrievals are obtained at 45 km resolution at nadir in a swath about 1,500 km wide (Susskind et al., 2014). Level 3 data are gridded Level 2 swath retrieval products of geophysical variables and quality parameters, averaged and binned into 1x1-degree grid cells (Tian et al., 2017). The study utilizes AIRS daily total column water vapor (TCWV) averaged from daily observations of ascending and descending Level 3 gridded data sets.

AIRS retrievals are available for scenes with approximately 70% effective cloud fraction (the product of cloud coverage and infrared emissivity), or about 70% of all scenes observed (Susskind et al., 2014). AIRS retrievals include water vapor information for cloudy scenes because the cloud-clearing retrieval methodology combines information from nine 15 km-wide infrared scenes to remove the cloud contribution at 45 km (Susskind et al., 2014). As a result, the approximate 70% coverage for AIRS is far higher than typical clear sky occurrence of a few percent at 45 km scales (Guillaume et al., 2019). Cloud clearing, and the large number of AIRS channels provide information not obtainable with broad spectral satellite instrument (Fan et al., 2023). While some cloud types are rarely sampled by AIRS, including deep convective clouds (Yue et al., 2013), these occur infrequently and do not significantly affect the monthly TCWV statistics considered in this study (Wong et al., 2015). The effects of cloud-induce sampling in AIRS is also discussed in Tian et al. (2019). The climatology from AIRS is broadly consistent with other data sets (Schröder et al., 2018), except for small mean relative differences whose values are not know. Also, a 1 × 1 degree grid box contains approximately four 45-km wide AIRS observations, so only grid boxes with complete cloud cover will not contain AIRS information. Other studies have demonstrated the value of using AIRS water vapor to reconstruct high resolution datasets over the Tibetan Plateau (Wang et al., 2021) and Antarctica (Fan et al., 2023), and in moist convective environments over oceans (Abraham and Goldblatt, 2023). AIRS cannot not fully resolve the diurnal cycle, which can be as large as 10% or more of the mean state for tropical conditions (Radhakrishna et al., 2022). However, twice-daily samples of a sinusoid with diurnal period (24 h) average to zero, so do not affect the time mean values (though overtones of the diurnal period will alias onto lower frequencies). As Radhakrishna et al. (2022) show, the diurnal variability of TCWV is nearly sinusoidal of period 24 h, so diurnal sampling effects are small in AIRS TCWV. Together, cloud-induced sampling and diurnal effects will contribute an estimated 10% of the signal in monthly TCWV statistics from AIRS (Wong et al., 2015; Tian et al., 2019). In comparison, the climatological signals shown below can vary by an order of magnitude or more. In summary, the AIRS TCWV in this study is representative of the large-scale, slowly varying total water vapor, and its interactions with nearby convection at daily to monthly

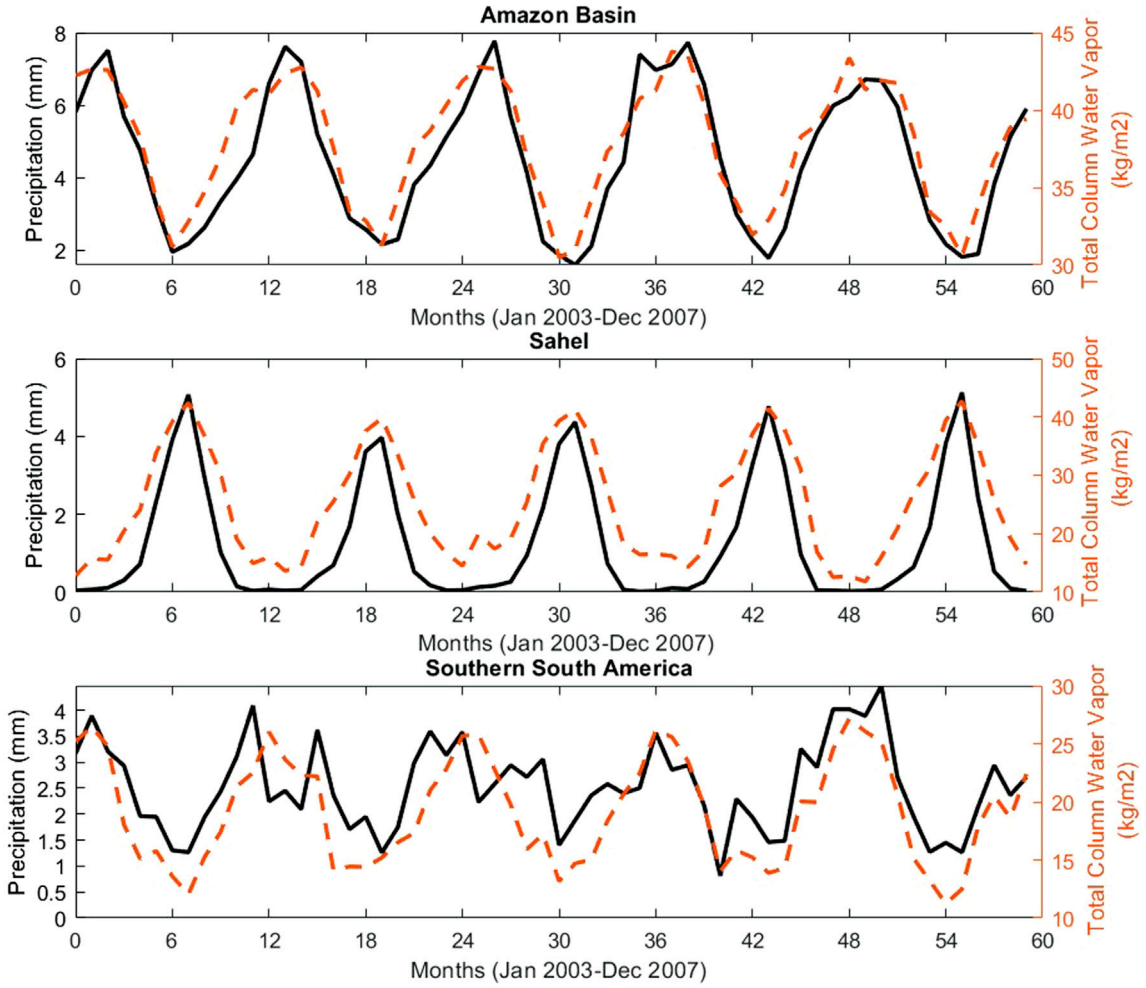

FIGURE 2
Time series of monthly precipitation and TCWV over three Land regions.

scales, but not water vapor within and under clouds where rain is occurring.

2.2.2 Precipitation

Precipitation data are from the 3B42 (Daily) and 3B43 (Monthly) Version 7 TRMM Multi-satellite Precipitation Analysis (TMPA) Rainfall Estimate Product 3B42/3B43 Version 7 (TRMM) (Huffman et al., 2010; Tropical Rainfall Measuring Mission TRMM, 2011). TRMM launched in November 1997 as a joint mission between NASA and the Japan Aerospace Exploration Agency to monitor and study tropical rainfall. The TRMM goal is to understand the distribution and variability of precipitation within the tropical climate system; and the interaction between water vapor, clouds, and precipitation (NASA, 2015). The 3B42 dataset is produced by merging satellite rainfall estimates with rain gauge data into gridded estimates. This product gives 3-hourly precipitation estimates using microwave, TRMM imager (TMI) precipitation, infrared, and rain gauge adjustments. 3B43 is a monthly version of the 3B42 dataset. For brevity, we address this dataset as TRMM. The spatial coverage of 3B42 (Daily) extends to the −50/+50 latitude and all longitudes. The temporal resolution is 3-hourly data. The spatial resolution is on a 0.25 × 0.25-degree grid. The TRMM satellite operated from 1997 to 2015 before transitioning to the Global Precipitation Measurement (GPM) satellite (TRMM. Goddard Space Flight Center Distributed Active Archive Center GSFC DAAC, 2015). For initial results, we select the beginning of 2003 to allow a one-year gap in data collection from the Aqua satellite, and before the transition to GPM. Given that these two daily data sets of water vapor and precipitation have different spatial resolutions, we take averages of all gridded values within each study area to derive daily values during their overlapping period of 1 January 2003, to 31 December 2007. This period overlaps a year after the start of AIRS in 2002 and before the end of TRMM to ensure consistency with our data.

2.3 Methodology

Previous studies highlight the broader relationship between precipitation and column and vertical structures of water vapor (Bretherton et al., 2004; Holloway and Neelin, 2009; Holloway and Neelin, 2010; Muller, 2013; Schiro et al., 2016). In this study, we

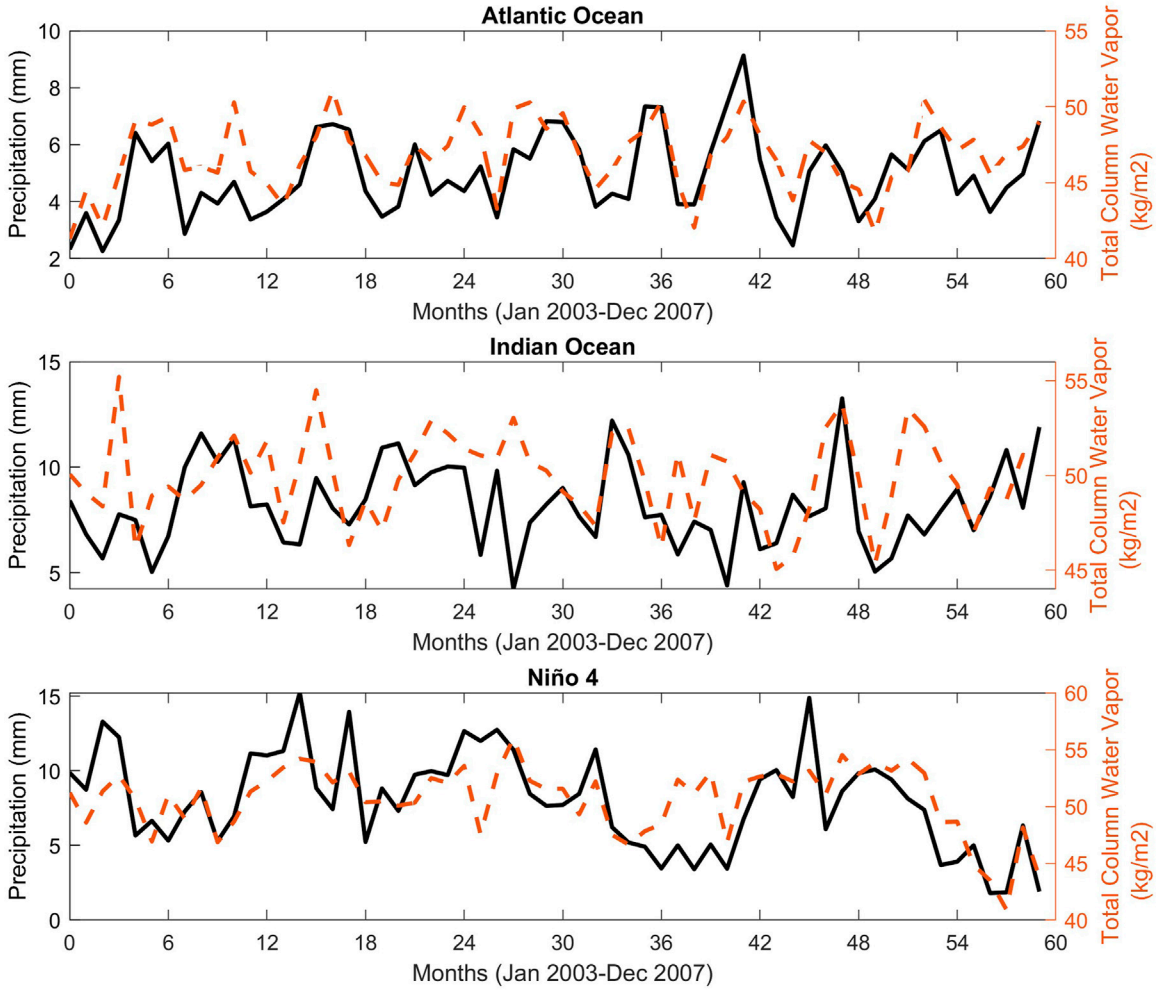

FIGURE 3
Time series of monthly precipitation and TCWV over three Ocean regions.

provide a localized approach to these connections over multiple tropical land and ocean areas at daily and monthly time scales. The monthly time scale examines the general relationship between the water vapor and precipitation over different parts of the tropical oceans and (sub)tropical land areas from a climatological perspective. The daily time scale reveals the in-depth relationship between the precipitation intensity and occurrences in response to the water vapor content simultaneously.

2.3.1 Rate of change

We plot monthly time series of TCWV and precipitation to examine the seasonality and visualize the variability of these two variables at each locality (Figures 2, 3). To quantify the rate of change in monthly mean precipitation intensity with TCWV, we adopt Ye et al. (2017) and Lenderink and Van Meijgaard (2008) calculation method for non-linear relationship (Eq. 1). It is an exponential regression used by fitting a least square linear regression to the logarithm of precipitation (Lenderink and Van Meijgaard, 2008; Ye et al., 2017):

$$p_{rate} = b(1+a)^{d(TCWV)}$$

TABLE 2 Designates the groupings for the precipitation intensities based on percentiles.

Group 1	1–20th percentile
Group 2	21–40th percentile
Group 3	41–60th percentile
Group 4	61–80th percentile
Group 5	81–100th percentile

Where p_{rate} is the daily mean precipitation intensity in response to daily TCWV change, a is the constant rate of increase in daily precipitation intensity, and d(TCWV) is the change in total column water vapor. We applied a logarithmic operation on the equation and fit a least squared linear regression to obtain the rate of change in precipitation intensity with TCWV. After calculating the rate of change, we convert this into percent of change for clarity and easy comparison among different study sites and with other studies.

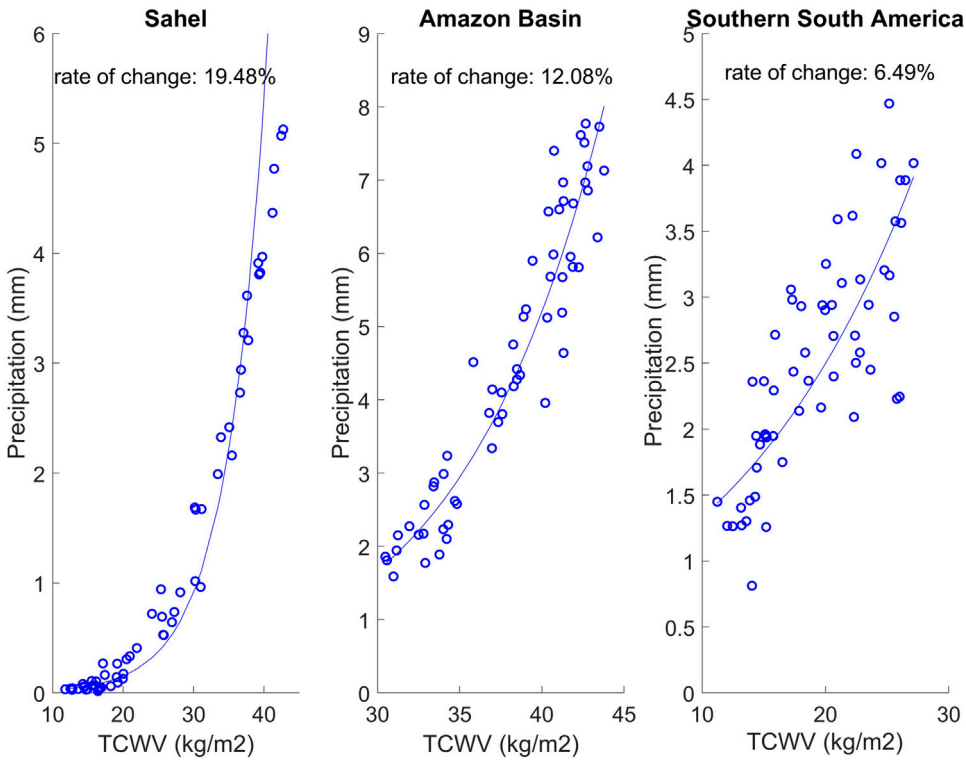

FIGURE 4
Monthly mean precipitation intensity versus TCWV at three Land regions.

2.3.2 Stratified precipitation intensity distribution based on TCWV

For an in-depth examination of the relationship between daily precipitation intensity and TCWV, we stratify daily precipitation intensity into five groups at each location: lower than 20th, 21st-40th, 41st-60th, 61st-80th, and higher than 80th percentiles (Table 2). Then, we pair each day with its corresponding daily TCWV and plot the distribution of occurrence of the five precipitation intensity groups based on their corresponding daily TCWV. This way, we visualize the distribution of daily precipitation intensity in response to the TCWV values for different locations. This information determines which precipitation intensity is most likely to occur at specific TCWV for different localities.

3 Results

3.1 Monthly TCWV vs. precipitation

Figure 2 presents the time series of monthly mean TRMM rainfall and AIRS TCWV for the land regions. For the Amazon region, there is a significant seasonal pattern of both precipitation intensity and TCWV, as shown in Figure 2. The wet season tends to occur in December-February and dry season during June-August. The peak precipitation coincides with peak TCWV. Similar to the Amazon, Sahel also depicts a seasonal pattern of precipitation and TCWV. The peak wet season appears to occur in June and the dry season in November to January. The TCWV and precipitation follow each other very closely as seasons progress, especially in the peak wet month of the year. After these wet months, the values drastically decrease when rainfall is low or not present during November and December months. The southern South America region (Figure 2) also displays seasonality, but with more variation in precipitation than Amazon Basin and Sahel. Southern South America TCWV shows much lower water vapor values but with a similar seasonal variation to that of Amazon.

Figure 3 illustrates a time series of monthly mean TRMM rainfall and AIRS TCWV over ocean regions. Compared to the land regions (Figure 2), the seasonality associated with the TCWV, and precipitation intensity appears to be much less evident in the ocean regions (Figure 3). In the Atlantic Ocean region, the peak of precipitation does not necessarily correspond to the peak of TCWV. Similarly, there is a difficulty discerning a seasonal pattern in TCWV and precipitation in the Indian Ocean and Niño 4 regions. There is more variability in the precipitation and TCWV compared to the land regions.

3.2 Rate of change

Figure 4 illustrates the relationship between TCWV and monthly mean precipitation intensity for land regions including Amazon, Sahel, and Southern South America. Sahel has the greatest rate of change in precipitation for 1 kg/m^2 TCWV, there is an increase in monthly precipitation intensity, resulting in 19.48% change. This strong correspondence may be due to Sahel's drier climate. The second greatest rate of change occurs in the Amazon region at 12.08%. The smallest rate of change occurs in the southern

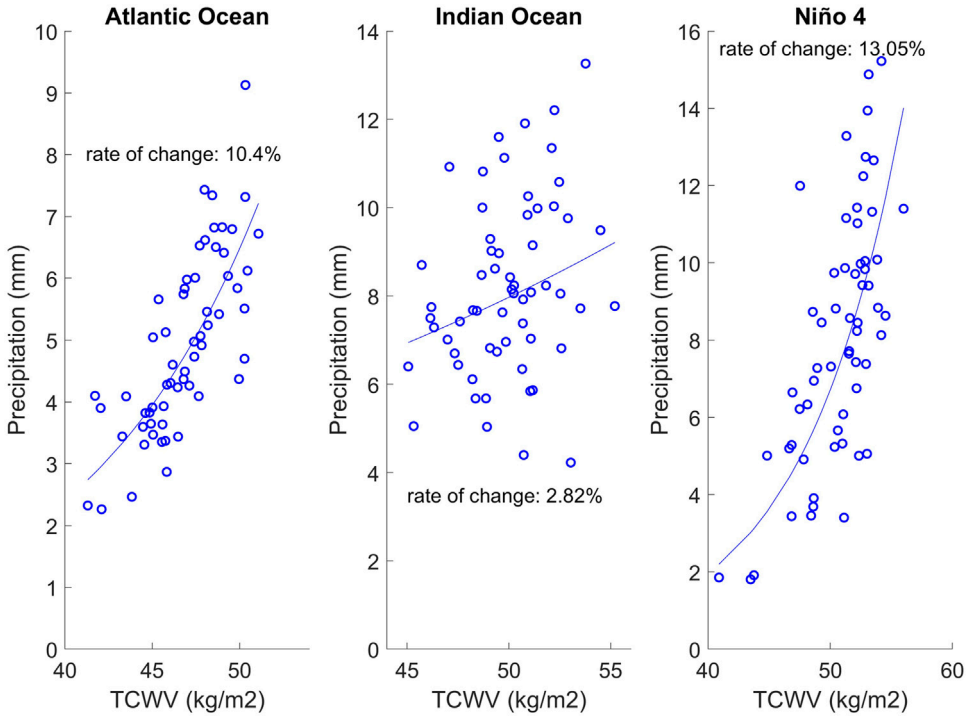

FIGURE 5
Monthly mean precipitation intensity versus TCWV at three Ocean regions.

South American region at 6.49%. Sahel and southern South America have similar warm season climates; however, these regions have a difference in rate of change, illustrating the distinct precipitation processes regarding the precipitation-moisture response. Generally, we expect the rate of change in land location to be greater supported by other studies highlighting the large change over land (Ye et al., 2017).

Figure 5 shows the relationship between TCWV and monthly mean precipitation intensity for ocean regions including Atlantic Ocean, Indian Ocean, and Niño 4. Niño 4 has the largest rate of change at 13.05%, followed by the Atlantic Ocean at 10.4%. The Indian Ocean has the smallest rate of change at 2.82% with the largest spread of data points, depicting a weaker relationship between TCWV and precipitation intensity. This aligns with observations by Bretherton et al. (2004) that precipitation has a minimal response to water vapor in the Indian Ocean region compared to the other selected ocean regions.

3.3 Stratified precipitation intensity distribution

Figure 6 illustrates the occurrence distribution of five different precipitation intensity groups in corresponding TCWV for six study regions. Table 3 provides each study region's precipitation percentile values for five precipitation intensity groups. Based on the Amazon Basin results (Figure 6A), the higher the values of daily TCWV, the greater likelihood of higher precipitation intensity events. The lowest precipitation intensity below the 20th percentile (Group 1) peaks at TCWV of 31 kg/m^2. The 21–40th percentile precipitation (Group 2), peaks at TCWV of 34 kg/m^2. The precipitation intensity at 41–60th percentile (Group 3), peaks at 37 kg/m^2. For precipitation intensity at 61–80th percentile (Group 4), the peak is at 39 kg/m^2 TCWV. Lastly, precipitation intensity higher than 80th percentile (Group 5), peaks at 41 kg/m^2 water vapor. The highest precipitation intensities (Group 5) show the narrowest distribution range for the Amazon Basin with no occurrence below 30 kg/m^2 TCWV.

The occurrence of various daily averaged precipitation intensities in the Sahel region is shown in Figure 6B. This is the greatest sensitivity to water vapor of any region considered in this study. Compared to the Amazon Basin, the distribution of precipitation intensity is well separated based on water vapor, with very little overlap between lowest and highest percentiles, the blue and red curves, respectively. In Figure 6B, the lowest 20th percentile (Group 1), peaking at 13 kg/m^2. The 21–40th percentile (Group 2) peaks at 14 kg/m^2. For the 41–60th percentile (Group 3), the peak water vapor is 24 kg/m^2. The water vapor peaks at 30 kg/m^2 for the 61–80th percentile (Group 4). Water vapor peaks at 36 kg/m^2 for the highest percentile rainfall occurrence (Group 5). The distribution shape is roughly similar among different groups, but with the top and bottom 20th percentile extremes being slightly narrower.

The precipitation intensity is less sensitive to water vapor in the southern South American region (Figure 6C). This result suggests high-intensity precipitation sometimes happens during very low value of TCWV, and that low-intensity precipitation days may have very high TCWV. However, the general shift from the lowest intensity group to the highest intensity group with increasing TCWV is still apparent. For Group 1, the water vapor value peaks at 12 kg/m^2. Group 2 peaks at 15 kg/m^2. The highest water vapor value for Group 3 is 16 kg/m^2. Group 4 peaks at 21 kg/m^2, Group 5 also peaks between 21 and 22 kg/m^2.

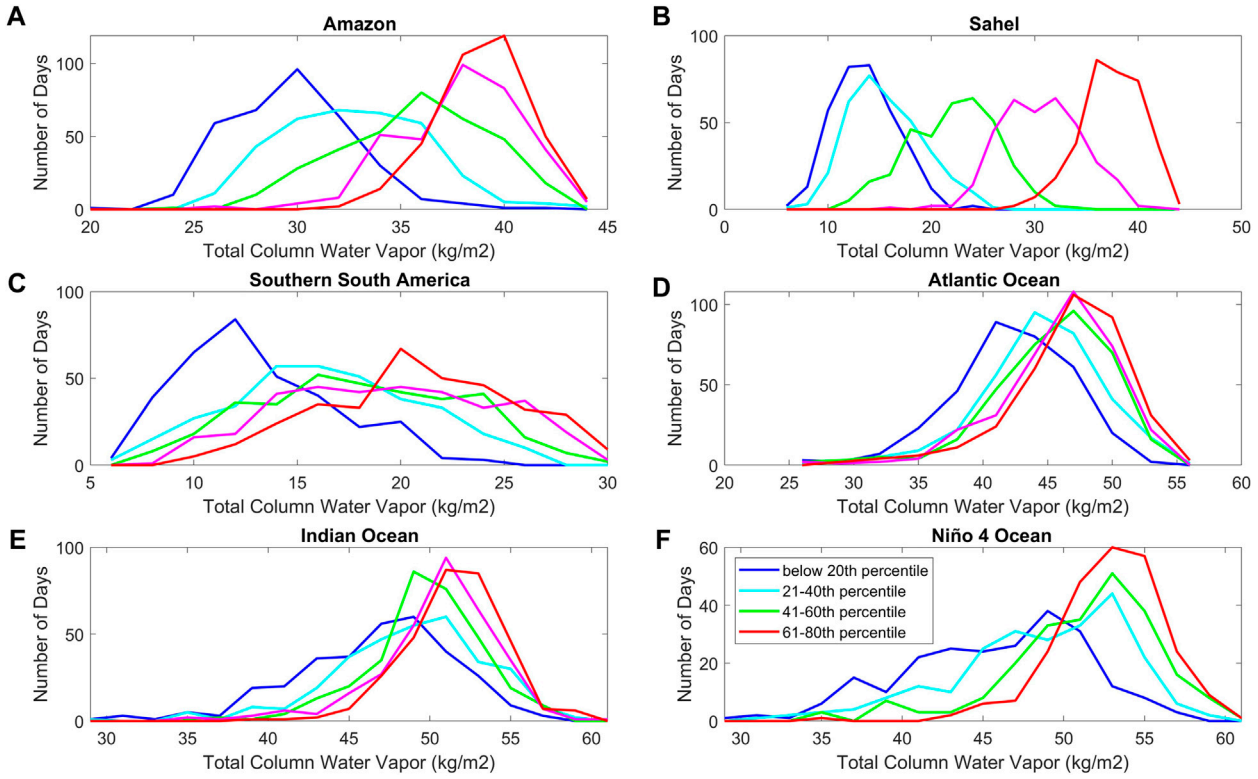

FIGURE 6
Distribution of ranked precipitation occurrence intensity versus TCWV for six study regions, including **(A)** Amazon, **(B)** Sahel, **(C)** Southern South America, **(D)** Atlantic Ocean, **(E)** Indian Ocean, and **(F)** Niño 4 Ocean.

TABLE 3 Percentiles of daily precipitation values (in mm) for six regions in this study.

Locations	Sahel	Amazon basin	Southern South America	Atlantic ocean	Indian ocean	Niño 4
20th Percentile	0.77	53.1	10.6	33.7	41.6	21.5
40th Percentile	3.4	86.4	27.6	71.3	97.1	61.4
60th Percentile	19.6	123.5	55.7	113.9	180.2	142.5
80th Percentile	63.4	158.6	104.8	191	326.1	322.2
100th Percentile	226.7	291.7	447.68	745.1	1,091.2	2,147.5

Compared to the land regions, the precipitation over the Atlantic Ocean (Figure 6D), is less sensitive to TCWV, especially at higher intensity groups. The distributions of precipitation occurrence almost overlap among Groups 3, 4, and 5. They all peak at 47 kg/m^2. The TCWV peaks at 40 kg/m^2 for Group 1, and the Group 2 peaks at 44 kg/m^2. This distribution suggests water vapor has little control of the precipitation intensity above the 40th percentile over the tropical Atlantic region.

The occurrence of precipitation intensity over the Indian Ocean (Figure 6E) is relatively unresponsive to the water vapor, as was seen over the Atlantic Ocean region (Figure 6D). The most likely values of TCWV associated with the following groups are: Group 1 at 47 kg/m^2, Group 2 at 51 kg/m^2, Group 3 at 49 kg/m^2, and Group 4 and 5 at 50 kg/m^2. The shape of distribution tends to narrow as water vapor increases, especially for Groups 3, 4, and 5.

The occurrence of different precipitation intensities in the Niño 4 region varies only slightly with TCWV (Figure 6F). This is consistent with other oceanic regions (Figures 6D, E), and contrasts with land regions (Figures 6A–C). Niño 4 Group 1 peaks at 49 kg/m^2. The highest water vapor peak for Groups 2–5 is 53 kg/m^2. There are very few differences in occurrence distributions between Groups 4 and 5. This distribution suggests that precipitation intensity occurrences higher than the 60th percentile do not respond to the TCWV change above a threshold of about 45 kg/m^2.

The occurrence distribution for Niño 4 location (Figure 6F) is quite like that of the Indian Ocean (Figure 6E) but with even less response to water vapor. Niño 4 Group 1 peaks at low TCWV of 37 kg/m^2 (Figure 6F) and spreads more broadly across the entire range of water vapor. Groups 2–5 peak at a similar value of around

54 kg/m^2; however, the distribution becomes narrower as the precipitation intensity group increases.

4 Discussion

This study expands previous knowledge on the relationships and geographic effects of tropical precipitation intensity response to TCWV utilizing satellite observations.

We find that the daily precipitation intensity over tropical lands has more sensitivity to TCWV than over tropical oceans. Results over tropical land detail a well-sorted pattern of increased occurrences of higher daily precipitation intensity as TCWV increases. Similarly, Liang et al. (2020) found that increases in precipitable water vapor accompany precipitation occurrence.

In Sahel, precipitation has the greatest sensitivity to water vapor change, where the rate of change is 19.48% per each 1 kg/m^2 of TCWV increases at monthly time scale. The higher sensitivity to water vapor could be due to the arid climate of the Sahel. We also notice a seasonal component of rainfall and TCWV in the Sahel during June -September (Figure 2). If a dry environment is a factor in sensitivity, we would expect that the southern South American area would show similar behavior. However, rainfall is less sensitive to water vapor there, suggesting fundamentally different precipitation processes in the Sahel and southern South America.

For the study areas over the ocean, the precipitation intensity occurrence does not show strong response to water vapor, especially in the Indian Ocean and Niño 4 regions: a wider range of water vapor changes over the ocean regions does not appear to control precipitation intensities. Oceanic precipitation intensities above the 40th percentiles are insensitive to the increase of water vapor above threshold values. These are consistent with the smaller change rates of monthly precipitation intensities with TCWV between 2%–13.1% among these tropical ocean regions.

Daily data is necessary to examine the occurrence distributions for different precipitation intensities. We find precipitation intensity occurrences over land regions are more sensitive to water vapor changes compared to the ocean regions. These differences indicate that changes in water vapor impact precipitation differently over land and ocean. These relationships are further confirmed by the distribution of occurrences of precipitation intensity. Forecasts of precipitation over tropical land can rely on water vapor as a predictor of precipitation intensity and occurrence. The highest land precipitation intensity occurrences are associated with higher values of TCWV. Knowing the difference between precipitation intensities over (sub)tropical land and ocean may aid water resource planning. More importantly, this study contributes to understanding the precipitation-moisture over multiple scales.

Data availability statement

The original contributions presented in the study are included in the article/Supplementary Material, further inquiries can be directed to the corresponding author.

Author contributions

SJ: Conceptualization, Data curation, Formal Analysis, Investigation, Methodology, Visualization, Writing–original draft, Writing–review and editing. HY: Conceptualization, Funding acquisition, Methodology, Supervision, Writing–review and editing. EF: Conceptualization, Funding acquisition, Methodology, Supervision, Writing–review and editing. JL: Conceptualization, Funding acquisition, Methodology, Supervision, Writing–review and editing.

Funding

The author(s) declare financial support was received for the research, authorship, and/or publication of this article. This research was funded by the NASA Minority University Research and Education Project (MUREP) Institutional Research Opportunity under Grant (NNX15AQ06A) and NASA's Making Earth System Data Records for Use in Research Environments (MEaSUREs) program.

Acknowledgments

The authors would like to thank the support of NASA DIRECT-STEM, AIRS group at the Jet Propulsion Laboratory, California Institute of Technology, and colleagues.

Conflict of interest

The authors declare that the research was conducted in the absence of any commercial or financial relationships that could be construed as a potential conflict of interest.

Publisher's note

References

Abraham, C., and Goldblatt, C. (2023). Changes in relative humidity profiles over earth's oceans in a warming climate: a satellite-data-based inference. *J. Atmos. Sci.* 80 (7), 1847–1866. doi:10.1175/jas-d-22-0119.1

Ahmed, F., and Schumacher, C. (2015). Convective and stratiform components of the precipitation-moisture relationship. *Geophys Res. Lett.* 42 (23). doi:10.1002/2015GL066957

Ahmed, F., and Schumacher, C. (2017). Geographical differences in the tropical precipitation-moisture relationship and rain intensity onset. *Geophys Res. Lett.* 44 (2), 1114–1122. doi:10.1002/2016gl071980

AIRS project (2019). *Aqua/AIRS L3 daily standard physical retrieval (AIRS-only) 1 degree x 1 degree V7.0.* Greenbelt, MD, USA: Goddard Earth Sciences Data and Information Services Center GES DISC. doi:10.5067/UO3Q64CTTS1U

Bao, J., Sherwood, S. C., Alexander, L. V., and Evans, J. P. (2017). Future increases in extreme precipitation exceed observed scaling rates. *Nat. Clim. Change* 7 (2), 128–132. doi:10.1038/nclimate3201

Bevis, M., Businger, S., Herring, T. A., Rocken, C., Anthes, R. A., and Ware, R. H. (1992). GPS meteorology: remote sensing of atmospheric water vapor using the global positioning system. *J. Geophys Res.* 97 (D14), 15787–15801. doi:10.1029/92jd01517

Bretherton, C. S., Peters, M. E., and Back, L. E. (2004). Relationships between water vapor path and precipitation over the tropical oceans. *J. Clim.* 17 (7), 1517–1528. doi:10.1175/1520-0442(2004)017<1517:rbwvpa>2.0.co;2

Chahine, M. T., Pagano, T. S., Aumann, H. H., Atlas, R., Barnet, C., Blaisdell, J., et al. (2006). AIRS improving weather forecasting and providing new data on greenhouse gases. *Am. Meteorol. Soc.* 87, 911–926. doi:10.1175/bams-87-7-911

Chen, B., Liu, C., and Mapes, B. E. (2017b). Relationships between large precipitating systems and atmospheric factors at a grid scale. *J. Atmos. Sci.* 74 (2), 531–552. doi:10.1175/jas-d-16-0049.1

Chen, B., Liu, Z., Wong, W. K., and Woo, W. C. (2017a). Detecting water vapor variability during heavy precipitation events in Hong Kong using the GPS tomographic technique. *J. Atmos. Ocean. Technol.* 34 (5), 1001–1019. doi:10.1175/jtech-d-16-0115.1

Donat, M. G., Lowry, A. L., Alexander, L. V., O'Gorman, P. A., and Maher, N. (2016). More extreme precipitation in the world's dry and wet regions. *Nat. Clim. Change* 6 (5), 508–513. doi:10.1038/nclimate2941

Fan, R., Zeng, Z., Wang, X., Zhang, L., Cheng, W., and Ding, M. (2023). Comprehensive evaluation and comparison of AIRS, VASS, and VIRR water vapor products over Antarctica. *J. Geophys Res. Atmos.* 128 (23), e2023JD039221. doi:10.1029/2023jd039221

Guillaume, A., Kahn, B. H., Fetzer, E. J., Yue, Q., Manipon, G. J., Wilson, B. D., et al. (2019). Footprint-scale cloud type mixtures and their impacts on Atmospheric Infrared Sounder cloud property retrievals. *Atmos. Meas. Tech.* 12 (8), 4361–4377. doi:10.5194/amt-12-4361-2019

Holloway, C. E., and Neelin, D. J. (2009). Moisture vertical structure, column water vapor, and tropical deep convection. *J. Atmos. Sci.* 66 (6), 1665–1683. doi:10.1175/2008jas2806.1

Holloway, C. E., and Neelin, J. D. (2010). Temporal relations of column water vapor and tropical precipitation. *J. Atmos. Sci.* 67 (4), 1091–1105. doi:10.1175/2009jas3284.1

Huffman, G. J., Adler, R. F., Bolvin, D. T., and Nelkin, E. J. (2010). "The TRMM multi-satellite precipitation analysis (TMPA)," in *Satellite rainfall applications for Surface hydrology* (Netherlands: Springer), 3–22.

Kuo, Y. H., Neelin, J. D., and Mechoso, C. R. (2017). Tropical convective transition statistics and causality in the water vapor–precipitation relation. *J. Atmos. Sci.* 74 (3), 915–931. doi:10.1175/jas-d-16-0182.1

Lenderink, G., and Van Meijgaard, E. (2008). Increase in hourly precipitation extremes beyond expectations from temperature changes. *Nat. Geosci.* 18 (8), 511–514. doi:10.1038/ngeo262

Liang, H., Zhang, Y., Cao, L., and Cao, Y. (2020). Temporal relations between precipitable water vapour and precipitation during wet seasons based on nearly two decades of data from the Lhasa River valley, Tibetan Plateau. *Int. J. Climatol.* 40 (3), 1656–1668. doi:10.1002/joc.6293

Muller, C. J. (2013). Impact of convective organization on the response of tropical precipitation extremes to warming. *J. Clim.* 26 (14), 5028–5043. doi:10.1175/jcli-d-12-00655.1

NASA (2015). The tropical rainfall measuring mission (TRMM). *NASA Glob. Precip. Meas. Mission*. Available at: https://gpm.nasa.gov/missions/trmm

Neelin, J. D., Martinez-Villalobos, C., Stechmann, S. N., Ahmed, F., Chen, G., Norris, J. M., et al. (2022). Precipitation extremes and water vapor: relationships in current climate and implications for climate change. *Curr. Clim. Change Rep.* 8 (1), 17–33. doi:10.1007/s40641-021-00177-z

O'Gorman, P. A., and Schneider, T. (2009). The physical basis for increases in precipitation extremes in simulations of 21st-century climate change. *Proc. Natl. Acad. Sci. U. S. A.* 106 (35), 14773–14777. doi:10.1073/pnas.0907610106

Powell, S. W. (2019). Observing possible thermodynamic controls on tropical marine rainfall in moist environments. *J. Atmos. Sci.* 76 (12), 3737–3751. doi:10.1175/jas-d-19-0144.1

Radhakrishna, B., Fabry, F., Braun, J. J., and Van Hove, T. (2015). Precipitable water from GPS over the continental United States: diurnal cycle, intercomparisons with NARR, and link with convective initiation. *J. Clim.* 28 (7), 2584–2599. doi:10.1175/jcli-d-14-00366.1

Radhakrishna, B., and Rao, T. N. (2021). Diurnal variation of rainfall in the presence of large- and small-scale precipitating systems during different monsoon seasons over a complex terrain (gadanki) region. *J. Appl. Meteorol. Climatol.* doi:10.1175/jamc-d-20-0269.1

Radhakrishna, B., Rao, T. N., and Chandrakanth, G. S. V. (2022). Total column water vapor from INSAT-3D: assessments with ground-based GNSS receivers and GMI datasets at different temporal scales. *IEEE Trans. Geosci. Remote Sens.* 60, 1–8. doi:10.1109/tgrs.2022.3200716

Roderick, T. P., Wasko, C., and Sharma, A. (2019). Atmospheric moisture measurements explain increases in tropical rainfall extremes. *Geophys Res. Lett.* 46 (3), 1375–1382. doi:10.1029/2018gl080833

Rushley, S. S., Kim, D., Bretherton, C. S., and Ahn, M. S. (2018). Reexamining the nonlinear moisture-precipitation relationship over the tropical oceans. *Geophys Res. Lett.* 45 (2), 1133–1140. doi:10.1002/2017gl076296

Schiro, K. A., Ahmed, F., Giangrande, S. E., and Neelin, J. D. (2018). GoAmazon2014/5 campaign points to deep-inflow approach to deep convection across scales. *Proc. Natl. Acad. Sci.* 115 (18), 4577–4582. doi:10.1073/pnas.1719842115

Schiro, K. A., Neelin, J. D., Adams, D. K., and Lintner, B. R. (2016). Deep convection and column water vapor over tropical land versus tropical ocean: a comparison between the amazon and the tropical Western Pacific. *J. Atmos. Sci.* 73 (10), 4043–4063. doi:10.1175/jas-d-16-0119.1

Schröder, M., Lockhoff, M., Fell, F., Forsythe, J., Trent, T., Bennartz, R., et al. (2018). The GEWEX Water Vapor Assessment archive of water vapour products from satellite observations and reanalyses. *Earth Syst. Sci. Data* 10 (2), 1093–1117. doi:10.5194/essd-10-1093-2018

Sun, Y., Solomon, S., Dai, A., and Portmann, R. W. (2007). How often will it rain?. *J. Clim.* 20 (19), 4801–4818. doi:10.1175/jcli4263.1

Susskind, J., Blaisdell, J., and Iredell, L. (2014). Improved methodology for surface and atmospheric soundings, error estimates, and quality control procedures: the atmospheric infrared sounder science team version-6 retrieval algorithm. *J. Appl. Remote Sens.* 8, 084994. doi:10.1117/1.jrs.8.084994

Tian, B., Fetzer, E. J., and Manning, E. M. (2019). The atmospheric infrared sounder Obs4MIPs version 2 data set. *Earth Space Sci.* 6 (2), 324–333. doi:10.1029/2018ea000508

Tian, B., Manning, E., Fetzer, E., Olsen, E., and Wong, S. (2017). *AIRS/AMSU/HSB version 6 level 3 product user guide*.

Trenberth, K. (2011). Changes in precipitation with climate change. *Clim. Res.* 47 (1), 123–138. doi:10.3354/cr00953

Trenberth, K. E., Dai, A., Rasmussen, R. M., and Parsons, D. B. (2003). The changing character of precipitation. *Bull. Am. Meteorol. Soc.* 84 (9), 1205–1218. doi:10.1175/bams-84-9-1205

TRMM. Goddard Space Flight Center Distributed Active Archive Center (GSFC DAAC) (2015). The tropical rainfall measuring mission (TRMM) | NASA global precipitation measurement mission. Available at: https://gpm.nasa.gov/missions/trmm.

Troller, M., Geiger, A., Brockmann, E., Bettems, J. M., Bürki, B., and Kahle, H. G. (2006). Tomographic determination of the spatial distribution of water vapor using GPS observations. *Adv. Space Res.* 37 (12), 2211–2217. doi:10.1016/j.asr.2005.07.002

Tropical Rainfall Measuring Mission (TRMM) (2011). "Goddard Earth sciences data and information services center (GES DISC)," in *TRMM (TMPA/3B43) rainfall estimate L3 1 month 0.25 degree x 0.25 degree V7*. Available at: https://disc.gsfc.nasa.gov/datasets/TRMM_3B43_7/summary.

Van Baelen, J., Reverdy, M., Tridon, F., Labbouz, L., Dick, G., Bender, M., et al. (2011). On the relationship between water vapour field evolution and the life cycle of precipitation systems. *Q. J. R. Meteorol. Soc.* 137 (Suppl. 1), 204–223. doi:10.1002/qj.785

Wang, Z., Sun, M., Yao, X., Zhang, L., and Zhang, H. (2021). Spatiotemporal variations of water vapor content and its relationship with meteorological elements in the third Pole. *Water* 13 (13), 1856. doi:10.3390/w13131856

Wong, S., Fetzer, E. J., Schreier, M., Manipon, G., Fishbein, E. F., Kahn, B. H., et al. (2015). Cloud-induced uncertainties in AIRS and ECMWF temperature and specific humidity. *J. Geophys Res. Atmos.* 120 (5), 1880–1901. doi:10.1002/2014jd022440

Ye, H., Fetzer, E. J., Wong, S., Behrangi, A., Olsen, E. T., Cohen, J., et al. (2014). Impact of increased water vapor on precipitation efficiency over northern Eurasia. *Geophys Res. Lett.* 41 (8), 2941–2947. doi:10.1002/2014gl059830

Ye, H., Fetzer, E. J., Wong, S., Behrangi, A., Yang, D., and Lambrigtson, B. H. (2015). Increasing atmospheric water vapor and higher daily precipitation intensity over northern Eurasia. *Geophys Res. Lett.* 42 (21), 9404–9410. doi:10.1002/2015gl066104

Ye, H., Fetzer, E. J., Wong, S., and Lambrigtsen, B. H. (2017). Rapid decadal convective precipitation increase over Eurasia during the last three decades of the 20th century. *Sci. Adv.* 3 (1), e1600944. doi:10.1126/sciadv.1600944

Yue, Q., Fetzer, E. J., Kahn, B. H., Wong, S., Manipon, G., Guillaume, A., et al. (2013). Cloud-state-dependent sampling in AIRS observations based on CloudSat cloud classification. *J. Clim.* 26 (21), 8357–8377. doi:10.1175/jcli-d-13-00065.1

Zhang, F., Feng, P., Barriot, J. P., Hopuare, M., and Sichoix, L. (2018). "Correlation between integrated precipitable water vapor and precipitated water during the heavy rainfall event of february 2018 in the tahiti Island (South pacific)," in Proceedings of the 2018 International Conference on Earth Observations and Societal Impacts (ICEO&SI 2018), Hsinchu, Taiwan, 1–3 July 2018. Available at: https://www.researchgate.net/publication/325429291_Correlation_Between_Integrated_Precipitable_Water_Vapor_and_Precipitated_Water_During_the_Heavy_Rainfall_Event_of_February_2018_in_the_Tahiti_Island_South_Pacific.

frontiers | Frontiers in Environmental Science

TYPE Original Research
PUBLISHED 21 May 2024
DOI 10.3389/fenvs.2024.1387672

OPEN ACCESS

EDITED BY
Haipeng Yu,
Chinese Academy of Sciences (CAS), China

REVIEWED BY
Murat Yakar,
Mersin University, Mersin, Türkiye
Shanyou Zhu,
Nanjing University of Information Science and Technology, China

*CORRESPONDENCE
Xiaochun Luo,
ntlxc9@163.com

RECEIVED 18 February 2024
ACCEPTED 08 April 2024
PUBLISHED 21 May 2024

CITATION
Shi X, Sun M and Luo X (2024), Comparative analysis of near-surface and surface urban heat islands in the Yangtze River Delta region. *Front. Environ. Sci.* 12:1387672. doi: 10.3389/fenvs.2024.1387672

Comparative analysis of near-surface and surface urban heat islands in the Yangtze River Delta region

Xiao Shi[1,2], Ming Sun[2] and Xiaochun Luo[2]*

[1]China Meteorological Administration Transportation Meteorology Key Laboratory, China Meteorological Administration, Beijing, China, [2]Jiangsu Meteorological Services Center, Jiangsu Provincial Meteorological Bureau, Nanjing, China

Compared with surface temperature, the near-surface temperature is more related with human health. However, extensive researches have been conducted on the UHI effect globally using surface temperature considering its accessibility. In this study, a comparative analysis of near-surface and surface urban heat islands in the Yangtze River Delta Region is investigated. This study first proposed a spatialization method suitable for air temperature in highly urbanized areas with complex land cover. Based on this method, a dataset of 1-km gridded air temperature is developed, and an in-depth analysis of the changes of near-surface and surface heat island is further carried out. Results show that both the near-surface urban heat island intensity (NSUHII) and surface urban heat island intensity (SUHII) are rather strong over the past 20 years, presenting similar spatial distributions as well. However, in the rapidly expanding urban areas especially during summer and winter seasons, the difference in magnitude and time variations (R) between NSUHII and SUHII are pronounced. Hence, adaptions and mitigation strategies on NSUHI and SUHI should be developed and implemented separately in such occasions, which is especially important for developed areas such as Yangtze River Delta Region.

KEYWORDS

air temperature estimation, land surface temperature, random forest, urban heat island, remote sensing

1 Introduction

Primarily triggered by climate change and the intricate interplay between land surface and atmospheric systems, the heat island effect in urban landscapes takes shape (Krayenhoff et al., 2018; Lu et al., 2023). Climate change has led to an imbalanced distribution of water and heat, leading to a surge in extreme high-temperature occurrences in certain regions. Concurrently, as urbanization rapidly advances, urban spaces and their populations expand exponentially, accompanied by profound shifts in land-use patterns (Aliyazıcıoğlu et al., 2021; Topaloglu, 2022; Morsy and Hadi, 2022). These changes, by manipulating surface albedo and water evaporation, disrupt the equilibrium of surface heat budgets, encompassing both the sensible and latent heat exchanges between land and atmosphere, as well as vertical water vapor transport. Consequently, these alterations reshape meteorological variables like temperature and humidity within the lower atmospheric stratum. Ultimately, this gives rise to a remarkable phenomenon where urban temperatures significantly outstrip those in neighboring rural areas, thus giving

birth to the urban heat island effect (UHI) (Manley, 1959; Parry& Chandler, 1966; Oke, 1982; Zhang et al., 2023). Featured by significant spatio-temporal variations and substantial side effects, the UHI effect imposes an obvious impact on regional climate, energy consumption, air pollution and human health (Shahmohamadi et al., 2011; Zhang et al., 2023). In addition, extreme weather events have become increasingly frequent under the context of climate change, which further exacerbate the UHI effect (Shi et al., 2021; Lou et al., 2023). Hence, it is crucial to accurately describe and quantify the UHI effect for the urban sustainable development.

In recent years, extensive researches have been conducted on the UHI effect globally (Ramakreshnan et al., 2019; Han et al., 2020; Hu et al., 2023). Traditional UHI studies primarily use the air temperature data observed at meteorological stations (referred to as near-surface UHIs) (Liu et al., 2021). The observed air temperature data have the advantages of high temporal resolution and high precision, which are widely regarded as the "ground truth" by scholars from various fields (Wang et al., 2016; Abbas and Ismael, 2020). However, sparsely distributed meteorological stations struggle to meet the research needs for various types of UHI effects, leading to uncertainties in the calculation of UHI effects.

Satellite remote sensing enables fast observation of UHI with spatio-temporal continuity. Currently, the UHI studies mostly focus on the LST-related surface heat island effect (Chen et al., 2016; Peng et al., 2016; Wang et al., 2021). The spatial and temporal variations of SUHI have been documented, the SUHI intensity varies greatly by cities, seasons according to previous studies (Imhoff et al., 2010; Yao et al., 2018; Meng et al., 2023). In addition, the long term trends of SUHI and associated drivers have been also investigated. Yao et al. (2018) pointed out significant increasing trends of SUHII in China and increased non-agriculture population and decreasing vegetation were important reasons for increased SUHII. Wang et al. (2021) pointed out anthropogenic factors are considered the most important ones in determining SUHI in the Yangtze River Delta.

With respect to human health and comfort, the near-surface temperature is more direct than surface temperature because human skin is directly in contact with the atmosphere rather than the land surface (Anniballe et al., 2014; Nanayakkara et al., 2023). However, there are still some gaps in studies of near-surface urban heat island, mainly because the near surface temperature cannot be retrieved by remote sensing method. Most of current studies on near-surface urban heat island are based on sparsely distributed meteorological stations, which may have some uncertainties (Shi et al., 2024).

Numerous studies have revealed a mutual interaction between the air temperature and the LST from the energy balance perspective (Liu et al., 2020; Luo et al., 2023; Yao, 2020). However, this interaction is relatively complex considering the physical differences and natural environments between them, which lead to discrepancies when describing the urban thermal effects, and may cause uncertainties for evaluating the impact of urbanization on environment. Weak relationships were reported in both vegetated, barren lands (Xiong et al., 2017) and urban area, especially during the daytime (Yang et al., 2020; Yao et al., 2021). Up to now, there is still a lack of research on comprehensively analyzing the spatio-temporal variation differences between near-surface heat island effects and surface heat island effects within the same study area from different perspectives.

The objective of this study is to investigate and analyze the characteristics of the near-surface UHI and surface UHI in the Yangtze River Delta region based on grid scale air temperature using machine learning method and remote sensing land surface temperatures. The remainder of this paper is organized as follows. Section 2 provides a detailed introduction to the study area, data information and methods used in this study. Section 3 analyzes the accuracy of remote sensing estimation of air temperature, and further investigates the spatial distributions, interrelationships and variation trends of near-surface UHI intensity (NSUHII) and surface UHI intensity (SUHII). Section 4 discusses the strengths and limitations of this study. Finally, the main conclusions are summarized in Section 5.

2 Materials and methods

2.1 Study area

The Yangtze River Delta (YRD) region is located in the east of China and has an area covers 358,000 square kilometers (Figure 1A). It is one of the three major urban agglomerations (the Beijing-Tianjin-Hebei, the Yangtze River Delta, and the Pearl River Delta) in China (Liu et al., 2017). The overall terrain in the northern part of the study area mainly consists of plain areas, while many mountainous areas are located in the southwestern and southeast part of the study area. The climate over the study area is dominated by the East Asian monsoon with four distinct seasons.

It consists of three provinces (Jiangsu, Zhejiang and Anhui) and one municipality (Shanghai), with a total of 41 cities (Figure 1B). Mega-cities including Shanghai, Hangzhou, Nanjing and Suzhou are located in this region, with a permanent population accounting for nearly 1/6 of the entire country and an economic aggregate constituting nearly 1/4 of the national total (Sun et al., 2019).

During the urbanization process, this region has undergone dramatic changes in land cover (Jin et al., 2021), where the UHI effect has also become increasingly intense and more severe. In addition, relevant studies have indicated that this region has experienced significant warming trend (Shi et al., 2021). Under the combined influences of climate warming and the rapid expansion of urban areas, the variations of thermal environment in this region have imposed a profound impact on both the ecological environment and social economy (Wang et al., 2021; Yang and Pan, 2011). Hence, it is crucial to study the spatio-temporal variation characteristics of the thermal environment in this region.

2.2 Data

The maximum air temperature data for the 2001–2018 period are obtained from 199 national ground meteorological stations, which are provided by the National Meteorological Information Center of China Meteorological Administration. This dataset was subjected to strict quality control procedures including spatial and internal consistency checks, identification of outliers, and manual revision of erroneous data (Chen et al., 2021). The locations of meteorological stations are shown in Figure 1B.

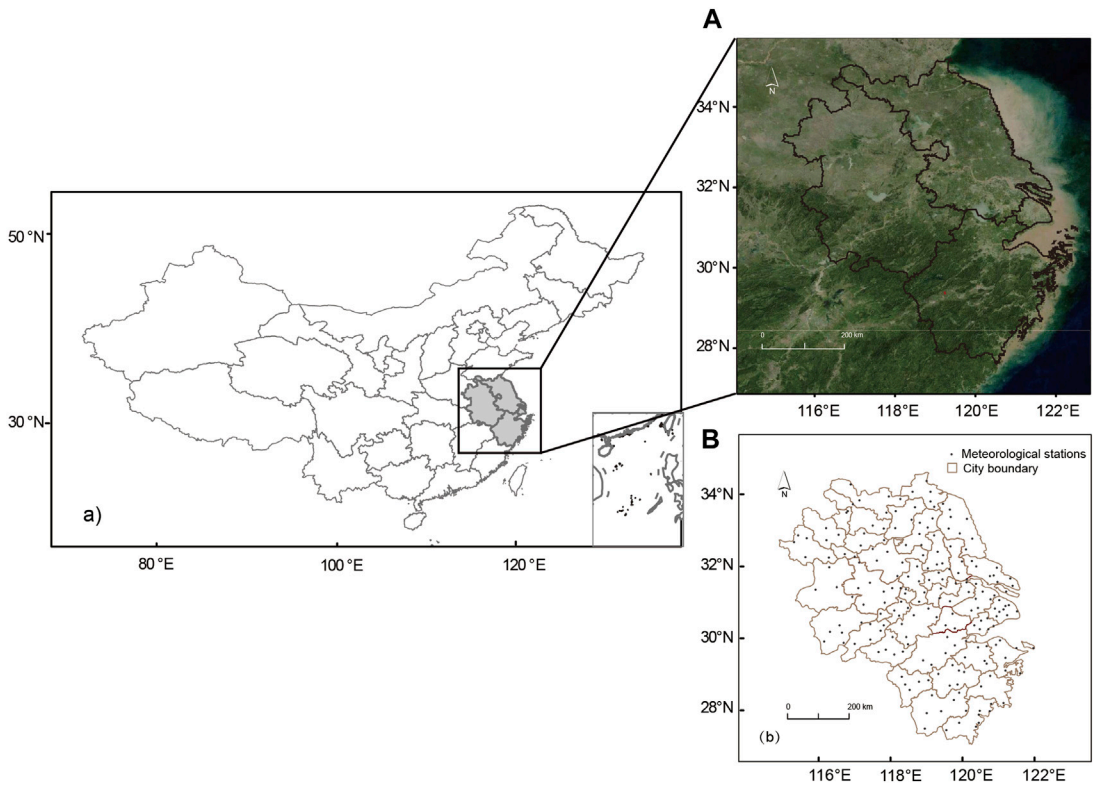

FIGURE 1
Study area **(A)** and the spatial distribution of meteorological stations **(B)**.

Terra Moderate Resolution Imaging Spectroradiometer (MODIS) is a sensor onboard Terra and Aqua platforms. The MOD11A2 product is an 8-day composite dataset with a spatial resolution of 1 km (Niu et al., 2020; Su et al., 2013; Wang et al., 2023). In this study, we obtained daytime LST, nighttime LST, clear_sky_days and clear_sky_nights data from MOD11A2. In addition, we calculate the rate of clear day (R_D) and night (R_N) from clear_sky_days and clear_sky_nights data, which are defined as the percentage of days and nights with clear sky. The surface reflectance from MOD09GA product provides the daily reflectance of bands 1–7 with 500-m spatial resolution. It is considered to derived the normalized difference vegetation index (NDVI) and the modified normalized difference water index (MNDWI) in this study, which are input parameters to estimate the air temperature are calculated using this data. The MCD12Q1 land cover type products combined Terra and Aqua data at yearly intervals and with 500-m spatial resolution (Yang and Huang, 2021; Hua and Chen, 2013).

The global nighttime light data during 2001–2018 is obtained from the National Polar-orbiting Partnership (NPP)/Visible-Infrared Imaging Radiometer Suite (VIIRS) data provided by the United States National Oceanic and Atmospheric Administration Earth Observation Group (Li et al., 2020). In addition, to calculate the solar radiation, which is an input parameter for remote sensing estimation, elevation data from the Shuttle Radar Topography Mission (SRTM) is also used. The data specifics used in this study are shown in Table 1.

2.3 Methods

2.3.1 Air temperature estimation

The core principle of remote sensing estimation for air temperature is to use the relationship between station-observed air temperatures and corresponding independent variables at a certain grid point to predict the air temperature values on this grid. Specifically, the monthly-averaged maximum air temperature from meteorological observation stations is selected as the dependent variable for the estimation models. Eight different types of land surface factors (LST_D, LST_N, R_D, R_N, NDVI, MNDWI, DEM, extraterrestrial solar radiation) are chosen as independent variables in the remote sensing estimation process of air temperature.

Extraterrestrial solar radiation is an important parameter for evaluating solar energy resources, which refers to the solar radiation that can be received by the earth's surface without considering the influence of the atmosphere. Here we use the distributed modeling of extraterrestrial solar radiation over rugged terrains proposed by (Zeng et al., 2005) and to calculate monthly average extraterrestrial solar radiation in study area. Extraterrestrial solar radiation on the slope is determined by geography, topographic features and astronomical factors (solar declination, hour Angle). The daily extraterrestrial solar radiation is calculated as follows (Eqs 1–9):

TABLE 1 Data and related information used in this study.

Variable	Source	Parameter	Time period	Spatial resolution	Temporal resolution	Data use
Maximum air temperature	Ground station	AT	2001–2018	/	1 day	Input parameter of remote sensing estimation
Daytime LST	MOD11A2	LST_D	2001–2018	1 km	8 days	Input parameter of remote sensing estimation\Comparison with AT
Nighttime LST	MOD11A2	LST_N	2001–2018	1 km	8 days	Input parameter of remote sensing estimation
Clear_sky_days	MOD11A2	Rate of clear Day (R_D)	2001–2018	1 km	8 days	
Clear_sky_nights	MOD11A2	Rate of clear night (R_N)	2001–2018	1 km	8 days	
Surface reflectance	MOD09GA	NDVI, MNDWI	2001–2018	0.5 km	1 day	Input parameter of remote sensing estimation\identification of the rural background
Land cover	MCD12Q1	/	2001–2018	0.5 km	1 year	Identification of the rural background
Elevation (DEM)	The Shuttle Radar Topography Mission (SRTM)	extraterrestrial solar radiation	2008	90 m	/	Input parameter of remote sensing estimation\identification of the rural background
Nighttime light	Composite NPP/VIIRS data	/	2001–2018	30 m	1 year	Identification of the rural background

$$\mathrm{Ws} = \frac{T}{2\pi} I_0 E_0 \left[u \sin\delta \left(\omega_{ss} - \omega_{sr}\right) + v \cos\delta \left(\sin\omega_{ss} - \sin\omega_{sr}\right) + w \cos\delta \left(\cos\omega_{ss} - \cos\omega_{sr}\right)\right] \quad (1)$$

W_s is extraterrestrial solar radiation, T is the length of 1 day (1,140 min), I_0 is solar constant (0.082 $MJ{\cdot}m^{-2}{\cdot}min^{-1}$), E_0 is correction coefficient of sun-earth distance. u, v, and w are the feature factors related to terrain. δ is the declination of the sun, ω is the hour angle (positive to the west and negative to the east from noon in true solar time), ω_{sr} and ω_{ss} are the sunrise and sunset hours respectively.

$$u = \sin\varphi\cos\alpha - \cos\varphi\sin\alpha\cos\beta \quad (2)$$

$$v = \sin\varphi\sin\alpha\cos\beta + \cos\varphi\cos\alpha \quad (3)$$

$$w = \sin\alpha\sin\beta \quad (4)$$

The declination of the sun and correction coefficient of sun-earth distance E_0 can be calculated as follows:

$$\delta = 0.006894 - 0.399512\cos\tau + 0.072075\sin\tau - 0.006799\cos 2\tau + 0.000896\sin 2\tau - 0.002689\cos 3\tau + 0.001516\sin 3\tau \quad (5)$$

$$E_0 = 1.000109 + 0.033494\cos\tau + 0.001472\sin\tau + 0.000768\cos 2\tau + 0.000079\sin 2\tau \quad (6)$$

Where τ is the daily angle and expressed in radians and can be calculated by days D_n.

$$\tau = 2\pi(D_n - 1)/365 \quad (7)$$

$$\omega_{ss} = \arccos\left(-\tan\varphi\tan\delta\right) \quad (8)$$

$$\omega_{sr} = -\omega_{ss} \quad (9)$$

Furthermore, four machine learning methods of the Multiple Linear Regression (MLR), Back-Propagation Neural Networks (BPNN), Support Vector Machine (SVM) and Random Forest (RF) are used to fit the relationship between the dependent variable and independent variables at the station scale. 10-fold cross-validation method is used to assess the fitness of selected predictors by comparing the observed and estimated air temperatures. Subsequently, the four models output four datasets of 1-km gridded monthly-averaged maximum air temperature by taking the 1-km independent variable data as the input. Since this study mainly focus on the comparison between near-surface and surface urban heat islands, detailed information about the air temperature estimation process will not be discussed in this study.

2.3.2 Urban heat island evaluation

To compare and analyze the similarities and differences between near-surface and surface heat island, NSUHII and SUHII are employed. The NSUHII and SUHII are used to quantify the near-surface and surface UHI effect, as follows (Eqs 10, 11):

$$\mathrm{NSUHII}_i = AT_i - \frac{1}{n}\sum_{j=1}^{n} ATb_j \quad (10)$$

$$\mathrm{SUHII}_i = LST_i - \frac{1}{n}\sum_{j=1}^{n} LSTb_j \quad (11)$$

Where NSUHIIi and SUHIIi refer the near-surface and surface urban heat intensity in pixel i, AT_i and LST_i refer the air temperature and LST in pixel i, n is the total number of rural background effective pixels. ATb_j and $LSTb_j$ represent the air temperature and LST of the corresponding rural background, respectively (Liu et al., 2017).

The appropriate selection of suburban farmland background is the key to calculate urban heat island intensity. For different cities in large urban agglomerations, it is not advisable choosing the same rural background to calculate the temperature difference between

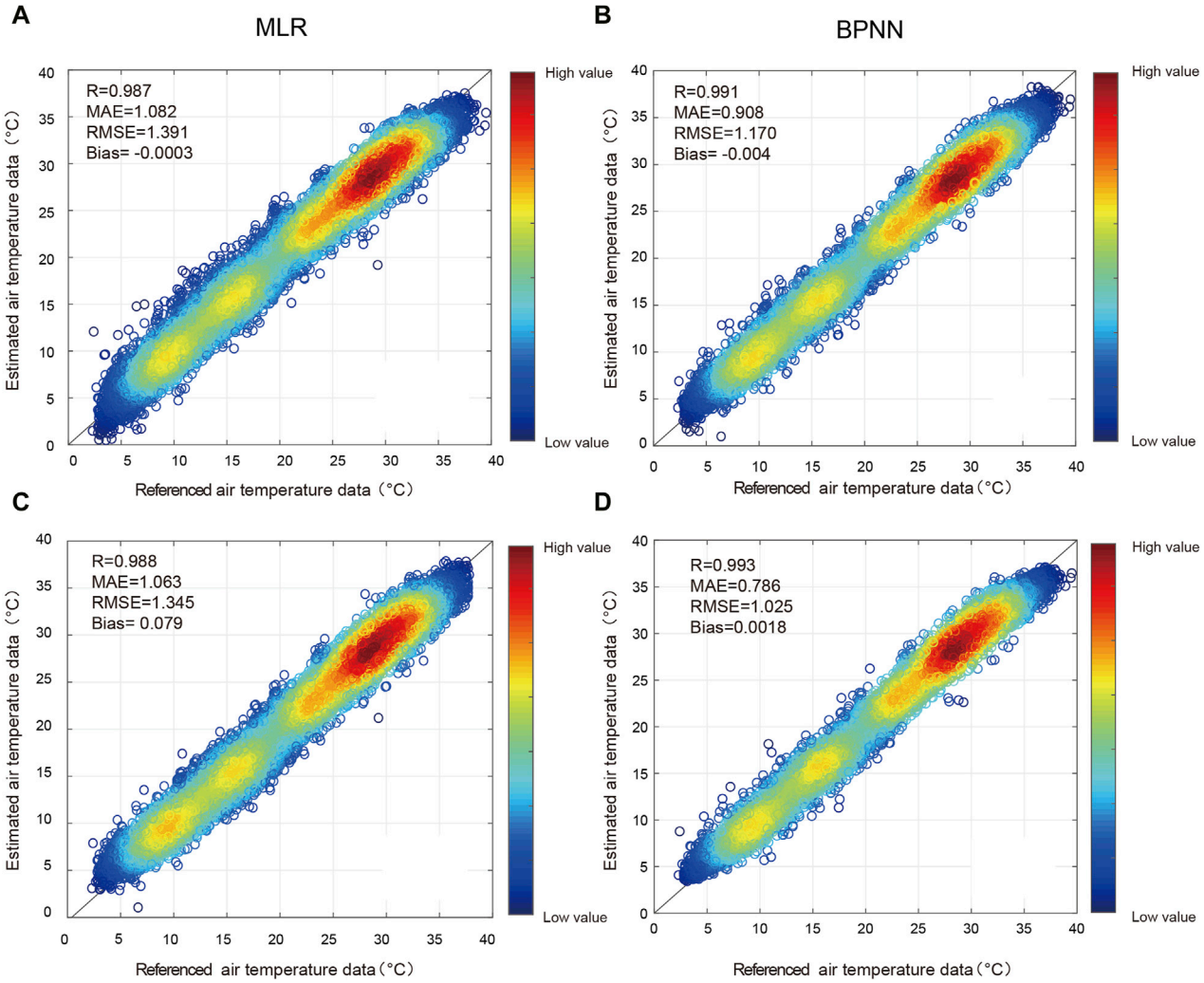

FIGURE 2
10-fold cross-validation accuracies of air temperature estimation based on MLR **(A)**, BPNN **(B)**, SVM **(C)** and RF **(D)** methods.

urban and rural areas to get the urban heat island intensity (Shi et al., 2021). We use the method proposed by (Liu et al., 2017) to determine the farmland background pixels of each city by combining four criteria: land cover, NDVI, night light index and elevation difference relative to urban central areas. 1) In terms of land cover type, the rural area is selected as the background pixel according to the land cover type of farmland; 2) The annual maximum NDVI ≥0.7 is used as the ideal value to determine the rural background; 3) The night light index ≤15 identifies areas unaffected by human activity; 4) The altitude difference from the city <50 m is preferred to reduce the terrain effect on the heat island intensity. The spatial distributions of land cover type of 2018, annual maximum NDVI of 2018, night light index of 2018 and altitude difference from the city are shown in Supplementary Figure S1.

2.3.3 Trend analysis

The non-parametric statistics of Theil-Sen slope (Sen, 1968) is used to determine the linear trend of NSUHII and SUHII during 2001–2018. It is a more robust estimator than the least-square method because it is insensitive to outliers and extreme values, which leading to the robust performance in time series variation trend estimation (Svilicic et al., 2016). The TS estimator is expressed as Eq. 12:

$$TS_{slope} = median\left(\frac{x_j - x_i}{t_j - t_i}\right) \quad (12)$$

where median denotes the median function, x_i and x_j are the data values at times i and j, respectively, and t_i and t_j are the corresponding time series with lengths of n and $i < j < n$, respectively.

3 Results

3.1 Accuracy analysis of estimation results

Figure 2 shows the density scatter plot between estimated air temperature data and the referenced air temperature data.

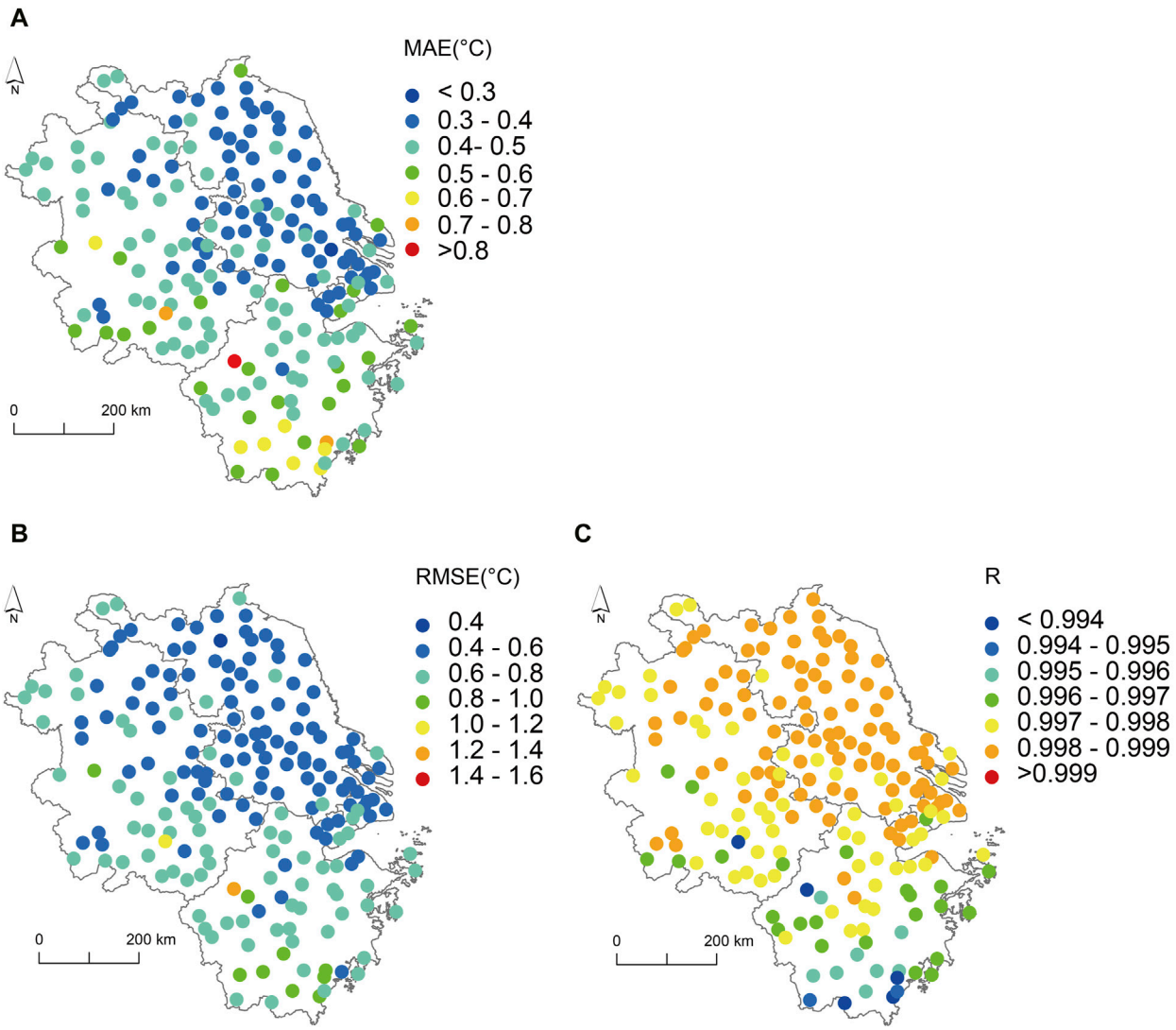

FIGURE 3
Spatial distributions of maximum air temperature estimation accuracy based on random forest: **(A)** MAE, **(B)** RMSE, **(C)** R.

Apparently, the linear relationship of these four scatter plots are close to 1:1 lines and the variation ranges of air temperature are similar. However, the outliers of RF method seems to be least among the other three methods, indicating the relatively higher estimated accuracy. The 10-fold cross-validation accuracies of the 1-km gridded air temperature data estimated using four methods (Figure 2) also demonstrate that the RF model outperforms three other models with highest correlation coefficient, least MAE and RMSE. In addition, the spatial distributions of RF-based estimation also indicate that the results are more reasonable than other three methods (Supplementary Figure S2).

Based on the observations from 199 meteorological stations, the accuracy of the 1-km gridded air temperature data estimated using the RF is assessed, as shown in Figure 3. It can be seen that the MAEs and RMSEs are relatively smaller over the entire study area. Particularly, the MAEs and RMSEs in the majority areas of Jiangsu Province are relatively smaller than in Zhejiang Province. This may be attributed to the uniform underlying surface in Jiangsu Province where most areas are relatively flat plains, which is conducive to improving the accuracy of the RF-based estimation model. While the larger MAEs and RMSEs in the southern part of Zhejiang Province are mainly associated with its complex terrains due to numerous mountain ranges. The R values between the estimations and the observations at all stations in the study area are quite high, with the values exceeding 0.995 at most stations. It indicates a good consistency in the temporal variations of air temperature between the estimations and the observations. Consequently, the 1-km gridded air temperature data derived from RF model proves to be an ideal choice for studying the UHIs.

3.2 Spatial distributions of NSUHII and SUHII

Using the 1-km gridded air temperature data from air temperature estimation and daytime LST data from the 8-day

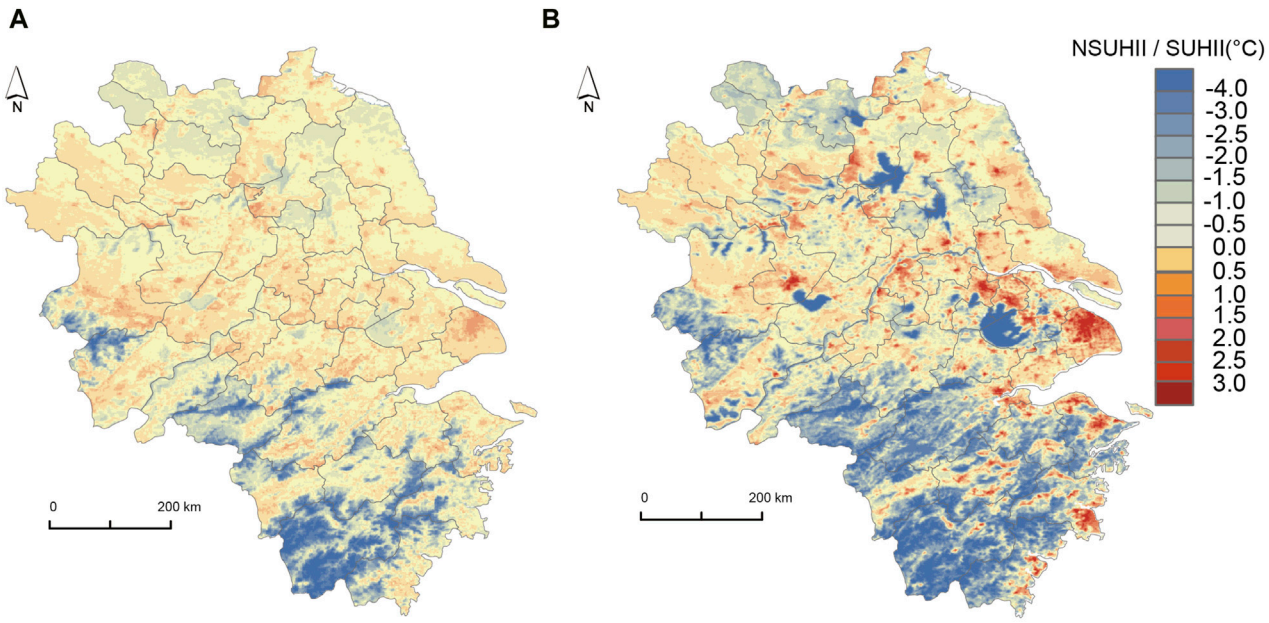

FIGURE 4
Spatial distributions of NSUHII **(A)** and SUHII **(B)** during 2001–2018.

composite (MODIS) LST product, monthly average NSUHII and SUHII can be derived. Figure 4 illustrates the spatial distributions of NSUHII and SUHII in the study area during 2001–2018. In general, both NSUHII and SUHII are rather strong in the study area over the past 20 years, presenting similar spatial distributions. Higher UHI effect are observed over the YRD core cities such as Shanghai, Nanjing, Taizhou, indicating that both the air temperatures and near surface temperatures in these areas are higher than those of farmland background areas. Noticeable cool island effect is found in mountainous areas, demonstrating the relatively lower temperature compared with those of farmland background areas. However, the SUHII exhibits higher intensity and a broader range of both heat and cool island effects than the NSUHII. The highest NSUHII is recorded in Shanghai City, reaching up to 2.8°C while the highest value of SUHII is found in Taizhou City with SUHII value up to 4.8°C. In addition, the cool island effect of surface temperature is more pronounced over water bodies compare with near surface temperature.

Previous studies have demonstrated that the LST and air temperature are both representations of thermal environment, which impact each other through the land-atmosphere interaction. To better understand the relationship between the SUHII and NSUHII, this study calculates the annual mean differences and monthly correlation coefficient (R) between the two. Figure 5A reveals that in most areas, the annual mean SUHII is higher than the annual mean NSUHII, with the major differences ranging from 0°C to 2°C. The instances where the NSUHII is significantly higher than the SUHII (−2~ −6°C) are mainly observed in areas with water bodies as the dominant land cover. The reason may be that the cooling effect of water bodies on the LST is relatively direct and pronounced, while the air temperature above water bodies is regulated by the process of latent heat exchange through evaporation, which is relatively indirect and slow. It is also evident that pixels with the SUHII significantly higher than the NSUHII are mainly located in the central urban areas of the core cities in the YRD region (Shanghai, Wuxi, Hangzhou, etc.). Due to the rapid urbanization in these regions, the impervious surfaces are rapidly expanded, which also leads to a great difference between the SUHII and NSUHII. The largest differences between the two are found in summer, while their values are relatively similar in winter, as shown in Supplementary Figure S3. The seasonal variation is also related to the increase in total radiation in summer. The increase in radiation results in the enhanced radiation absorbed by impervious surfaces, leading to a significant LST increase. However, the increase in radiation has no significant impact on the air temperature increase, thereby causing a larger difference between the two in summer.

Figure 5B displays the spatial distribution of R between annual mean SUHII and NSUHII in the study area from 2001 to 2018. In terms of the R between annual mean SUHII and NSUHII, it is found that the SUHII and NSUHII are positively correlated in most regions, with the R values being rather high ($R > 0.6$). The R values larger than 0.9 are primarily in the southern part of the study area, mainly caused by the higher values in spring (Supplementary Figure S4). In contrast, the R values are smaller ($0 < R < 0.3$) in the core cities of the YRD region, indicating that there is a certain degree of correlation in the temporal variation between the SUHII and NSUHII in this region, but there are still some differences. The correlations are the weakest in winter, while strongest in spring (Supplementary Figure S4). It is attributed to the fact that the atmospheric circulation that affects the energy transfer between the surface and near-surface is relatively weaker in winter, resulting a weaker interaction between SUHII and NSUHII. While in summer, the temperature background field is too dominant, diminishing the influence of LST on air temperature. In contrast, the temperature background field is weaker in spring, and the temperature fluctuations are pronounced, resulting in the strongest values.

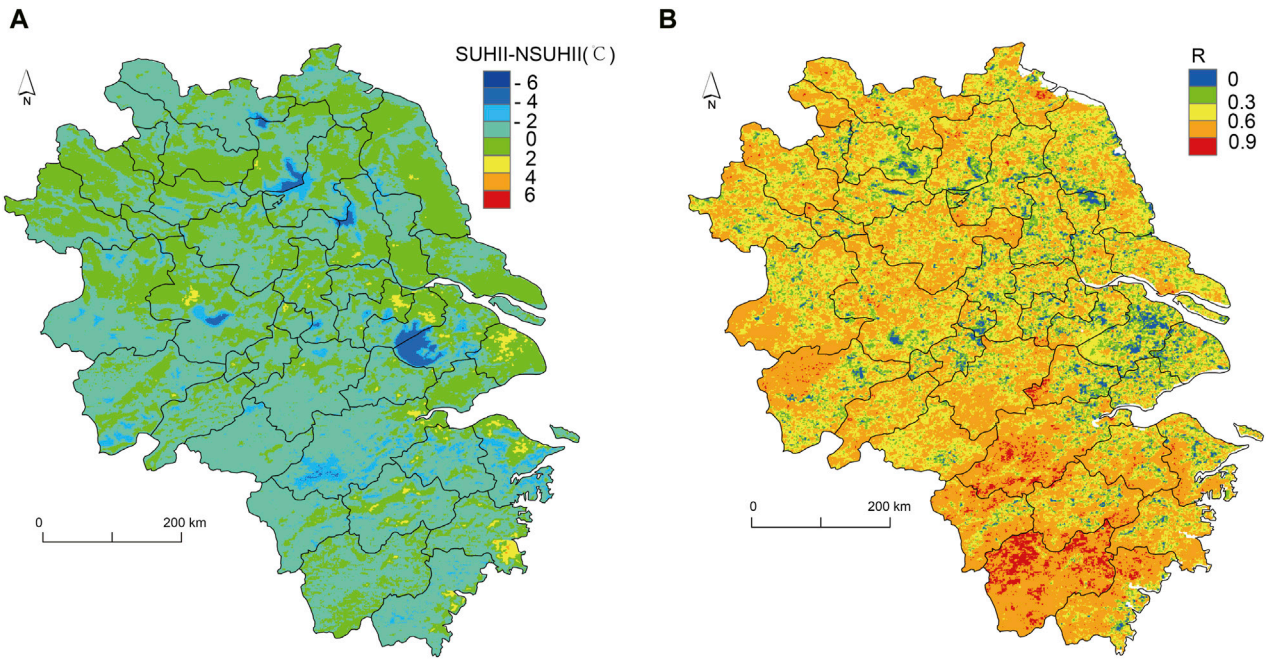

FIGURE 5
(A) Spatial distribution of differences between the annual mean SUHII and NSUHII during 2001–2018. **(B)** Spatial distribution of correlation coefficients between the annual SUHII and NSUHII from 2001 to 2018.

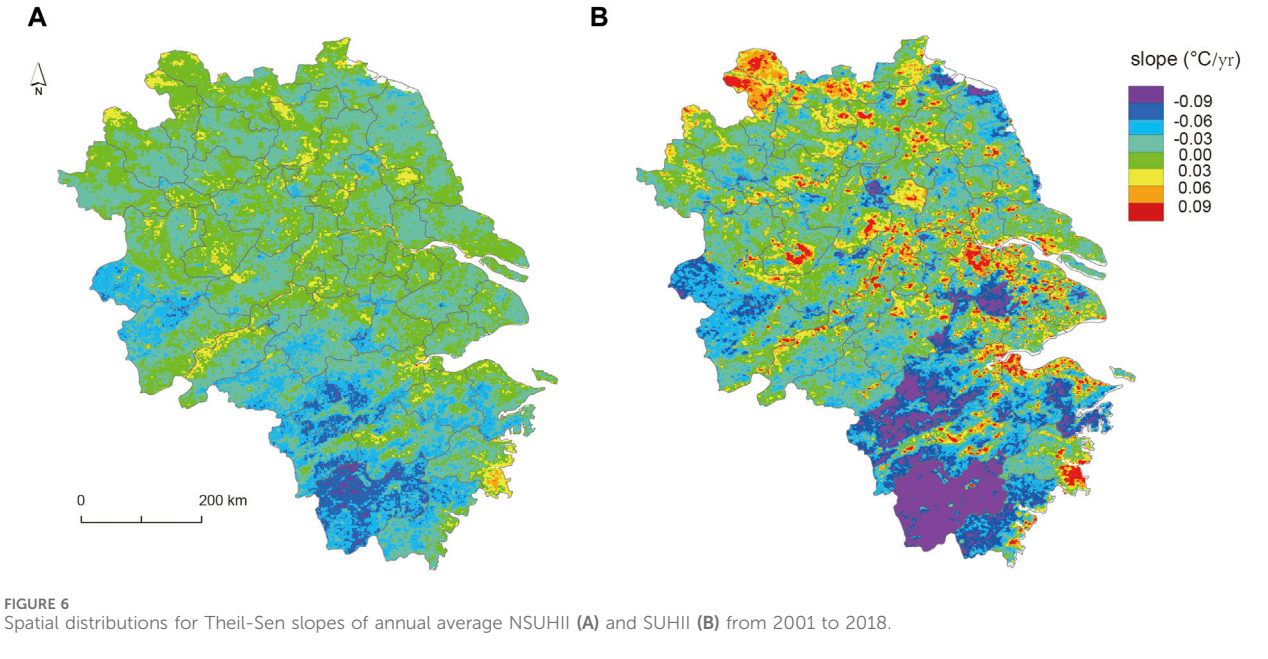

FIGURE 6
Spatial distributions for Theil-Sen slopes of annual average NSUHII **(A)** and SUHII **(B)** from 2001 to 2018.

3.3 Temporal variations in NSUHII and SUHII

To better understand the variation characteristics in the long-term time series of NSUHII and SUHII as well as the differences in between, the Theil-Sen slopes of NSUHII and SUHII during 2001–2018 are calculated in the study area, as shown in Figure 6. Positive (negative) trends indicate that the warming rate of air temperature in pixels is higher (lower) than that of corresponding pixels under agricultural background.

In the study area, the variation trends of NSUHII present an uneven distribution, with most regions showing relatively weak warming trends (0–0.03°C/yr). Specifically, the warming trends in

TABLE 2 Information of three typical urban areas (2023).

City	Urban size	Population (million)	City area (square kilometers)	Urban built-up area (square kilometers)
Shanghai	Mega city	24.7589	6,340	860.2
Wuxi	Super city	7.4908	4,627.47	356
Jiaxing	Type I big city	5.551	3,915	163.42

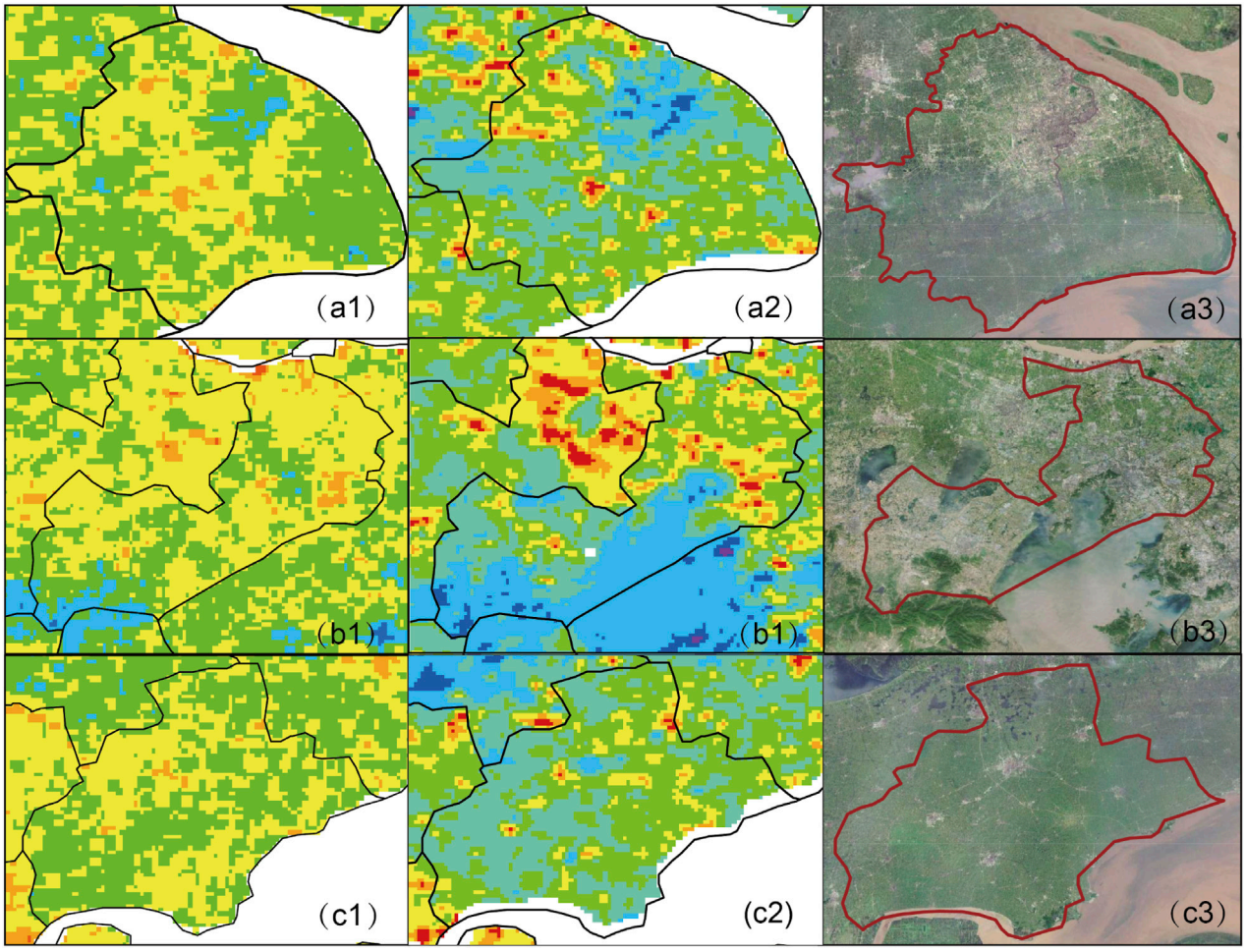

FIGURE 7
Spatial distributions for Theil-Sen slopes of the multi-year average NSUHII **(A1,B1,C1)** and SUHII in typical cities in the YRD region from 2001 to 2018 **(A2,B2,C2)** and corresponding remote sensing images **(A3,B3,C3)**.

most of the northern part are slightly higher than those of farmland background areas. Regions with a rapid increase (0.03–0.09°C/yr) in NSUHII are scatteredly distributed in a few areas of each city. Particularly, the areas with rapid increases (>0.09°C/yr) in NSUHII are mainly located in parts of Chizhou and Taizhou Cities in the central and southern parts of the study area, suggesting that the warming rates in these areas are significantly higher than those of farmland background areas. Areas with a cooling trend are mainly found in mountainous regions, with the trend values exceeding −0.06°C/yr.

Compared with the NSUHII, the urban heat island phenomenon is more pronounced in terms of surface temperature than near-surface temperature. The variation trends of SUHII are more significant in urban, mountainous and aquatic areas, resulting in greater spatial distribution differences. Approximately half of the study area exhibits an increasing trend in UHI effects, regions with increasing trends higher than 0.06°C/yr are mainly located in the northern, middle and part of the southern area. The SUHII with the highest warming trend is found in Hefei City, reaching 0.42°C/yr, while the fastest cooling trend is observed in the Taihu region of Suzhou City, reaching −0.24°C/yr. The large variation trends in the SUHII may be associated with changes in vegetation cover. During 2001–2018, as the urbanization accelerates, some

vegetation is replaced by impervious surface, which in turn accelerates the changes in SUHII.

Concerning the different urban sizes, population levels, city area and urban built-up area (Table 2), three cities-Shanghai, Wuxi and Jiaxing are selected as typical urban areas. The differences between NSUHII and SUHII variations in these three typical areas are further investigated, as shown in Figure 7.

According to the remote sensing images (Figure 7A3), the central urban area of Shanghai City exhibits relatively smaller variation trends of NSUHII (Figure 7A1) and SUIHII (Figure 7A2). Various factors may contribute to this phenomenon, such as the increase in green areas within the central urban area and the reconstruction of old urban districts in mega-cities like Shanghai, leading to a decrease in the warming rate within the central urban area.

For Wuxi City, deviations are observed between the distribution of NSUHII and SUHII. While most areas exhibit a slow warming rate (0.03–0.06°C/yr) in the NSUHII (Figure 7B1), the SUHII (Figure 7B2) in the central urban area shows a significantly larger warming trend (0.06–0.12°C/yr) than the areas outside the central urban region and water bodies. Wuxi City is one of the top 10 cities by gross domestic product in the YRD region, and its central urban area has undergone rapid development over the past 2 decades. The slow warming trend in the NSUHII demonstrating that the urbanization in Wuxi City has not had a significant impact on the NSUHII.

In Jiaxing City, the variation trends of NSUHII (Figure 7C1) and SUHII (Figure 7C2) in the central urban area are comparable to those outside the central urban area, with some regions showing a weak warming trend. This phenomenon may be attributed to the fact that Jiaxing City belongs to Type I large city, which has a smaller population and slower economic development in comparison to mega-cities.

Overall, over the past 2 decades, both near-surface and surface UHI effects in the study area have been developing intensely and exhibit an obvious increase trend. The areas with the largest increase rates are not necessarily the most developed regions but rather the fastest developing ones. The increase rate of near-surface NSUHII is smaller than that of SUHII.

4 Discussion

Generally, most UHI effect is monitored by satellite remote sensing, which spatial distribution and trends have been widely studied on global, regional and city scale. The study of near-surface UHI effect is normally studied using air temperature data from meteorological stations at 2 m above the ground due to the lack of data. In this study, a spatialization method suitable for air temperature in complex and highly urbanized areas is determined. The RF-based estimation method has good accuracy and outperforms three other remote sensing estimation methods. Hence, it serves as an ideal high-resolution air temperature dataset for studying the UHI effects. This method retains the advantages of station observations in terms of temporal resolution and high precision, and makes up for its disadvantage of spatial discontinuity, thereby achieving good gridding effect. Previous studies also use several machine learning methods for air temperature estimation in different places, however, the estimation accuracies were not as good as this study (Yao et al., 2021). For example, (Yang et al., 2023), also used SVM and RF methods in air temperature estimation in China. Though RF and SVM outperform other methods in in Yang's study, MAE and RMSE values for RF (RMSE = 2.01, MAE = 1.36) and SVM (RMSE = 2.33, MAE = 1.58) are still larger than results in this study. With the development of machine learning techniques, new deep learning models such as long short-term memory (LSTM) and XGboost are continually emerging (Reichstein et al., 2019; Amato et al., 2020; Yang et al., 2023). Meanwhile, the dense observation stations and new remote sensing data lay the foundations for further enhancing the accuracy of gridded datasets of air temperature. Therefore, research on near-surface UHI effects based on station observed air temperature should move towards the way of greater precision and refinement (Liu et al., 2021; Bird et al., 2022).

The spatial distributions and temporal variations of near-surface UHIs and surface UHIs are quite consistent. Although the SUHII and NSUHII are closely related, there are still certain differences especially in the rapidly expanding urban areas and in summer. The SUHII is mainly influenced by surface properties, including vegetation cover, reflectance and anthropogenic heat, whereas the NSUHII is influenced not only by surface properties but also by meteorological elements under local climate (Arnfield, 2003; Liu et al., 2020). Previous studies have suggested that both SUHII and NSUHII can be used to characterize human comfort, but the NSUHII is a more accurate representation (Yao et al., 2021). In addition, the continuous increase in thermal environments exerts pressure on human health and energy consumption (Zhang et al., 2023), which thus should be given enough attention. Therefore, more attention should be paid to the study of NSUHII and driving factors so as to find applicable mitigation strategies. Previous studies generally analyzed the NSUHII and SUHII effect based on several meteorological stations to represent the air temperature of the entire urban or rural area (Sun et al., 2020; Hu et al., 2019). However, this kind of comparison may cause great uncertainty considering the location and number of stations.

This study only focuses on the UHI effect with respect to daily maximum air temperature, without considering daily minimum air temperature or nighttime UHI effects. However, numerous studies have shown that there are significant differences between nighttime and daytime UHI effects (Sun et al., 2020). Therefore, relevant research can be conducted on the nighttime UHI effect in the future.

5 Conclusion

In this study, a spatialization method suitable for air temperature in complex and highly urbanized areas is determined. Specifically, the 1-km gridded air temperature data derived from RF method and LST data from the Moderate-resolution Imaging Spectroradiometer are used to analyze the spatial distribution characteristics of NSUHII and SUHII in the YRD region over the past 2 decades. The results show that both the

NSUHII and SUHII are rather strong in the study area over the past 20 years, presenting similar spatial distributions. The situation that the NSUHII is higher than the SUHII with significant differences appears over water bodies, while the situation of SUHII higher than the NSUHII is often found in the core areas of rapidly urbanizing cities in the YRD, and the differences are more prominent in summer. Although there is a certain degree of correlation between the temporal variations of SUHII and NSUHII, some discrepancies still exists. Notably, the R values between them are relatively lower in the core areas of rapidly urbanizing cities in the Yangtze River Delta region, with the lowest in winter. From 2001 to 2018, most areas in the study region witnessed an increase in both NSUHII and SUHII, especially in regions with rapid urbanization. However, the area with the largest increase rate is not necessarily the most developed region but the fastest developed one. In well-developed cities, the increase rates in the central urban areas are lower than those in the surrounding regions.

Data availability statement

The raw data supporting the conclusion of this article will be made available by the authors, without undue reservation.

Author contributions

XS: Writing–original draft, Writing–review and editing. MS: Validation, Visualization, Writing–original draft. XL: Conceptualization, Writing–review and editing.

Funding

The author(s) declare that financial support was received for the research, authorship, and/or publication of this article. This research was funded by Jiangsu Province Marine Science and Technology Innovation Project (JSZRHYKJ202307) and Jiangsu Meteorological Bureau Scientific research project (KM202408 and KZ202303).

Conflict of interest

The authors declare that the research was conducted in the absence of any commercial or financial relationships that could be construed as a potential conflict of interest.

Publisher's note

All claims expressed in this article are solely those of the authors and do not necessarily represent those of their affiliated organizations, or those of the publisher, the editors and the reviewers. Any product that may be evaluated in this article, or claim that may be made by its manufacturer, is not guaranteed or endorsed by the publisher.

Supplementary material

The Supplementary Material for this article can be found online at: https://www.frontiersin.org/articles/10.3389/fenvs.2024.1387672/full#supplementary-material

References

Abbas, W., and Ismael, H. (2020). Assessment of constructing canopy urban heat island temperatures from thermal images: an integrated multi-scale approach. *Sci. Afr.* 10, e00607. doi:10.1016/j.sciaf.2020.e00607

Aliyazıcıoğlu, K., Beker, F., Topaloğlu, R. H., Bilgilioğlu, B. B., and Çömert, R. (2021). Temporal monitoring of land use/land cover change İn Kahramanmaraş City. *Turkish J. Eng.* 5 (3), 134–140. doi:10.31127/tuje.707156

Amato, F., Guignard, F., Robert, S., and Kanevski, M. (2020). A novel framework for spatio-temporal prediction of environmental data using deep learning. *Sci. Rep.* 10 (1), 22243–22311. doi:10.1038/s41598-020-79148-7

Anniballe, R., Bonafoni, S., and Pichierri, M. (2014). Spatial and temporal trends of the surface and air heat island over Milan using MODIS data. *Remote Sens. Environ.* 150, 163–171. doi:10.1016/j.rse.2014.05.005

Arnfield, A. J. (2003). Two decades of urban climate research: a review of turbulence, exchanges of energy and water, and the urban heat island. *Int. J. Climatol.* 23 (1), 1–26. doi:10.1002/joc.859

Bird, D. N., Banzhaf, E., Knopp, J., Wu, W., and Jones, L. (2022). Combining spatial and TemporalData to create a fine-resolution daily urban air temperature product from remote sensing land surface temperature (LST) data. *Atmosphere* 13, 1152. doi:10.3390/atmos13071152

Chen, L., Jiang, R., and Xiang, W. N. (2016). Surface heat island in Shanghai and its relationship with urban development from 1989 to 2013. *Adv. Meteorology* 2016, 1–15. doi:10.1155/2016/9782686

Chen, Y., Liang, S., Ma, H., Li, B., He, T., and Wang, Q. (2021). An all-sky 1 km daily land surface air temperature product over mainland China for 2003-2019 from MODIS and ancillary data. *Earth Syst. Sci. Data* 13, 4241–4261. doi:10.5194/essd-13-4241-2021

Han, J., Liu, J., Liu, L., and Ye, Y. (2020). Spatiotemporal changes in the urban heat island intensity of distinct local climate zones: case study of zhongshan district, dalian, China. *Complexity* 2020, 1–9. doi:10.1155/2020/8820338

Hu, Y., Hou, M., Jia, G., Zhao, C., Zhen, X., and Xu, Y. (2019). Comparison of surface and canopy urban heat islands within megacities of eastern China. *ISPRS Journal of Photogrammetry and Remote Sensing* 156, 160–168.

Hu, Y., Li, H., Amir Siddique, M., and Liu, D. (2023). Assessing the impact of spatiotemporal land cover changes on the urban heat islands in developing cities with landsat data: a case study in zhanjiang. *Atmosphere* 14, 1716. doi:10.3390/atmos14121716

Hua, W. J., and Chen, H. S. (2013). Impacts of regional-scale land use/land cover change on diurnal temperature range. *Adv. Clim. Change Res.* 4, 166–172. doi:10.3724/SP.J.1248.2013.166

Imhoff, M. L., Zhang, P., Wolfe, R. E., and Bounoua, L. (2010). Remote sensing of the urban heat island effect across biomes in the continental USA. *Remote Sens. Environ.* 114, 504–513. doi:10.1016/j.rse.2009.10.008

Jin, X., Jiang, P., Du, H., Chen, D., and Li, M. (2021). Response of local temperature variation to land cover and land use intensity changes in China over the last 30 years. *Clim. Change* 164 (3–4), 34–20. doi:10.1007/s10584-021-02955-y

Krayenhoff, E. S., Moustaoui, M., Broadbent, A. M., Gupta, V., and Georgescu, M. (2018). Diurnal interaction between urban expansion, climate change and adaptation in US cities.*Nat. Clim. Change* 8 (12), 1097, 1103. doi:10.1038/s41558-018-0320-9

Li, X., Zhou, Y., Zhao, M., and Zhao, X. (2020). A harmonized global nighttime light dataset 1992–2018. *Sci. Data* 7 (1), 168–169. doi:10.1038/s41597-020-0510-y

Liu, K., Li, X., Wang, S., and Li, Y. (2020). Investigating the impacts of driving factors on urban heat islands in southern China from 2003 to 2015. *J. Clean. Prod.* 254, 120141. doi:10.1016/j.jclepro.2020.120141

Liu, Y., Xu, Y., Weng, F., Zhang, F., and Shu, W. (2021). Impacts of urban spatial layout and scale on local climate: a case study in Beijing. *Sustain. Cities Soc.* 68 (January), 102767. doi:10.1016/j.scs.2021.102767

Liu, Y. H., Fang, X., Xu, Y., Zhang, S., and Luan, Q. (2017). Assessment of surface urban heat island across China ' s three main urban agglomerations. *Theor. Appl. Climatol.* 133, 473–488. doi:10.1007/s00704-017-2197-3

Lou, D., Shi, X., Ullah, W., Shi, D., Li, C., Chai, Y., et al. (2023). Long-term changes in observed soil temperature over Poyang Lake Basin, China, during 1960–2016. *Theor. Appl. Climatol.* 154, 717–731. doi:10.1007/s00704-023-04522-0

Lu, W., Zhang, D., Ren, Q., Qi, T., and He, C. (2023). Impacts of future urban expansion on natural habitats will intensify in China: scenario analysis with the improved LUSD-urban model. *Landsc. Ecol.* 38, 2547–2567. doi:10.1007/s10980-023-01740-9

Luo, F., Yang, Y., Zong, L., and Bi, X. (2023). The interactions between urban heat island and heat waves amplify urban warming in Guangzhou, China: roles of urban ventilation and local climate zones. *Front. Environ. Sci.* 11, 1084473. doi:10.3389/fenvs.2023.1084473

Manley, G. (1959). On the frequency of snowfall in metropolitan England. *Q. J. R. Meteorological Soc.* 84, 70–72. doi:10.1002/qj.49708435910

Meng, F., Yan, S., Tian, G., and Wang, Y. (2023). Surface urban heat island effect and its spatiotemporal dynamics in metropolitan area: a case study in the Zhengzhou metropolitan area, China. *Front. Environ. Sci.* 11, 1247046. doi:10.3389/fenvs.2023.1247046

Morsy, S., and Hadi, M. (2022). Impact of land use/land cover on land surface temperature and its relationship with spectral indices in Dakahlia Governorate, Egypt. *Int. J. Eng. Geosciences* 7 (3), 272–282. doi:10.26833/ijeg.978961

Nanayakkara, S., Wang, W., Cao, J., Wang, J., and Zhou, W. (2023). Analysis of urban heat island effect, HeatStress and public health in colombo,Sri Lanka and shenzhen, China. *Atmosphere* 14, 839. doi:10.3390/atmos14050839

Niu, L., Tang, R., Jiang, Y., and Zhou, X. (2020). Spatiotemporal patterns and drivers of the surface urban heat island in 36 major cities in China: a comparison of two different methods for delineating rural areas. *Sustainability* 12, 478. doi:10.3390/su12020478

Oke, T. R. (1982). The energetic basis of the urban heat island. *Q. J. R. Meteorological Soc.* 108 (455), 1–24. doi:10.1002/qj.49710845502

Parry, M., and Chandler, T. J. (1966). The climate of london. *Geogr. Journa* 132 (1), 84. doi:10.2307/1793062

Peng, J., Xie, P., Liu, Y., and Ma, J. (2016). Urban thermal environment dynamics and associated landscape pattern factors: a case study in the Beijing metropolitan region. *Remote Sens. Environ.* 173, 145–155. doi:10.1016/j.rse.2015.11.027

Ramakreshnan, L., Aghamohammadi, N., Fong, C. S., Ghaffarianhoseini, A., Wong, L. P., and Sulaiman, N. M. (2019). Empirical study on temporal variations of canopy-level Urban Heat Island effect in the tropical city of Greater Kuala Lumpur. *Sustain. Cities Soc.* 44 (November 2018), 748–762. doi:10.1016/j.scs.2018.10.039

Reichstein, M., Camps-Valls, G., Stevens, B., Jung, M., Denzler, J., Carvalhais, N., et al. (2019). Deep learning and process understanding for data-driven Earth system science. *Nature* 566 (7743), 195–204. doi:10.1038/s41586-019-0912-1

Sen, P. K. (1968). Estimates of the regression coefficient based on kendall's tau. *J. Am. Stat. Assoc.* 63 (324), 1379–1389. doi:10.1080/01621459.1968.10480934

Shahmohamadi, P., Che-Ani, A. I., Maulud, K. N. A., Tawil, N. M., and Abdullah, N. A. G. (2011). The impact of anthropogenic heat on formation of urban heat island and energy consumption balance. *Urban Stud. Res.* 2011, 1–9. doi:10.1155/2011/497524

Shi, T., Liu, L., Wen, X., and Qi, P. (2024). Research progress on the synergies between heat waves and canopy urban heat island and their driving factors. *Front. Environ. Sci.* 12, 1363837. doi:10.3389/fenvs.2024.1363837

Shi, X., Xu, Y., Wang, G., Liu, Y., Wei, X., and Hu, X. (2021). Spatiotemporal variations in the urban heat islands across the coastal cities in the Yangtze River Delta, China. *Mar. Geod.* 44 (5), 467–484. doi:10.1080/01490419.2021.1897716

Su, Z., De Rosnay, P., Wen, J., Wang, L., and Zeng, Y. (2013). Evaluation of ECMWF's soil moisture analyses using observations on the Tibetan Plateau. *J. Geophys. Res. Atmos.* 118 (11), 5304–5318. doi:10.1002/jgrd.50468

Sun, T., Sun, R., and Chen, L. (2020). The trend inconsistency between land surface temperature and near surface air temperature in assessing Urban heat island effects. *Remote Sens.* 12 (8), 1271. doi:10.3390/RS12081271

Sun, Y., Gao, C., Li, J., Wang, R., and Liu, J. (2019). Evaluating urban heat island intensity and its associated determinants of towns and cities continuum in the Yangtze River Delta Urban Agglomerations. *Sustain. Cities Soc.* 50 (January), 101659. doi:10.1016/j.scs.2019.101659

Svilicic, P., Vucetic, V., Filic, S., and Smolic, A. (2016). Soil temperature regime and vulnerability due to extreme soil temperatures in Croatia. *Theor. Appl. Climatol.* 126, 247–263. doi:10.1007/s00704-015-1558-z

Topaloglu, R. H. (2022). Investigation of Land Use/Land Cover change in Mersin using geographical object-based image analysis (GEOBIA). *Adv. Remote Sens.* 2 (2), 40–46. Available at: https://publish.mersin.edu.tr/index.php/arsej/article/view/247.

Wang, H., Yue, C., and Luyssaert, S. (2023). Reconciling different approaches to quantifying land surface temperature impacts of afforestation using satellite observations. *Biogeosciences* 20, 75–92. doi:10.5194/bg-20-75-2023

Wang, J., Qingming, Z., Guo, H., and Jin, Z. (2016). Characterizing the spatial dynamics of land surface temperature–impervious surface fraction relationship. *Int. J. Appl. Earth Observation Geoinformation* 45, 55–65. doi:10.1016/j.jag.2015.11.006

Wang, Z., Meng, Q., Allam, M., Hu, D., Zhang, L., and Menenti, M. (2021). Environmental and anthropogenic drivers of surface urban heat island intensity: a case-study in the Yangtze River Delta, China. *Ecol. Indic.* 128, 107845. doi:10.1016/j.ecolind.2021.107845

Xiong, J., Thenkabail, P. S., Gumma, M. K., Teluguntla, P., Poehnelt, J., Congalton, R. G., et al. (2017). Automated cropland mapping of continental Africa using Google Earth Engine cloud computing. *ISPRS J. Photogrammetry Remote Sens.* 126, 225–244. doi:10.1016/j.isprsjprs.2017.01.019

Yang, C., Yan, F., and Zhang, S. (2020). Comparison of land surface and air temperatures for quantifying summer and winter urban heat island in a snow climate city. *J. Environ. Manag.* 265 (March), 110563. doi:10.1016/j.jenvman.2020.110563

Yang, D., Zhong, S., Mei, X., Ye, X., Niu, F., and Zhong, W. (2023). A comparative study of several popular models for near-land surface air temperature estimation. *Remote Sens.* 15 (4), 1136. doi:10.3390/rs15041136

Yang, J., and Huang, X. (2021). The 30 m annual land cover dataset and its dynamics in China from 1990 to 2019. *Earth Syst. Sci. Data* 13 (8), 3907–3925. doi:10.5194/essd-13-3907-2021

Yang, Y., and Pan, P. (2011). Research on the impact of impervious surface area on urban heat island in Jiangsu Province. *Int. Symposium Lidar Radar Mapp. 2011 Technol. Appl.* 8286, 82861P. doi:10.1117/12.912517

Yao, L., Sun, S., Song, C., Li, J., Xu, W., and Xu, Y. (2021a). Understanding the spatiotemporal pattern of the urban heat island footprint in the context of urbanization, a case study in Beijing, China. *Appl. Geogr.* 133 (June), 102496. doi:10.1016/j.apgeog.2021.102496

Yao, R., Wang, L., Huang, X., Li, L., Sun, J., Wu, X., et al. (2020). Developing a temporally accurate air temperature dataset for Mainland China. *Sci. Total Environ.* 706, 136037. doi:10.1016/j.scitotenv.2019.136037

Yao, R., Wang, L., Huang, X., Liu, Y., Niu, Z., Wang, S., et al. (2021b). Long-term trends of surface and canopy layer urban heat island intensity in 272 cities in the mainland of China. *Sci. Total Environ.* 772, 145607. doi:10.1016/j.scitotenv.2021.145607

Yao, R., Wang, L., Huang, X., Zhang, W., Li, J., and Niu, Z. (2018). Interannual variations in surface urban heat island intensity and associated drivers in China. *J. Environ. Manag.* 222, 86–94. doi:10.1016/j.jenvman.2018.05.024

Zeng, Y., Qiu, X. F., and Liu, S. M. (2005). Distributed modeling of extraterrestrial solar radiation over rugged terrains. *Chin. J .Geophys Chin.* 48 (5), 1028–1033.

Zhang, J., Tu, L., and Shi, B. (2023a). Spatiotemporal patterns of the application of surface urban heat island intensity calculation methods. *Atmosphere* 14, 1580. doi:10.3390/atmos14101580

Zhang, Y., Cai, H., Zhu, T., Guo, X., Zeng, J., and Huang, L. (2023b). Impact of land use changes on the land surface thermal environment in Nanchang, Jiangxi province, China. *Front. Environ. Sci.* 11, 1227682. doi:10.3389/fenvs.2023.1227682

Frontiers in
Environmental Science

Explores the anthropogenic impact on our natural world

An innovative journal that advances knowledge of the natural world and its intersections with human society. It supports the formulation of policies that lead to a more inhabitable and sustainable world.

Discover the latest Research Topics

See more →

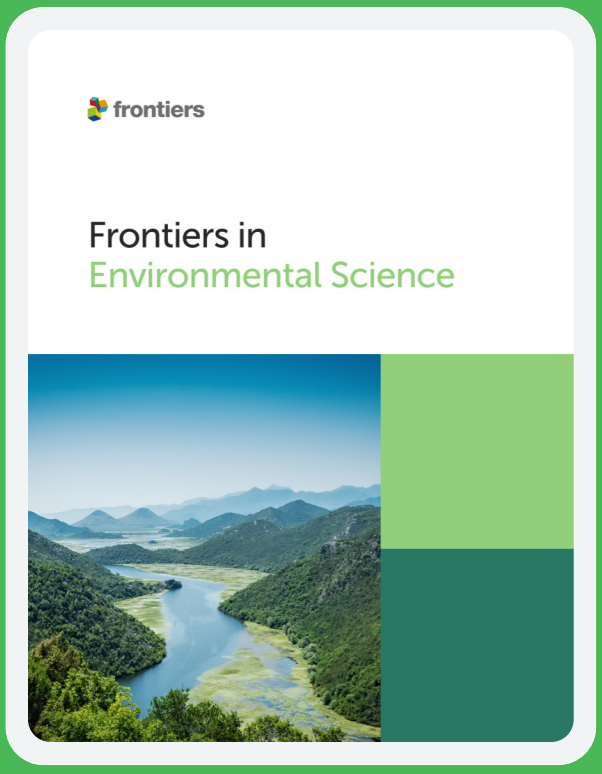

Frontiers

Avenue du Tribunal-Fédéral 34
1005 Lausanne, Switzerland
frontiersin.org

Contact us

+41 (0)21 510 17 00
frontiersin.org/about/contact